LEVERAGING NATURAL DYNAMICAL STRUCTURES TO EXPLORE MULTI-BODY SYSTEMS

A Dissertation

Submitted to the Faculty

of

Purdue University

by

Natasha Bosanac

In Partial Fulfillment of the

Requirements for the Degree

of

Doctor of Philosophy

August 2016

Purdue University

West Lafayette, Indiana

ACKNOWLEDGMENTS

First and foremost, I would like to express gratitude towards my family for their endless support. Mum, none of this would have been possible without everything you have done for me over the years. Along this journey, you have listened to me, encouraged me, stood up for me, advised me and welcomed me home to defrost every winter. More importantly, you raised me to have the strength and courage to follow my dreams (despite the many obstacles) and supported the decisions I have made along the way, even when they took me to the other side of the world. For these things and many more, I am continually grateful.

Next, I have an incredible appreciation for my advisor, Professor Kathleen C. Howell. Working with you has changed me: you have taught me so much about astrodynamics, research and education; continually challenged and supported me; provided me with many new and exciting opportunities as well as the freedom to pursue my interests; patiently edited countless pages of my writing; trusted me with increasing responsibilities; and have gone above and beyond in helping to prepare me for my future in academia. I am endlessly grateful for everything you have done for me, and have thoroughly enjoyed these last several years.

I would also like to acknowledge Professor Ephraim Fischbach in the Physics department. Given his experience with many-body forces in nuclear physics, he first presented the idea of studying orbital dynamics under the influence of a three-body interaction to Professor Howell and me. It feels like yesterday that the three of us sat down and you drew a triangle to explain this force. A seemingly simple question turned into such an interesting and challenging problem that has benefited from our inherently interdisciplinary approach. I have thoroughly enjoyed working with you and appreciate all the knowledge you have shared about academia along the way.

Through my work on spacecraft trajectory design over the last few years via the development of an orbit catalog and, more recently, the construction of a trajectory design framework, I have had the privilege of working with Dave Folta at NASA Goddard Space Flight Center. Thank you for answering my many questions, teaching me about the practical aspects of spacecraft trajectory design, the many interesting discussions last summer, and enabling a number of exciting opportunities. It has been an absolute pleasure working with you.

In addition, I would like to thank my committee members, Professor Longuski and Professor Minton for their interesting questions and feedback. Past and present members of the research group also deserve recognition. Even though we come from so many different places and backgrounds, the collaborative atmosphere within our research group fosters unique and interesting conversations. I am also appreciative to the close friends I have made during my time at Purdue: for your friendship, support and for always keeping me laughing.

Finally, I would like to thank the Computational Science and Engineering program for providing me with a Lynn Fellowship and the Department of Aeronautics and Astronautics for subsequently supporting me with teaching and research assistantships. In addition, I am grateful to the Zonta International Amelia Earhart Fellowship, as well as NASA grants NNX13AM17G and NNX13AH02G which supported my research in spacecraft trajectory design within the Earth-Moon system. This dissertation would not have been possible without their generosity, and I am grateful to each of them.

TABLE OF CONTENTS

Page

Page

LIST OF FIGURES

Figure Page

Figure Page

Figure Page

Figure Page

ABSTRACT

Bosanac, Natasha Ph.D., Purdue University, August 2016. Leveraging Natural Dynamical Structures to Explore Multi-Body Systems. Major Professor: Kathleen C. Howell.

Multi-body systems have become the target of an increasing number of mission concepts and observations, supplying further information about the composition, origin and dynamical environment of bodies within the solar system and beyond. In many of these scenarios, identification and characterization of the particular solutions that exist in a circular restricted three-body model is valuable. This insight into the underlying natural dynamical structures is achieved via the application of dynamical systems techniques. One application of such analysis is trajectory design for CubeSats, which are intended to explore cislunar space and other planetary systems. These increasingly complex mission objectives necessitate innovative trajectory design strategies for spacecraft within our solar system, as well as the capability for rapid and well-informed redesign. Accordingly, a trajectory design framework is constructed using dynamical systems techniques and demonstrated for the Lunar IceCube mission. An additional application explored in this investigation involves the motion of an exoplanet near a binary star system. Due to the strong gravitational field near a binary star, physicists have previously leveraged these systems as testbeds for examining the validity of gravitational and relativistic theories. In this investigation, a preliminary analysis into the effect of an additional three-body interaction on the dynamical environment near a large mass ratio binary system is conducted. As demonstrated through both of these sample applications, identification and characterization of the natural particular solutions that exist within a multi-body system supports a well-informed and guided analysis.

1. INTRODUCTION

With recent scientific interest into the composition, origin and dynamical environment of bodies both within the solar system and beyond, multi-body systems have become the target of an increasing number of mission concepts and observations. In many of these scenarios, a foundational understanding of the available natural dynamical structures is valuable. For instance, the potential for asteroids to be gravitationally mapped or mined in-orbit for resources has motivated the development of various mission scenarios [1]. Among the expansive array of asteroids that have been observed and catalogued, approximately 16% are members of binary or triple systems, providing a variety of potential targets for both large and small spacecraft [2]. Small satellites, which have advanced significantly with the emergence of CubeSats, are also intended to explore cislunar space and other planetary systems [3], [4]. CubeSats typically possess a small propulsive capability and, as secondary payloads, are subject to significant uncertainty in their deployment state. As a result, a foundational understanding of the natural dynamical structures that are available within the nonlinear and chaotic environment of multi-body systems enables the design of complex paths for spacecraft within our solar system, as well as rapid and well-informed redesign. Similar knowledge of the natural underlying dynamical structures within multi-body systems is also useful in binary star systems. In fact, with improved observational capabilities and techniques, an increasing number of exoplanets have been discovered to orbit in binary star systems, comprised of stars at various stages of their lifetime [5]. Observational data is often used to predict the orbits and masses of these companion bodies which follow natural motions that exist within the chaotic and nonlinear dynamical environment of a binary system [6]. This orbital information may also be useful to predict the bounds on the strength of any additional force

contributions. In each of these scenarios, identification and characterization of the underlying dynamical structures in a binary system is warranted.

An exploration of the natural dynamics that are available within a multi-body system is enabled by the computation and analysis of particular solutions within a simplified dynamical model. Consider the examples of an exoplanet within a binary star system or a spacecraft within the Earth-Moon system. In these scenarios, the two primary bodies (e.g., the two stars or the Earth and Moon) can be modeled as point masses traveling along circular orbits around their mutual barycenter. For systems in which these assumptions are approximately valid, the Circular Restricted Three-Body Problem (CR3BP) provides a reasonable prediction of the possible motions for an infinitesimally small body (e.g., an exoplanet or a spacecraft) near the two primaries. Although this autonomous dynamical model is nonlinear and chaotic, four types of steady-state solutions exist when viewed from a frame that rotates with the two primaries: equilibrium points, periodic orbits, quasi-periodic trajectories and chaotic paths. Analysis of each of these types of motion provides significant insight into the underlying dynamical structures within a multi-body system. For instance, equilibrium points, which represent constant solutions to the differential equations, possess manifolds that impact the existence and characteristics of trajectories within various regions of the phase space. A periodic orbit, however, is a time-varying solution that is characterized by repeating motion. Since the CR3BP is autonomous and conservative, these periodic orbits exist within continuous families that form an underlying structure: a stable orbit attracts or bounds nearby motion, while trajectories near an unstable orbit depart its vicinity. In fact, identifying periodic orbits and evaluating their stability delivers significant insight into the dynamics within a multi-body system. For instance, stable periodic orbits possess a center manifold that is comprised of families of quasi-periodic trajectories that are bounded and trace out the surface of a torus. In contrast to these bounded particular solutions, chaotic motion associated with a multi-body gravitational environment enables natural transport between various regions of the phase space. Together, these four types of solutions are

useful in a variety of scenarios, including the identification of potential motions of an exoplanet within a binary star system, the characterization of modified dynamical fields and the construction of a trajectory design framework for a small spacecraft.

Knowledge of the underlying dynamical structures enables a preliminary analysis into the impact of an additional autonomous force contribution on the dynamical environment near a binary system. Given the absence of experimental data gathered within the vicinity of a binary star, for example, it is possible that the dynamical field within this system might not be accurately modeled solely using pairwise gravitational forces. In this investigation, the presence of an additional three-body interaction is considered. Many-body forces are not an entirely new concept; the importance of three-body interactions in accurately modeling force fields on the atomic scale is well established in nuclear physics [7]. On a much larger scale, the motion of a small body orbiting a binary system serves as a new and interesting application for examining the characteristics of a three-body interaction in orbital dynamics [8], [9], [10].

To explore the effect of a three-body interaction, periodic motions in the vicinity of a large mass ratio binary system are first examined within the context of the CR3BP and, then, in an extended model labeled the Modified Circular Restricted Three-Body Problem (MCR3BP) [8]. In a binary system, the paths followed by comparatively small bodies are influenced by periodic orbits, which contribute to an underlying structure by attracting, bounding or repelling trajectories in their vicinity. The identification of stable orbits near a binary star system, for instance, may aid in modeling exoplanet motion that persists over a long time interval. Unstable orbits, however, could be exploited in a preliminary analysis of matter ejected from or captured by the system. Stability analysis can be employed to identify suitable periodic orbits in each of these sample applications. Furthermore, the evolution of stability along a family of orbits also supports locating bifurcations, indicating structural changes or the formation of new families. In this investigation, an assessment of the evolution of periodic orbits enables the identification of any key signatures identifying a three-body interaction, which may result in a unique effect on the potential motions of an exoplanet.

To visualize the stability across a given family of orbits, at various values of the natural parameters of the system, a two-dimensional representation is constructed in this investigation for various families in the vicinity of the binary [11]. Structural changes are identified and analyzed in both the CR3BP and the MCR3BP, supplemented by the application of dynamical systems theory. Changes in the physical configuration of periodic orbits along a family, identified via these stability representations, are then explored using discrete variational mechanics [10]. This mathematical technique is numerically applied to the search for values of the system parameters that correspond to the existence of a natural trajectory resembling a given reference path. A comparison between the geometries of the computed and reference orbits is then conducted to aid in identifying and exploring potential effects of an additional autonomous force contribution that does not mimic the behavior in response to varying the energy constant or the mass ratio of the binary.

By leveraging natural structures that exist in a simplified, autonomous dynamical model, a rapid and well-informed process for constructing a trajectory for a low-thrust enabled small spacecraft is also developed. As an example application, consider Lunar IceCube, a CubeSat mission that is designed to detect and observe water and other volatiles near the lunar poles. These observations are required to occur from an elliptical and highly inclined orbit around the Moon. Currently, Lunar IceCube is scheduled for launch as a secondary payload onboard the upcoming Exploration Mission-1 vehicle. Following deployment, the spacecraft is placed on a highly energetic path that naturally departs the Earth-Moon system. However, as demonstrated via existing point solutions, the onboard low-thrust engine can be successfully leveraged, along with exploitation of the multi-body gravitational environment, to deliver the spacecraft to the final science orbit [12]. As the deployment conditions and spacecraft hardware parameters evolve, a strategy for rapid exploration of the trajectory design space is warranted.

Techniques from dynamical systems theory support the construction of a framework for designing complex paths for a CubeSat with limited propulsive capability

and constrained departure conditions [12]. In particular, Poincaré mapping strategies are employed in a circular restricted model of the Sun-Earth system to predict the availability and geometry of natural solutions that connect the deployment state to captured motion around the Moon. Insight from particular solutions that exist within a simplified natural gravitational environment supports the prediction of bounds on the motion. The developed trajectory design framework enables the construction of an initial guess prior to corrections in a low-thrust-enabled point mass ephemeris model. The resulting continuous trajectory provides a starting point for subsequent corrections in an operational-level modeling environment and, potentially, optimization. This capability to rapidly design an intricate path for a small spacecraft enables redesign as the deployment information and spacecraft hardware parameters are updated throughout the development and operational phases of the mission. Furthermore, a dynamical systems approach supports the exploration of the complex trajectory design space within a chaotic multi-body dynamical environment [13].

1.1 Previous Contributions

1.1.1 Dynamical Model

The CR3BP is leveraged in this investigation due to the extensive set of tools and techniques that have been developed to construct and visualize a solution for an assumed massless body. The configuration for the restricted three-body problem was first introduced by Leonhard Euler in 1772 in his second lunar theory [14]. In this work, Euler formulated the model with respect to a rotating coordinate system and demonstrated the existence of the collinear equilibrium points. During the same year, Joseph Louis Lagrange determined the location of the equilateral equilibrium points. Later, in 1836, Carl Gustav Jacob Jacobi contributed to the development of the CR3BP through the proposal of a single integral of the motion, labeled the Jacobi constant [15]. George Hill then used this knowledge in 1878 to prove the existence of

the zero velocity curves that bound regions of allowable motion for a comparatively small, third body [16].

Significant contributions to the identification and visualization of particular solutions in the CR3BP originated with Henri Poincaré who conceived the basic foundational concept for the Poincaré map, also labeled the first return map, in 1881 [14]. This invaluable tool yields a lower-dimensional representation of the dynamics in a continuous-time system. With this work as a foundation, Poincaré explored the influence of particular solutions (including periodic and quasi-periodic orbits) on the dynamics in their vicinity, also identifying the presence of chaotic motion in the CR3BP. He published his preliminary findings in 1899 in *Les Méthodes Nouvelles de la Mécanique Céleste* [17]. The contributions of Poincaré have served as a framework for the development of the tools used today in dynamical systems theory.

1.1.2 Visualization of the Stability Evolution of Periodic Orbits

Stability analysis of families of periodic orbits has been widely employed in recent years in astrodynamics to supplement the exploration of the dynamical environment near binary systems. Such analysis has been applied to various systems over the last several decades: from the Sun-planet systems commonly examined within the solar system, to nearly equal mass binaries. The linear stability of orbits at selected values of the mass ratio has been used extensively in the CR3BP to predict the sensitivity to perturbations for various purposes, such as characterizing orbits, detecting the existence of manifolds and for locating bifurcations [18], [19], [20], [21], [22]. Recent work by Folta, Bosanac, Guzzetti and Howell has demonstrated the use of the stability index, among other characteristic parameters, to aid in the construction of an interactive catalog of periodic orbits in the Earth-Moon system for mission design applications [13], [23]. By analyzing the stability index across various families, further insight into the dynamics near a periodic orbit may emerge: instability indicates that manifolds may be used to reduce the cost of transfers into a given periodic or-

bit, while stability suggests that nearby quasi-periodic solutions exist and may be exploited, potentially reducing the cost and difficulty of stationkeeping relative to an exact periodic orbit. Another example involves work by Lara, Russell and Villac, examining the stability evolution of several well-known simply periodic orbits in the Jupiter-Europa system to locate orbits that may provide long-term stability [24]. Orbits that are linearly stable in the CR3BP may retain characteristics of boundedness in an ephemeris model, a property that is favorable in the design of missions to Europa. In this analysis, Lara, Russell and Villac fix the value of μ and analyze the stability index as a function of the Jacobi constant. However, analysis of the stability evolution along a family at a single value of the mass ratio may not reveal any sensitivities to uncertainty in the value of the mass ratio. Lara and Russell investigate the effect of the mass ratio on the evolution of a prograde family of orbits near the smaller primary [25]. At several distinct values of the mass ratio, separate plots of the stability evolution of the selected family are depicted. Lara and Russell note the occurrence of structural changes along the family as the value of μ is varied. These structural changes are often indicated by a change in the shape of the stability curves. However, plotting the stability curve on separate diagrams for a large number of mass ratios can be cumbersome and difficult to visualize.

To visualize the stability across a given family of orbits at various mass ratios, a two-dimensional representation, similar to an exclusion plot, is introduced. Exclusion plots are often used in physics to depict constraints on combinations of parameters. This concept is extended to represent the stability of periodic orbits in the vicinity of binary systems as a natural parameter of the system is varied. The figures constructed in this investigation resemble Benest's original stability diagrams, but with significant modifications [26], [27], [28], [29]. Benest constructs stability representations as a linear function of the mass ratio and a configuration space variable at a fixed point along the orbit. Stability is qualitatively indicated for orbits along the family and minimum and maximum stability indices are located within the two-parameter space.

These plots facilitate a straightforward visualization of the stability evolution along the family and the identification of any structural changes that may occur.

1.1.3 Discrete Variational Mechanics

Discrete variational mechanics is leveraged in this investigation for orbit computation. As opposed to collocation or a multiple-shooting method, which require the continuous dynamics of a system be exactly satisfied at a discrete set of nodes or along multiple trajectory arcs, the discrete variational methodology begins with a discretization of the action integral [30]. Developed primarily for the purpose of optimal control, discrete variational principles rely on the definition of a discrete action and derivation of the discrete Euler-Lagrange equations [31], [32]. A discrete version of Hamilton's principle, which involves the variation of the discrete action summation only at a finite set of nodes along a discretized path, is used to constrain the motion within a dynamical system [31]. Numerical implementation of this concept via a constrained optimization problem was first proposed by Junge, Marsden and Ober-Blöbaum [33]. This method does not require integration, and may alleviate the effect of numerical sensitivities induced by a poor initial guess.

Discrete variational mechanics has been employed in a variety of applications both within astrodynamics and other disciplines. The most common use of discrete variational mechanics is in the construction of variational integrators, often used to compute the paths followed by mechanical systems. For conservative systems, these integrators possess the favorable properties of symplecticity and momentum-preservation, as well as often exhibiting good behavior in the evolution of the system energy [31], [34]. Rather than formulating a variational integrator, discrete variational principles can be employed to construct a constrained optimization problem where the discrete Euler-Lagrange equations provide a set of constraints that enforces the system dynamics. In the context of astrodynamics, this concept has been applied to various scenarios and models. For instance, Ober-Blöbaum, Junge and Marsden have

used discrete variational mechanics to construct a low-thrust transfer in a two-body problem [30]. In addition, Ober-Blöbaum has used discrete variational mechanics to model the configuration of multiple spacecraft in formation-flying problems in the CR3BP [35]. Other work has involved the low-thrust control of spacecraft in the Sun-Earth system using multi-objective optimization [36], [37]. In the context of more complex models, Moore has applied discrete variational mechanics to the computation of low-thrust transfers in a four-body problem, constructed using manifolds and orbits from two patched three-body problems [34]. Each of these sample applications involves using discrete variational mechanics to compute controlled paths. However, in this investigation, these concepts are applied to the calculation of natural periodic orbits.

1.1.4 Many-Body Force

The modeling of a three-body interaction within the context of orbital dynamics is inspired by analogous electromagnetic interactions in quantum physics. In 1948, Richard P. Feynman introduced Feynman diagrams. In nuclear physics, these graphical representations have been used to illustrate the possible combinations of interactions within a system of multiple particles [38]. Each configuration can be analyzed to recover certain properties of the system, including the potential function. For a sample system of two electrically-charged particles, Coulomb's inverse square law is recovered by modeling pairwise exchanges of photons [39].

If more than two particles are considered, many-body interactions may also be postulated using Feynman diagrams. The resulting hypotheses have led to the explanation of physically observable phenemona in nuclear physics. One example is the inconsistency between the observed half life of Carbon-14 and the half-life computed using a two-body force model [40]. In this scenario, three-body forces contribute significantly to an otherwise underestimated quantity.

Analogously, the gravitational interactions in an orbital dynamics problem may also be modeled using Feynman diagrams. Representation of the possible interactions between three masses, such as those within a binary star system with a smaller companion, leads to the proposal of three-body interactions added to the inverse-square gravity force proposed by Sir Isaac Newton in 1687 in *Philosophiae Naturalis Principia Mathematica*. Using an appropriately constructed Feynman diagram, this additional potential contribution may be initially modeled as proportional to the product of the distances between the three bodies.

1.2 Thesis Overview

This study is organized as follows:

- Chapter 2: The dynamical model for natural motion of an infinitesimally small body within a binary system is formulated using the circular restricted three-body problem. Following the derivation of the equations of motion, the integral of motion known as the Jacobi constant is identified. Particular solutions, in the form of equilibrium points and zero velocity curves, are explored and developed within the context of the circular restricted three-body problem as an indicator of the bounds on the motion.

- Chapter 3: Particular solutions in the form of continuous families of periodic and quasi-periodic trajectories are defined and associated computational techniques are summarized. For periodic orbits, stability is defined using the state transition matrix. As a natural parameter is varied along a family of orbits, qualitative changes in the stability correspond to the occurrence of a bifurcation, signaling a change in the nearby dynamics. These periodic orbits are computed via a differential corrections algorithm based on a multiple-shooting scheme as well as pseudo-arclength continuation. Quasi-periodic motion is then defined and computed using a method that leverages an invariance condition. Associated with these bounded dynamical structures are manifolds: for orbits that

possess stable and unstable modes, these manifold structures are exploited to describe both the flow in various regions of the phase space, and the formation and existence of families of periodic orbits

- Chapter 4: To visualize the stability evolution across a family of periodic orbits as the relative masses of the two primaries comprising a binary system are varied, a two-dimensional composite stability representation is constructed. These plots leverage a qualitative measure of the orbital stability, represented via various colors. In this section, stability plots are constructed for the following simply-periodic families in the restricted problem at large mass ratios: distant retrograde orbits about the larger primary; distant and low prograde orbits about the larger primary; retrograde orbits that encircle both primaries; and Lyapunov orbits about a collinear equilibrium point.

- Chapter 5: A discrete variational methodology is explored and implemented to simultaneously solve for a periodic orbit that resembles a given reference path as well as the associated natural parameters describing the dynamical environment. First, variational principles are presented for continuous time systems. Then, these concepts are extended to accommodate discrete time. A constrained optimization problem, resembling an existing methodology in the discipline of optimal control, is formulated to compute a natural periodic orbit within a simplified, autonomous model of a binary system.

- Chapter 6: Identification and characterization of particular solutions is employed to explore the impact of an additional three-body interaction on the dynamical environment near a binary system. A dynamical model is derived based on the circular restricted three-body problem, but augmented by the additional force contribution. In this modified dynamical environment, the existence and characteristics of equilibrium points and families of periodic orbits are summarized and explained. Through the identification of qualitative changes to natural particular solutions for the behavior of an infinitesimal body, a guided

and well-informed exploration of the effect of an additional autonomous force contribution is completed.

- Chapter 7: Dynamical systems techniques are employed to construct a trajectory design framework for a CubeSat with limited propulsive capability and constrained departure conditions. The differential equations for low-thrust enabled motion in a point mass ephemeris model are derived. Using this dynamical model, a differential corrections algorithm is formulated to correct an initial guess trajectory. A trajectory design framework is then developed for the Lunar IceCube spacecraft by decomposing the transfer into three segments and selecting arcs in each segment to enable assembly of an initial guess. Potential transfer options are assessed in a natural gravitational environment and identified via dynamical systems theory and Poincaré mapping strategies. The utility of this framework is then demonstrated by constructing a sample trajectory that delivers the Lunar IceCube spacecraft from a highly energetic deployment state to captured motion in the lunar vicinity. By leveraging dynamical systems techniques, a complex path is designed for a spacecraft with limited propulsive capability and significant uncertainty in the initial conditions.

- Chapter 8: A summary of the results of this investigation is presented, followed by recommendations for extending the analysis for each of the two applications: exploration of the influence of a three-body interaction on the dynamics of an infinitesimally small body temporarily captured within a binary system, and the application of dynamical systems techniques to the design of a low-thrust enabled trajectory for a CubeSat.

2. DYNAMICAL MODEL

To facilitate exploration of the dynamical structures within multi-body systems, a variety of models is leveraged. First, the CR3BP reflects the motion of a particle of negligible mass in the vicinity of two primary bodies, assumed to traverse circular orbits about their mutual barycenter. This model is well-known within the astrodynamics community and has provided researchers with an autonomous approximation to the dynamics within multi-body systems such as the Earth-Moon and Sun-Earth systems, as well as binary star systems. In fact, the dynamical structures that exist in the CR3BP have supplied rapid and valuable insight into the fundamental motions within these multi-body systems, informing both spacecraft trajectory design procedures and the study of natural transport. Motion within multi-body systems, as predicted by the CR3BP, can also be transitioned to higher-fidelity models including an ephemeris model which considers the true non-Keplerian motion of bodies within a system. Many techniques consistent with dynamical systems theory have been developed by previous researchers to identify, visualize and characterize solutions that exist within multi-body systems. These techniques are leveraged and adapted in this investigation for two applications: to explore the effect of an additional autonomous force contribution on the motion of an exoplanet near a binary system and to enable the construction of a trajectory design framework for a small spacecraft within the Sun-Earth-Moon system.

2.1 Circular Restricted Three-Body Problem

In modeling the dynamical environment near a binary system, the motion of a body of interest, P_3, due to the pairwise gravitational attraction of each of two primaries, P_1 and P_2, is considered. These two massive components of the binary, P_i,

each possess a mass $\tilde{M}_i$. Figure 2.1 depicts the configuration of these three bodies in an inertial reference frame, $\hat{X}\hat{Y}\hat{Z}$, with a fixed origin at point O. The position vector locating P_3 with respect to the origin is expressed as $\bar{R}_3 = X\hat{X} + Y\hat{Y} + Z\hat{Z}$, while P_1 and P_2 are, respectively, located relative to the origin using the vectors $\bar{R}_1 = X_1\hat{X} + Y_1\hat{Y} + Z_1\hat{Z}$ and $\bar{R}_2 = X_2\hat{X} + Y_2\hat{Y} + Z_2\hat{Z}$. Figure 2.1 also portrays the relative position vectors $\bar{R}_{ij} = (X_j - X_i)\hat{X} + (Y_j - Y_i)\hat{Y} + (Z_j - Z_i)\hat{Z}$ which locate body P_j with respect to body P_i. In this investigation, note that an overbar identifies a vector, while the notation $\hat{(.)}$ represents a unit vector.

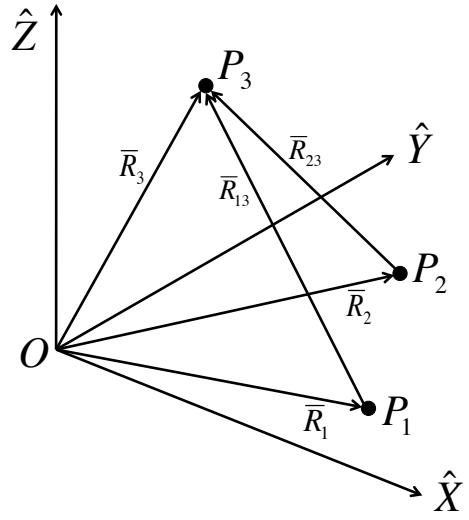

Fig. 2.1. Definition of the inertial coordinate frame and the position vectors locating each of the bodies in the CR3BP.

Given this system configuration, derivation of the differential equations governing the motion of P_3 in the CR3BP begins with a definition of the potential function, as expressed in the inertial frame. The scalar potential of P_3, per unit mass, is comprised of the following terms:

$$\tilde{U}_3 = \frac{\tilde{G}\tilde{M}_1}{\tilde{R}_{13}} + \frac{\tilde{G}\tilde{M}_2}{\tilde{R}_{23}} \tag{2.1}$$

where the tilde denotes dimensional quantities, and $\tilde{G}$ is the universal gravitational constant. From the definition of the potential function in Eq. (2.1), the equations

of motion for P_3 are derived relative to an inertial observer. A potential function depending solely upon position variables is differentiated to determine the force per unit mass, $\bar{F}_i$, acting on body P_i such that:

$$\bar{F}_i = \bar{\nabla}_i \tilde{U}_i = \bar{\tilde{R}}_i'' \tag{2.2}$$

where $\tilde{U}_i$ reflects the terms in the potential function that are functions of the coordinates locating body P_i. Then, $\bar{\nabla}_i(.)$ is a vector operator, and derivatives with respect to an inertial observer are denoted with a prime, $(.)'$. Although P_3 is the body of interest, this relationship applies to any of the three bodies. Assuming that P_3 is located using the inertial coordinate triad $(\tilde{X}, \tilde{Y}, \tilde{Z})$ as indicated in Figure 2.1, the partial derivatives of the potential function $\tilde{U}_3$ yield the force components in each of the inertial directions:

$$\begin{aligned} \frac{\partial \tilde{U}_3}{\partial \tilde{X}} &= \frac{\partial}{\partial \tilde{X}} \left(\frac{\tilde{G}\tilde{M}_1}{\tilde{R}_{13}} + \frac{\tilde{G}\tilde{M}_2}{\tilde{R}_{23}} \right) \\ &= -\frac{\tilde{G}\tilde{M}_1(\tilde{X} - \tilde{X}_1)}{\tilde{R}_{13}^3} - \frac{\tilde{G}\tilde{M}_2(\tilde{X} - \tilde{X}_2)}{\tilde{R}_{23}^3} \end{aligned} \tag{2.3}$$

$$\begin{aligned} \frac{\partial \tilde{U}_3}{\partial \tilde{Y}} &= \frac{\partial}{\partial \tilde{Y}} \left(\frac{\tilde{G}\tilde{M}_1}{\tilde{R}_{13}} + \frac{\tilde{G}\tilde{M}_2}{\tilde{R}_{23}} \right) \\ &= -\frac{\tilde{G}\tilde{M}_1(\tilde{Y} - \tilde{Y}_1)}{\tilde{R}_{13}^3} - \frac{\tilde{G}\tilde{M}_2(\tilde{Y} - \tilde{Y}_2)}{\tilde{R}_{23}^3} \end{aligned} \tag{2.4}$$

$$\begin{aligned} \frac{\partial \tilde{U}_3}{\partial \tilde{Z}} &= \frac{\partial}{\partial \tilde{Z}} \left(\frac{\tilde{G}\tilde{M}_1}{\tilde{R}_{13}} + \frac{\tilde{G}\tilde{M}_2}{\tilde{R}_{23}} \right) \\ &= -\frac{\tilde{G}\tilde{M}_1(\tilde{Z} - \tilde{Z}_1)}{\tilde{R}_{13}^3} - \frac{\tilde{G}\tilde{M}_2(\tilde{Z} - \tilde{Z}_2)}{\tilde{R}_{23}^3} \end{aligned} \tag{2.5}$$

where $\tilde{R}_{j3} = \sqrt{(\tilde{X} - \tilde{X}_j)^2 + (\tilde{Y} - \tilde{Y}_j)^2 + (\tilde{Z} - \tilde{Z}_j)^2}$ is the distance between P_j and P_3, for $j = 1, 2$. Since these partial derivatives are equal to the forces acting in each of the inertial directions, differentiating the pairwise gravitational potential terms recovers the well-known resultant inverse-square gravitational force. The equations

of motion for P_3 with respect to an inertially fixed observer are subsequently obtained by inserting these partial derivatives into Eq. (2.2):

$$\tilde{X}'' = -\frac{\tilde{G}\tilde{M}_1(\tilde{X}-\tilde{X}_1)}{\tilde{R}_{13}^3} - \frac{\tilde{G}\tilde{M}_2(\tilde{X}-\tilde{X}_2)}{\tilde{R}_{23}^3} \tag{2.6}$$

$$\tilde{Y}'' = -\frac{\tilde{G}\tilde{M}_1(\tilde{Y}-\tilde{Y}_1)}{\tilde{R}_{13}^3} - \frac{\tilde{G}\tilde{M}_2(\tilde{Y}-\tilde{Y}_2)}{\tilde{R}_{23}^3} \tag{2.7}$$

$$\tilde{Z}'' = -\frac{\tilde{G}\tilde{M}_1(\tilde{Z}-\tilde{Z}_1)}{\tilde{R}_{13}^3} - \frac{\tilde{G}\tilde{M}_2(\tilde{Z}-\tilde{Z}_2)}{\tilde{R}_{23}^3} \tag{2.8}$$

Together, these expressions comprise the equations of motion for P_3 as formulated in an inertial frame. Determining the position and velocity time histories governing the behavior of P_3 with respect to an inertially fixed point requires the simultaneous solution of the position and velocity for all three bodies. Combining Eq. (2.6)-(2.8) with similar equations of motion for P_1 and P_2 results in 18 scalar first-order differential equations. An analytical solution, therefore, requires 18 constants. However, only 10 integrals of the motion are known to exist: six from the conservation of linear momentum, three from the conservation of angular momentum and one from the conservation of energy. Reformulating the problem to model the relative motion of P_3 with respect to a primary reduces the number of first-order scalar differential equations to 12. However, the number of integrals still remains insufficient and, thus, no analytical solution is available.

In the absence of an analytical solution, the introduction of simplifying assumptions and a reformulation of the equations of motion supplies valuable insight into the behavior of P_3. First, the third body is assumed to possess infinitesimal mass in comparison to P_1 and P_2. Such an assumption is reasonable when modeling a spacecraft orbiting within the Earth-Moon system or an exoplanet near a binary star system. Incorporating this assumption into the three-body problem results in the center of mass of the three-body system being located along the line between the two massive primaries. The system barycenter, an inertially fixed location, is conveniently selected to be the origin of the $\hat{X}\hat{Y}\hat{Z}$ coordinate frame. Since the infinitesimal third body does not influence the motion of P_1 and P_2, the primaries trace out closed

conics about their mutual barycenter. For an arbitrary conic, the distance between P_1 and P_2 is time-dependent, resulting in complexities in visualizing the motion of P_3 with respect to the primaries. To eliminate the pulsation of the primaries and the time-dependence of their rotation rate, P_1 and P_2 are assumed to move on circular orbits. The locations of P_1 and P_2 are, therefore, known for all time.

To extend the analysis to systems of various relative mass ratios, it is convenient to rewrite the equations of motion using a set of nondimensional system parameters. Length quantities are normalized using the constant distance between the two primaries as a reference, denoted l^*:

$$l^* = \tilde{D}_1 + \tilde{D}_2$$

where $\tilde{D}_i$ is the distance from the system barycenter to each of the two primaries, respectively. Since the two primaries are assumed to follow circular orbits, the nondimensional distance between P_1 and P_2 is constant at a value of unity. The characteristic mass quantity, m^*, is the sum of the masses of the primaries, while time is nondimensionalized with t^* such that the mean motion of the primaries is equal to unity. These characteristic quantities are evaluated as:

$$m^* = \tilde{M}_1 + \tilde{M}_2$$

$$t^* = \left(\frac{(\tilde{D}_1 + \tilde{D}_2)^3}{\tilde{G}(\tilde{M}_1 + \tilde{M}_2)} \right)^{1/2}$$

The characteristic mass quantity yields nondimensional mass values for P_1 and P_2 equal to $(1 - \mu)$ and μ, respectively, where μ is defined as:

$$\mu = \frac{\tilde{M}_2}{m^*}$$

Leveraging these characteristic quantities, the nondimensional potential of P_3 reduces to the following expression:

$$U_3 = \frac{1 - \mu}{R_{13}} + \frac{\mu}{R_{23}}$$

where R_{13} and R_{23} are the nondimensional distances between P_3 and each of the two primaries. Similarly, Eq. (2.6)-(2.8) can be written using nondimensional variables to produce the following equations of motion relative to an inertial observer:

$$X'' = -\frac{(1-\mu)(X+\mu\cos(t))}{R_{13}^3} - \frac{\mu(X-(1-\mu)\cos(t))}{R_{23}^3} \tag{2.9}$$

$$Y'' = -\frac{(1-\mu)(Y+\mu\sin(t))}{R_{13}^3} - \frac{\mu(Y-(1-\mu)\sin(t))}{R_{23}^3} \tag{2.10}$$

$$Z'' = -\frac{(1-\mu)Z}{R_{13}^3} - \frac{\mu Z}{R_{23}^3} \tag{2.11}$$

These expressions still include time-dependent terms locating P_1 and P_2, which add complexity to the identification of equilibrium and other particular solutions, as well as the visualization of trajectories.

To convert the CR3BP equations of motion into a form that is autonomous, a rotating frame is leveraged. In particular, this coordinate frame, $\hat{x}\hat{y}\hat{z}$, is defined as portrayed in Figure 2.2 such that the $\hat{x}$ unit vector is directed from P_1 towards P_2. Since the primaries are assumed to follow circular orbits about their mutual barycenter, the $P_1 - P_2$ line rotates at a constant, nondimensional rate of unity about the $+\hat{Z}$ axis. The $\hat{z}$ unit vector is defined in a direction that is normal to the $P_1 - P_2$ orbit plane and parallel to the orbital angular momentum. This right-handed triad is completed by appropriately defining $\hat{y}$ within the plane of motion of the primaries and perpendicular to $\hat{x}$. In the rotating frame, the location of P_3, (x, y, z), is written in terms of its inertial nondimensional coordinates (X, Y, Z) as:

$$\begin{bmatrix} x \\ y \\ z \end{bmatrix} = \begin{bmatrix} cos(t) & sin(t) & 0 \\ -sin(t) & cos(t) & 0 \\ 0 & 0 & 1 \end{bmatrix} \begin{bmatrix} X \\ Y \\ Z \end{bmatrix}$$

Using this transformation, the fixed locations of the two primaries, P_1 and P_2, expressed in nondimensional rotating coordinates are, respectively, $(x_1, y_1, z_1) = (-\mu, 0, 0)$ and $(x_2, y_2, z_2) = (1-\mu, 0, 0)$. In addition, the position vectors, $\bar{r}_1 = (x+\mu)\hat{x}+y\hat{y}+z\hat{z}$ and $\bar{r}_2 = (x-1+\mu)\hat{x}+y\hat{y}+z\hat{z}$, locate P_3 with respect to the two primaries.

The equations of motion of P_3 in terms of rotating coordinates are developed by rewriting the derivatives with respect to a rotating observer. Recall that the angular

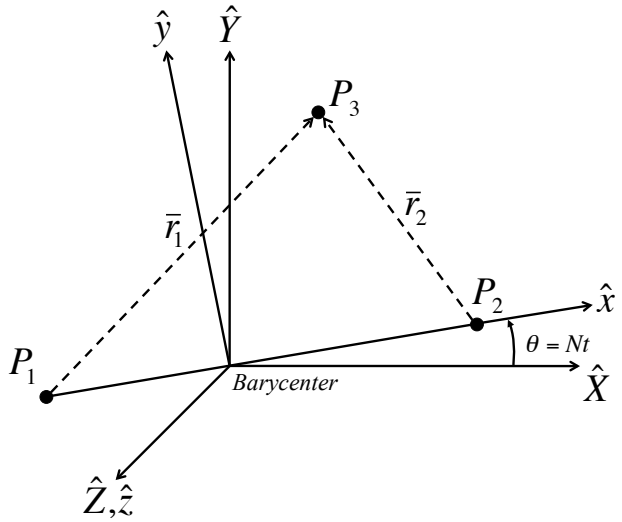

Fig. 2.2. Definition of the rotating coordinate frame which rotates with respect to the inertial frame at a nondimensional rate of $N = 1$ about the $\hat{Z}$-axis.

velocity of the rotating frame with respect to the inertial frame is in the $\hat{z}$ direction, with a nondimensional magnitude of unity. Thus, the acceleration of P_3 is expressed as the second derivative of the position vector, $\bar{r} = x\hat{x} + y\hat{y} + z\hat{z}$, with respect to an inertial observer, and the kinematic expansion yields:

$$\bar{r}'' = (\ddot{x} - 2\dot{y} - x)\hat{x} + (\ddot{y} + 2\dot{x} - y)\hat{y} + \ddot{z}\hat{z}$$

where $\dot{(.)}$ represents a time derivative with respect to an observer in the rotating frame. Using this result, the equations of motion, given in Eq. (2.6)-(2.8), are expressed in terms of rotating coordinates as:

$$\ddot{x} = 2\dot{y} + x - \frac{(1-\mu)(x+\mu)}{r_1^3} - \frac{\mu(x-1+\mu)}{r_2^3} \tag{2.12}$$

$$\ddot{y} = -2\dot{x} + y - \frac{(1-\mu)y}{r_1^3} - \frac{\mu y}{r_2^3} \tag{2.13}$$

$$\ddot{z} = -\frac{(1-\mu)z}{r_1^3} - \frac{\mu z}{r_2^3} \tag{2.14}$$

where $r_1 = \sqrt{(x+\mu)^2 + y^2 + z^2}$ and $r_2 = \sqrt{(x-1+\mu)^2 + y^2 + z^2}$ are the nondimensional distances between P_3 and each of the primaries. Although there is no analytical solution to the CR3BP equations of motion, these three second-order differential equations can be transformed into six first-order differential equations and numerically integrated using initial conditions for $(x, y, z, \dot{x}, \dot{y}, \dot{z})^T$.

2.1.1 Integral of Motion

From conservation of energy, a constant energy integral exists when the CR3BP equations of motion are formulated in a rotating frame. The equations of motion, Eq. (2.12)-(2.14), can be written in the form:

$$\ddot{x} - 2\dot{y} = \frac{\partial U^*}{\partial x} \tag{2.15}$$

$$\ddot{y} + 2\dot{x} = \frac{\partial U^*}{\partial y} \tag{2.16}$$

$$\ddot{z} = \frac{\partial U^*}{\partial z} \tag{2.17}$$

where U^* is defined as the pseudopotential function:

$$U^* = \frac{1}{2}(x^2 + y^2) + \frac{1-\mu}{r_1} + \frac{\mu}{r_2} \tag{2.18}$$

which includes additional terms due to the rotation of the $\hat{x}\hat{y}\hat{z}$ coordinate frame. To derive the energy integral, the dot product of the acceleration and velocity vectors, $(\ddot{x}, \ddot{y}, \ddot{z})^T$ and $(\dot{x}, \dot{y}, \dot{z})^T$, produces the following relationship:

$$\dot{x}\ddot{x} + \dot{y}\ddot{y} + \dot{z}\ddot{z} = \frac{\partial U^*}{\partial x}\dot{x} + \frac{\partial U^*}{\partial y}\dot{y} + \frac{\partial U^*}{\partial z}\dot{z}$$

which, when integrated, is equivalent to:

$$\frac{1}{2}v^2 = \int dU^* - \frac{dU^*}{dt}$$

where $v^2 = \dot{x}^2 + \dot{y}^2 + \dot{z}^2$. Since the pseudopotential function is autonomous, its derivative with respect to time is always equal to zero. An energy integral, C, labeled the Jacobi constant is, therefore, defined as:

$$v^2 = 2U^* - C$$

This expression reveals that increasing C is equivalent to decreasing the physical energy of P_3 relative to the three-body system. Rearranging this expression, the constant of integration is written in terms of the state variables, expressed in the rotating frame, as:

$$C = x^2 + y^2 + \frac{2(1-\mu)}{r_1} + \frac{2\mu}{r_2} - \dot{x}^2 - \dot{y}^2 - \dot{z}^2 \tag{2.19}$$

Since the CR3BP is an autonomous model of the pairwise gravitational interactions acting on P_3 due to the presence of the two primaries, this energy integral remains constant along any natural solution to the equations of motion.

2.1.2 Equilibrium Points

Despite the lack of an analytical solution, significant insight into the dynamics in the CR3BP emerges from particular solutions, including equilibrium points. These constant solutions to the equations of motion exist in the phase space, $(x, y, z, \dot{x}, \dot{y}, \dot{z})^T$, with a velocity and acceleration of zero. Under these conditions, the equations of motion, Eq. (2.15)-(2.17), simplify to:

$$\frac{\partial U^*}{\partial x} = \frac{\partial U^*}{\partial y} = \frac{\partial U^*}{\partial z} = 0$$

Equilibrium points in the rotating frame are, therefore, determined as stationary points of the pseudopotential function, U^*.

Five intervals for the possible locations of the equilibrium points are identified by examining these partial derivatives. When $z = 0$, the partial derivative of U^* with respect to z, denoted U_z^*, is equal to zero, placing all five equilibrium points within the plane of motion of the primaries. If the y coordinate is zero, providing $U_y^* = 0$, there are three intervals in which an equilibrium point could potentially exist:

$$(x+\mu) > 0, (x-1+\mu) > 0$$

$$(x+\mu) < 0, (x-1+\mu) < 0$$

$$(x+\mu) > 0, (x-1+\mu) < 0$$

Equilibrium points within these regions are computed by numerically locating stationary points of the pseudopotential function, given initial guesses in each of the three intervals. Two additional equilibrium points exist above and below the x-axis and are located by solving for the stationary points of the pseudopotential written in terms of the variables r_1 and r_2. Due to the form of U^*, these two equilibrium points are located symmetrically across the x-axis.

In the CR3BP, there are five well-known equilibrium points, all in the plane of motion of the two primaries: three collinear points located along the x-axis, and two equilateral points with a nonzero component in the $\hat{y}$ direction, located such that $r_1 = r_2 = 1$ [15]. These five equilibrium points are labeled L_i, for $i = 1, 2, 3, 4, 5$. The location of the equilibrium points with respect to the primaries, located via gray filled circles, in the rotating frame appear as red diamonds in Figure 2.3 for $\mu = 0.30$, and are labeled consistent with the conventional numbering for each point. While these equilibrium points represent constant solutions to the equations of motion, additional types of steady-state solutions also exist. Each of these motions can be examined using concepts from dynamical systems theory.

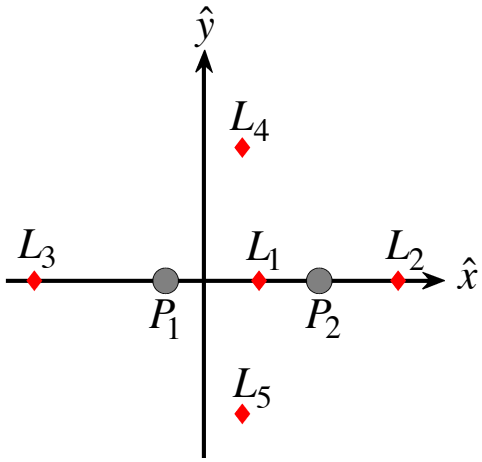

Fig. 2.3. Equilibrium points in the CR3BP relative to the two primaries, with sample locations corresponding to $\mu = 0.30$.

2.1.3 Zero Velocity Surfaces

At a given energy level, natural solutions that emerge in the CR3BP may be restricted to limited regions of the phase space. In fact, an infinite set of points that possesses a velocity of zero (and nonzero acceleration) relative to the rotating frame defines boundaries on the motion, labeled zero velocity surfaces [41]. To identify these boundaries, the energy constant derived in Eq. (2.19) is rearranged to isolate the magnitude of the velocity:

$$\dot{x}^2 + \dot{y}^2 + \dot{z}^2 = x^2 + y^2 + \frac{2(1-\mu)}{r_1} + \frac{2\mu}{r_2} - C$$

When the speed is equal to zero, an infinite set of points described by a state vector in the form $(x, y, z, 0, 0, 0)^T$, satisfies the following expression for a given value of the energy constant, C:

$$x^2 + y^2 + \frac{2(1-\mu)}{r_1} + \frac{2\mu}{r_2} = C$$

Together, these points form a surface in three-dimensional space. On either side of these surfaces, the square of the velocity is either positive or negative. The zero velocity surfaces therefore separate regions in the phase space with either real or imaginary velocity magnitudes. Given that imaginary speeds are not physically valid, zero velocity surfaces separate regions of allowable and forbidden motion. Accordingly, the zero velocity surfaces cannot be crossed. Thus, zero velocity surfaces are useful in visualizing regions that bound the motion for P_3. In the case of solely planar motion, the intersections of these surfaces with the plane of motion of the primaries form zero velocity curves. As an example, Figure 2.4 depicts the zero velocity curves at the four specific values of C that correspond to the five equilibrium points in the CR3BP at a mass ratio $\mu = 0.30$. The dark shaded regions are forbidden to motion, and white space represents allowable regions of motion for P_3. In this figure, equilibrium points are colored red and the two primaries are represented by blue circles. Since the primaries are modeled as point masses, their sizing in this figure is purely illustrative. When P_3 is located in the vicinity of either primary, it is in the "interior region", while

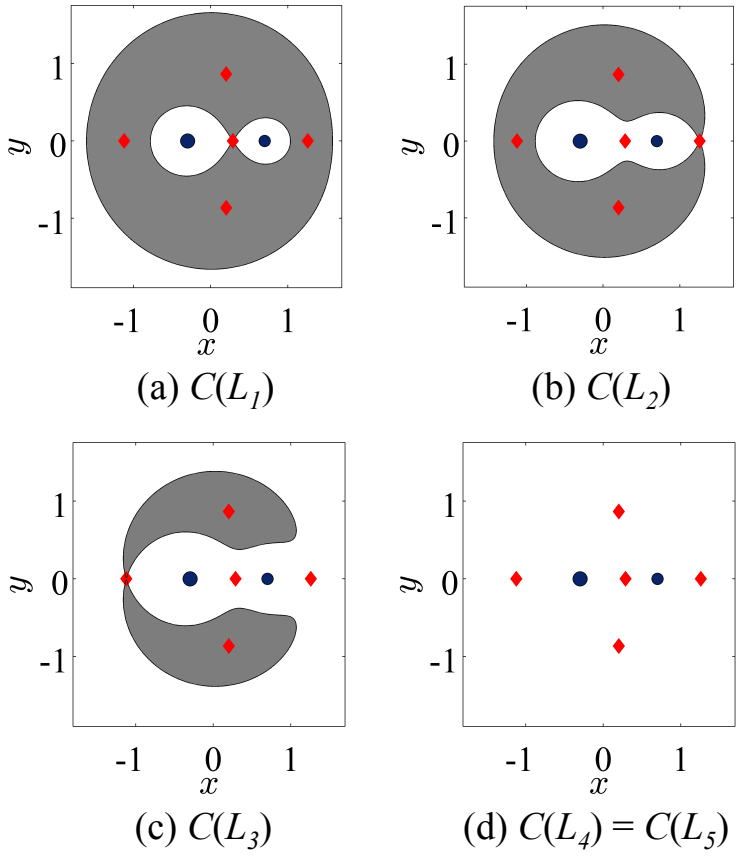

Fig. 2.4. Zero Velocity Curves of the CR3BP for energy integrals evaluated at the equilibrium points, where $C(L_1) > C(L_2) > C(L_3) > C(L_4)$, for $\mu = 0.30$.

the "exterior region" encompasses areas in the configuration space that are outside the zero velocity curves.

Analysis of the zero velocity curves across a range of energy levels reveals the regions that P_3 can traverse along a natural, planar trajectory. From a value $C = C(L_1)$, raising the energy level, or, equivalently, decreasing the value of C, results in growth of the allowable interior regions. Beginning at a constant of motion that is higher than $C(L_1)$, P_3 can move near one of the primaries or in the exterior region, beyond the zero velocity curves. When the constant of motion is lowered below that of L_1, P_3 is able to move between the vicinity of P_1 and P_2 or exterior to the zero

velocity curves, but not between all regions of the phase space. Decreasing the value of the constant further, below $C(L_2)$, P_3 may move between the vicinity of either primary and the exterior region. Any exchange between the exterior and interior regions at this energy level occurs in the vicinity of L_2, i.e., the L_2 gateway. If the energy constant is slightly below $C(L_3)$, further interchange between the interior and exterior region may now potentially occur through the L_3 gateway. When the energy constant is reduced to a value below that of L_4 or L_5, P_3 can move anywhere within the plane of the primaries. At these higher values of the energy constant, zero velocity surfaces still exist above and below the $z = 0$ plane. Accordingly, while motion in the plane is unrestricted at low values of C, P_3 is still bounded by zero velocity surfaces in three-dimensional space. The zero velocity curves do not, however, offer insight into the form of the infinite solutions present in the allowable regions, including periodic orbits, quasi-periodic trajectories, manifolds, and chaotic motion. Rather, additional techniques, derived from dynamical systems theory, must be employed to locate particular solutions with desired characteristics.

3. PARTICULAR SOLUTIONS

Since the nonlinear equations of motion in the CR3BP are nonintegrable and autonomous, four types of steady-state solutions exist: equilibrium points, periodic orbits, quasi-periodic orbits, and chaotic motion [42]. Sample solutions of each type are plotted in Figure 3.1(a)-(d) in configuration space. Recall that, in the CR3BP, the locations of the five equilibrium points are fixed for given values of the natural parameters. A periodic orbit, however, is a time-varying solution that is characterized by repeating motion. Since the CR3BP is autonomous and conservative, these periodic orbits exist within continuous families that form an underlying structure: a stable orbit attracts or bounds nearby motion, while trajectories near an unstable orbit depart its vicinity [19]. In fact, identifying periodic orbits and evaluating their stability delivers significant insight into the dynamics within a multi-body system. For instance, stable periodic orbits possess a center manifold that is comprised of families of quasi-periodic orbits, that are bounded and trace out the surface of a torus [15]. In contrast to these bounded particular solutions, chaotic motion associated with a multi-body gravitational environment enables natural transport between various regions of the phase space. Together, these four types of motions are useful in a variety of scenarios, including the identification of potential motions of an exoplanet within a binary star system, the characterization of modified dynamical fields, and the design of complex paths for a spacecraft subject to various mission constraints.

3.1 Periodic Orbits

Within the autonomous dynamical field modeled in the CR3BP, families of periodic solutions exist, as viewed relative to the rotating frame, in various regions of the phase space [15]. Each one-dimensional periodic orbit is characterized by re-

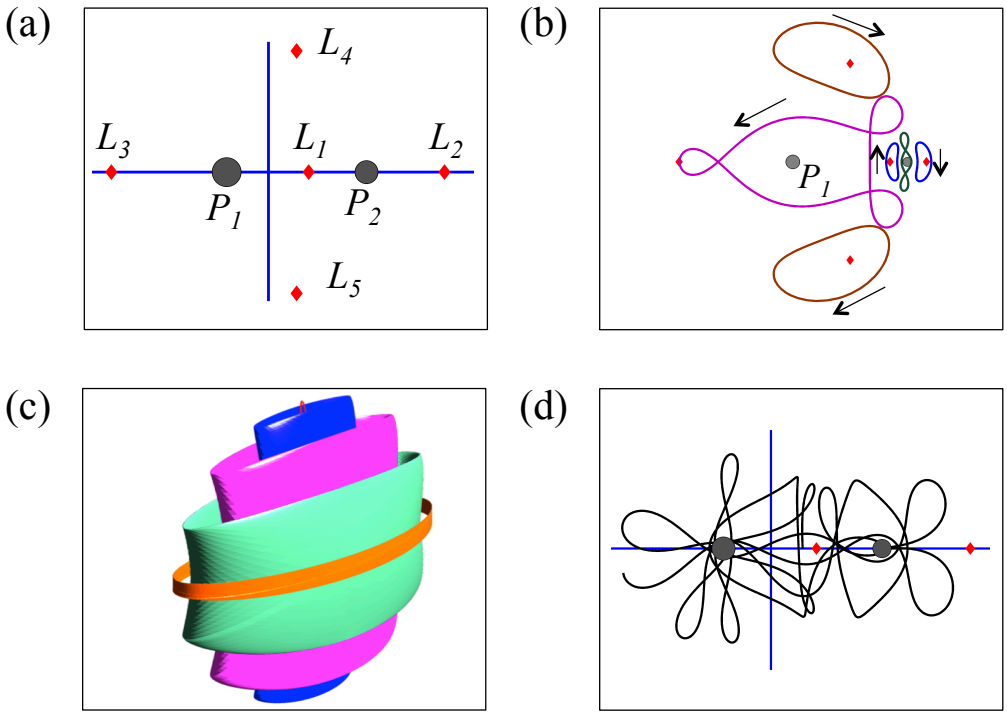

Fig. 3.1. Sample particular solutions in the CR3BP, including: (a) equilibrium points, (b) periodic orbits, (c) quasi-periodic trajectories, and (d) chaotic motion.

peating motion such that any state represented in the form $\bar{x} = [x, y, z, \dot{x}, \dot{y}, \dot{z}]^T$, as expressed in rotating coordinates, lies along a periodic orbit if it satisfies the condition $\bar{x}(t) = \bar{x}(t + T)$ when integrated over a time T. The minimum positive value of T for which this condition is satisfied is labeled the period [42]. Note that an orbit that is periodic in the rotating frame is only periodic in the inertial frame if the orbital period is a rational multiple of the period of the primaries. As viewed in the rotating coordinate system, a period-q orbit encircles the primaries, or an equilibrium point, q times during one period. Examples of this nomenclature appear in Figure 3.2: a period-1 orbit in Figure 3.2(a) encircles P_2 once and, in Figure 3.2(b), a period-3 orbit completes three clockwise revolutions about both primaries. In general, to an observer in the rotating frame, a period-q orbit can travel about a reference location in any direction. Recall that the primaries move with an orbital angular momentum vector

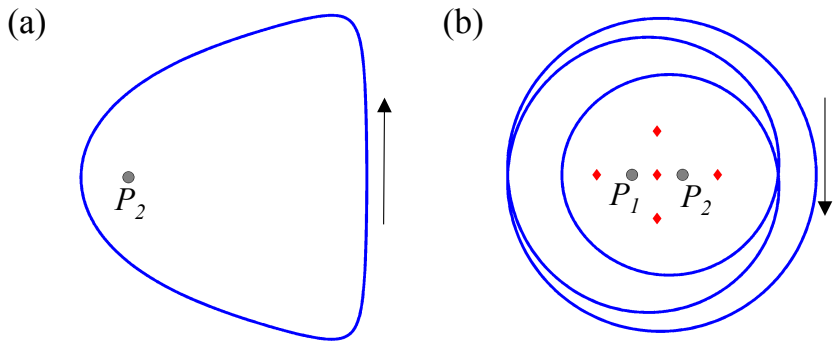

Fig. 3.2. A (a) planar period-1 orbit and (b) planar period-3 orbit plotted in the rotating frame.

parallel to the $+\hat{Z}$-direction in the inertial frame, or equivalently, in the $+\hat{z}$-direction as defined in the rotating frame. This angular momentum vector is employed as a reference when describing the direction of motion of a trajectory as viewed in the rotating frame. An arbitrary trajectory, representing the path of particle P in the vicinity of a reference point, appears as a black arc in Figure 3.3. At any time t_1 along the path, the state describing the position and velocity of P, relative to the primary P_i and with respect to the rotating frame, is represented by the vector $\bar{x}_{1,P_i}$. This six-dimensional relative state vector, $\bar{x}_{1,P_i}$, expressed in rotating coordinates, is comprised of the three-dimensional relative vectors of position, $\bar{r}$, and velocity, $\bar{v}$, as illustrated. Then, the specific relative angular momentum for the motion of P, as formulated in the rotating frame with respect to the reference primary, is evaluated at t_1 as the cross product $\bar{H} = \bar{r} \times \bar{v}$. An arc with an instantaneous angular momentum vector in the $+\hat{z}$-direction is prograde with respect to the selected primary, while an instantaneous angular momentum in the $-\hat{z}$-direction corresponds to a retrograde path. In the rotating frame, a periodic orbit can appear to wind about one of the primaries in an entirely prograde or retrograde direction, or a particle moving along a periodic path can alternate between the two directions as it encircles one or both of the primaries. When viewed by an observer from the $+\hat{z}$-direction, the period-1

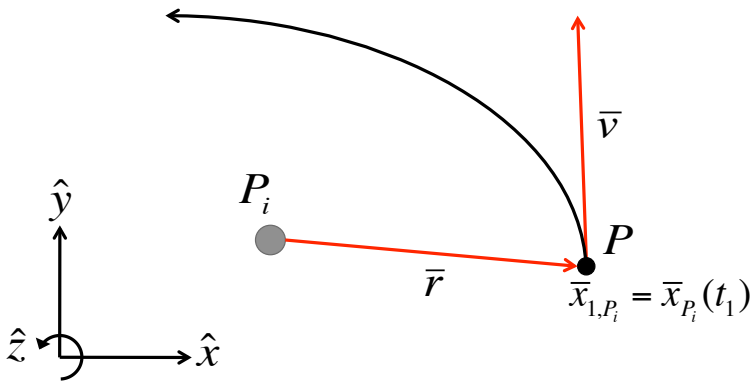

Fig. 3.3. Definition of position and velocity vectors with respect to one of the primaries in the rotating frame.

orbit in Figure 3.2(a) reflects motion that is counterclockwise about P_2. Since the associated relative angular momentum vector is parallel to the $+\hat{z}$-direction, this periodic orbit is defined as prograde with respect to P_2. Similarly, the period-3 orbit in Figure 3.2(b) is classified as retrograde with respect to both P_1 and P_2.

3.1.1 Stability

Orbital stability is typically deduced from the monodromy matrix, defined as the state transition matrix propagated for precisely one period of the orbit [41]. Given a reference periodic orbit, a neighboring solution is approximated using first-order variational equations. To demonstrate this process, consider a sample reference path, $\bar{x}_R(t)$ associated with an initial condition $\bar{x}_R(t_0)$, as depicted in Figure 3.4. After introducing a variation $\delta\bar{x}(t_0)$ in the initial state and numerically integrating forward (or backward) in time, the resulting perturbed trajectory is evaluated as:

$$\bar{x}(t) = \bar{x}_R(t) + \delta\bar{x}(t)$$

Since each solution in the CR3BP is unique, integrating both the reference and the perturbed initial states results in two distinct paths. Consequently, at a time t_f, the

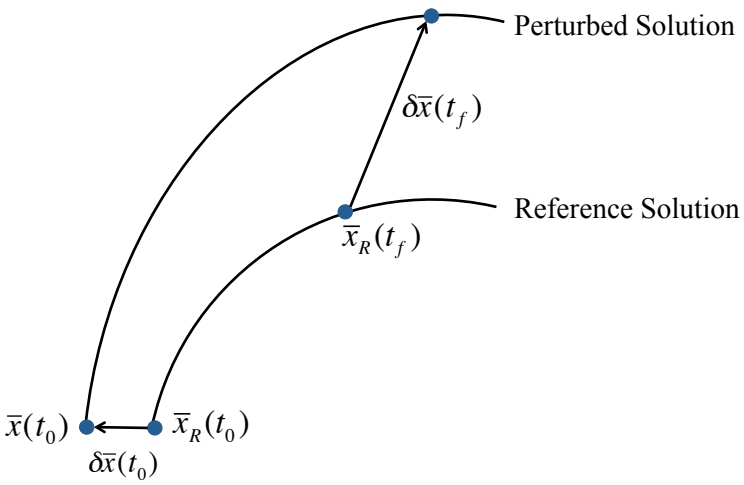

Fig. 3.4. Deviation in states at times t_0 and t_f along a reference path and a nearby perturbed trajectory.

states along these two paths are not equal and their difference, $\delta\bar{x}(t_f)$, is estimated using a first-order Taylor series expansion about the reference arc. Leveraging the variation relative to the reference path, the general equations of motion are expressed in first-order form as:

$$\dot{\bar{x}} = \dot{\bar{x}}_R + \delta\dot{\bar{x}} = \bar{f}(\bar{x}_R + \delta\bar{x})$$

where $\bar{f}$ represents the nonlinear differential equations in the CR3BP. A Taylor series expansion about the reference trajectory yields the first-order terms:

$$\dot{\bar{x}} \approx \bar{f}(\bar{x}_R, t) + \left.\frac{\partial \bar{f}}{\partial \bar{x}}\right|_{\bar{x}_R} \delta\bar{x}$$

which simplifies to the linear vector variational equation:

$$\delta\dot{\bar{x}} \approx \left.\frac{\partial \bar{f}}{\partial \bar{x}}\right|_{\bar{x}_R} \delta\bar{x} \tag{3.1}$$

Solutions to this equation are of the form:

$$\delta\bar{x}(t) = \mathbf{\Phi}(t, t_0)\delta\bar{x}(t_0) \tag{3.2}$$

where $\mathbf{\Phi}(t, t_0)$ denotes the state transition matrix (STM) [41]. Analysis of this relationship reveals that the STM is essentially a linear mapping from t_0 to a time t.

Substituting this solution into Eq. (3.1) produces the first-order matrix differential equation for the STM:

$$\dot{\boldsymbol{\Phi}}(t,t_0) = \left.\frac{\partial \bar{f}}{\partial \bar{x}}\right|_{\bar{x}_R} \boldsymbol{\Phi}(t,t_0) \tag{3.3}$$

with the initial condition $\boldsymbol{\Phi}(t_0,t_0) = \boldsymbol{I}_{6\times 6}$, where $\boldsymbol{I}_{6\times 6}$ represents the 6×6 identity matrix [43]. The elements of the STM can, therefore, be appended to the state vector along the reference trajectory and simultaneously integrated.

Properties of the STM, such as its inherent decomposition into the product of intermediate STMs and its symplectic form, are useful in a variety of scenarios, including the assessment and reduction of the error associated with numerical integration of the STM over long time intervals. First, consider Eq. (3.2) rewritten at time t_f as:

$$\delta\bar{x}(t_f) = \boldsymbol{\Phi}(t_f,t_0)\delta\bar{x}(t_0) \tag{3.4}$$

Consecutively employing the chain rule and substituting the variations at intermediate times produces the equivalent expression:

$$\delta\bar{x}(t_f) = \boldsymbol{\Phi}(t_f,t_{f-1})\boldsymbol{\Phi}(t_{f-1},t_{f-2})....\boldsymbol{\Phi}(t_1,t_0)\delta\bar{x}(t_0) \tag{3.5}$$

Combining Eq. (3.4) and (3.5) reveals that an STM, $\boldsymbol{\Phi}(t_f,t_0)$, can be computed as the product of intermediate STMs:

$$\boldsymbol{\Phi}(t_f,t_0) = \boldsymbol{\Phi}(t_f,t_{f-1})\boldsymbol{\Phi}(t_{f-1},t_{f-2}).....\boldsymbol{\Phi}(t_2,t_1)\boldsymbol{\Phi}(t_1,t_0) \tag{3.6}$$

where $t_0 < t_1 ... < t_{f-1} < t_f$. This property is often leveraged within a multiple shooting algorithm to compute the state transition matrix along a trajectory that has been discretized into several arcs, potentially offering a reduced measure of the numerical error in comparison to integration of the STM over one longer time interval. Additional useful properties of the STM are deduced as a consequence of its symplecticity. For a $2n \times 2n$ matrix, $\boldsymbol{S}$, to be considered symplectic, it must satisfy the condition:

$$\boldsymbol{S}^T\boldsymbol{J}\boldsymbol{S} = \boldsymbol{J} \tag{3.7}$$

where $\boldsymbol{J}$ is defined as the constant $2n \times 2n$ matrix:

$$\boldsymbol{J} = \begin{bmatrix} \boldsymbol{0}_{n\times n} & \boldsymbol{I}_{n\times n} \\ -\boldsymbol{I}_{n\times n} & \boldsymbol{0}_{n\times n} \end{bmatrix}$$

In this matrix, $\boldsymbol{I}_{n\times n}$ is the $n \times n$ identity matrix and $\mathbf{0}_{n\times n}$ is an $n \times n$ matrix of zeros [41]. If $\boldsymbol{S}$ is a symplectic transformation matrix, it preserves many properties of the flow, including the volume of the phase space. Since the STM is initially equal to the identity matrix, it is symplectic at t_0. To determine whether the STM satisfies this condition at any other time t, the time derivative of the symplectic condition is analyzed. Using the chain rule, this derivative is equal to:

$$\frac{d}{dt}\left(\boldsymbol{\Phi}(t,t_0)^T\boldsymbol{J}\boldsymbol{\Phi}(t,t_0)\right) = \dot{\boldsymbol{\Phi}}(t,t_0)^T\boldsymbol{J}\boldsymbol{\Phi}(t,t_0) + \boldsymbol{\Phi}(t,t_0)^T\boldsymbol{J}\dot{\boldsymbol{\Phi}}(t,t_0)$$

Substituting the first-order differential equation for the STM into this expression:

$$\begin{aligned}\frac{d}{dt}\left(\boldsymbol{\Phi}(t,t_0)^T\boldsymbol{J}\boldsymbol{\Phi}(t,t_0)\right) &= \boldsymbol{\Phi}(t,t_0)^T\left.\frac{\partial\bar{f}}{\partial\bar{x}}\right|_{\bar{x}_R}^T\boldsymbol{J}\boldsymbol{\Phi}(t,t_0) + \boldsymbol{\Phi}(t,t_0)^T\boldsymbol{J}\left.\frac{\partial\bar{f}}{\partial\bar{x}}\right|_{\bar{x}_R}\boldsymbol{\Phi}(t,t_0)\\ &= \boldsymbol{\Phi}(t,t_0)^T\left[\left.\frac{\partial\bar{f}}{\partial\bar{x}}\right|_{\bar{x}_R}^T\boldsymbol{J} + \boldsymbol{J}\left.\frac{\partial\bar{f}}{\partial\bar{x}}\right|_{\bar{x}_R}\right]\boldsymbol{\Phi}(t,t_0) \qquad (3.8)\end{aligned}$$

Recall that $\left.\frac{\partial\bar{f}}{\partial\bar{x}}\right|_{\bar{x}_R}$ is a matrix representing the derivative of the six first-order nonlinear differential equations with respect to the state vector, evaluated on $\bar{x}_R(t)$. Given the form of $\left.\frac{\partial\bar{f}}{\partial\bar{x}}\right|_{\bar{x}_R}$ for a Hamiltonian system, this matrix satisfies the following relationship:

$$\boldsymbol{J}\left.\frac{\partial\bar{f}}{\partial\bar{x}}\right|_{\bar{x}_R} = -\left.\frac{\partial\bar{f}}{\partial\bar{x}}\right|_{\bar{x}_R}^T\boldsymbol{J}$$

Substituting this relationship into Eq. (3.8), the time derivative of $\boldsymbol{\Phi}(t,t_0)^T\boldsymbol{J}\boldsymbol{\Phi}(t,t_0)$ is equal to zero for any time t. Since the initial STM is symplectic, it is also symplectic for all time [41]. As a direct result of this property, the determinant of the STM is theoretically always equal to a constant value of unity, enabling evaluation of the numerical error incurred during propagation of the STM along a natural trajectory.

The symplectic nature of the STM is leveraged to explore the eigenvalues of the STM. Substituting the STM into the symplectic condition in Eq. (3.7) and rearranging, such that $\boldsymbol{J}$ reflects a similarity transformation, the STM satisfies:

$$\boldsymbol{\Phi}(t,t_0)^T = \boldsymbol{J}^{-1}\boldsymbol{\Phi}(t,t_0)^{-1}\boldsymbol{J} \qquad (3.9)$$

This relationship reveals that $\mathbf{\Phi}(t,t_0)^T$ and $\mathbf{\Phi}(t,t_0)^{-1}$ are similar matrices. Denoting the $2n$ eigenvalues of $\mathbf{\Phi}(t,t_0)$, and equivalently $\mathbf{\Phi}(t,t_0)^T$, as λ_i, the eigenvalues of $\mathbf{\Phi}(t,t_0)^{-1}$ must be equal to $1/\lambda_i$. Since similar matrices possess eigenvalues that are equal, the eigenvalues of the STM must occur in reciprocal pairs λ_i and $1/\lambda_i$ [41].

Since the STM represents the sensitivity of a solution at a time downstream to perturbations in the initial state, its eigenvalues offer information about trajectories in the vicinity of the reference path $\bar{x}_R(t)$. Thus, for trajectory computations, simultaneous integration of the state, $\bar{x}(t)$, and the STM, $\mathbf{\Phi}(t,t_0)$, is useful. Given the nonlinearity of the system, the accuracy of the STM is limited for integration over long time intervals, or for a prediction of the motion resulting from large perturbations. In fact, the accuracy of the STM is typically monitored by comparing the determinant of the STM to unity, supplying a measure of the numerical error incurred during a numerical integration process.

The stability of a periodic orbit is deduced from the eigenvalues of the monodromy matrix, defined as the STM propagated for precisely one period of the orbit [41]. Recall that the general solution to the variational equations of motion, linearized relative to the given periodic orbit, is written as:

$$\delta\bar{x}(t) = \mathbf{\Phi}(t,t_0)\delta\bar{x}(t_0)$$

where $\delta\bar{x}(t_0)$ is the variation with respect to the initial state along the orbit [43]. In contrast to constant coefficient matrices that are straightforwardly decomposed into eigenvalues and eigenvectors to assess stability, a different strategy is necessary to determine the modes of behavior in the vicinity of a time-dependent periodic solution. Via Floquet theory, the time-varying STM is decomposed into the following form:

$$\mathbf{\Phi}(t,t_0) = \boldsymbol{F}(t)e^{\Omega t}\boldsymbol{F}(t_0)^{-1}$$

where $\boldsymbol{F}(t)$ is a periodic matrix and the diagonal elements of Ω are the Poincaré exponents, Ω_i, for $i = [1,6]$. The initial value of $\boldsymbol{F}(t)$ at $t_0 = 0$ is available by evaluating this decomposition after one period, T, and noting that $\boldsymbol{F}(T) = \boldsymbol{F}(0)$:

$$\mathbf{\Phi}(T,0) = \boldsymbol{F}(0)e^{\Omega T}\boldsymbol{F}(0)^{-1} \tag{3.10}$$

Since $e^{\Omega T}$ is a diagonal matrix, $\boldsymbol{F}(0)$ is formed from the eigenvectors of the monodromy matrix and the Poincaré exponents that are related to the eigenvalues of the monodromy matrix such that $\lambda_i = \pm e^{\Omega_i T}$. Thus, the eigenvalues of the monodromy matrix are the modes corresponding to the linear dynamics in the vicinity of the periodic orbit.

While the nontrivial eigenvalues of the monodromy matrix reflect the characteristics of the underlying linear system, they also supply insight into the stability of the periodic orbit in the original, nonlinear system. Given a reference periodic trajectory, $\bar{x}_{PO}(t)$, the Lyapunov definition of stability decomposes a stability assessment of this solution into three classes:

- A reference solution is stable if a nearby solution, $\bar{x}(t)$, remains bounded and there exists a reasonable, positive constant $\epsilon > 0$ such that $\left|\left|\bar{x}(t) - \bar{x}_{PO}(t)\right|\right| \leq \epsilon$ for all time.

- A reference solution is asymptotically stable if a nearby solution, $\bar{x}(t)$, converges to the reference trajectory such that $\lim_{t\to\infty} \left|\left|\bar{x}(t) - \bar{x}_{PO}(t)\right|\right| = 0$.

- A reference solution is unstable if a nearby solution, $\bar{x}(t)$, diverges from the reference solution over time.

Thus, this definition of stability is based on the concept of boundedness [15]. Analyzing the eigenvalues of the monodromy matrix enables an assessment of the nonlinear stability of the periodic reference orbit using this definition [43]. Each periodic orbit possesses a monodromy matrix that can be decomposed into six eigenvalues and their associated eigenvectors. Two of the eigenvalues are equal to one; one of these modes corresponds to the eigenvector direction along the periodic orbit and the eigenvector corresponding to the second unit eigenvalue is directed along the family of orbits [41]. The other two pairs of nontrivial eigenvalues are typically represented in the form $\lambda = a \pm bi$, in terms of two real numbers, a and b. Two possible forms for each nontrivial eigenvalue of the monodromy matrix emerge:

- $\lambda_{1,2} = a \pm bi$: complex roots occur in conjugate pairs. When these eigenvalues lie on the unit circle, motion in the vicinity of the reference solution is bounded, i.e., the solution neither approaches nor departs the reference path over time.

- $\lambda_1 = a$, $\lambda_2 = 1/a$: real roots correspond to exponential growth or decay of the variation between the reference and perturbed paths over time. An eigenvalue of $|\lambda| > 1$ indicates an unstable mode, while an eigenvalue of $|\lambda| \leq 1$ corresponds to the stable mode.

Using these classifications, oscillatory modes are indicated by a nontrivial pair of complex or imaginary eigenvalues, $\lambda_1, \lambda_2 = a \pm bi$, that lie on the unit circle, while nontrivial eigenvalues in the form $|\lambda_1| > 1$ and $|\lambda_2| < 1$ emerge when the periodic orbits possess an unstable mode [41].

Although the magnitude of a real eigenvalue reflects a measure of the convergence or divergence of the nearby flow with respect to a reference trajectory, the sign of the eigenvalue indicates the relative direction of motion. To demonstrate this concept, consider a periodic orbit that possesses one real pair of eigenvalues, including a stable mode corresponding to $\lambda_1 = +a < 1$. As sketched in Figure 3.5(a), the presence of a stable mode described by a positive eigenvalue causes nearby gray trajectories to approach the reference periodic orbit, in blue, with an even number of twists about the orbit. If, however, the stable mode is indicated by a negative real eigenvalue of $\lambda_1 = -a > -1$, the behavior of the nearby flow is qualitatively different. In fact, as illustrated in Figure 3.5(b), a stable negative mode reflects the twisting of nearby trajectories an odd number of times around the periodic orbit, analogous to motion along a Mobius strip [44].

Employing a stability index enables straightforward visualization of the evolution of a pair of eigenvalues for the monodromy matrix for periodic orbits along a given family. In fact, the stability index leveraged in this investigation is defined as the sum of two eigenvalues in a pair, equal to:

$$s = \lambda_1 + \lambda_2 \tag{3.11}$$

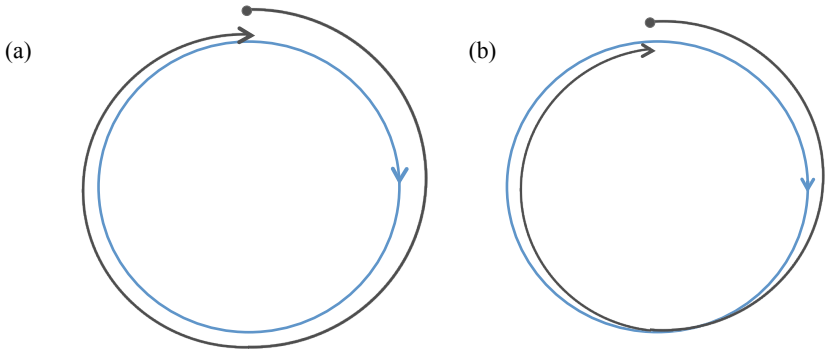

Fig. 3.5. Illustration of the motion in the vicinity of the blue periodic orbit. Nearby gray trajectories are governed by the mode corresponding to (a) a stable, positive eigenvalue and (b) a stable, negative eigenvalue.

Given the form of this expression, s is a real number, even for two eigenvalues that are, in fact, complex conjugates. As an example, the critical eigenvalues $\lambda_1, \lambda_2 = +1, +1$ correspond to the stability index $s = 2$, while eigenvalues equal to $\lambda_1, \lambda_2 = +i, -i$ produce a stability index of $s = 0$. In addition to enabling visualization of the evolution of the eigenvalues of periodic orbits along a family, the stability index is also employed to locate potential bifurcations.

3.1.2 Bifurcations

In the CR3BP, periodic orbits exist in families that, for a constant mass ratio, depend upon the energy constant as it evolves along the family. Varying C, the natural parameter, directly modifies the vector field, $\bar{f}(\bar{x})$, and, therefore, its infinite set of solutions. A local bifurcation occurs if a change in the energy constant results in a change in the qualitative behavior of the trajectories in the vicinity of a periodic orbit. In dynamical systems, a bifurcation may result in a change in the stability of the periodic orbits along a family, the formation of a new family of periodic orbits, or termination of the current family [45].

Since the stability of a periodic orbit reflects the behavior of nearby trajectories, local bifurcations are detected and characterized by monitoring the nontrivial eigenvalues of the monodromy matrix corresponding to each periodic orbit along a family. Recall that the monodromy matrix of a periodic orbit in three-dimensional space can be decomposed into three pairs of eigenvalues: one trivial pair indicating periodicity and the existence of a family of orbits, and two nontrivial pairs that reflect the stability of the orbit. In the complex plane, the nontrivial eigenvalues are located with respect to the unit circle, as illustrated in Figure 3.6. Nontrivial and complex eigenvalues that are located on the red unit circle possess a magnitude of unity, and indicate the existence of oscillatory modes. A pair of reciprocal eigenvalues that are located off the unit circle, however, indicate the presence of one unstable mode ($|\lambda| > 1$) and one stable mode ($|\lambda| < 1$) governing motion in the vicinity of the periodic orbit. As a pair of nontrivial eigenvalues, or, equivalently, the stability index, passes through any critical values, a bifurcation occurs.

Although many bifurcations exist in dynamical systems, two types are of particular interest within the dynamical environment that is the focus of this investigation:

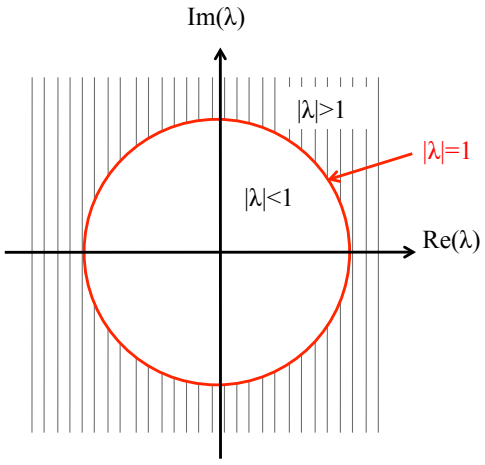

Fig. 3.6. Magnitude of the eigenvalues in the complex plane with respect to the unit circle, colored red.

tangent and period-multiplying bifurcations. The nontrivial eigenvalues reflecting the stability of the periodic orbits on either side of these bifurcations are depicted in the complex plane in Figure 3.7: the pair of eigenvalues are blue on one side and green on the opposite side of the bifurcation, with the critical value plotted in red. Each type of bifurcation is associated with a particular change in the characteristics of the dynamics in the neighborhood of the periodic orbits in a family.

A family of periodic orbits undergoes a tangent bifurcation when the orbital stability changes as a parameter evolves, e.g., the energy constant. During this type of local bifurcation, the nontrivial eigenvalues of the monodromy matrix pass through the critical values $\lambda_1 = \lambda_2 = +1, +1$. Simultaneously, the stability index passes through $s = 2$. The tangent bifurcation is further classified into three types [45]:

- Fold bifurcation: The orbits along a single family shift in terms of their stability, neither creating nor intersecting any other families.
- Pitchfork bifurcation: As the stability of the periodic orbits along a family changes, two additional families of similar period are formed. These new families of orbits possess the same stability as members of the original family prior to the bifurcation.

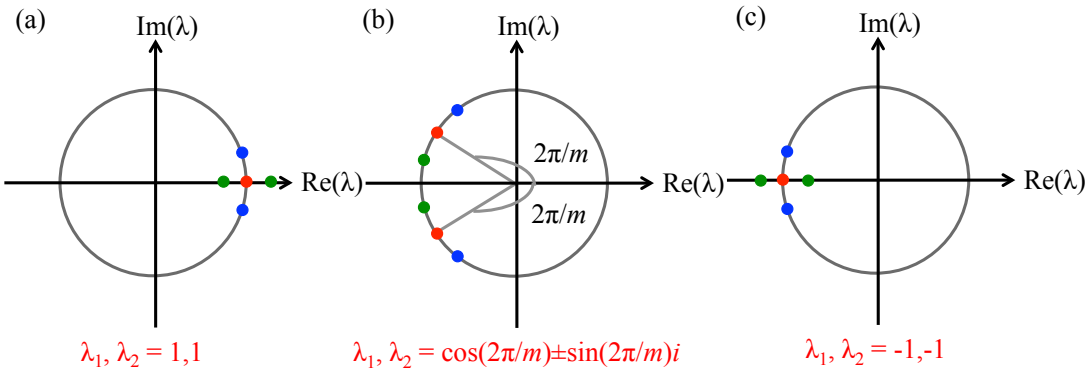

Fig. 3.7. Eigenvalues on either side of a (a) tangent bifurcation, (b) period-multiplying bifurcation for a multiplicative factor m and (c) period-doubling bifurcation (leading to a stability change).

- Transcritical bifurcation: A family of stable orbits intersects a family of unstable orbits. At the intersection, i.e., the common orbit, the two families exchange stability characteristics.

Across each type of tangent bifurcation, the eigenvalues that reflect the stability of orbits along a family transition between the unit circle and the real axis, as depicted in Figure 3.7(a).

During a period-multiplying bifurcation, a family of period-mq orbits emerges from a family of period-q orbits. At the critical value of the natural parameter, the orbit located at the intersection of the two families is equivalently described as a period-mq orbit or a period-q orbit traced out m times. Accordingly, the monodromy matrix of the period-mq orbit is expressed in terms of the monodromy matrix of the period-q orbit as:

$$\begin{aligned} \mathbf{\Phi}_{mq}(mT,0) &= \mathbf{\Phi}_q(mT,(m-1)T)\mathbf{\Phi}_q((m-1)T,(m-2)T)...\mathbf{\Phi}_q(2T,T)\mathbf{\Phi}_q(T,0) \\ &= [\mathbf{\Phi}_q(T,0)]^m \end{aligned}$$

where T is the period of the period-q orbit, and the subscript identifies the corresponding orbit. Decomposing these two monodromy matrices via Floquet theory, the modes of the period-mq orbit are expressed in terms of the modes of the period-q orbit as:

$$\lambda_{mq} = \lambda_q^m \tag{3.12}$$

At the period-multiplying bifurcation, the monodromy matrix of a planar period-mq orbit has two trivial pairs of eigenvalues: one pair corresponding to the periodicity of orbits along a family and the other pair signifying its intersection with another family. Since $\lambda_{mq} = 1$ for the first period-mq orbit in the family, a period-multiplying bifurcation with multiplicity m occurs when the eigenvalues of the monodromy matrices of period-q orbits along a family pass through the first and $(m-1)$-th complex roots of unity, as sketched in Figure 3.7(b) [46]. Therefore, this bifurcation is detected when the eigenvalues are equal to:

$$\lambda_1, \lambda_2 = \cos\left(\frac{2\pi}{m}\right) \pm \sin\left(\frac{2\pi}{m}\right) i \tag{3.13}$$

or, equivalently, when the value of the stability index is:

$$s = 2\cos\left(\frac{2\pi}{m}\right) \tag{3.14}$$

Since the stability index does not reflect the imaginary components of any complex conjugate eigenvalues, confirmation of a period-multiplying bifurcation requires verification that the eigenvalues do not split off the unit circle after passing through the corresponding roots of unity; such behavior corresponds to a Krein collision.

One limiting case of the period-multiplying bifurcation is particularly pertinent to this investigation: the period-doubling bifurcation that is accompanied by a change in the orbital stability. A period-doubling bifurcation is detected when a pair of eigenvalues passes through $\lambda_1, \lambda_2 = -1, -1$, and, therefore, corresponds to a critical value of the stability index, such that $s = -2$. As depicted in Figure 3.7(c), the orbits on one side of the bifurcation possess two nontrivial eigenvalues located on the unit circle. On the opposite side of the bifurcation, however, the eigenvalues of the monodromy matrix are located on the real axis, i.e., $\lambda_1 < -1$ and $\lambda_2 > -1$. In addition to a change in the qualitative stability characteristics of periodic orbits along a family, this bifurcation also indicates the intersection of the current period-q family with an additional family of period-$2q$ orbits [45].

3.1.3 Differential Corrections as an Orbit Computation Strategy

Since the equations of motion are not solvable analytically, a periodic orbit, or a trajectory with a set of desired characteristics, is traditionally computed via the formulation of a two-point boundary value problem. Various numerical methods are available to solve a problem of this form and new approaches are emerging as computational capabilities rapidly expand. However, given the nonuniform dynamical sensitivity in the CR3BP, shooting methods are employed in this investigation to compute a single periodic orbit; such a straightforward method is particularly efficient when the orbit is simply symmetric. From a single periodic solution, continuation methods are used to identify neighboring solutions along a family.

Consider a reference solution to a system of first-order nonlinear differential equations, $\dot{\bar{x}} = \bar{f}(\bar{x}(t))$, given an initial condition, $\bar{x}^*(t_1)$. Integrating this initial condition forward to a time t_2 supplies a path with a final state vector $\bar{x}^*(t_2)$. Although the elements comprising this final state vector generally do not meet a specified set of constraints, an alternative trajectory within its vicinity may satisfy the requirements, particularly if the integration time is allowed to vary. Modifying the reference initial condition by a variation $\delta\bar{x}(t_1)$ can produce a distinctly different path that, when integrated until a time $t_2 + \delta t_2$, satisfies a given set of boundary conditions. The trajectory, $\bar{x}_d(t)$, therefore, represents a solution to a two-point boundary value problem.

Numerous implementation strategies are available for numerical shooting schemes, with each strategy possessing advantages and disadvantages for a particular application. In this investigation, the numerical implementation recasts the two point boundary value problem as a vectorial root-finding problem, with the formulation based on a discrete set of free variables and constraints. At the initial point along the path, n_1 components of the state vector $\bar{x}^*(t_1)$ are required. The values of these components are subject to c_1 discrete constraints. Subtracting the number of constraints from the number of components in the initial state, there are $f_1 = n_1 - c_1$ free variables to be specified [47]. These free variables form an f_1-dimensional vector, $\bar{V}$:

$$\bar{V} = \left[\; V_1, V_2, ..., V_{f_1} \; \right]^T$$

Given the c_1 boundary conditions, this vector completely specifies the initial state, $\bar{x}^*(t_1)$. The n_1 equations of motion are then integrated forward from the initial state for a time $t_2 - t_1$ to obtain the final state, $\bar{x}^*(t_2)$. Depending on the accuracy of the initial guess for the free variables, $\bar{x}^*(t_2)$ may not satisfy the c_2 scalar constraints imposed at the boundaries of the trajectory. Accordingly, a c_2-dimensional vector, $\bar{F}$, is defined such that its scalar components, $F_i(\bar{V})$, capture any violations of the independent boundary conditions along a given arc:

$$\bar{F} = \left[\; F_1(\bar{V}), F_2(\bar{V}), ..., F_{c_2}(\bar{V}) \; \right]^T$$

The individual scalar constraints, applied at t_1 and t_2, are formulated such that $F_i(\bar{V}) = 0$. Consequently, the vector that satisfies $\bar{F} = \bar{0}$, to within a reasonably small tolerance, is denoted $\bar{V}_d$ and describes the desired solution [47].

To determine the vector, $\bar{V}_d$, that represents the solution that satisfies each of the boundary conditions within $\bar{F}$, an iterative update procedure is employed. An initial guess for the free variables, $\bar{V}^0$, is first specified. This initial guess is obtained through a variety of methods, dependent upon the application of interest. Assuming that the initial guess is sufficiently accurate, a Taylor series expansion relative to $\bar{V}^0$, that is, the initial guess for the vector of free variables that represents the initial state along a desired arc. Retaining only first-order terms, this expansion is written as:

$$\bar{F}(\bar{V}_d) \approx \bar{F}(\bar{V}^0) + D\bar{F}(\bar{V}^0) \cdot (\bar{V}_d - \bar{V}^0) \tag{3.15}$$

where $D\bar{F}(\bar{V}^0)$ is a Jacobian matrix comprised of the partial derivatives of the constraint vector with respect to the elements of $\bar{V}$:

$$D\bar{F}(\bar{V}) = \begin{bmatrix} \frac{\partial F_1}{\partial V_1} & \cdots & \frac{\partial F_1}{\partial V_{f_1}} \\ \vdots & \ddots & \vdots \\ \frac{\partial F_{c_2}}{\partial V_1} & \cdots & \frac{\partial F_{c_2}}{\partial V_{f_1}} \end{bmatrix} \tag{3.16}$$

Since the vector $\bar{F}$ is equal to the zero vector when the set of free variables deliver the desired solution, Eq. (3.15) simplifies to:

$$\bar{0} \approx \bar{F}(\bar{V}^0) + D\bar{F}(\bar{V}^0) \cdot (\bar{V}_d - \bar{V}^0) \tag{3.17}$$

Since Eq. (3.15) is truncated, the procedure to solve for $\bar{V}_d$ is iterative and the approach for solving this first-order expression for $\bar{V}_d$ depends upon the number of independent constraints compared with the number of free variables. If the number of free variables equals the number of constraints at t_2, that is, $f_1 = c_2$, the Jacobian matrix is square and invertible. Rearranging the Taylor series expansion, a first-order update equation is obtained:

$$\bar{V}_d = \bar{V}^0 - (D\bar{F}(\bar{V}^0))^{-1}\bar{F}(\bar{V}^0)$$

Generalizing, the update equation at any iteration i is, therefore, expressed as:

$$\bar{V}^{i+1} = \bar{V}^{i} - (D\bar{F}(\bar{V}^{i}))^{-1}\bar{F}(\bar{V}^{i}) \tag{3.18}$$

If, however, there are more free variables than constraints, i.e., $f_1 > c_2$, infinitely many solutions satisfy the boundary conditions [47]. Selecting the minimum-norm solution, one of many options for solving Eq. (3.17), minimizes the distance between $\bar{V}^{i}$ and $\bar{V}^{i+1}$. For the minimum norm solution, the first-order update equation at iteration i is equal to:

$$\bar{V}^{i+1} = \bar{V}^{i} - D\bar{F}(\bar{V}^{i})^{T}[D\bar{F}(\bar{V}^{i}) \cdot D\bar{F}(\bar{V}^{i})^{T}]^{-1}\bar{F}(\bar{V}^{i}) \tag{3.19}$$

Although the rectangular Jacobian matrix $D\bar{F}(\bar{V}^{i})$ is not invertible, multiplying by its transpose produces a square, symmetric matrix that can be inverted.

The update equations, Eq. (3.18) and Eq. (3.19), resemble a vector formulation of the well-known Newton's method, a fixed-point iteration scheme that updates the approximation to a root using the first derivative of the function. Assuming that an initial guess is sufficiently close to the root of $\bar{F}$, Newton's method exhibits second-order convergence over subsequent iterations [48]. Comparing the magnitude of the error vector at iterations i and $i+1$, the ratio:

$$\frac{||\bar{F}(\bar{V}^{i+1})||}{||\bar{F}(\bar{V}^{i})||^{2}}$$

should approach a constant value, demonstrating the quadratic convergence of this fixed point iteration scheme [48].

3.1.4 Multiple Shooting Algorithm

Although a periodic orbit within the multi-body dynamical environment described by the CR3BP can be computed using a variety of techniques, a multiple shooting algorithm is leveraged in this investigation. Common alternative procedures for computing a periodic orbit in the CR3BP include: exploiting a truncated normal form representation of a center manifold, finite difference methods, and collocation [49], [50], [51]. Nevertheless, a multiple shooting scheme employs intermediate

nodes that are distributed along an initial guess. Simultaneously integrating the states at each of these nodes produces multiple arcs that comprise the initial guess for a periodic orbit. This concept is sketched in Figure 3.8 for an arbitrary periodic orbit decomposed into seven arcs. The states at the nodes, represented as red dots, form the initial guess, labeled $\bar{x}^*(t_i)$, for $i = 1...7$. Integrating each six-dimensional node state for a time δt_i yields seven arcs, each with endpoints $\bar{x}^*(t_i + \delta t_i)$ that are denoted by blue dots. The discontinuities between the beginning and end points of neighboring arcs are identified by the dashed arrows. A multiple shooting algorithm eliminates these discontinuities to within a specified tolerance, and the corrected states, $\bar{x}(t_i)$, lie on the nearby periodic solution, represented as a blue dashed path. This particular numerical scheme for solving a two-point boundary value problem is typically leveraged in the computation of a periodic orbit in the CR3BP given a reasonable initial guess. One advantage of using a multiple shooting scheme is the

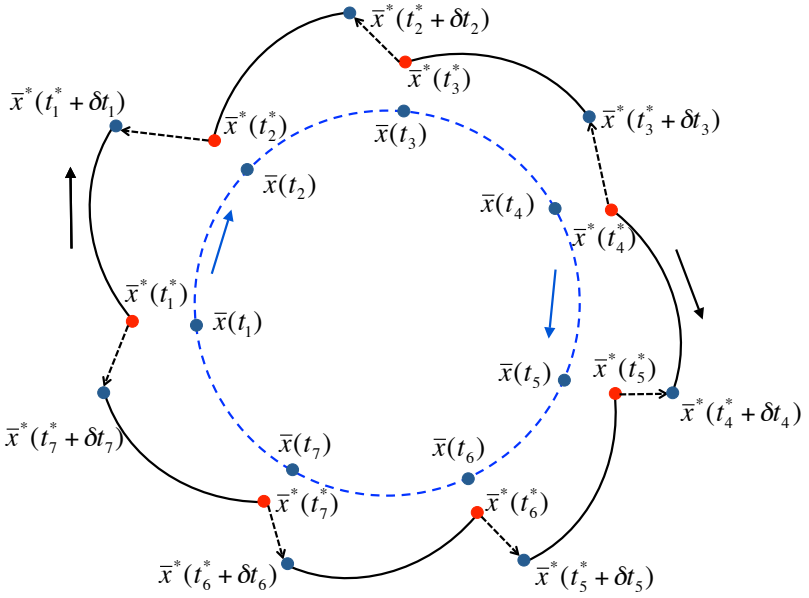

Fig. 3.8. Illustration of variable time multiple shooting formulation to target a periodic orbit.

reduction of error in the numerically-computed monodromy matrix. Recall that the monodromy matrix represents the sensitivity of the final state along the reference orbit, with respect to changes in an initial state $\bar{x}^*(t_1)$. Using the decomposition property of the STM in Eq. (3.6), the monodromy matrix is computed as the product of the STMs corresponding to n intermediate arcs along a path or arc, integrated for a time $\delta t_i = (t_{i+1} - t_i)$. The determinant of the assembled monodromy matrix may be closer to unity than the determinant of the monodromy matrix constructed through the continuous integration of the STM over a complete orbital period.

Consider a multiple shooting algorithm formulated to target a periodic orbit using n nodes equally spaced in time. Specification of the initial state along each arc, therefore, contributes six elements per node to the free variable vector, along with an additional variable for the integration time over each arc, t_{int}. Thus, the free variable vector, $\bar{V}$, can be defined as:

$$\bar{V} = [\bar{x}^*(t_1), \bar{x}^*(t_2), ..., \bar{x}^*(t_n), t_{int}]^T$$

where $t_j = (j-1)t_{int}$ is the time at the j-th node. The $6n+1$ free variables contained within $\bar{V}$, therefore, define a set of n arcs integrated over equal time intervals.

To target a natural trajectory that is continuous and periodic, discrete constraints are enforced between neighboring arcs. A continuity constraint of the form $\bar{x}^*(t_i + t_{int}) = \bar{x}^*(t_{i+1})$ is applied to all six states corresponding to each of the intermediate nodes, where $i = [1, n-1]$. Additionally, for these arcs to converge to a periodic solution, an explicit continuity constraint is applied to join the endpoint of the final arc and the first node. Since the Jacobi constant is conserved along a sequence of continuous and natural arcs, periodicity requires continuity over only five of the six state vector components at this boundary. Furthermore, to reduce any difficulties in convergence due to the nonuniquness of nodes distributed around a periodic orbit, an additional constraint is applied to the location of the first node. For this example, the first node along an initial guess for a periodic orbit is placed on the $y = 0$ line; assuming the periodic orbit crosses this plane, such a constraint does not impact the result. Addition of this constraint also ensures that the nullspace of the Jacobian

matrix is one-dimensional, which will enable the straightforward application of a pseudo-arclength continuation method to compute additional orbits along the family. Nevertheless, the constraint vector, $\bar{F}$, then takes the form:

$$\bar{F} = \begin{bmatrix} x^*(t_1 + t_{int}) - x^*(t_2) \\ y^*(t_1 + t_{int}) - y^*(t_2) \\ z^*(t_1 + t_{int}) - z^*(t_2) \\ \dot{x}^*(t_1 + t_{int}) - \dot{x}^*(t_2) \\ \dot{y}^*(t_1 + t_{int}) - \dot{y}^*(t_2) \\ \dot{z}^*(t_1 + t_{int}) - \dot{z}^*(t_2) \\ \vdots \\ x^*(t_n + t_{int}) - x^*(t_1) \\ y^*(t_n + t_{int}) - y^*(t_1) \\ z^*(t_n + t_{int}) - z^*(t_1) \\ \dot{x}^*(t_n + t_{int}) - \dot{x}^*(t_1) \\ \dot{z}^*(t_n + t_{int}) - \dot{z}^*(t_1) \\ y^*(t_1) \end{bmatrix} \tag{3.20}$$

These constraints are analytical expressions of the free variables, and are, therefore, straightforwardly differentiated to determine the Jacobian matrix as:

$$D\bar{F}(\bar{V}) = \begin{bmatrix} \frac{\partial \bar{x}^*(t_1+t_{int})}{\partial \bar{x}^*(t_1)} & -\mathbf{I}_{6\times 6} & \mathbf{0}_{6\times 6} & \cdots & \mathbf{0}_{6\times 6} & \frac{\partial \bar{x}^*(t_1+t_{int})}{\partial t_{int}} \\ \mathbf{0}_{6\times 6} & \frac{\partial \bar{x}^*(t_2+t_{int})}{\partial \bar{x}^*(t_2)} & -\mathbf{I}_{6\times 6} & \cdots & \mathbf{0}_{6\times 6} & \frac{\partial \bar{x}^*(t_2+t_{int})}{\partial t_{int}} \\ \vdots & & & & & \vdots \\ -\mathbf{H}_{5\times 6} & \mathbf{0}_{5\times 6} & \mathbf{0}_{5\times 6} & \cdots & \frac{\partial \bar{q}_2(t_n+t_{int})}{\partial \bar{x}^*(t_1)} & \frac{\partial \bar{q}_2(t_n+t_{int})}{\partial t_{int}} \\ [0\ 1\ 0\ 0\ 0\ 0] & \mathbf{0}_{1\times 6} & \mathbf{0}_{1\times 6} & \cdots & \mathbf{0}_{1\times 6} & 0 \end{bmatrix} \tag{3.21}$$

where $\bar{q}_2(t_i) = [x(t_i), y(t_i), z(t_i), \dot{x}(t_i), \dot{z}(t_i)]^T$, $\mathbf{I}_{6\times 6}$ is the 6×6 identity vector, $\mathbf{H}_{5\times 6}$ is the $\mathbf{I}_{6\times 6}$ matrix with the fifth row removed, and $\mathbf{0}_{i\times j}$ indicates an $i \times j$ matrix of zeros. By leveraging the STM, as well as the time derivative of the state vector, elements involving partial derivatives can be rewritten as follows:

$$\frac{\partial \bar{x}^*(t_i + t_{int})}{\partial \bar{x}^*(t_i)} = \mathbf{\Phi}(t_i + t_{int}, t_i) \qquad \frac{\partial \bar{x}^*(t_i + t_{int})}{\partial t_{int}} = \dot{\bar{x}}^*(t_i + t_{int}) \tag{3.22}$$

where $\mathbf{\Phi}(t_i + t_{int}, t_i)$ is the STM integrated along the i-th segment. Given that the number of constraints is less than the number of free variables, the update equation in Eq. (3.19) is applied at each iteration of the targeting scheme.

The multiple shooting algorithm employed in this analysis is tested on a prograde orbit encircling P_2 in the CR3BP, at a mass ratio of $\mu = 0.50$. In Figure 3.9(a), an initial guess comprised of five arcs is plotted in black. The initial nodes associated with these arcs, equally spaced in time, are represented as blue filled circles, while the endpoints along the arcs are represented as red open circles. Since the initial and final points corresponding to the five arcs do not coincide, this initial guess is clearly discontinuous. After six iterations of the multiple shooting algorithm, the free variable vector converges to the periodic orbit plotted in blue in Figure 3.9(b), with a black arrow representing the direction of motion along the path. The initial guess in this example has an error vector with an l_2-norm of $||F||_2 \approx 0.40$; this level of the error reflects an initial guess that is significantly far from a true solution. Thus, the algorithm requires a few iterations before the guess is sufficiently close to the true solution for quadratic convergence to be observed. The converged solution satisfies the continuity, periodicity and energy constraints to within a nondimensional tolerance on the order of 10^{-14}. When computing a periodic orbit in the CR3BP, a minimum acceptable value of the tolerance applied to the constraint vector may be selected through a variety of methods, including an assessment of the discontinuity between the beginning and end of the path when computed via a single integration over the entire orbital period. Additionally, the determinant of the final monodromy matrix is equal to unity with an accuracy on the order of 10^{-11}. This converged solution, therefore, represents a prograde periodic orbit about P_2 with a period of approximately 3.725 nondimensional time units.

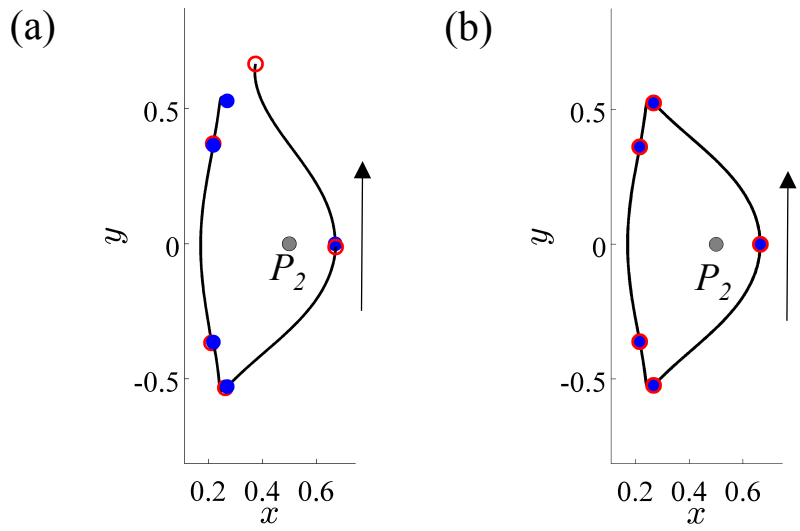

Fig. 3.9. Computation of a prograde periodic orbit around P_2 for $\mu = 0.50$ via a continuous time multiple-shooting scheme.

3.1.5 Numerical Continuation

A single periodic solution that belongs to a continuous, one-parameter family in the CR3BP can be exploited to obtain information representing other members of the family. Assuming that a parameter representing a family of orbits evolves smoothly, various continuation strategies are available for determining the solutions comprising each family, including natural parameter continuation and psuedo-arclength continuation. As depicted in the conceptual schematic in Figure 3.10(a), natural parameter continuation assumes knowledge of a periodic solution described by the free-variable vector, $\bar{V}$, at some value of a natural, frequently physical, parameter, p^*. In its most basic application, this known solution, represented as a blue dot located along the one-parameter curve, is used as an initial guess for a nearby orbit that possesses a value of the natural parameter equal to $p^* + \delta p$ and lies within the same family. The actual solution at this value of the natural parameter is represented as a red dot. Since the convergence of a solution using Newton's method requires a good initial guess, the

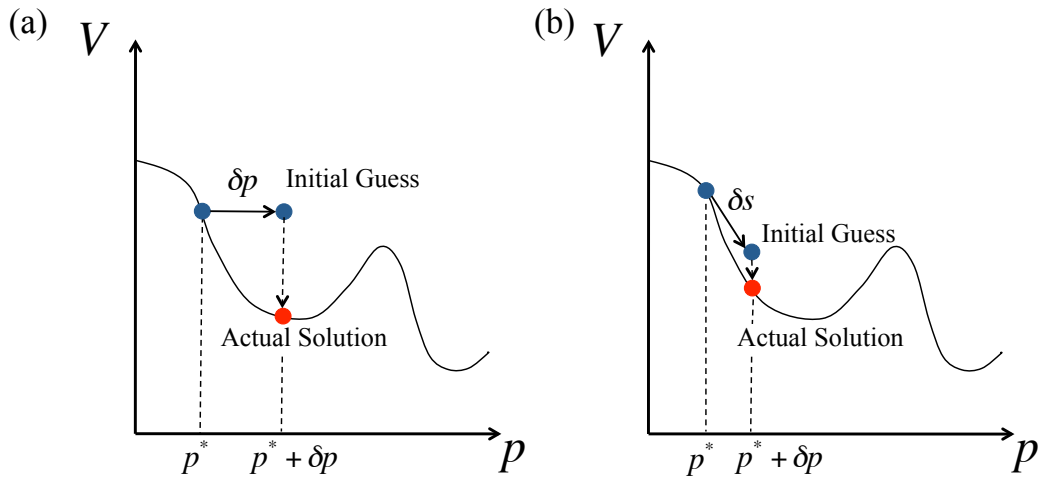

Fig. 3.10. Sample illustration of (a) natural parameter continuation and (b) pseudo-arclength continuation process.

success of a natural parameter continuation process depends upon the step size, δp, that is appropriate for the local slope of the solution curve. Psuedo-arclength continuation, however, incorporates knowledge of the gradient of this curve at p^* to predict a nearby solution [52]. As sketched in Figure 3.10(b), the initial guess is constructed by moving along the tangent vector using a distance δs. In fact, this tangent vector lies in the nullspace of the Jacobian matrix of the corrections algorithm, evaluated at the known solution. Accordingly, a pseudo-arclength continuation procedure often exhibits better convergence than true natural parameter continuation. In fact, if the direction in which the family evolves is not known a priori, a pseudo-arclength procedure can leverage the dynamical evolution more effectively. Thus, pseudo-arclength parameter continuation is employed in this investigation to construct a family of periodic or quasi-periodic solutions, in combination with a multiple shooting strategy to update the solution predicted at each step.

To demonstrate the computation of a family of periodic orbits, a large retrograde orbit in the exterior region for $\mu = 0.30$ is used as an initial solution to demonstrate the pseudo-arclength continuation method. Twenty members of the same family are

plotted in the rotating frame in Figure 3.11, each with a Jacobi constant value, C, within the range 3.885 to 5.705. The black arrow depicts the direction of motion along the orbits, while the blue arrow signifies the direction of an increasing energy constant for orbits within the family; the two primaries are indicated by the black dots. Computation of a family of periodic orbits in the CR3BP using this type of continuation process requires that the arclength, δs, is selected based on the dynamical properties, including: the geometry of the orbits, the presence of equilibrium points in the vicinity of the solution, changes in the orbital stability along the family, and the slope of a one-parameter curve representing the family in the solution space. Since this subset of orbits along the family possesses a simple geometry that remains far from the primaries and any equilibrium points, an arclength of $\delta s = 0.5$ nondimensional units is selected. As the shape and properties of the family of orbits evolves, the size of the arclength may be adjusted.

In constructing a family of periodic orbits, the targeting algorithm may sometimes fail to compute the next family member; due to divergence, the algorithm may converge to a solution belonging to another distinct family. Such behavior may occur

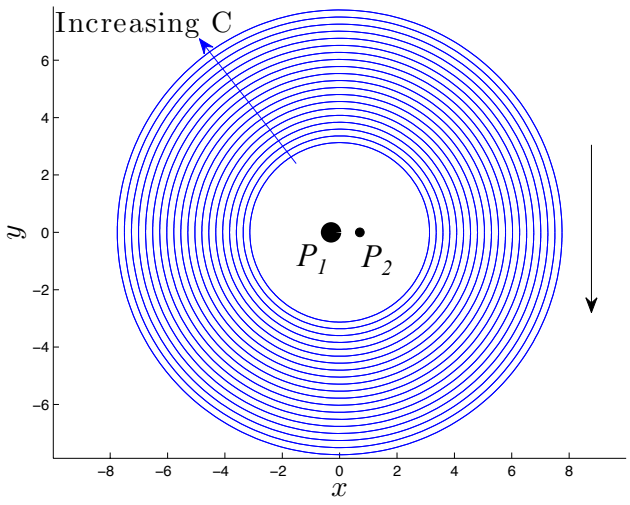

Fig. 3.11. Twenty members of a family of retrograde periodic orbits in the exterior region in the CR3BP for $\mu = 0.30$.

if the step size results in an initial guess that is either too far from the true solution for convergence, or the newly predicted initial guess is actually closer to solutions in another family. An adaptive step size procedure can be implemented, for example, by reducing the arc-length if the targeting algorithm does not converge within a given number of iterations. Alternatively, the numerical computation of a periodic orbit at a given energy level may not be successful because the family has terminated. Recording and analyzing the stability of each orbit during the continuation process can aid in ascertaining whether a family has terminated, evolved to a different family, or, perhaps, encountered a numerical issue that is not related to the physical evolution of the family. This check can also be accomplished through visualization of the dynamical environment in the vicinity of the periodic orbits along the family. In fact, an appropriately constructed discrete-time system that preserves periodicity may elucidate the stability and form of the periodic solutions of interest.

3.2 Quasi-Periodic Orbits

Stable periodic orbits are typically surrounded by quasi-periodic trajectories, corresponding to nonperiodic, bounded motion that lies on the surface of a torus [19]. As illustrated in Figure 3.12, the closed surface of a two-dimensional torus, outlined in grey, is generated as the product of two circles [43]. The central circle, highlighted in red, is associated with a nearby periodic orbit, while the blue circle corresponds to a transverse rotation. Each two-dimensional quasi-periodic trajectory, is, therefore, parametrically defined using two incommensurate, fundamental frequencies [15]. When these two frequencies, ω_1 and ω_2, are commensurate, their ratio is equal to the ratio of two integers: a limiting case that corresponds to a periodic orbit. Nevertheless, a periodic orbit with nearby oscillatory motion, as predicted by a pair of eigenvalues that lie on the unit circle, is associated with a family of quasi-periodic trajectories. Although tori inherit the behavior of a nearby periodic orbit, their characteristics can evolve significantly along the family. Accordingly, analysis of quasi-

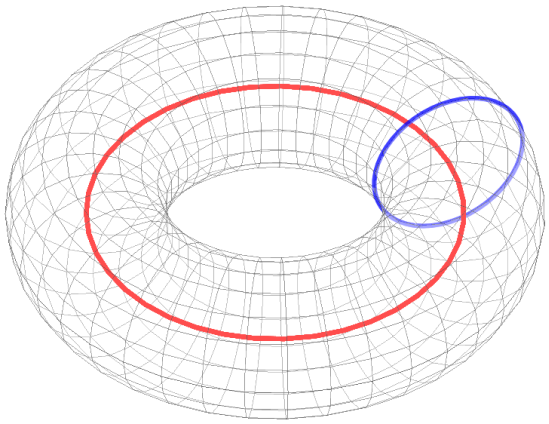

Fig. 3.12. A two-dimensional torus, the product of two circles.

periodic motion is valuable in a variety of scenarios: from the design of trajectories that must meet a given set of mission requirements, to the identification of regions of stable, bounded motion for an exoplanet that persists near a binary star system over a long time interval.

3.2.1 Computation via an Invariance Condition

In this investigation, quasi-periodic trajectories are computed using a method initially presented by Olikara and Scheeres that leverages an invariance condition and a multiple shooting formulation [53]. To numerically compute each torus along a family, a stroboscopic mapping technique is employed and relies on the definition of an invariant circle formed by the intersection of the torus with a higher-dimensional plane. To visualize this definition, consider the gray conceptual representation of a toroidal surface as depicted in Figure 3.13, along with the invariant circle, highlighted in red. A state along this invariant circle, colored purple, is integrated forward for a time $T_1 = 2\pi/\omega_1$. The final state, colored blue, also lies along the invariant circle and experiences a rotation by an angle of $\rho = 2\pi\omega_2/\omega_1$. Accordingly, the invariant

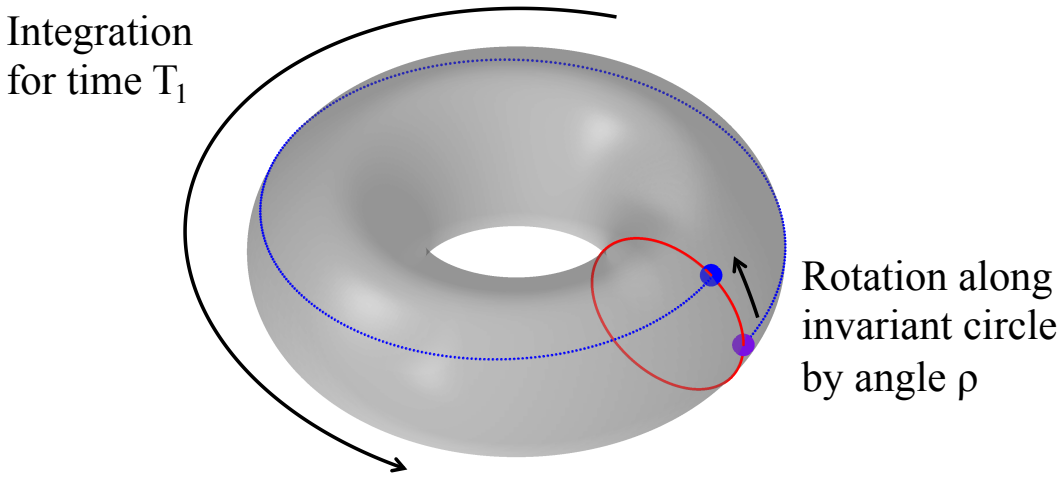

Fig. 3.13. Invariant circle (red) illustrated for a two-dimensional torus (gray surface). A single state along the circle (purple), when integrated forward in time for a time T_1 (blue), returns to the invariant circle and undergoes a rotation by angle ρ.

circle is formed by the set of states which, when integrated for a time T_1, return to the same circle in the six-dimensional phase space. As formulated by Olikara and Scheeres, this concept of an invariant circle is leveraged for numerical computation of a torus.

The procedure for computing tori is implemented numerically using a combination of differential corrections and continuation, following the approach demonstrated by Olikara and Scheeres [53]. A state, $\bar{v}_{QP}$, that lies on the surface of a two-dimensional torus in the CR3BP is expressed as a function of the angular variables in each of the central and transverse directions, i.e., θ_1 and θ_2, respectively. Along a torus, each of these angular coordinates varies at a constant rate equivalent to the nonresonant frequencies, ω_1 and ω_2. The time derivative of the state, $\bar{v}_{QP}(\theta_1, \theta_2)$, produces the following relationship between the angular variables, the associated frequencies, and the

system of differential equations, $\bar{f}(\bar{v}_{QP}, \theta_1, \theta_2, \mu)$, for motion along a two-dimensional torus in the CR3BP:

$$\dot{\bar{v}}_{QP}(\theta_1, \theta_2) = \frac{\partial \bar{v}_{QP}}{\partial \theta_1}\frac{d\theta_1}{dt} + \frac{\partial \bar{v}_{QP}}{\partial \theta_2}\frac{d\theta_2}{dt} = \frac{\partial \bar{v}_{QP}}{\partial \theta_1}\omega_1 + \frac{\partial \bar{v}_{QP}}{\partial \theta_2}\omega_2 = \bar{f}(\bar{v}_{QP}, \theta_1, \theta_2, \mu) \quad (3.23)$$

Furthermore, integration of this state, $\bar{v}_{QP}(\theta_1, \theta_2)$, for the time, T_1, is equivalently described via the following stroboscopic mapping:

$$\bar{v}_{QP}(\theta_1, \theta_2 + \rho) = \bar{F}_{QP}(\bar{v}_{QP}(\theta_1, \theta_2), \theta_1, \theta_2, T_1, \rho, \mu)$$

reflecting the periodicity of the angular variable θ_1 after a time T_1 and a rotation consistent with the transverse direction on the torus by the angle ρ. By leveraging this stroboscopic mapping, the problem of constructing a quasi-periodic trajectory is recast as the search for an invariant circle and, therefore, a fixed point. Consider, for a fixed value of $\theta_1 = \phi$, a state along the invariant circle, located at a value of the transverse angular coordinate, θ_2, that is labeled as:

$$\bar{u}_{QP}(\theta_2) = \bar{v}_{QP}(\phi, \theta_2)$$

Every state along this invariant circle, $\bar{u}_{QP}(\theta_2)$, when integrated forward for a time T_1, returns to the invariant circle and undergoes a rotation ρ. Thus, a torus is recovered upon identification of a set of states $\bar{u}_{QP}(\theta_2)$ that exactly repeat after a time T_1, following a reverse rotation, such that:

$$\boldsymbol{R}(-\rho)\bar{u}_{QP}(\theta_2 + \rho) = \bar{u}_{QP}(\theta_2) \quad (3.24)$$

where $\boldsymbol{R}(-\rho)$ is a matrix that rotates the state around the invariant circle by the angle $-\rho$ in the transverse direction. Then, this search for an invariant circle is expressed mathematically via the following invariance condition:

$$\boldsymbol{R}(-\rho)\bar{F}_{QP}(\bar{u}_{QP}(\theta_2), \theta_1, \theta_2, T_1, \rho, \mu) - \bar{u}_{QP}(\theta_2) = \bar{0} \quad (3.25)$$

Accordingly, quasi-periodic motion, is computed through identification of an invariant circle using a numerical root-finding algorithm, such as Newton's method.

To compute a generating torus near a reference periodic orbit with a nontrivial center subspace, an initial guess for the invariant circle is generated [53]. First, a single six-dimensional fixed point, $\bar{x}_f$, is selected along the periodic orbit. For this fixed point, the monodromy matrix is computed and, subsequently, the eigenvectors associated with the pair of complex conjugate eigenvalues of interest, λ_c and $\bar{\lambda}_c$. The real and imaginary components of the eigenvector, $\bar{e}_c$, are then employed in a linear approximation to construct an initial guess for an invariant circle along a nearby torus. This approximation to the set of states that lie along the invariant circle, $\bar{u}^0_{QP}(\theta_2)$, is constructed as:

$$\bar{u}^0_{QP}(\theta_2) = \bar{x}_f + \epsilon \left(\mathrm{Re}\left[\bar{e}_c\right] \cos(\theta_2) - \mathrm{Im}\left[\bar{e}_c\right] \sin(\theta_2) \right) \tag{3.26}$$

for N equally spaced values of $\theta_2 = [0, 2\pi/N, ..., 2\pi(N-1)/N]$, and ϵ, which denotes the size of the invariant circle relative to the periodic orbit. Information from the reference periodic orbit is also leveraged to create an initial guess for the stroboscopic mapping time and the rotation angle. For a sufficiently small value of ϵ, the eigenvalue corresponding to the oscillatory mode, λ_c, supplies a good guess for the rotation angle, such that $\rho \approx \mathrm{Re}[-i\ln(\lambda_c)]$, while the orbital period of the reference orbit is used to initialize the stroboscopic mapping time, $T_1 \approx T$.

A Fourier series expansion is leveraged to describe states along the invariant circle and, subsequently, construct the rotation matrix. First, each state along the invariant circle is approximated via a truncated Fourier series as:

$$\bar{u}_{QP}(\theta_2) \approx \sum_{m=-(N-1)/2}^{(N-1)/2} \bar{\Gamma}_m e^{im\theta_2} \tag{3.27}$$

where $\bar{\Gamma}_m$ is the complex-valued Fourier series coefficient vector with components in each of the six dimensions of the phase space. These vector coefficients, $\bar{\Gamma}_m$ are evaluated using the discrete Fourier transform via the following matrix relationship:

$$\boldsymbol{\Gamma} = \boldsymbol{D}\boldsymbol{u}_{QP} \tag{3.28}$$

where $\mathbf{\Gamma}$ is an $N \times 6$ matrix of the Fourier series coefficients, $\bar{\Gamma}_m$, $\boldsymbol{u}_{QP}$ is an $N \times 6$ matrix of the states along the invariant circle, $\bar{u}_{QP}(\theta_2)$, and $\boldsymbol{D}$ is a matrix consisting of the following elements:

$$D_{m,p} = \frac{1}{N} e^{-iK_m 2\pi(p-1)/N}$$

for $m, p = [1, N]$ and $K = [-(N-1)/2, ..., -1, 0, 1..., (N-1)/2]$. This series expansion enables computation of the rotation matrix $\boldsymbol{R}(-\rho)$ which is used to reverse the natural rotation for motion along the surface of a torus. In particular, this real rotation matrix is computed as follows:

$$\boldsymbol{R}(-\rho) = \boldsymbol{D}^{-1}\boldsymbol{Q}(-\rho)\boldsymbol{D}$$

for an $N \times N$ complex diagonal matrix, $\boldsymbol{Q}$, with elements $Q_{m,m}(-\rho) = e^{-iK(m)\rho}$. This Fourier series representation of the states along the invariant circle enables construction of the rotation matrix and, therefore, the invariance condition.

To solve the nonlinear invariance condition via root-finding, Newton's method is employed [53]. By linearizing the invariance condition in Eq. (3.25) with respect to a state on the invariant circle, $\bar{u}_R$, along with the stroboscopic mapping time and the rotation angle, the following first-order expansion is recovered:

$$\boldsymbol{R}(-\rho)\Big|_{\bar{u}_R}\left(\frac{\partial \bar{F}_{QP}}{\partial \bar{x}}\Big|_{\bar{u}_R}\delta\bar{u}_{QP} + \frac{\partial \bar{F}_{QP}}{\partial T_1}\Big|_{\bar{u}_R}\delta T_1\right) + \frac{\partial\left(\boldsymbol{R}(-\rho)\bar{F}_{QP}\right)}{\partial\rho}\Big|_{\bar{u}_R}\delta\rho - \delta\bar{u}_{QP} = \bar{0}$$

for $\bar{x} = [x, y, z, \dot{x}, \dot{y}, \dot{z}]^T$. Since $\bar{F}_{QP}$ does not explicitly depend upon ρ, this expression reduces to:

$$\boldsymbol{R}(-\rho)\Big|_{\bar{u}_R}\left(\frac{\partial \bar{F}_{QP}}{\partial \bar{x}}\Big|_{\bar{u}_R}\delta\bar{u}_{QP} + \frac{\partial \bar{F}_{QP}}{\partial T_1}\Big|_{\bar{u}_R}\delta T_1\right) + \frac{\partial \boldsymbol{R}(-\rho)}{\partial\rho}\bar{F}_{QP}\Big|_{\bar{u}_R}\delta\rho - \delta\bar{u}_{QP} = \bar{0} \quad (3.29)$$

Each of the partial derivatives in this linear expansion can be computed using information about the state and the STM, $\mathbf{\Phi}(T_1, 0)$, associated with integrating the invariant circle forward for a time T_1:

$$\frac{\partial \bar{F}_{QP}}{\partial \bar{x}} = \mathbf{\Phi}(T_1, 0) \qquad \frac{\partial \bar{F}_{QP}}{\partial T_1} = \dot{\bar{u}}_R(T_1) \qquad \frac{\partial \boldsymbol{R}(-\rho)]}{\partial\rho}\bar{F}_{QP} = \boldsymbol{D}^{-1}\frac{\partial \boldsymbol{Q}}{\partial\rho}\boldsymbol{D}\bar{u}_R(T_1)$$

where $\bar{u}_R(T_1)$ is a state along the invariant circle propagated forward for a time T_1. A differential corrections process using the linear approximation in Eq. (3.29) enables the determination of the states around the invariant circle, along with the stroboscopic mapping time, T_1, and rotation angle, ρ, that satisfy the invariance condition.

Due to the sensitivity associated with employing the STM to correct the states integrated over a sufficiently long time interval, a multiple shooting method is also incorporated into the torus computation algorithm [53]. This process is illustrated in Figure 3.14. The gray surface represents the torus, which is divided into $(n+1)$ segments. The discretized invariant circle is colored purple in Figure 3.14. Each of the N discretized states along the purple invariant curve is propagated forward for a time $T_1/(n+1)$, producing an intermediate set of N states along the torus. This process is repeated for n intermediate circles along the torus, as depicted in red in Figure 3.14. At each intermediate circle, $6N$ constraints enforcing full state continu-

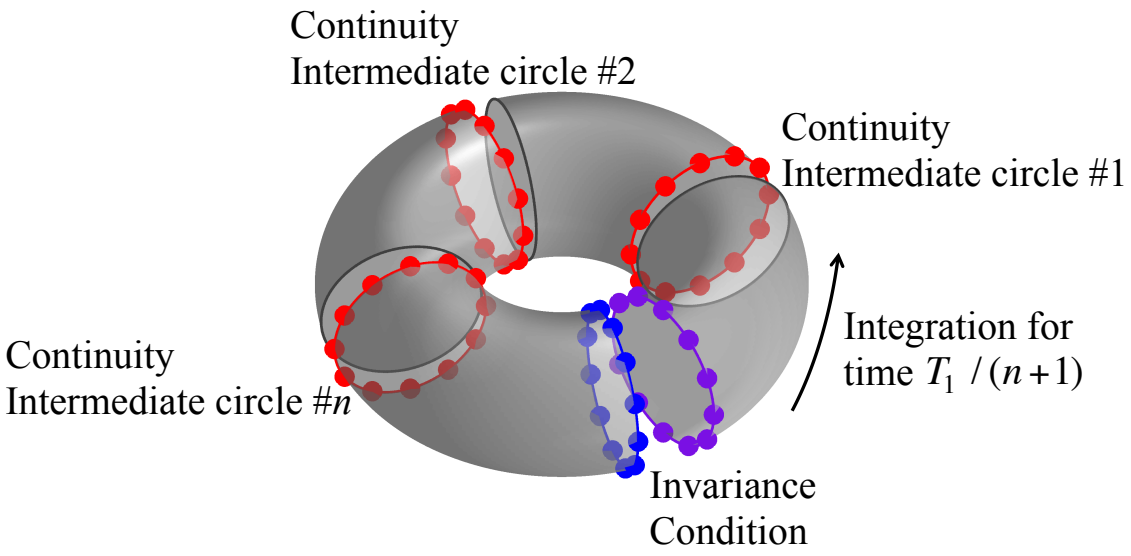

Fig. 3.14. Invariant circle (purple) illustrated for a two-dimensional torus (gray surface). Intermediate circles are indicated along the torus (red), as well as the states at the end of the final segment (blue). By enforcing continuity between each intermediate segment as well as the invariance condition, a torus is constructed.

ity are applied, thereby reducing the numerical sensitivity of this methodology when computing a torus in a chaotic nonlinear system. At the end of the final segment along the torus, each state lies along a curve, colored blue in Figure 3.14. For the torus to be closed and to exist in the CR3BP, each of the final states along this blue curve must lie along the invariant circle. Furthermore, after rotating this blue curve by an angle of $-\rho$, each state along the final invariant circle must coincide exactly with the corresponding state along the initial invariant circle, colored purple, producing $6N$ additional constraints to enforce the invariance condition in Eq. (3.25). An additional constraint is applied to ensure that the average value of the Jacobi constant corresponding to each state along the invariant circle is equivalent to a desired value of the Jacobi constant [53]. Depending upon the application, this constraint may be optional. Furthermore, constraints are also applied to fix the location of the invariant circle in the θ_1 coordinate, mitigating numerical issues associated with nonuniqueness of the invariant circle along the central axis of the torus. During the differential corrections process, this set of constraints is satisfied to within a specified tolerance by tuning the following variables: T_1, ρ, the N six-dimensional states along the invariant circle, and the N six-dimensional states along each of the n intermediate circles around the torus. Once a generating torus has been recovered, additional tori along the family are computed for a fixed Jacobi constant using pseudo-arclength continuation. This continuation method is repeated either until the family of tori is computed in its entirety, or the frequencies ω_1 and ω_2 approach a resonant ratio. This procedure, leveraging multiple-shooting and pseudo-arclength continuation, along with the invariance condition, enables the computation of a family of quasi-periodic trajectories.

As an example of the utility of numerically computing quasi-periodic motion via the invariance condition, consider a reference periodic orbit within the Earth-Moon L_1 vertical family. The sample periodic orbit, displayed in black in Figure 3.15 possesses an orbital period of approximately 12.19 days and a Jacobi constant of $C = 3.18126$. Using the monodromy matrix, this periodic orbit possesses a nontrivial

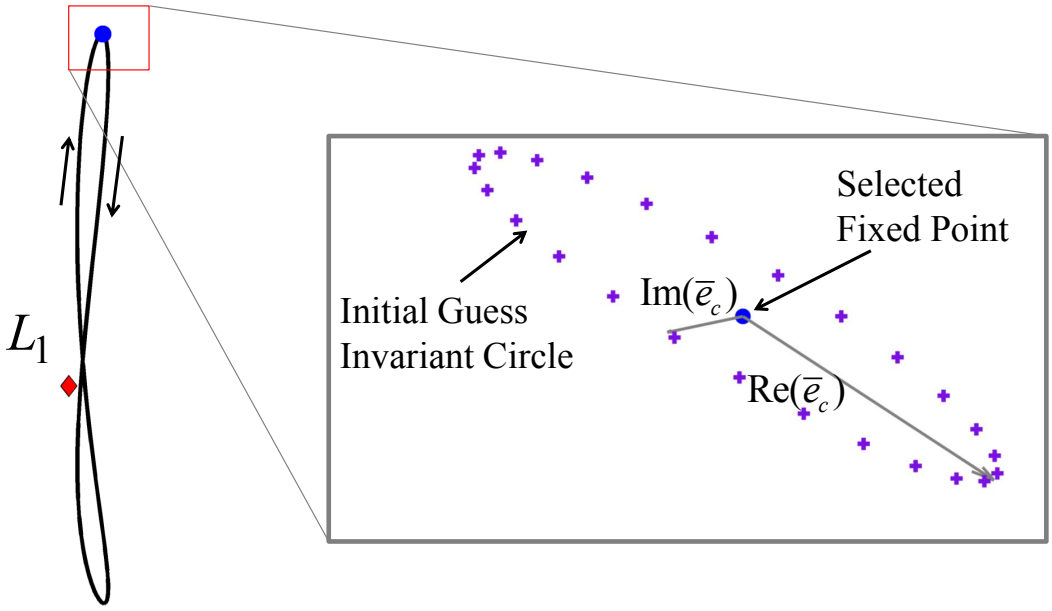

Fig. 3.15. Sample Earth-Moon L_1 vertical orbit with an orbital period of 12.19 days, along with an initial guess for an invariant circle near the selected fixed point (inset).

pair of complex conjugate eigenvalues equal to $\lambda_{c,1} = 0.97576 + 0.21885i$, $\lambda_{c,2} = 0.97576 - 0.21885i$. Since these eigenvalues lie on the unit circle, they indicate the existence of a family of quasi-periodic trajectories. Next, a fixed point, indicated by a blue filled circle in Figure 3.15, is selected at the maximum positive z location along the periodic orbit. At this location, the eigenvector corresponding to the complex mode $\lambda_{c,1}$ is used to construct an initial guess for the invariant circle via Eq. (3.26) for $N = 25$ equally spaced angles in the θ_2 coordinate and a nondimensional value of $\epsilon = 1 \times 10^{-5}$. This initial guess for the invariant circle is plotted in configuration space using purple crosses in the inset image within Figure 3.15, along with the associated fixed point. Then, initial guesses for the stroboscopic mapping time and the rotation angle are approximated using the orbital period and the complex eigenvalue to equal the following values:

$$T_1 \approx T = 2.7941 \qquad \rho \approx 2\pi\omega_2/\omega_1 = 0.22064 \tag{3.30}$$

Along the central axis, the torus is discretized to produce $n = 3$ intermediate circles by integrating each of the 25 states along the initial guess for the invariant circle in increments of 3.048 days. The initial guesses for T_1, ρ, the invariant circle, and the three intermediate circles are then corrected by leveraging the invariance condition along with a multiple shooting method. This generating solution for quasi-periodic motion closely resembles the reference periodic orbit. However, this generating solution is used to compute additional members within the family via pseudo-arclength continuation. For instance, sample tori that exist within this family, each possessing a Jacobi constant of $C = 3.18126$, are plotted in Figure 3.16. At the selected Jacobi constant, the family of tori originate at the L_1 vertical periodic orbit and terminate at the corresponding L_1 Lyapunov periodic orbit. In fact, the evolution of the quasi-periodic orbits that lie along the displayed tori can significantly differ from the reference periodic orbit. Accordingly, quasi-periodic solutions offer alternative orbit options that may be actively incorporated into the design of complex paths for spacecraft subject to mission constraints, or the identification of possible motions of an exoplanet captured within a binary star system.

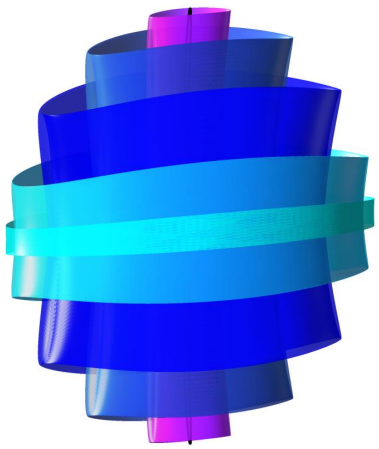

Fig. 3.16. Sample Earth-Moon L_1 vertical quasi-periodic orbits each possessing the same Jacobi constant as the reference periodic orbit, $C = 3.18126$, and plotted in configuration space.

3.3 Manifolds

Manifold structures departing and approaching unstable periodic and quasi-periodic orbits can guide the flow in various regions of the phase space, as well as influence the formation and existence of families of periodic orbits. Consider, for this example, a periodic orbit that is unstable and possesses one pair of stable and unstable modes, indicated by the eigenvalues $|\lambda_S| < 1$ and $|\lambda_U| > 1$. Accordingly, this unstable periodic orbit possesses natural flow that departs or approaches the orbit along unstable and stable manifolds, respectively. The associated manifold structures are generated by first discretizing the orbit into numerous fixed points. A small step is then introduced in the direction of the corresponding eigenvectors at each fixed point, $\bar{x}_{PO}$, to produce initial conditions for the stable and unstable manifold structures, $\bar{x}_{S,0}$ and $\bar{x}_{U,0}$, respectively:

$$\bar{x}_{S,0} = \bar{x}_{PO} \pm d \cdot \bar{e}_S \qquad \bar{x}_{U,0} = \bar{x}_{PO} \pm d \cdot \bar{e}_U \tag{3.31}$$

where $\bar{e}_S$ and $\bar{e}_U$ are the stable and unstable eigenvectors computed from the monodromy matrix at the fixed point of interest and normalized by the magnitude of the position components, while d is a sufficiently small real-valued number. Then, the unstable and stable manifold structures are computed by propagating these initial conditions forward and backward in time, respectively [41]. Sample planar manifold structures are displayed in Figure 3.17 for an L_1 Lyapunov orbit in the Sun-Earth system. In this projection onto the configuration space, the periodic orbit is displayed in black, while L_1 is indicated by a red diamond and the Earth is displayed as a black circle. The stable manifold (blue) corresponds to planar motion that naturally flows into the periodic orbit, while the unstable manifold structure (green) includes planar trajectories that naturally depart the orbit. When propagated for a sufficiently long time interval, these manifolds trace out complex paths in the six-dimensional phase space and may be leveraged in the design of low-cost or free transfers between various regions of a multi-body system.

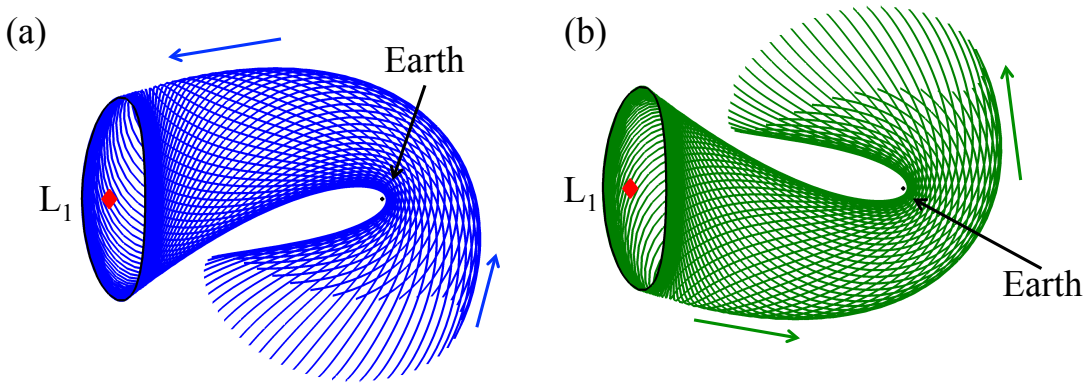

Fig. 3.17. (a) Stable and (b) unstable manifolds associated with an L_1 Lyapunov orbit in the Sun-Earth system.

Natural manifold structures are also valuable in exploring the existence of a variety of periodic orbits as the natural parameters of the dynamical system are varied. In fact, two types of periodic orbit families exist, and are distinguished by their formation process: regular and irregular periodic orbits. As described by Contopoulos, regular orbits are those emerging as a result of bifurcations from a central periodic orbit. Irregular orbits, however, are formed close to the homoclinic and heteroclinic tangles of the manifolds corresponding to unstable periodic orbits [19]. Such families are generated at a tangent bifurcation as a pair of stable and unstable periodic orbits. This observation suggests that manifolds also play a key role in governing the existence and evolution of other families of periodic orbits.

3.4 Poincaré Mapping

To construct a Poincaré map from a system of differential equations, the concept of a surface of section is introduced. Consider the system of six scalar autonomous, nonlinear differential equations represented in vector form:

$$\dot{\bar{x}} = \bar{f}(\bar{x})$$

with initial conditions $\bar{x}_0 = [x_0, y_0, z_0, \dot{x}_0, \dot{y}_0, \dot{z}_0]^T$. Integrating these differential equations forward from a time t_0 to t produces a solution, $\bar{x}(\bar{x}_0, t)$, or equivalently, a continuous time flow, $\phi_t(\bar{x}_0)$ [42]. For solely planar motion, the four-dimensional phase space of the flow is reduced to three dimensions by considering initial conditions at a given energy: if three of the four coordinates x_0, y_0, $\dot{x}_0$ and $\dot{y}_0$ are known, the fourth coordinate is determined from the Jacobi constant [19]. Then, a smooth surface of section, Σ, is selected such that the flow is transverse to the hyperplane [42]. As illustrated in Figure 3.18, the flow through $\bar{x}_0$ is propagated forward or backward in time. Its first intersection with the surface of section is denoted the Poincaré map, P, such that $\bar{x}_0 \rightarrow P(\bar{x}_0)$. Subsequently, the n-th intersection of the flow with the surface of section is denoted $P^n(\bar{x}_0)$, crossing the surface of section in either the positive or negative direction. A two-sided map records crossings in both the positive and negative directions while a one-sided map records only crossings in one direction: an important distinction that is critical when defining the map [42]. Since the flow at a given energy level crosses the hyperplane transversally, the discrete time mapping P

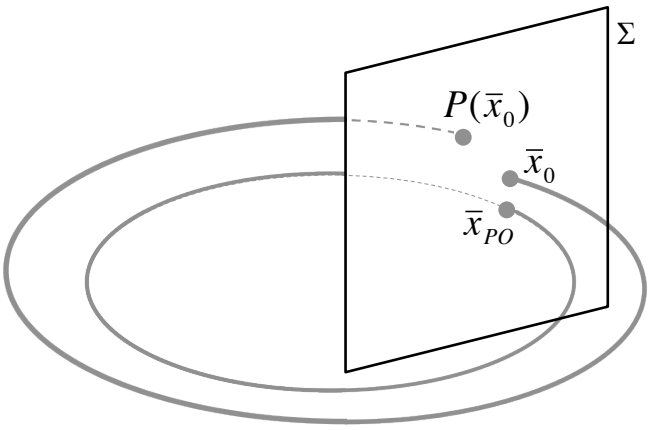

Fig. 3.18. From the initial state $\bar{x}_0$ in Σ, the mapping $\bar{x}_0 \rightarrow P(\bar{x}_0)$ represents the intersection of the surface of section as the first return of the flow through $P(\bar{x}_0)$.

possesses a dimension of two. In comparison to the original system of continuous time differential equations, the reduction in the dimension of the phase space significantly simplifies visualization of the flow, while preserving many of the physical properties of the continuous-time solutions that intersect the surface of section. Properties that are preserved by the mapping P include stability and periodicity. As depicted in Figure 3.18, a periodic orbit repeatedly crosses the surface of section at the intersection labeled $\bar{x}_{PO}$, exhibiting periodicity in the discrete-time mapping and is labeled a fixed point in the flow. A stable, periodic, continuous time solution, for example, is also stable and periodic in the discrete time system.

There are numerous possible options for a surface of section, dependent upon the desired application. For instance, a physical plane in configuration space such as a section at $y = 0$ has been explored extensively in the CR3BP, as many planar trajectories tend to revolve around the primaries, successively crossing the x-axis [19]. One limitation when employing a $y = 0$ surface of section, however, is that information is only retained for trajectories revolving around the primaries. Trajectories that do not cross the x-axis, such as those that tightly orbit L_4, are not preserved in the transformation between the differential equations and this particular discrete mapping. Alternative definitions for a surface of section include time, a function or an event, such as periapsis or apoapsis [54], [55], [56]. Periapsis occurs along a trajectory at a locally minimum distance relative to a given central body, while apoapsis occurs at the locally maximum distance. At each apse, the radial velocity is equal to zero. Accordingly, the position and velocity vectors relative to the central body must be perpendicular and, in the rotating frame of the CR3BP, the following orthogonality condition is satisfied:

$$(x - x_{Pi})\dot{x} + y\dot{y} + z\dot{z} = 0 \tag{3.32}$$

where x_{Pi} is the x-coordinate of the primary of interest, P_i, located along the x-axis. When this condition is satisfied along a trajectory, an apse occurs [56]. The radial acceleration and, therefore, the time derivative of this orthogonality condition, can

be used to classify the apse as an apoapsis or a periapsis. In combination with Eq. (3.32), a periapsis occurs when the following condition is satisfied:

$$\dot{x}^2 + \dot{y}^2 + \dot{z}^2 + (x - x_{Pi})\ddot{x} + y\ddot{y} + z\ddot{z} \geq 0 \tag{3.33}$$

while an apoapsis occurs when:

$$\dot{x}^2 + \dot{y}^2 + \dot{z}^2 + (x - x_{Pi})\ddot{x} + y\ddot{y} + z\ddot{z} \leq 0 \tag{3.34}$$

Depending upon the apse of interest, one of these conditions, along with Eq. (3.32), can be used to define a surface of section. A periapsis or apoapsis Poincaré map can reflect motion in various regions of configuration space, and may be useful for trajectory design applications [54], [55]. While there are various options for a surface of section, an appropriate definition is selected based upon the application and characteristics of the trajectories of interest.

3.4.1 Identification of Map Structures

A Poincaré map can elucidate the form of various types of solutions present at a particular energy level in the CR3BP, while also offering a qualitative assessment of the behavior of nearby trajectories. Consider, for example, three types of dynamical structures captured on a Poincaré map: periodic orbits, quasi-periodic trajectories, and stable or unstable manifold structures.

Period-q orbits repeat after every period, appearing as q points on an appropriately defined one-sided map. Two examples of the representations of periodic orbits on a Poincaré map are illustrated in Figures 3.19 and 3.20. The first figure highlights the map for a simple planar period-1 orbit and a planar period-4 orbit appears in the second figure. On the left in both figures, the trajectories are depicted intersecting a conceptual representation of a surface of section, Σ. These intersections are isolated and plotted on the one-sided Poincaré map on the right. Behavior near the points of intersection with the surface of section qualitatively describes the orbital stability.

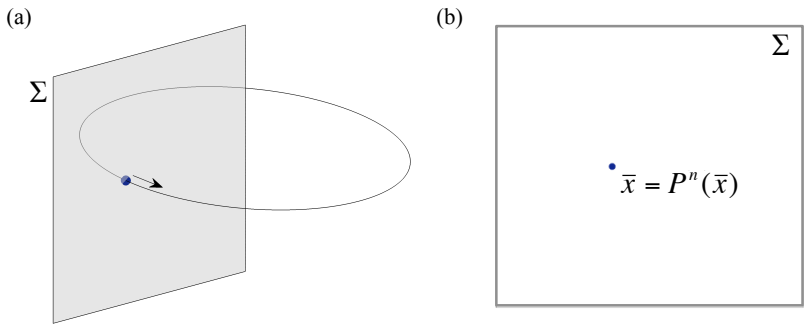

Fig. 3.19. Period-1 orbit (a) intersecting a surface of section and (b) represented as a fixed point on the resulting Poincaré map.

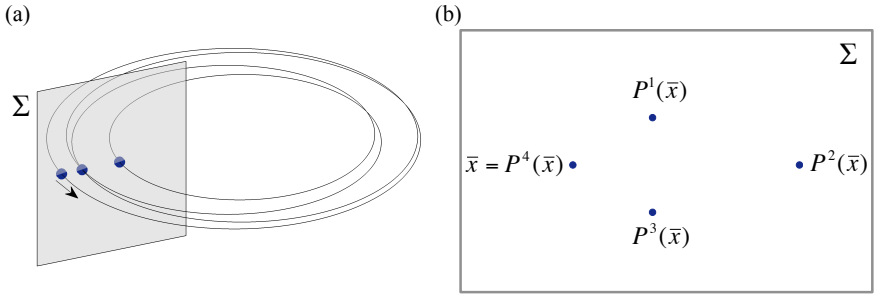

Fig. 3.20. Period-4 orbit (a) intersecting a surface of section and (b) represented as four successive points on the resulting Poincaré map.

If a period-q orbit is stable, it is surrounded by an infinite number of quasi-periodic trajectories in its vicinity. Since quasi-periodic motion traces out the surface of a torus, it appears as a series of q closed curves on the map [42]. Within each of these curves lies one of the q points corresponding to the periodic orbit at the center of the torus. As an example, Figure 3.21(a) depicts the intersection of a quasi-periodic orbit with a surface of section. On a one-sided map, such as the map in Figure 3.21(b), the quasi-periodic orbit is represented as a single curve with a fixed point corresponding to a period-1 orbit at its center.

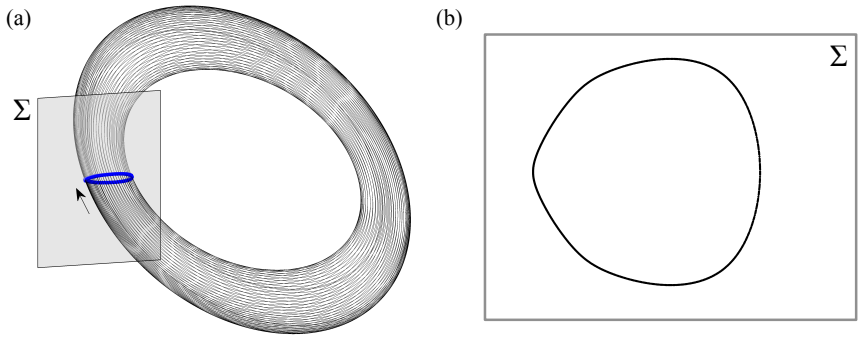

Fig. 3.21. Quasi-periodic orbit (a) intersecting a surface of section and (b) represented as a closed curve consisting of successive points on the resulting Poincaré map.

Since perturbations to an unstable orbit depart the vicinity of the orbit relatively quickly, unstable orbits are usually only identifiable on a map when they are embedded between stable islands. As illustrated in Figure 3.22, each of the q points correspond to an unstable periodic orbit that is located at an intersection of a separatrix on the map. In dynamical systems, a separatrix is a boundary between two different types of behavior, such as higher-order stable islands embedded within the two invariant curves corresponding to quasi-periodic motion. Unstable orbits can, therefore, be identified when they lie between stable islands. When surrounded by chaos, however, unstable orbits are not generally associated with any discernible structures on a Poincaré map because chaotic trajectories randomly intersect the map, forming a "dusty region", as depicted in Figure 3.23 [19].

To further demonstrate the value of Poincaré mapping techniques in enabling straightforward visualization, consider a planar stable manifold structure associated with an L_1 Lyapunov orbit in the Sun-Earth system at a Jacobi constant value of $C = 3.000884$. Trajectories along this manifold are propagated backwards in time until their first intersection with an apoapsis surface of section, defined with respect to the Earth. This dynamical structure (blue) is plotted in configuration space in Figure

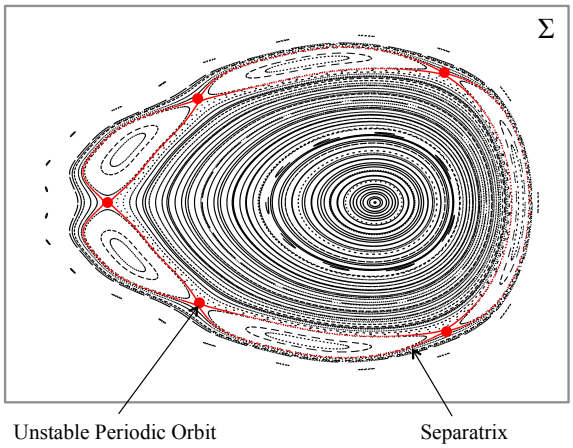

Fig. 3.22. A map featuring a central stable island with embedded higher order islands. Red dots correspond to an unstable period-5 orbit, located where the red separatrix intersects.

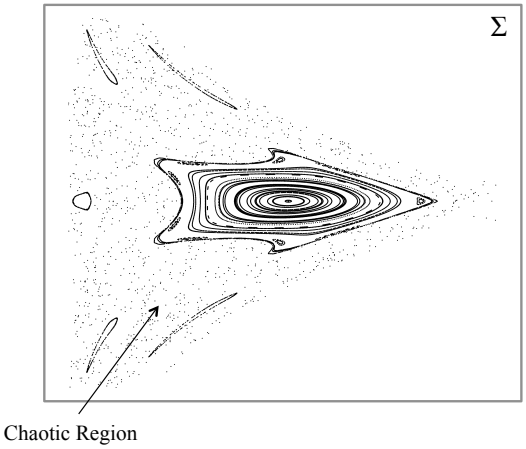

Fig. 3.23. Dusty regions on a map between stable islands, corresponding to chaotic orbits.

3.24(a), along with the associated periodic orbit (black). The Sun-Earth L_1 point, as well as the Earth, are also located on this plot, while arrows indicate the direction of motion along the stable manifold in forward time. By leveraging an apoapsis surface of section, the first apoapses along the associated surface, colored magenta, can be

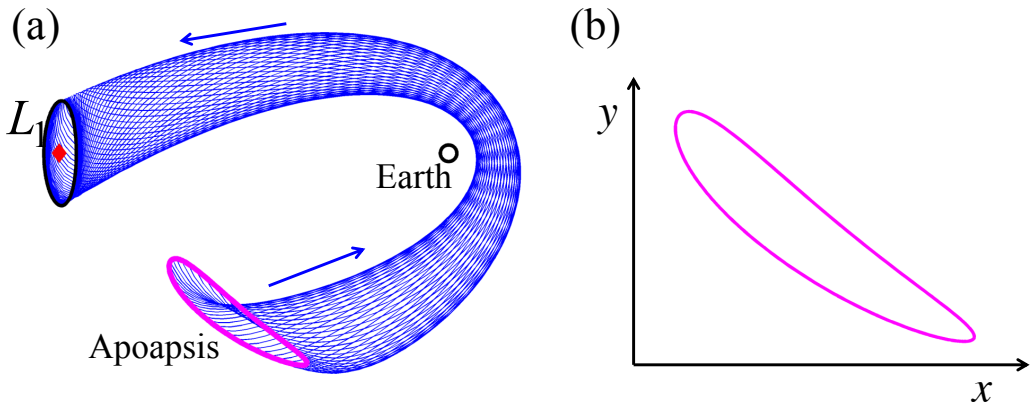

Fig. 3.24. Representation of a planar stable manifold tube associated with an L_1 Lyapunov orbit in the Sun-Earth system in (a) configuration space and (b) on a two-dimensional apoapsis map.

completely represented as a curve on a Poincaré map in the xy configuration space, as depicted in Figure 3.24(b). Recall that each state along the planar stable manifold tube exists within a four dimensional phase space. However, due to the energy and surface of section constraints, only two state variables are required to completely describe each planar apoapsis on the stable manifold structure. Specifically, the map in Figure 3.24(b) is portrayed in two-dimensional xy configuration space to enable an intuitive visualization. Furthermore, this structure on the map also offers insight into the fate of a planar state, $\bar{x} = [x, y, \dot{x}, \dot{y}]^T$, within its vicinity. For instance, states that lie inside this curve in all four dimensions produce trajectories that depart the Earth vicinity through the Sun-Earth L_1 gateway, while states outside of the magenta curve of apoapses do not. Alternatively, the resulting trajectories may remain within the Earth vicinity for at least one revolution around the Earth, or pass through the L_2 gateway. Such qualitative analysis of the behavior of trajectories that lie near manifold structures is enabled by the application of Poincaré mapping strategies and is valuable in the design of complex spacecraft trajectories.

4. EVOLUTION OF PERIODIC ORBIT FAMILIES IN THE RESTRICTED PROBLEM

As the natural parameters in a dynamical system are varied, the existence and evolution of families of periodic orbits may be impacted. Recall that in the CR3BP, these families of periodic orbits contribute to an underlying dynamical structure formed by attracting, bounding or repelling trajectories in their vicinity. In fact, the existence, form and stability of these periodic orbits impact the availability of long-term stable motions or natural pathways for transfers between various regions of space. Such insight into the available dynamics within a multi-body system across a range of natural parameters is valuable in a variety of scenarios, including the search for potential exoplanetary motions near binary stars or the design of complex paths for spacecraft within a system that possesses a mass ratio that is not accurately known. Accordingly, structural changes that occur along a family of periodic orbits are investigated by leveraging stability analyses to locate bifurcations.

To visualize the stability evolution across a given family of orbits at various mass ratios, a two-dimensional representation, similar to an exclusion plot, is introduced [11]. Exclusion plots are often used in physics to depict constraints on combinations of parameters [57]. This concept is extended to represent the stability of periodic orbits in the vicinity of binary systems on a two-dimensional plot as a point colored by the type of linear stability it exhibits. The resulting composite stability representation corresponding to a specified family, over a range of natural parameters, offers an elegant and straightforward visualization of the orbital stability of members across the family, thereby enabling the detection of any structural changes, or bifurcations. The figures constructed in this investigation resemble Benest's original stability diagrams [26], [27], [28], [29]. However, key differences exist, including: the use of the orbital period as a constant comparable quantity, a mixed linear-log scale for the

mass ratio and the application to a wider variety of families. In fact, in this section, exclusion plots are constructed for the following simply-periodic families in the restricted problem at mass ratios in the range $\mu = [0.10, 0.50]$: distant retrograde orbits about the larger primary; distant and low prograde orbits about the larger primary; retrograde orbits that encircle both primaries; and Lyapunov orbits about L_1 [11]. As a comparison to the Sun-planet and planet-moon systems commonly examined in the solar system, as well as binaries with less evenly distributed masses, these composite stability representations are also extended to include, where applicable, mass ratios in the range $\mu = [1 \times 10^{-6}, 0.10)$. In addition, many structural changes identified using a composite stability representation of selected families in the restricted problem are examined using concepts from dynamical systems theory [11]. In later sections of this investigation, composite stability representations are also leveraged to examine the impact of an additional force contribution on the underlying dynamics within a binary system.

To visualize the stability of a family of periodic orbits across a range of natural parameters, such as the mass ratio in the restricted problem, a qualitative measure of the stability along a family is employed. Consider, for this investigation, only planar periodic orbits. At a specified value of the mass ratio, the in-plane and out-of-plane stability indices corresponding to periodic orbits along a family can each be plotted as a function of a continuously-varying natural parameter. Although it is nonunique, the orbital period serves as an intuitive characteristic quantity. In fact, in the search for exoplanets about binary systems using eclipse-timing or pulse-detection, the period may be an orbital parameter that can be accurately deduced, to within a multiplicative factor, without significant limiting assumptions. The in-plane and out-of-plane stability indices across a family of orbits at a given mass ratio each form a single curve when plotted against the orbital period. Often, the stability index along these curves exhibits a number of turning points and a large range of values. Simultaneously plotting these complex curves at various values of the mass ratio can hinder any exploration of the stability characteristics along the family. Accordingly,

a simplified representation of the stability in a two-parameter space, such as (μ, T), enables clearer visualization, and aids in the examination of the stability evolution across the family. To demonstrate this process, consider the stability index along a retrograde family of orbits in the exterior region of the restricted problem, encircling both primaries at a mass ratio of $\mu = 0.10$. Three sample orbits along this family are plotted in Figure 4.1(a) using individual colors to provide clarity. The direction of motion along these orbits is indicated by an arrow and the primaries are located by gray-filled diamonds. A zoomed-in view of the in-plane stability along this family as a function of the orbital period is displayed on the right in Figure 4.1(b). As evident from the figure, this family possesses an intricate stability curve. However, since the eigenvalues of the monodromy matrix reflect a linear approximation of the dynamics, they can only be used to qualitatively determine the type of stability exhibited by a periodic orbit in the nonlinear dynamical environment in the CR3BP. In particular, each orbit is classified using the stability index, s: stable, for $s = [-2, 2]$; positive unstable, for $s > 2$; and negative unstable, for $s < -2$. The point representing a single periodic orbit in the two-parameter space, (μ, T), can, therefore, be colored by the type of stability it exhibits. In this investigation, a stable orbit is assigned the color blue, a positive unstable orbit is colored red and negative instability is represented by the color purple. A composite stability representation, for a single value of the mass ratio, μ, appears in Figure 4.2 to summarize the stability information. Since multiple periodic orbits may possess the same orbital period, points corresponding to stable periodic orbits are brought to the front in each plot for this investigation, as they may correspond to the motion of interest when identifying potential stable motions, for example, of an exoplanet. Through examination of the stability curve, the retrograde exterior family consists of members with each of the three types of stability. Accordingly, at a mass ratio of $\mu = 0.10$, this family will contribute a single line consisting of blue, red and purple intervals to a composite stability representation in the two-parameter (μ, T) space, as displayed in Figure 4.2. Thus, a complex curve encompassing a large range of values of s is reduced to a single line that is overlaid

for various mass ratios within a specified range, forming a useful, two-dimensional composite stability representation. These plots are developed further for various families in the CR3BP and analyzed from the perspective of identifying potential stable motions of an exoplanet near a binary star system. For each type of orbit, examination of structural changes along a family is supported by the use of techniques from dynamical systems theory.

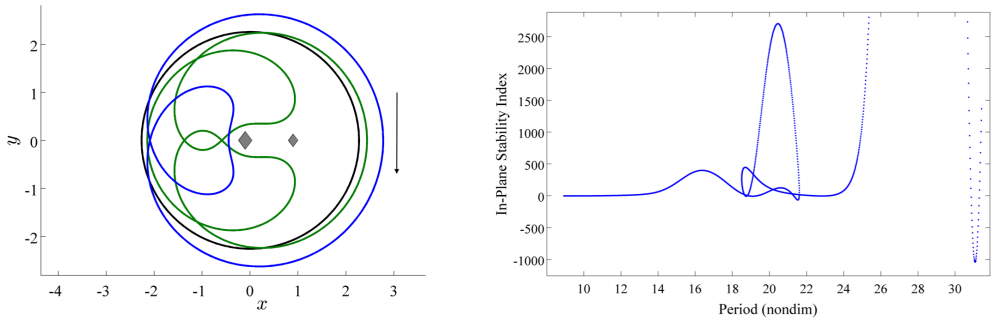

(a) Selected orbits plotted in configuration space.

(b) Zoomed-in view of the in-plane stability index.

Fig. 4.1. Stability of retrograde exterior family for a mass ratio of $\mu = 0.10$.

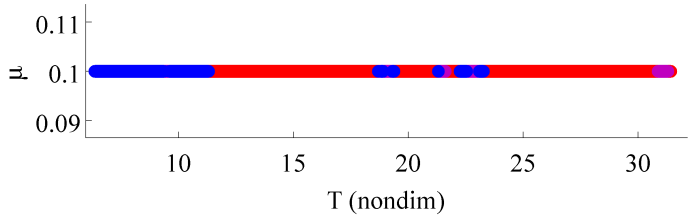

Fig. 4.2. Colored representation of the in-plane stability index along the retrograde exterior family at $\mu = 0.10$.

4.1 Retrograde Circumbinary Orbits

Consider a simply-periodic family of retrograde orbits that exists in the exterior region in the CR3BP to motivate the utility of composite stability representations and to demonstrate the construction of each plot. The corresponding stability representation for a subset of this family possessing periods below 20 nondimensional time units, is depicted in Figures 4.3(a) and 4.3(b) for the in-plane and out-of-plane stability, respectively. To limit the computational time and effort, members of each family are only computed until they pass through a predefined maximum period, pass within some radius of either primary, or become difficult to compute numerically. Since the dynamics in the CR3BP are nonlinear, each family may possess turning points that introduce multiple members with the same period. Recall that stable orbits are located within the blue regions of these composite representations, while negative instability is indicated by purple structures and positive unstable orbits are located within the red regions. Colored structures, therefore, reflect the stability of periodic orbits along a family, as well as the occurrence of some bifurcations. If the family is closed or reduces to an equilibrium point, for example, these "dynamical barriers" are represented via gray shading, which indicates that the family cannot extend into a particular region of the (μ, T) space. Since the CR3BP is inherently nonlinear, it may not be possible to accurately predict the stability index across any portions of the family that are not computed. Accordingly, any white regions of the space, at a given value of μ, indicate that the family may not be computed in its entirety. Due to the possible existence of turning points along a family, periodic orbits that are not computed may exist at values of the orbital period either within or outside of the colored regions.

To facilitate visualization of the evolution of a family across a large range of mass ratios, a mixed linear-log scale is employed to represent μ on the vertical axis, with the mass ratios corresponding to sample systems as indicated. Specifically, mass ratios in the range $\mu = [0.10, 0.50]$ are plotted as a linear scale, while mass ratios in

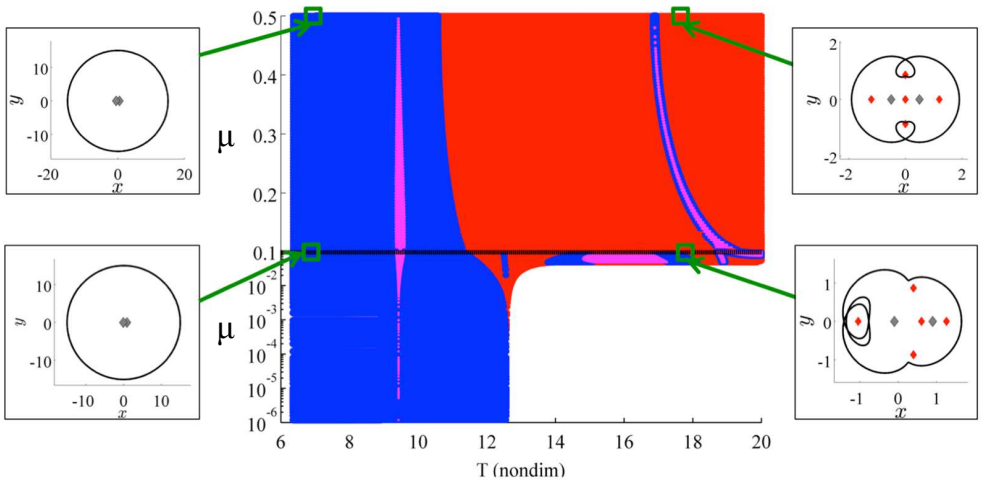

(a) In-plane stability.

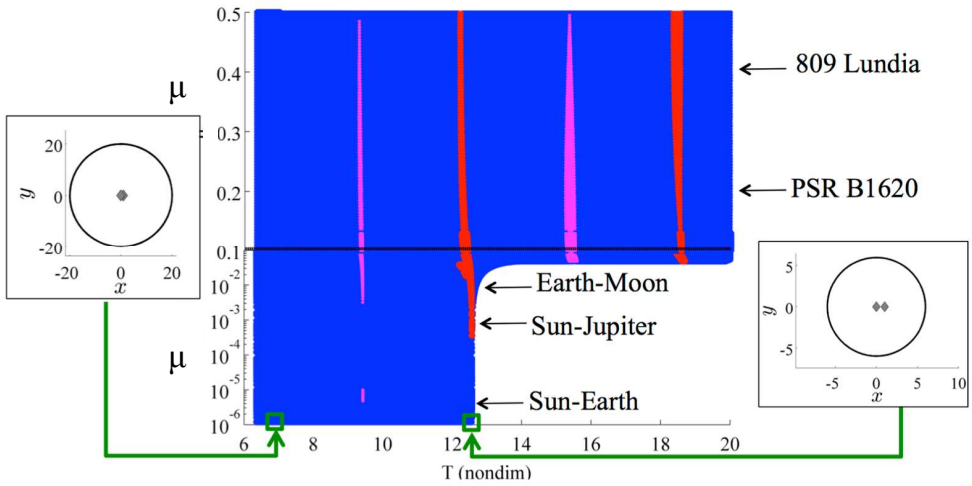

(b) Out-of-plane stability.

Fig. 4.3. Stability representation for retrograde orbits in the exterior region in the CR3BP. Orbital stability is indicated via color: stable (blue), positive unstable (red), and negative unstable (purple).

the range $\mu = [10^{-6}, 0.10)$ are displayed using a log scale. The boundary between these two scales is indicated by a black dashed line. For comparison, selected systems with a specific mass ratio are also identified on the plots that represent the three-dimensional stability index, such as in Figure 4.3(b). In particular, the mass ratio

that corresponds to the binary asteroid 809 Lundia is highlighted on the stability representation. This system, which consists of two V-type asteroids described by an approximate diameter of 6.4 km and separated by a distance of 15.8 km, possesses a mass ratio that is approximately equal to 0.41 [58]. In addition, the binary star system PSR B1620 is also indicated on the stability representation in Figure 4.3(b). Consisting of a pulsar and white dwarf separated by a distance of 0.77 AU, this binary system possesses a small captured planet, named PSR B1620-26. Given the inherent challenges associated with directly observing this planet, significant uncertainties in its characteristics and orbital motion still remain. This small companion is theorized to possess a mass of approximately 1-3 times the mass of Jupiter, with an orbital period of around 68 years, corresponding to a large semi-major axis of 20 AU [59]. Although the mass ratio of the inner binary is not exactly known, it is approximately equal to 0.20 [60]. In addition, sample periodic orbits are displayed in the margins of the composite stability representation at selected mass ratios and periods to reflect the configuration of selected members in physical space.

The composite representations in Figures 4.3(a) and 4.3(b) can be used to assess the effect of changes in the mass ratio on the range of values of the orbital period of stable members of the retrograde exterior family. First, consider the in-plane stability along this retrograde exterior family of orbits. These simply-periodic orbits do not collapse to a singularity. Instead, this irregular family is formed at its minimum energy value within the homoclinic tangles of the manifolds of the L_2 Lyapunov orbits. This minimum energy orbit does not occur at the minimum orbital period along the family but, rather, an intermediate value. At the formation of this family, a branch of stable and unstable orbits is created, a typical phenomenon in the formation of irregular orbits [19]. Since the Jacobi constant at the formation of this family is below the value corresponding to L_3, the L_2 manifolds can pass through the L_3 gateway. Accordingly, the tangle of stable and unstable manifolds that forms the retrograde exterior family of orbits may also involve the manifolds of the L_3 Lyapunov orbits. Such a distinction, however, is difficult to visualize at such large energies. As the

retrograde exterior family grows larger and its period simultaneously decreases to a limiting value, the stability index approaches a value of $s = +2$. Below periods of approximately $T = 11.3$ nondimensional time units, the majority of members of the retrograde exterior family are stable. There does, however, exist a thin band of negative instability centered about $T = 9.42$, where the stability curve plunges below $s = -2$, creating two planar, period-doubling bifurcations. The orbital periods corresponding to the left and right boundaries of this purple structure do not vary drastically across the range of mass ratios considered in this investigation. Furthermore, this region of negative unstable orbits still exists even at smaller values of the mass ratios consistent with the Sun-planet and planet-moon systems within our solar system. The blue region to the right of this purple structure is bound on its other side by a red region. Accordingly, the retrograde exterior family undergoes a variety of planar period-multiplying bifurcations as the stability index encompasses the range of values $s = [-2, 2]$. As the orbital period is increased, this evolution of the stability index corresponds to a pair of complex conjugate eigenvalues moving from -1 to +1, along the unit circle. Beyond a period of approximately 11.3 time units, the retrograde exterior family is predominantly unstable in the plane of motion of the primaries, for large values of the mass ratio. There is, however, a thin blue and purple structure that indicates the presence of stable members at a small range of high orbital periods, as the stability curve plunges below $s = -2$. Since this stable region is curved, and does not form a vertical band, the range of values of the orbital period corresponding to stable members of this family is sensitive to changes in large values of μ. Such insight may be valuable in the analysis of potential exoplanetary motions near a binary star. If, for example, the mass ratio of this binary star system is inaccurately known, it may be difficult to determine if, for a fixed orbital period between 16.84 and 19.37 nondimensional time units, simply-periodic retrograde motions that exhibit in-plane stability exist in the exterior region.

For large mass ratios in the range $\mu = [0.10, 0.50]$, the three-dimensional stability associated with the simply-periodic retrograde family of orbits in the exterior region

exhibits alternating structures that appear at almost regular intervals in the orbital period. By examination of Figure 4.3(b), members of this family are predominantly stable in a direction that is perpendicular to the plane of motion of the primaries. There are, however, thin regions of negative and positive instability that are embedded within this figure. The alternating configuration of these structures, which appear to almost repeat approximately every 2π time units in the orbital period, indicates that the out-of-plane stability index is oscillatory with respect to the orbital period. Further insight into this oscillatory behavior is gained through examination of the inertial view for selected retrograde exterior orbits. Consider one oscillation of the three-dimensional stability index, for $\mu = 0.30$, encompassing a subset of orbits with a period that increases by 2π time units across the selected range: in particular, orbits with a period in the range $T = [12, 18.28]$. Figure 4.4(a) displays the out-of-plane stability index across this range of the family, colored using the same color scheme as the composite stability representations. Three orbits, as indicated, are selected within this range: orbit 1 (red) is positive unstable, orbit 2 (purple) is negative unstable, and orbit 3 (blue) is stable. These three orbits are plotted in the rotating frame in Figure 4.4(b) with the primaries located using grey diamonds, while L_4 and L_5 are indicated via green diamonds. As the orbital period is increased across the selected range, the retrograde exterior family forms loops in the vicinity of L_4 and L_5. These loops eventually grow and encircle each of the two triangular equilibrium points. In an inertial frame, each loop corresponds to motion that is temporarily prograde, moving faster than the mean motion of the binary system. In Figure 4.4(c), the three selected orbits are plotted in an inertial frame, with the circular orbits of the primaries overlaid in black and green. The selected orbits appear to complete almost one additional revolution of the barycenter within one oscillation of the three-dimensional stability index. This observation appears consistent for subsequent oscillations of the out-of-plane stability curve, for values of μ where the orbital period of the retrograde exterior family expands and additional loops form in a fractal manner.

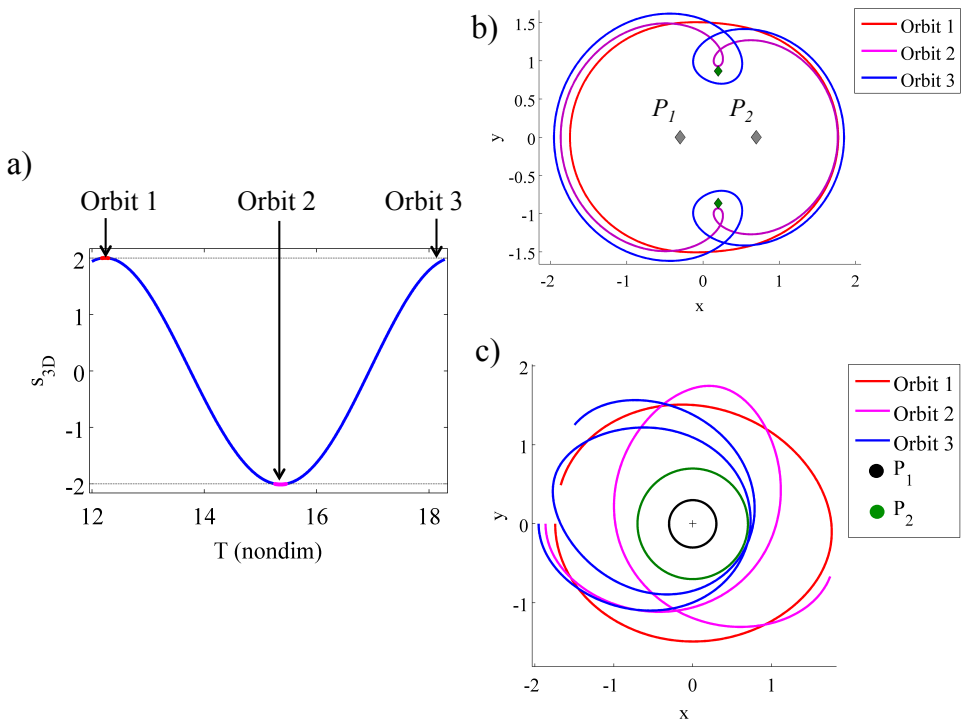

Fig. 4.4. Three members of the retrograde exterior family for $\mu = 0.30$, indicated along (a) one interval of the out-of-plane stability curve as a function of orbital period. Selected orbits are plotted in (b) the rotating frame and (c) an inertial frame.

Although the retrograde family of orbits in the exterior region extends to large values of the orbital period for mass ratios in the range $\mu = [0.10, 0.50]$, the same behavior does not occur below a critical value of the mass ratio, $\mu \approx 0.048$. In fact, a large white region appears in the composite stability representation in Figure 4.3 for mass ratios below this critical value. Note that the value $\mu \approx 0.048$ at which the retrograde family of orbits in the exterior region transition from nearly circular to exhibiting loops in the vicinity of L_4 and L_5 is slightly greater than the value of $\mu = 0.044$, for which planar periodic orbits are still observed near the triangular equilibrium points. Although L_4 and L_5 are only linearly stable for mass ratios less than 0.03852, previous work by Deprit has determined that nearby planar orbits still

exist for $0.03852 < \mu \leq 0.044$ [61]. Thus, the formation of loops near L_4 and L_5 along the retrograde exterior orbits for $\mu \geq 0.048$ and, therefore, the extension of the family to large orbital periods, appears to occur when the planar orbits near the triangular equilibrium points do not exist. To further explain the discontinuous reduction in the maximum orbital period, bifurcations along the family are sought. Accordingly, the in-plane stability index across the retrograde exterior family is plotted as a function of the orbital period for selected mass ratios close to the critical value, with a zoomed-in view displayed in Figure 4.5(a). Each stability index curve is colored by the corresponding mass ratio, as indicated by the colorbar on the right side of the plot. Approaching the critical mass ratio from above, at least two orbits along the family possess the same orbital period in the range $T = [13.5, 14.5]$, with a local minimum and a local maximum in the stability index occurring at $T \approx 14.1 \approx 9/2\pi$. As the mass ratio is reduced towards the critical value of μ, these local extrema approach a value of $s = +2$ at identical values of the orbital period. Accordingly, a collision of two tangent bifurcations occurs at the critical mass ratio, with the two portions of the family exchanging branches and separating. Upon application of a small perturbation to reduce the value of the mass ratio below its critical value, the two left branches of

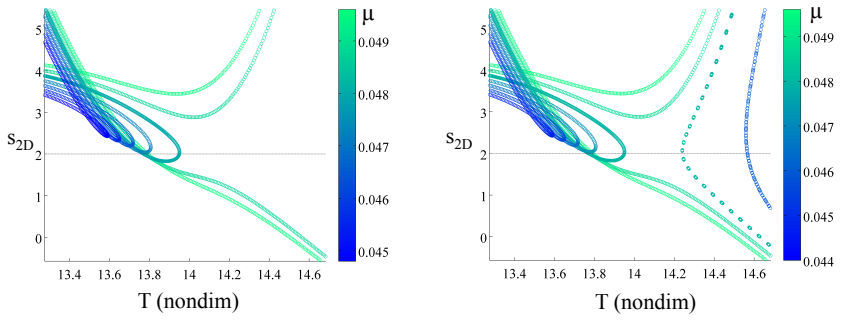

(a) Stability index across the original family.

(b) Stability index for two connected families.

Fig. 4.5. In-plane stability index along retrograde exterior family for mass ratios near the critical value of $\mu \approx 0.048$.

the family join and form a turning point below $T \approx 14.1$. This turning point occurs at lower values of the orbital period as the mass ratio is reduced further, offering an explanation for the discontinuous reduction in the maximum orbital period along the original retrograde exterior family, as observed in Figure 4.3. During the collision of bifurcations, the two righthand branches of the family also join to form a separate family of orbits. This new family of orbits is computed for mass ratios in the range $\mu = [1 \times 10^{-6}, 0.048)$ and its stability index at selected values of μ is plotted in Figure 4.5(b) alongside the stability curves of the original retrograde exterior family, thereby demonstrating the separation of the two portions of the family during the collision of bifurcations. From this knowledge of the occurrence of a bifurcation, the presence of a white region in the composite stability representation in Figure 4.3(a) may not necessarily be correlated with the absence of any large period orbits. Alternate families that have bifurcated from the original family at larger values of the mass ratio, in fact, fill part of the white region.

Given the evolution of the retrograde exterior family of orbits over the examined range of large mass ratios, composite stability representations can be used in a preliminary analysis to postulate the suitability of members of this family to describe stable motions of an exoplanet near a binary star system. Since small perturbations can influence the motion of an exoplanet both within and out of the plane of the relative orbits of the primaries, both stability indices are evaluated simultaneously. Assuming that orbits that are stable in the CR3BP are sought, the overlap of blue regions in both Figures 4.3(a) and 4.3(b) are identified. Note that the purple regions corresponding to orbits with negative instability for both in-plane and out-of-plane modes occur at similar periods near $T = 9.5$ across the range of mass ratios examined in this investigation. Aside from this small region, orbits in the retrograde exterior family with periods below approximately 10.5 nondimensional time units are, predominantly, stable both within and out of the plane. Such orbits, which exist far from the two primaries, may, therefore, be examined further in identifying potential circumbinary orbits for an exoplanet. Recall that one nondimensional length unit is

equal to the distance between the two primaries; for PSR B1620, these retrograde exterior orbits exist over 1.2 AU from the system barycenter, or further for lower period orbits. Within the binary environment, orbits that are unstable within the plane of motion of the primaries exist and might be utilized as a mechanism for capture or ejection of exoplanets. These orbits, located in the red or purple regions of Figure 4.3(b) and at large values of the orbital period, possess stable and unstable manifolds that can potentially facilitate natural transfer of matter between various regions in the vicinity of a binary system. Using the composite stability representations, this insight into the stability of a family of orbits is also available rapidly and straightforwardly for multiple binary star systems at a variety of mass ratios.

4.2 Retrograde Circumstellar Orbits Around The Largest Primary

Retrograde orbits that emanate from the singularity at P_1 also exist and may supply further insight into the behaviors that could be exhibited by an exoplanet in a circumstellar or S-type orbit, encircling one of the primaries [62]. This family of orbits, which can grow quite large in size at high orbital periods, exhibits a wide range of values for the in-plane stability index. Composite stability representations for the in-plane and out-of-plane stability indices across this planar family are plotted in Figure 4.6. At low periods, these orbits are close to circular with low altitudes relative to P_1, as depicted in the left margins of the stability representations. Note that for the sample binary system PSR B1620, its components are separated by a distance of 0.77 AU, which represents one nondimensional length unit. Although the small circular orbits plotted on the left in Figure 4.6(a) may be defined by an altitude lower than the radius of the pulsar in PSR B1620, these orbits may not intersect the surface of a primary body in an alternative system that possesses a similar mass ratio. These smaller orbits are, therefore, retained in the composite stability representation.

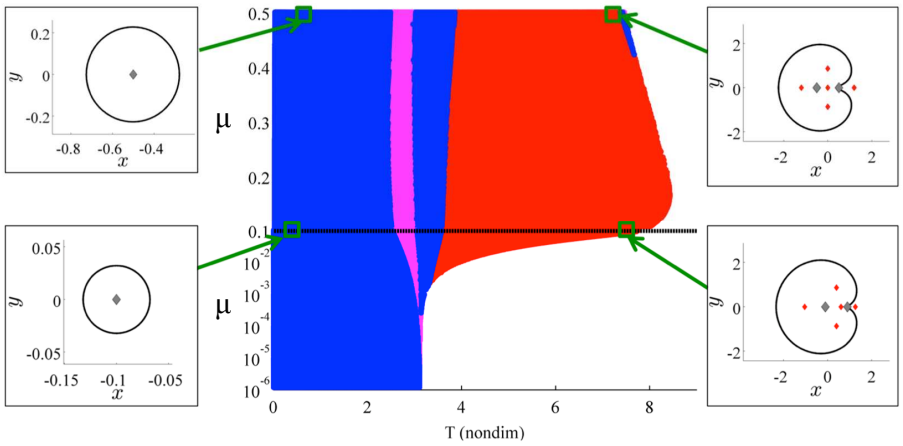

(a) In-plane stability.

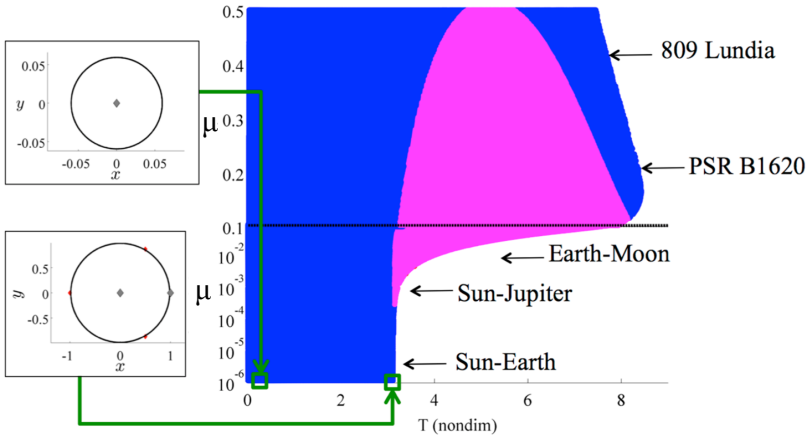

(b) Out-of-plane stability.

Fig. 4.6. Stability representation for retrograde orbits about the larger primary, P_1, in the CR3BP. Orbital stability is indicated via color: stable (blue), positive unstable (red), and negative unstable (purple).

As evidenced by the in-plane stability representation in Figure 4.6(a), a set of stable retrograde orbits exist at large mass ratios. In fact, the family is formed at the singularity corresponding to the location of P_1, indicating that the in-plane stability index approaches the value $s = +2$ as the period decreases. As the period increases, however, the orbits along this family appear more nonlinear in shape, extending further towards P_2 and beyond the locations of the equilateral points L_4 and L_5. At

periods just below $T = \pi$, a purple structure corresponding to negative instability appears. The left and right bounds of this purple structure indicate the presence of two planar period-doubling bifurcations at $s = -2$ that exist for mass ratios in the range $\mu = [0.10, 0.50]$. The presence of this purple region at small mass ratios may be related to the appearance of a purple region in the out-of-plane stability representation in Figure 4.6(b), which occurs at a similar value of the orbital period. The period-doubling bifurcation that occurs in three-dimensional space may influence the flow within the plane, inducing negative instability along the retrograde exterior family at nearby values of the mass ratio. This potential correlation between the two period-doubling bifurcations may cause the stability curve to plunge below the value $s = -2$; such correlation warrants further examination. Increasing the period even further, above $T \approx 3.9$, a region of positive instability exists, where the stability index evolves to a value greater than $s = +2$. Within the blue region, a wide variety of period-multiplying bifurcations occur as the planar stability index passes through the range $s = [-2, 2]$. At these bifurcations, higher-order planar, periodic orbits intersect this family. Such orbits may possess a physical configuration similar to the simply-periodic retrograde orbits about P_1, but with different frequencies and stability properties that warrant further investigation. Note that, for large mass ratios, at periods larger than $T = 7$ nondimensional time units, the orbits closely approach the smaller primary and are difficult to compute numerically. This computational difficulty may contribute to the presence of a large white region on the righthand side of Figure 4.6(a). A similar phenomenon is also observed at small mass ratios, for a smaller maximum orbital period. From these observations using composite stability representations, it is evident that the in-plane stability of the retrograde P_1 family across the range $\mu = [0.10, 0.50]$ is relatively insensitive to changes in the mass ratio, as the colored structures appear similar to thick vertical bands. For smaller mass ratios, however, the family becomes predominantly stable within the xy-plane. Over the computed portion of the family, the purple, blue and red structures that exist at larger periods converge as the mass ratio approaches $\mu = 10^{-5}$ from above, which is close to the

mass ratio of the Uranus-Titania system. At these smaller mass ratios, the retrograde family of orbits encircling the larger primary are predominantly stable.

The retrograde family about P_1 exhibits a simple variation in the out-of-plane of stability, as depicted in Figure 4.6(b). In fact, this figure is predominantly blue with one large purple structure corresponding to negative instability. Accordingly, there are two period-doubling bifurcations that bound this large region and exist for all mass ratios in the range $\mu = [0.10, 0.50]$. As the retrograde P_1 orbits reduce in size towards the singularity at P_1, the out-of-plane stability index approaches, from below, a value of $s = +2$. The stable region corresponding to smaller periods, therefore, suggests the existence of a wide variety of three-dimensional period-multiplying bifurcations as the stability index encompasses the range $s = [-2, 2]$. The orbits that are produced from these bifurcations evolve out of the plane. At smaller mass ratios, below the critical value $\mu = 10^{-4}$, which is close to the mass ratio of the Sun-Saturn system, the two period-doubling bifurcations disappear within the range of orbits computed along the family. Thus, for mass ratios smaller than this critical value, the members of the computed portions of the family appear to predominantly exhibit stability out of the plane of the primaries. Above this critical value, however, it is evident that, for orbital periods above $T = \pi$, changes in the mass ratio significantly affect the range of orbital periods corresponding to members of the family that are stable out of the plane of motion of the primaries.

Combining the observations from both the in-plane and out-of-plane stability assessments of the retrograde P_1 orbits at large mass ratios, portions of this family may be further examined for identification of stable circumstellar orbits of an exoplanet about a binary star system with an inaccurately known large mass ratio. In particular, it is observed that the stable regions in each exclusion plot overlap for periods below approximately 2.5 nondimensional units. Accordingly, and perhaps not surprisingly, orbits with a period below this value exhibit stability in all directions and may be less sensitive to perturbations than larger retrograde orbits. There also exists another interval of orbits along the family exhibiting total stability. At smaller mass ratios,

this range shrinks and approaches a value of $T \approx \pi$. As the mass ratio is increased to the limiting value of $\mu = 0.50$, this range grows in size to encompass orbital periods between $T \approx 3$ and $T \approx 3.9$. Depending upon the radii of the components of the binary system of interest, there may be some members within either of these intervals along the family that do not intersect the primaries. Correspondingly, candidate exoplanet orbits may be identified for further examination in a higher fidelity model that incorporates additional effects and forces.

4.3 Retrograde Circumstellar Orbits Around The Smallest Primary

In the vicinity of the smaller primary, there exist planar orbits that encircle the body in a retrograde direction, commonly denoted the distant retrograde orbits (DROs). At relatively small mass ratios, such as $\mu \approx 0.012$ in the Earth-Moon system, these orbits exhibit in-plane stability across a wide range of orbital periods, potentially providing suitable candidate orbits for the placement of a long-term lunar infrastructure [13]. Using the composite stability representation in Figure 4.7(a) as a reference, it is clear that the stability across the DRO family is more varied for many large mass ratio binary systems. Note that the presence of a large white region at small values of the orbital period corresponds to portions of the DRO family possessing a periapsis with respect to P_2 that falls below a predefined minimum altitude, implemented to limit the required computational effort. Analysis of Figure 4.7(a) reveals that, for large mass ratios, a purple structure corresponding to negative instability appears near $T = \pi$. This orbital period corresponds to a 2:1 resonance with the period of the primaries. As the value of μ decreases, the two period-doubling bifurcations along the edge of this purple structure occur at higher values of the orbital period. In addition, the left and right bounds of the purple region merge at a critical value of the mass ratio. This evolution of the period-doubling bifurcations corresponds to the local minimum of the in-plane stability index occurring at less negative values of s, and passing through $s = -2$ at $\mu \approx 0.11$. At this critical mass

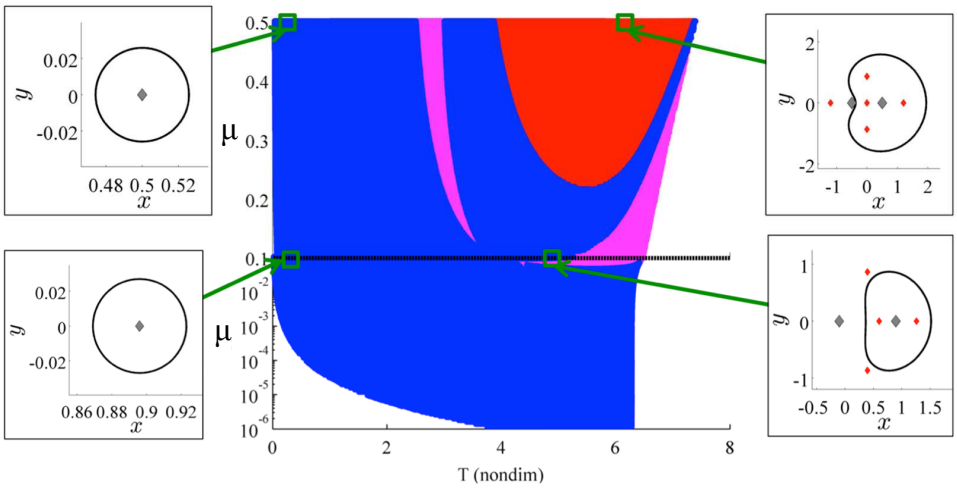

(a) In-plane stability.

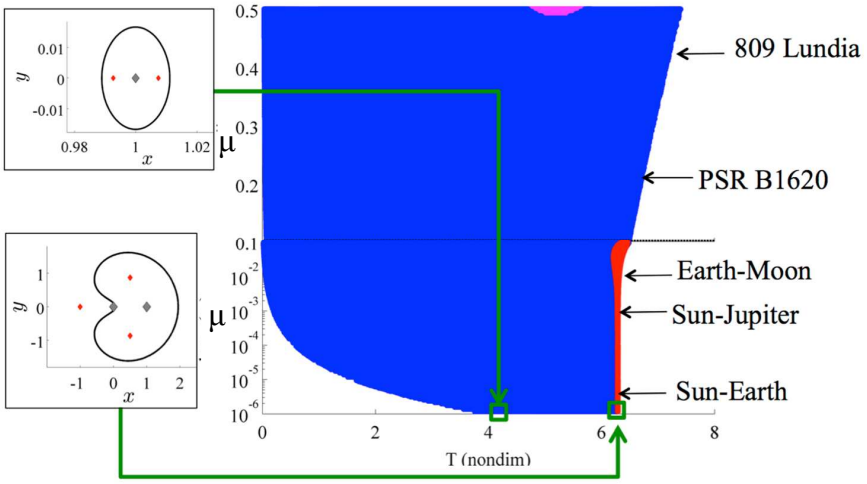

(b) Out-of-plane stability.

Fig. 4.7. Stability representation for retrograde orbits about P_2 in the CR3BP. Orbital stability is indicated via color: stable (blue), positive unstable (red), and negative unstable (purple).

ratio, the purple structure links to another structure of negative instability that exists at larger periods, for $\mu > 0.048$, and is potentially correlated to the disappearance of planar periodic orbits near L_4 at $\mu = 0.044$ [61]. As a reference, this critical value of $\mu \approx 0.048$ is larger than the mass ratio corresponding to the Earth-Moon system. Between the two regions of negative instability, the in-plane stability index

passes through $s = +2$ twice, creating a large red region of positive instability for sufficiently large mass ratios. As the mass ratio is decreased to a value of $\mu \approx 0.22$, the maximum value in the stability index decreases and passes through $s = +2$ as the two tangent bifurcations meet. Below this critical value of the mass ratio, the two tangent bifurcations disappear. Thus, composite stability representations reveal that the variation in the in-plane stability index that occurs at large mass ratios is significantly more complex than the stability exhibited by the DROs at the mass ratios consistent with the Sun-planet or planet-moon systems within the solar system.

In contrast to the planar behavior, the out-of-plane stability for orbits in the DRO family is largely homogeneous across all mass ratios. As displayed in Figure 4.7(b), the out-of-plane stability index predominantly possesses values in the range $s = [-2, +2]$. Noticeably, there is a small region of negative instability at mass ratios close to $\mu = 0.50$, centered at a period of $T \approx 5.2$. This structure reflects a stability index that plunges below $s = -2$, thereby forming two period-doubling bifurcations. Additionally, a structure corresponding to positive instability appears at small mass ratios below $\mu = 0.11$, for the largest periods along the regions in this family that are computed. The presence of this structure may be correlated to the occurrence of a close pass to the larger primary, as illustrated by the sample orbit plotted in the bottom inset image in Figure 4.7(b). This range of μ encompasses the value of μ corresponding to the Earth-Moon system, and many of the Sun-planet combinations in the solar system.

For motion in the vicinity of the smaller primary, combining the results of both in-plane and out-of-plane stability analyses for the retrograde family of orbits about P_2 reveals large ranges of orbital periods corresponding to stable members. Since this orbit family is predominantly stable in the $\hat{z}$ direction, its in-plane stability essentially governs the overall stability of its member orbits. At each value of the mass ratio, large and small, there remains a significant range of orbits that are stable in the CR3BP. Depending upon the physical configuration of the components of the desired binary, some of the stable members of this simply-periodic retrograde family of orbits

may not intersect or pass near the surface of either primary. Such orbits could serve as candidates for further examination in a higher-fidelity model that also incorporates any eccentricity of the inner binary orbit, as well as additional forces.

4.4 Prograde Circumstellar Orbits

Another type of simply-periodic circumstellar or S-type orbit that encircles the larger primary, P_1, includes two families of prograde orbits. These two families, plotted in Figure 4.8 at a sample mass ratio equal to $\mu = 0.30$, are labelled 'family 1' and 'family 2' in this investigation. The location of the largest primary is marked by a gray-filled circle and the direction of motion for both families is indicated by the arrows. Each family evolves with the mass ratio in an intriguing manner that is evident in their composite stability representations and clarified using the stable and unstable manifolds emanating from the L_1 Lyapunov orbits. Assuming the simplified and autonomous dynamical regime described by the CR3BP, composite stability representations are used to identify stable periodic orbits and, subsequently, hypothesize

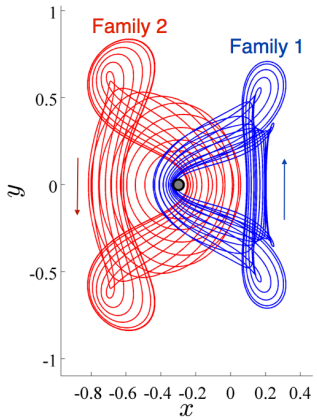

Fig. 4.8. Sample prograde orbits near the larger primary, P_1, in 'family 1' and 'family 2' for $\mu = 0.30$.

whether such prograde orbits could potentially describe the motion of a small body in the vicinity of a large mass ratio binary system.

To determine the viability of a small body exhibiting motion corresponding to 'family 1', the evolution of the in-plane stability index over various mass ratios is examined. As evident in the stability representation in Figure 4.9(a), the family closes (with the upper and lower bounds on the period indicated by the gray shaded regions) and disappears as the mass ratio approaches the value of $\mu \approx 0.26284$. The

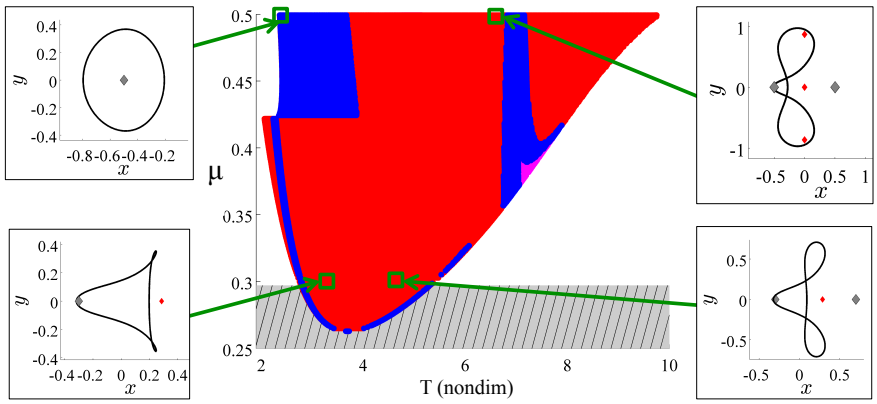

(a) In-plane stability.

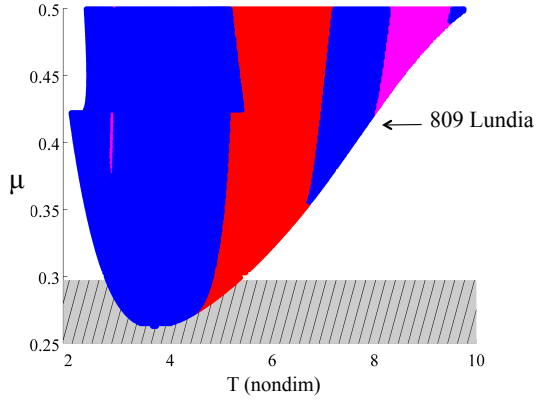

(b) Out-of-plane stability.

Fig. 4.9. Stability representation for 'family 1', comprised of prograde orbits about P_1. Orbital stability is indicated via color: stable (blue), positive unstable (red), and negative unstable (purple).

in-plane stability curves for selected mass ratios close to this critical μ value are plotted as a function of the period in Figure 4.10, with dotted lines located at $s = +2$ and $s = -2$. In this figure, it is clear that, for each period, two orbits exist in 'family 1' for the corresponding values of μ. For a system with a mass ratio of $\mu = 0.27$, stable members of the family exist close to the upper and lower bounds of the period. As the mass ratio is decreased towards the critical value, however, the minimum of the curve rises and passes through $s = -2$. At a nearby value of the mass ratio, the two period-doubling bifurcations at $s = -2$ disappear and result in a stable periodic orbit existing at each value of the period across the family. Thus, small blue structures appear at the bottom of the composite stability representation in Figure 4.9(a). This family may or may not be closed at all mass ratios; computational difficulties prevent examination of the entire family as the orbits closely approach P_1 for large mass ratios. Eventually, the two tangent bifurcations at the minimum and maximum period of the family collide, and the family no longer exists. Assuming that the dynamical environment near a binary system is adequately modeled via the CR3BP, and that close passes to the larger primary are permissible, this observation of the disappearance of 'family 1' at the critical μ value suggests that a small nearby

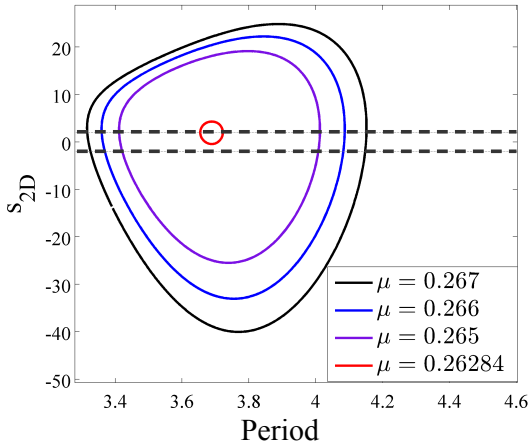

Fig. 4.10. In-plane stability index for 'family 1' at selected values of the mass ratio close to $\mu = 0.26284$.

body would not exhibit the behavior typical of this family for mass ratios below $\mu \approx 0.26284$. Since the composite stability representation in Figure 4.9(a) displays large red regions, this family is predominantly unstable in the plane of motion of the primaries. There is one small blue region at low periods corresponding to stable periodic orbits that occur at increasing values of the period as the mass ratio is decreased. In contrast, the composite stability representation in Figure 4.9(b) reveals that a large portion of the family, with orbital periods above 4.5 nondimensional time units, consists of members that are stable in response to perturbations that only excite out-of-plane modes. Using the insight gained from the composite stability representation, a small body that is, at some instant, captured in an orbit belonging to 'family 1' may only persist over long time intervals in the presence of in-plane and out-of-plane perturbations for specific small ranges of the orbital period. Furthermore, in a dynamical regime that is well-approximated via the CR3BP, the detection of a captured exoplanet exhibiting motion with a given orbital period and characteristics resembling the orbits in 'family 1' may be used to place significant bounds on the mass ratio of the binary system.

The disappearance of 'family 1' at the critical value of the mass ratio, $\mu \approx 0.26284$, is predictable through examination of nearby stable and unstable manifolds. The crossings of the manifolds of the L_1 Lyapunov orbit with the surface of section described by $y = 0$, are plotted on the maps represented in $(x, \dot{x})$ space in Figures 4.11(a) and 4.11(b). These manifolds are computed for a system with mass ratio $\mu = 0.26284$, close to the critical mass ratio, and a Jacobi constant value equal to $C = 3.165$. In Figure 4.11(a), crossings of the stable manifold with $\dot{y} < 0$ are colored blue, unstable manifold crossings with $\dot{y} < 0$ are colored red, black circles reflect the crossings of prograde orbits known to belong to 'family 1', and the black diamond locates P_1. In Figure 4.11(b), a similar color scheme applies for manifold crossings that possess a positive value of $\dot{y}$. These two zoomed-in views of the manifold crossings appear separately to supply sufficient visual clarity and to separate crossings of the hyperplane in each of the two possible directions. Although the manifold crossings actually form

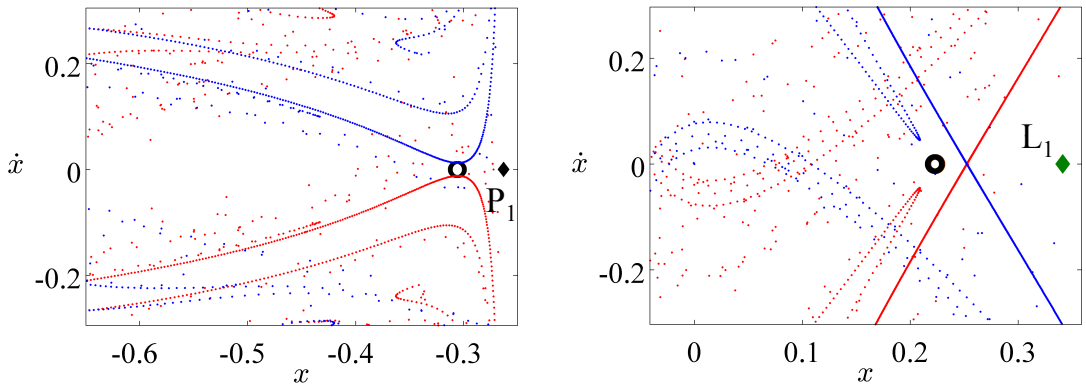

(a) Zoomed-in view of manifold crossings near P_1 with $\dot{y} < 0$.

(b) Zoomed-in view of the manifold crossings near P_1 with $\dot{y} > 0$.

Fig. 4.11. Visualization of flow near the stable (blue) and unstable (red) manifolds of the L_1 Lyapunov orbit with $C = 3.165$ in a system with $\mu = 0.26284$ to demonstrate the existence of 'family 1'.

closed curves, these curves appear to resemble dotted lines of larger spacing with subsequent revolutions of the two primaries, as the manifolds elongate. For both of these figures, the two black circles that are located at similar values of x, with $\dot{x} = 0$, correspond to the crossings of the $y = 0$ surface of section for the two periodic orbits in 'family 1' at the specified value of the Jacobi constant, $C = 3.165$. As evident from these two figures, these two periodic orbits are nestled between the stable and unstable manifolds of the L_1 Lyapunov orbits. Accordingly, these manifolds are examined at mass ratios lower than the critical value to explain the disappearance of 'family 1'. Figure 4.12 portrays the stable and unstable manifolds, plotted with the same color scheme as in Figure 4.11, of an L_1 Lyapunov orbit with a Jacobi constant value equal to $C = 3.155$ in a system with mass ratio $\mu = 0.26$. For periodic orbits in 'family 1' to exist at this mass ratio, such an orbit must possess two crossings of the surface of section $y = 0$ with $\dot{x} = 0$ in a similar region along the x-axis. This requirement of two perpendicular crossings (one with $\dot{y} < 0$ and the other possessing $\dot{y} > 0$) corresponds to the symmetry of orbits within this family. It is generally difficult to distinguish the

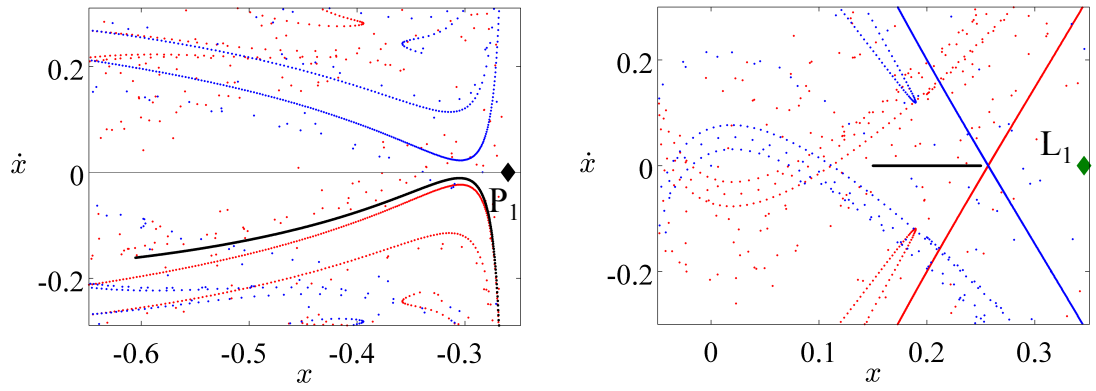

(a) Initial conditions seeded along $y = \dot{x} = 0$, with $\dot{y} < 0$.

(b) First return to $y = 0$, with $\dot{y} > 0$.

Fig. 4.12. Visualization of flow near the stable (blue) and unstable (red) manifolds of the L_1 Lyapunov orbit with $C = 3.155$ in a system with $\mu = 0.26$ demonstrating the disappearance of 'family 1'.

regions which lie within the crossings of a manifold as it encircles the primary. Thus, to search for periodic orbits with such crossings, that also lie close to the manifolds, initial conditions are seeded along the x-axis with $x = [0.15, 0.25]$ and $\dot{x} = 0$. The value of $\dot{y}$ at each point is selected to possess a magnitude that supplies the correct Jacobi constant, and a positive sign to recover prograde motion about P_1. These initial conditions, plotted as dark gray points in Figure 4.12(b), are integrated forward in time to their subsequent intersection of the hyperplane $y = 0$. The resulting map crossings, with $\dot{y} < 0$, are also displayed in Figure 4.12(a) as dark gray points. Note that the curve formed by these crossings does not intersect the hyperplane defined by $\dot{x} = 0$. Accordingly, the manifolds of the L_1 Lyapunov orbit no longer the guide the flow in a manner that allows the symmetric, simply periodic orbits of 'family 1' to exist. Thus, as illustrated, the existence and evolution of this family is reflected in the manifolds of the L_1 Lyapunov orbits.

In contrast to the disappearance of 'family 1' at $\mu \approx 0.26284$, 'family 2' continues to exist across the entire range of mass ratios that are examined within this inves-

tigation, and may supply potential orbits to describe the motion of a small body near a binary system with a mass ratio below this critical μ value. A similar analysis of the manifolds of the L_1 Lyapunov orbits reveals that orbits in 'family 2' are not destroyed at the critical mass ratio identified in 'family 1'. This observation is straightforwardly visualized using the composite stability representation displayed in Figure 4.13(a). In particular, this family is predominantly stable within the plane of motion of the primaries with two key purple structures emerging at sufficiently large periods, and meeting at $\mu \approx 0.236$. Recall that these structures represent regions of negative instability and are bound by period-doubling bifurcations at the edges. Slightly above the mass ratio $\mu \approx 0.236$, there exists a small oscillation in the in-plane stability index, centered about $s = -2$, that results in three period-doubling bifurcations. As the mass ratio is increased, the oscillation in the stability curve disappears to leave only one period-doubling bifurcation, and only one region of negative instability within the range of computable orbits along the family. The purple structure that exists at smaller periods disappears at $\mu \approx 10^{-3}$, just above the mass ratio of the Sun-Jupiter system. Below this critical value, 'family 2' exhibits stability for both in-plane and out-of-plane behavior. For the out-of-plane stability index, this prograde family of orbits is predominantly stable at large mass ratios. There is, however, one small region of negative instability that occurs just below the resonant period at $T = \pi$, and one small region of positive instability close to $T = 2\pi$. For both stability indices, the presence of stable members of 'family 2' with larger orbital periods appears more sensitive to variations in large values of the mass ratio than the smaller mass ratios corresponding to the Sun-planet combinations within the solar system. Since the mass ratio of a binary star system is usually not accurately known, or may shift over time due to mass exchange, the composite stability representations reveal that a large portion of this family may supply orbits that could describe stable motion of captured small bodies that persists in the vicinity of a binary over longer intervals of time.

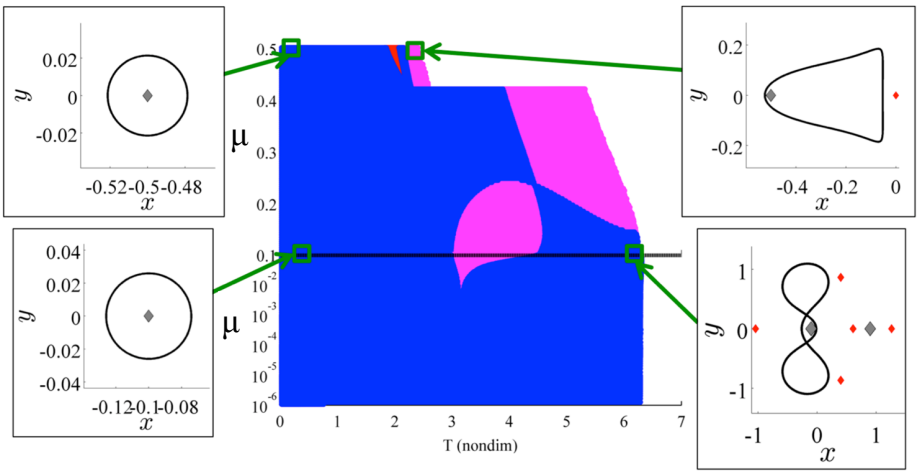

(a) In-plane stability.

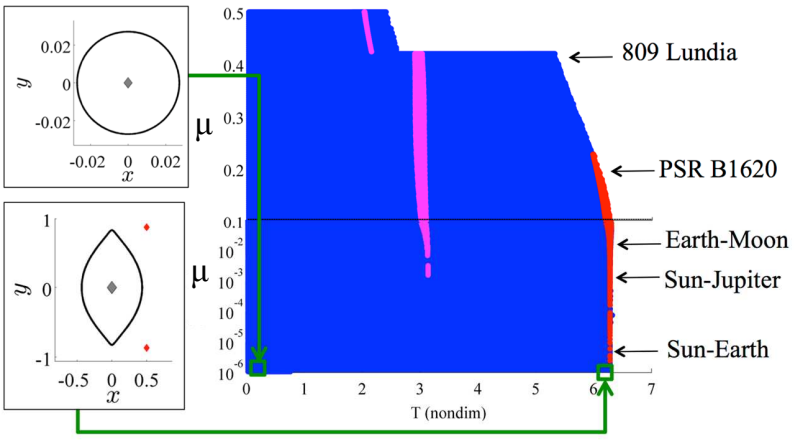

(b) Out-of-plane stability.

Fig. 4.13. Stability representation for 'family 2', consisting of prograde orbits about P_1. Orbital stability is indicated via color: stable (blue), positive unstable (red), and negative unstable (purple).

As evident in the composite stability representations, there also exist discontinuities in the stability indices corresponding to both 'family 1' and 'family 2' at a common critical mass ratio. These discontinuities occur at a mass ratio of $\mu \approx 0.4232$ and, again, appear correlated with the manifolds of the L_1 Lyapunov orbits. First,

it is valuable to view the stability curves for 'family 1' and 'family 2' at mass ratios just above and below the critical value, as plotted in Figure 4.14. From this figure, it is evident that, as the mass ratio passes through the critical value, the two tangent bifurcations at $s = +2$, that occur in each of the two families meet, causing a collision of bifurcations. In fact, in the local neighborhood of the tangent bifurcations in both families, the stability curve appears to resemble a set of asymptotes that meet at $s = +2$. For mass ratios below $\mu = 0.4232$, the top two branches of these asymptotes are linked to form 'family 1', and vice versa for 'family 2'. As the mass ratio is increased beyond the critical value, 'family 1' consists of the two left branches of these asymptotes, while 'family 2' is formed by the right asymptote branches. This exchange of periodic orbits between 'family 1' and 'family 2' is reflected by the discontinuities in the in-plane stability index in Figures 4.9(a) and 4.13(a). To explain this structural change in the two families, the manifolds of the L_1 Lyapunov orbits are examined at a value of the Jacobi constant equal to $C = 3.61$, which is close to the energy level at which the two tangent bifurcations merge. At $\mu = 0.42$, below the critical mass ratio, the stable and unstable manifolds are plotted in blue and red, respectively, in Figure 4.15(a) for crossings with $\dot{y} < 0$. The crossings of the stable

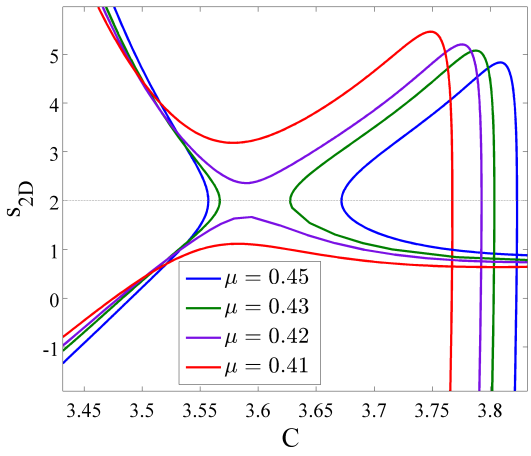

Fig. 4.14. In-plane stability index for 'family 2' at selected values of the mass ratio close to $\mu = 0.4232$.

and unstable manifolds with $\dot{y} > 0$ are plotted using the same color scheme in Figure 4.15(b). In Figure 4.15(a), purple circles represent the corresponding crossings of three periodic orbits: one that exists in 'family 2', and two that exist in 'family 1' (one of which possesses a large negative value of s for modes within the plane of motion of the primaries). A set of initial conditions can be seeded along the x-axis in this figure, for the specified value of the Jacobi constant, and propagated forward in time until the next intersection with the $y = 0$ surface of section. The returns to this map are overlaid in gray on Figure 4.15(b), with intersections of the line $\dot{x} = 0$ indicated by purple circles. Since the resulting curve intersects the x-axis in this figure three times, three symmetric prograde orbits exist at this mass ratio and are nestled within the homoclinic tangle of the manifolds of the L_1 Lyapunov orbit. Using Figure 4.14 as a reference, it is noted that for a mass ratio above the critical value, e.g., $\mu = 0.43$, only one periodic orbit should exist at $C = 3.61$, with a large negative value of s. This observation reflects the branches of 'family 1' and 'family 2' reconnecting such that there is a gap between, respectively, the local maximum and local minimum in the stability index across these two families; this gap appears to be located near $C = 3.61$. A set of initial conditions corresponding to perpendicular crossings of the hyperplane $y = 0$ with $\dot{y} > 0$, near the expected locations of the crossings of prograde periodic orbits, are plotted in Figure 4.16(b). Upon return to the map, with $\dot{y} < 0$, the resulting crossings form a curve that only intersects the $\dot{x} = 0$ line once, as portrayed in Figure 4.16(a). As such, the manifolds of the L_1 Lyapunov orbits apparently no longer guide the flow in their vicinity to produce three symmetric, simply periodic orbits. These dynamics in the vicinity of the manifolds clarify the changes in the structural configurations of both prograde families about P_1 near the observed critical mass ratio. Such exchange of the branches of these prograde families may influence the search for periodic orbits that possess a given orbital period and encircle the larger primary in a binary system with an inaccurately-known mass ratio near $\mu = 0.4232$.

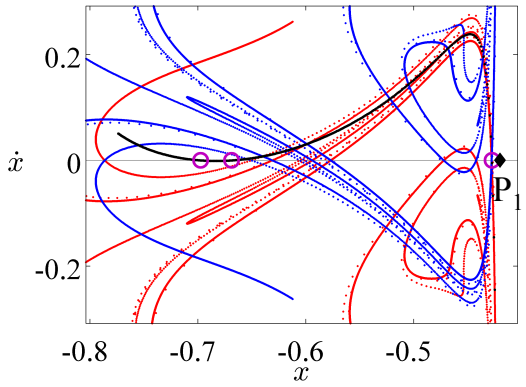

(a) Zoomed-in view of manifold crossings near P_1 with $\dot{y} < 0$.

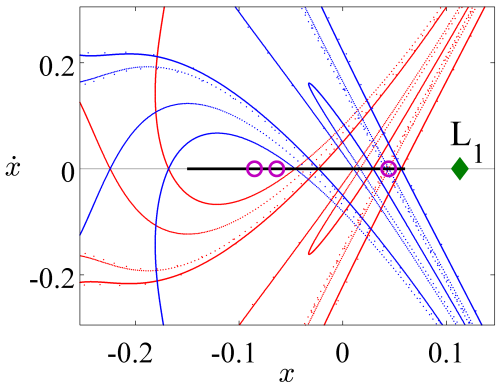

(b) Zoomed-in view of the manifold crossings near P_1 with $\dot{y} > 0$.

Fig. 4.15. Visualization of flow near the stable (blue) and unstable (red) manifolds of the L_1 Lyapunov orbit with $C = 3.61$ in a system with $\mu = 0.42$ to demonstrate the exchange of branches between 'family 1' and 'family 2'.

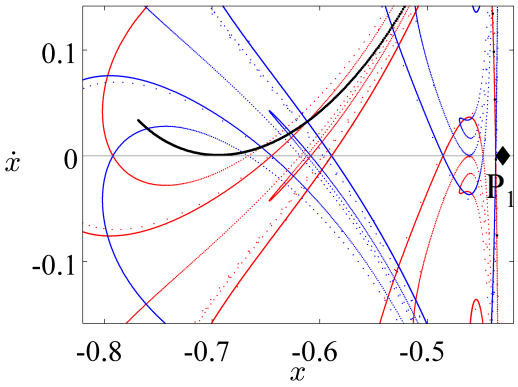

(a) Zoomed-in view of manifold crossings near P_1 with $\dot{y} < 0$.

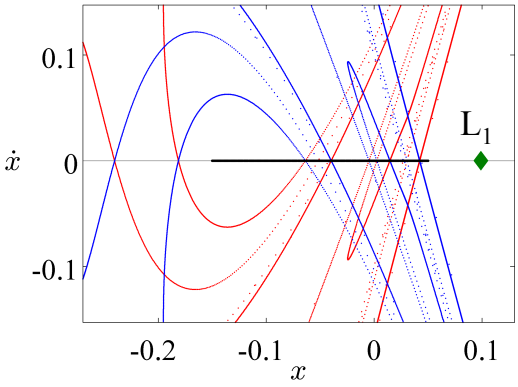

(b) Zoomed-in view of the manifold crossings near P_1 with $\dot{y} > 0$.

Fig. 4.16. Visualization of flow near the stable (blue) and unstable (red) manifolds of the L_1 Lyapunov orbit with $C = 3.61$ in a system with $\mu = 0.43$ to demonstrate the exchange of branches between 'family 1' and 'family 2'.

4.5 Libration Point Orbits

Another type of periodic motion to examine via exclusion plots, within the context of binary star systems, is the planar family of L_1 Lyapunov orbits. In the Earth-Moon system, these Lyapunov orbits are known to exhibit instability within the plane of motion of the primaries that, essentially, creates three-dimensional orbits, such as the halo and axial families, through bifurcations identified by the out-of-plane stability index. However, the behavior of the stability indices for large mass ratios appears to exhibit more variability than at the small mass ratios typically examined within the solar system.

The L_1 Lyapunov orbits, which are located between the two primaries, do not possess a pair of stable and unstable planar modes at each value of the orbital period for large values of the mass ratio. Using the composite stability representation in Figure 4.17(a) as a reference, it is evident that for orbital periods below 5 nondimensional units, members of the L_1 Lyapunov family possess stability indices with a magnitude greater than two. At larger values of the period, however, the in-plane stability curve plunges into and beyond the range of stability indices $s = [-2, 2]$. Accordingly, a purple region of negative instability appears, and is surrounded by blue regions corresponding to stable orbits. Although computational difficulties prohibit continuation across the entire family, it is possible that unstable orbits also exist at the same periods as the stable orbits. The presence of stable motion near the L_1 gateway may complicate an investigation of ejection or capture of matter from or into the vicinity of a binary with a large mass ratio. Out of the plane of motion of the primaries, however, the range of orbital periods corresponding to stable members of the L_1 Lyapunov family is less sensitive to changes in the mass ratio. From Figure 4.17(b), it is evident that the tangent bifurcations that form the well-known halo and axial families persist for large mass ratios. Additionally, the period doubling bifurcation that occurs at larger values of the orbital period is also present. One notable feature in this composite stability representation is the presence of an

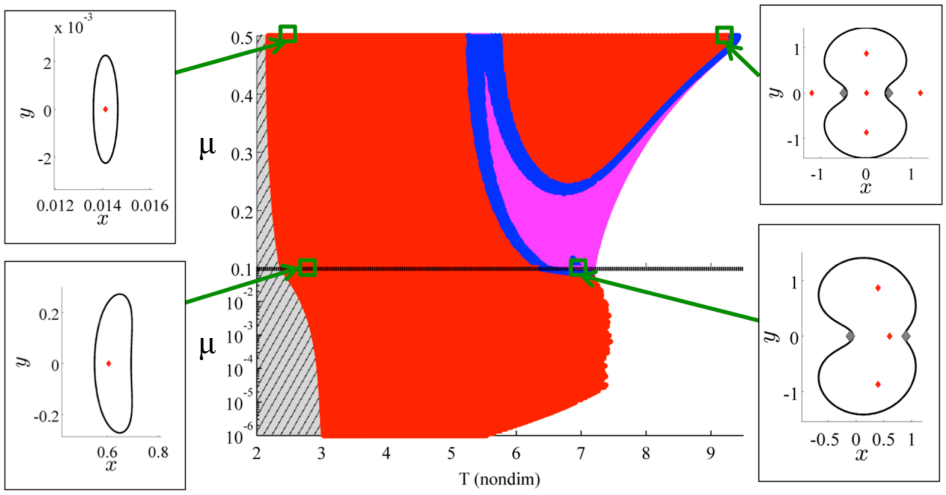

(a) In-plane stability.

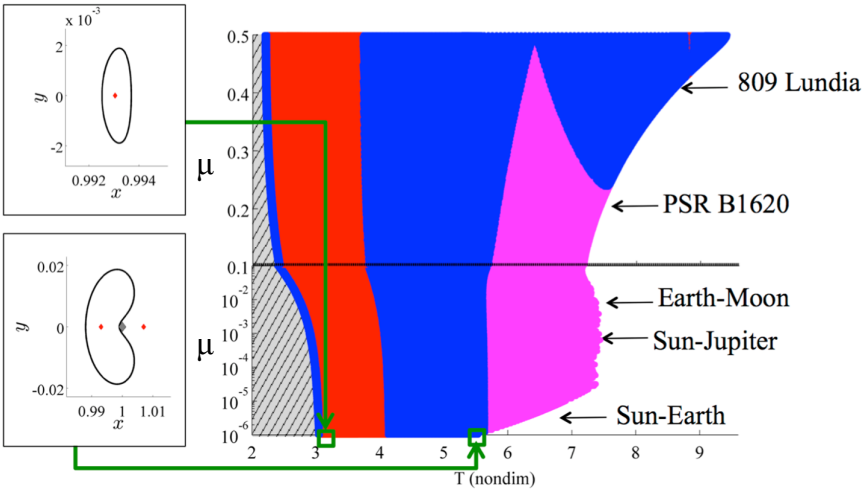

(b) Out-of-plane stability.

Fig. 4.17. Stability representation for L_1 Lyapunov orbits. Orbital stability is indicated via color: stable (blue), positive unstable (red), and negative unstable (purple).

additional blue, stable region for mass ratios larger than the value $\mu \approx 0.238$. Above this critical value, the two period-doubling bifurcations approach each other in orbital period and Jacobi constant with increasing values of μ. Combining both the in-plane and out-of-plane stability information for the L_1 Lyapunov family, there are

some small regions that indicate the presence of stable orbits. From the computed portions of this family, these regions exist for mass ratios above $\mu = 0.174$ and form small slivers at periods within the range $T = [5.28, 6.02]$. There is also a small region of total stability corresponding to larger orbital periods. Given that the range of orbital periods corresponding to these small regions evolves with the mass ratio, the detection of motion that resembles orbits in the L_1 Lyapunov family may be used to suggest bounds on a poorly known mass ratio for $\mu \geq 0.174$. Such insight, as gained from the composite stability representations of a variety of families in the CR3BP, may also allow for a rapid identification of potential motions of an exoplanet in the vicinity of a low-eccentricity binary star system, thereby guiding more numerically intensive analyses.

4.6 Survey of Associated Quasi-Periodic Motion

The stability representations constructed thus far enable the identification of stable orbits that possess a center manifold comprised of quasi-periodic trajectories. These bounded nonperiodic paths may be useful in predicting the behavior of an exoplanet that is, at least temporarily, captured within a binary system. In contrast to periodic orbits that are characterized by one fundamental frequency, quasi-periodic trajectories can be decomposed into multiple underlying frequencies. Accordingly, observational data of exoplanets following quasi-periodic paths may result in the detection of multiple fundamental frequencies. Such motions, which exist in families, may resemble the nearby stable orbit or appear distinctively different. Sample tori associated with quasi-periodic trajectories are computed using the methodology from Section 3.2.1 and applied within a binary system as described by $\mu = 0.30$. Figure 4.18 depicts sample tori for a large nearly circular retrograde orbit in the exterior region that possesses a Jacobi constant value equal to $C = 3.276$, with the direction of motion indicated by black arrows. In particular, Figure 4.18(a) features a planar path, tightly bound in the vicinity of the reference orbit, while Figure 4.18(b) dis-

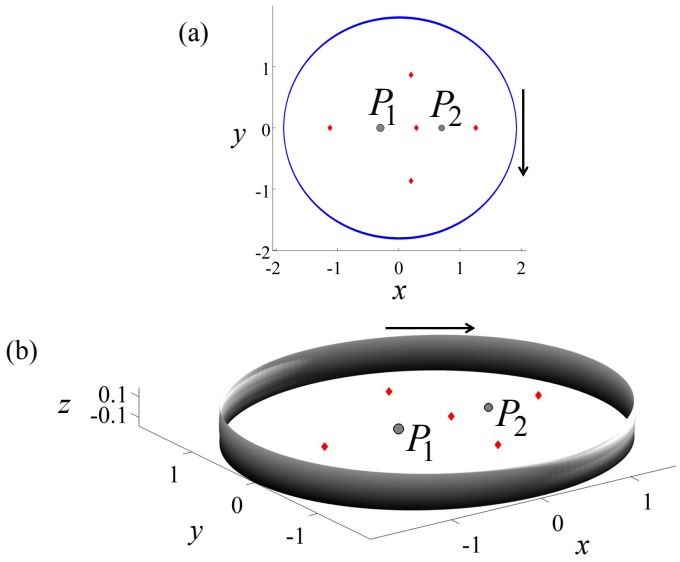

Fig. 4.18. Sample tori describing (a) planar and (b) spatial quasi-periodic motion near a retrograde exterior orbit at $C = 3.276$ for $\mu = 0.30$.

plays a torus that extends out of the plane of motion of the primaries. Next, sample tori associated with retrograde orbits about P_1 are plotted in configuration space in Figure 4.19 including (a) a planar path at $C = 0.7695$, one that closely resembles the reference periodic motion, (b) a three-dimensional path at $C = 0.6103$, and (c) a spatial trajectory at $C = 1.8941$. In each figure, the reference periodic orbit is plotted in red. While the three-dimensional torus in Figure 4.19(c) closely resembles the associated periodic orbit, Figure 4.19(b) features a torus that exhibits an interesting geometry due to the uneven distribution of the toroidal surface around the reference orbit. For instance, along the spatial path in Figure 4.19(b), on the side of the orbit that lies closest to P_2, the maximum out of plane excursion in configuration space is smaller than on the opposite side of the orbit. In addition, quasi-periodic orbits that lie near a retrograde orbit about P_2 at $C = 1.6420$ are plotted in Figure 4.20 for (a) a planar path and (b) an out of plane torus. In each case, the quasi-periodic trajectory exhibits a reasonably small deviation in behavior from the reference periodic orbit.

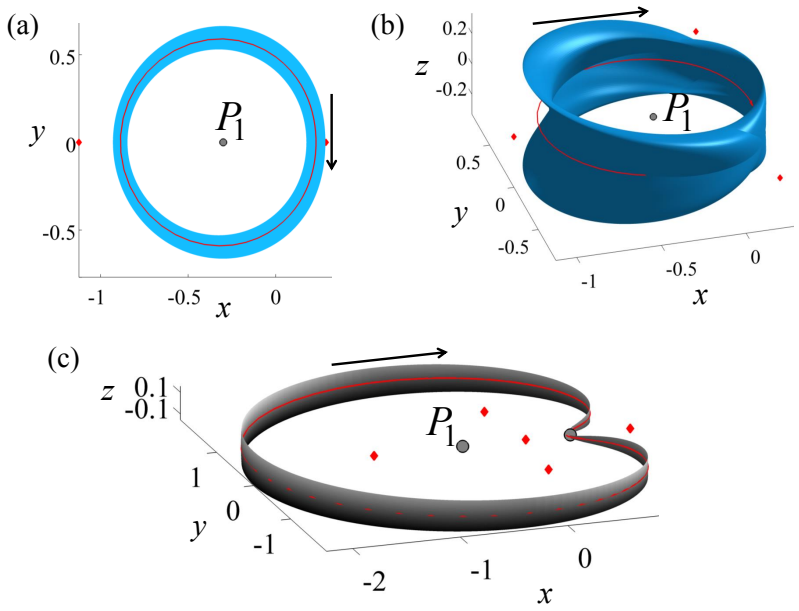

Fig. 4.19. Sample tori describing quasi-periodic motion near a retrograde orbit about P_1 for $\mu = 0.30$ including (a) a planar path at $C = 0.7695$, (b) a spatial path at $C = 0.6103$ and (c) a spatial trajectory at $C = 1.8941$.

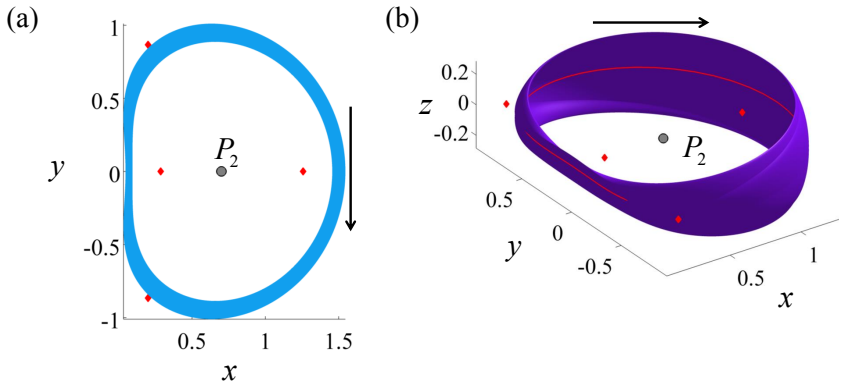

Fig. 4.20. Sample tori describing quasi-periodic motion near a retrograde orbit about P_2 at $C = 1.642$ for $\mu = 0.30$ including (a) a planar path and (b) a spatial path.

However, each path is described by an additional frequency that might be detected through the pulse timing measurements or other observational data. Next, sample tori near prograde orbits about P_1 are plotted in Figures 4.21 and 4.22. In each of these examples, the planar and spatial paths resemble the associated periodic orbits. However, the deviations from these reference paths could explain a detection of exoplanets that are instantaneously located beyond the radii expected from an analysis of purely periodic motion. Finally, multiple tori at a single value of the Jacobi constant, $C = 3.851$, for a reference periodic orbit in the L_1 Lyapunov family are displayed in Figure 4.23 from (a) an out of plane perspective and (b) a view looking down onto the plane of motion of the primaries. Note that not all members of the L_1 Lyapunov family are associated with tori such as those plotted in Figure 4.23. However, energy levels corresponding to those at which such motion is observed, the tori emanate from the reference L_1 Lyapunov orbit and continue to extend out of the plane until they collapse to a separate family of L_1 vertical orbits. Such motion that lies within the L_1 vicinity may exhibit characteristics inherited from two different families of periodic orbits. Although this survey of tori is not exhaustive, it offers a sample of the

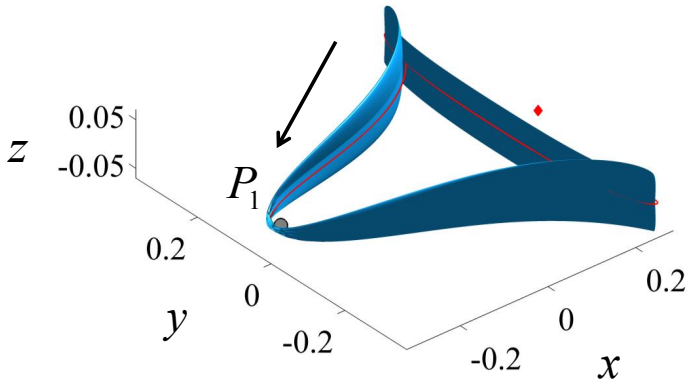

Fig. 4.21. Sample tori describing (a) planar and (b) spatial quasi-periodic motion near a prograde orbit about P_1 in 'family 1' for $\mu = 0.30$.

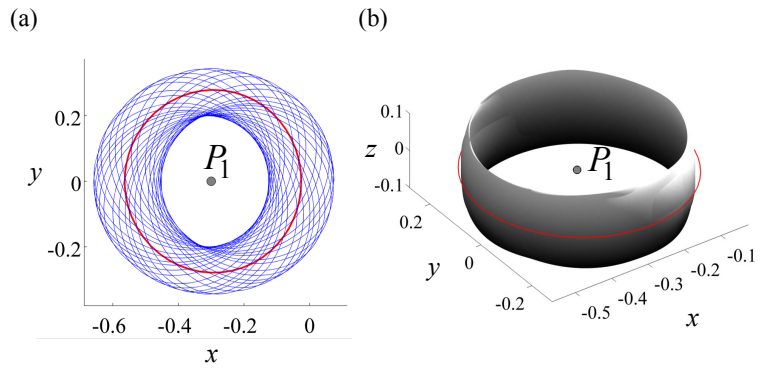

Fig. 4.22. Sample tori describing (a) planar and (b) spatial quasi-periodic motion near a low nearly circular prograde orbit at $C = 4.137$ for $\mu = 0.30$.

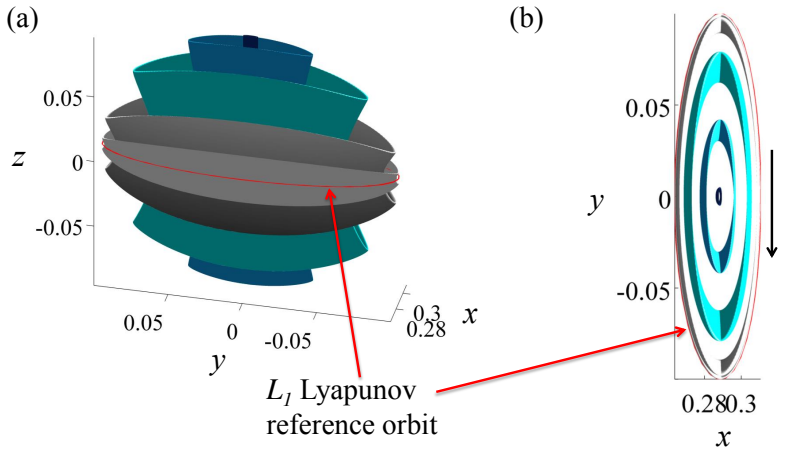

Fig. 4.23. Sample tori describing quasi-periodic motion near an L_1 Lyapunov orbit at $C = 3.851$ for $\mu = 0.30$.

types of ordered motion that exist within the phase space for a binary system with a large mass ratio. Furthermore, these sample quasi-periodic trajectories may support alternatives for describing the path of an exoplanet following motion that is bounded over a long time interval and described by multiple fundamental frequencies.

5. DISCRETE VARIATIONAL MECHANICS

To supplement the use of composite stability representations in observing changes in the periodic orbits along a family, discrete variational mechanics is employed to simultaneously solve for the periodic orbit that resembles a given reference path as well as the associated natural parameters describing the dynamical environment. As opposed to various numerical schemes, such as collocation or a multiple-shooting method, that require the continuous differential equations representing a dynamical system be exactly satisfied at a discrete set of nodes or along multiple trajectory arcs, the discrete variational methodology begins with a discretization of the action integral [30]. A discrete version of Hamilton's principle, which involves the variation only at a finite set of nodes along a discretized path, is used to constrain the motion as it evolves within a dynamical system [34]. These constraints are leveraged to construct a constrained optimization problem, possessing a formulation similar to discrete mechanics and optimal control (DMOC), for the computation of periodic orbits that possess a desired geometry, along with the associated values of the natural parameters. In contrast to multiple shooting, this methodology does not require numerical integration, and may alleviate the impact of numerical sensitivities induced by a poor initial guess in a chaotic system. To establish a framework for this methodology, some background is offered, followed by a discussion of the application of discrete variational mechanics to the construction of natural trajectories in the CR3BP. This technique is later employed to facilitate exploration of the influence of a three-body interaction on orbits within a binary star system.

5.1 Variational Principles for Continuous Time Systems

Prior to a discussion of discrete variational concepts, fundamental variational principles in Lagrangian mechanics are summarized within the context of continuous time systems. First, consider an autonomous mechanical system that can be described by a Lagrangian, $L(\bar{q}(t), \dot{\bar{q}}(t))$, for the m-dimensional generalized coordinate vector $\bar{q}$ and m-dimensional generalized velocity vector $\dot{\bar{q}}$. Integrating this continuous Lagrangian along a path from a time $t_0 = 0$ to a subsequent time t yields the following functional, typically identified as the action integral [63]:

$$A = \int_{t_0}^{t} L(\bar{q}(t), \dot{\bar{q}}(t))dt \tag{5.1}$$

By Hamilton's principle, any actual path $\bar{q}(t)$ in a holonomic system results in a stationary action integral with respect to path variations, for fixed endpoints [64]. For an autonomous mechanical system, this statement is expressed as:

$$\delta A = \delta \int_{t_0}^{t} L(\bar{q}(t), \dot{\bar{q}}(t))dt = \int_{t_0}^{t} \sum_{j=1}^{m} \left[\left(\frac{\partial L}{\partial q_j} - \frac{d}{dt} \left(\frac{\partial L}{\partial \dot{q}_j} \right) \right) \delta q_j \right] dt = 0 \tag{5.2}$$

For this statement to be true for all nonzero variations along the path $\bar{q}(t)$, the integrand of Eq. (5.2) must equal zero in each dimension of the configuration space, thereby recovering the continuous time Euler-Lagrange equations written as:

$$\frac{\partial L}{\partial q_j} - \frac{d}{dt} \left(\frac{\partial L}{\partial \dot{q}_j} \right) = 0 \tag{5.3}$$

for the j-th configuration space variable. Thus, a natural trajectory followed by a holonomic and autonomous continuous time system must satisfy the Euler-Lagrange equations, a well-known concept in Lagrangian mechanics [63].

5.2 Variational Principles for Discrete Time Systems

In the absence of an analytical solution for the motion of a system, only a discretely sampled path is available, requiring modification of the continuous variational concepts in Lagrangian mechanics to accommodate discrete time, as explored by Marsden

and West [31]. Sampling of a natural trajectory inherently occurs during numerical integration, or even observation. Consider, for this investigation, discrete sampling occurring N times at constant time intervals, of length h, for a total time $t = (N-1)h$. Then, a continuous vector path $\bar{q}(t)$ is approximated by a discrete path $\tilde{\bar{q}}$ described by the set of generalized coordinates $\bar{q}_i^* = \tilde{\bar{q}}(ih)$ where $i = 0, 1, ..., N-1$ [31]. Velocities along the path are replaced by finite difference approximations, such as $\dot{\bar{q}}_i^* \approx \frac{(\bar{q}_{i+1}^* - \bar{q}_i^*)}{h}$, which converge to the true velocity along a nonlinear path as h approaches an infinitesimally small value. Analogous to the theory associated with continuous time systems, a discrete time Lagrangian for an autonomous system can then be defined as $L_d(\bar{q}_i^*, \bar{q}_{i+1}^*, h)$, approximating the integral of the true Lagrangian, $L(\bar{q}(t), \dot{\bar{q}}(t))$, over the i-th time interval of length h as the system evolves from $\bar{q}_i^*$ to $\bar{q}_{i+1}^*$ [34]. Since $L_d(\bar{q}_i^*, \bar{q}_{i+1}^*, h)$ is assessed as a numerical integral, a quadrature rule must be selected to approximate the continuous dynamics of the system [31]. Once an expression for $L_d(\bar{q}_i^*, \bar{q}_{i+1}^*, h)$ is defined, a discrete action is then constructed using the summation of the discrete Lagrangian over all $N-1$ time intervals, such that:

$$A_d = \sum_{i=0}^{N-2} L_d(\bar{q}_i^*, \bar{q}_{i+1}^*, h) \approx \int_{t_0}^{t} L(\bar{q}(t), \dot{\bar{q}}(t))dt \tag{5.4}$$

Applying Hamilton's principle to this expression for the discrete action, and using summation by parts, a discrete time counterpart to Eq. (5.2) is available:

$$\begin{aligned}\delta A_d &= \delta \sum_{i=0}^{N-2} L_d(\bar{q}_i^*, \bar{q}_{i+1}^*, h) \\ &= \sum_{i=1}^{N-2} \sum_{j=1}^{m} \left[\left(\frac{\partial L_d(\bar{q}_i^*, \bar{q}_{i+1}^*, h)}{\partial q_{i,j}^*} + \frac{\partial L_d(\bar{q}_{i-1}^*, \bar{q}_i^*, h)}{\partial q_{i,j}^*} \right) \delta q_{i,j}^* \right] = 0\end{aligned}$$

where $q_{i,j}^*$ is the j-th configuration space variable at time t_i. From this expression, for the discrete action to be stationary with respect to all path variations, with fixed endpoints, the following discrete Euler-Lagrange equations must be satisfied across each time interval $[t_i, t_{i+1}]$. :

$$\frac{\partial L_d(\bar{q}_i^*, \bar{q}_{i+1}^*, h)}{\partial q_{i,j}^*} + \frac{\partial L_d(\bar{q}_{i-1}^*, \bar{q}_i^*, h)}{\partial q_{i,j}^*} = 0 \tag{5.5}$$

for $i = [1, N-2]$ and $j = [1, m]$. Note that this form of the discrete Euler-Lagrange equations is only true for holonomic autonomous systems with no external forcing, as is the case for the dynamical model employed in this investigation. Straightforward modifications to these discrete equations to accommodate forcing terms or nonautonomous Lagrangians, for example, are available and have been employed by numerous authors in previous works [31], [34].

5.3 Formulation of Constrained Optimization Problem

The concepts from discrete variational mechanics provide a set of constraints, in the form of the discrete Euler-Lagrange equations, that can be used in a constrained optimization problem to determine a discrete path minimizing a given objective function. In this investigation, however, the underlying formulation of discrete mechanics and optimal control is applied to the search for a natural trajectory (i.e., no required control forces) resembling a given reference path, along with the corresponding values of the parameters describing the dynamical field.

To construct an orbit with a desired geometry using a constrained optimization problem, an objective function is required. In a continuous time system, this objective function takes the form of an integral over the path $\bar{q}(t)$ from time $t_0 = 0$ to t, given by $J(\bar{q}, \dot{\bar{q}}) = \int_{t_0}^{t} C_c(\bar{q}(t), \dot{\bar{q}}(t))dt$, for some specified cost function C_c. However, this infinite-dimensional functional $J(\bar{q}, \dot{\bar{q}})$ is transformed into a finite-dimensional objective function by replacing the integral with a summation of discrete cost functions, each evaluated along the $N-1$ time intervals along the discrete path:

$$J_d(\tilde{\bar{q}}) = \sum_{i=0}^{N-2} C_d(\bar{q}_i^*, \bar{q}_{i+1}^*, h) \approx \int_{t_0}^{t} C_c(\bar{q}(t), \dot{\bar{q}}(t))dt \tag{5.6}$$

Since this approximation implies that the discrete cost function at the i-th node is a numerical integral of the continuous function C_c over the i-th time interval, a quadrature rule can be selected to produce an expression for $C_d(\bar{q}_i^*, \bar{q}_{i+1}^*, h)$ [34]. In the examples in this investigation, the desired solution should resemble a given reference path. Although a continuous cost function that enables the reproduction of a desired

geometry requires knowledge of the state variables along the current solution and the reference path, an appropriate expression could take a number of forms. For instance, a continuous cost function for each node located by a three-dimensional configuration space variable $\bar{q} = (q_1, ..., q_m)$, along the orbit could be defined using the distance from a corresponding point along the reference path, $\bar{q}_{ref} = (q_{1,ref}, ..., q_{m,ref})$, such that $C_c(\bar{q}, \bar{q}_{ref}) = \sum_{j=1}^{m}(q_j - q_{j,ref})^2$. Alternatively, a cost function could be defined using the difference between the velocities along the computed solution and the reference path. This candidate cost function could be expressed using each of the components of the velocity such that $C_c(\dot{\bar{q}}, \dot{\bar{q}}_{ref}) = \sum_{j=1}^{m}(\dot{q}_j - \dot{q}_{j,ref})^2$. A discrete cost function, $C_d(\bar{q}_i^*, \bar{q}_{i+1}^*, h)$, is then determined by applying a numerical integral to this continuous cost function, along with the finite difference approximations to the velocity components. The resulting objective function, constructed by summing $C_d(\bar{q}_i^*, \bar{q}_{i+1}^*, h)$ across all segments, is used within a constrained optimization problem to facilitate orbital computations.

To construct the constraint relationships that enforce natural motion within a dynamical force field, a discrete Lagrangian, approximating the integral of the exact Lagrangian over each of the $N-1$ segments between neighboring nodes, must first be defined. In this investigation, the numerical integral supplying the discrete Lagrangian is approximated using the midpoint rule:

$$L_d(\bar{q}_i^*, \bar{q}_{i+1}^*, h) = hL\left(\frac{\bar{q}_i^* + \bar{q}_{i+1}^*}{2}, \frac{\bar{q}_{i+1}^* - \bar{q}_i^*}{h}\right) \tag{5.7}$$

where L_d is constructed using the average of the position variables evaluated at both the left and right boundaries of the i-th segment, with a velocity that is calculated using a first-order finite differencing. For a given dynamical system, the associated continuous Lagrangian is employed to evaluate the discrete Lagrangian across each segment using the midpoint rule in Eq. (5.7). The resulting expressions for L_d over the i-th and (i-1)-th segments are then differentiated and combined using Eq. (5.5) to form the discrete Euler-Lagrange equations, which must be satisfied for all discrete path variations, given fixed endpoints.

Any discrete path that minimizes this objective function must also satisfy the discrete Euler-Lagrange equations, which reflect the dynamics of the system. A finite-dimensional constrained optimization problem for orbit computation within a dynamical field described by a vector of natural parameters, $\bar{\sigma}$, is summarized as:

$$\min \qquad J_d(\tilde{\bar{q}}) = \sum_{i=0}^{N-2} C_d(\bar{q}_i^*, \bar{q}_{i+1}^*, \bar{\sigma}, h)$$

subject to the constraints from Eq. (5.5), reflecting the system dynamics, for each dimension of the configuration space:

$$\frac{\partial L_d(\bar{q}_i^*, \bar{q}_{i+1}^*, \bar{\sigma}, h)}{\partial q_{i,j}^*} + \frac{\partial L_d(\bar{q}_{i-1}^*, \bar{q}_i^*, \bar{\sigma}, h)}{\partial q_{i,j}^*} = 0$$

for $i = [1, N-2]$, and $j = [1, m]$, where $q_{i,j}^*$ is the j-th configuration space variable evaluated at time t_i. At each of these interior nodes, the resulting constrained optimization problem can potentially affect the configuration space variables. Furthermore, h and the scalar components of the natural parameter vector $\bar{\sigma}$ are all assumed to be variables, thereby allowing modification of both the orbital period and the dynamical environment. To ensure periodicity along the approximate path, position and momentum continuity is enforced across the first and last time intervals using, respectively, equality constraints on the position variables and the discrete Euler-Lagrange equations. For each of the three dimensions within configuration space, the position constraint is expressed as:

$$q_{0,j}^* - q_{N-1,j}^* = 0$$

while momentum continuity is written as:

$$\frac{\partial L_d(\bar{q}_0^*, \bar{q}_1^*, \bar{\sigma}, h)}{\partial q_{0,j}^*} + \frac{\partial L_d(\bar{q}_{N-2}^*, \bar{q}_{N-1}^*, \bar{\sigma}, h)}{\partial q_{N-1,j}^*} = 0$$

for $j = [1, m]$. Together, these constraints enforce periodicity along the discrete approximation to a periodic orbit. Depending upon the application, either equality or inequality constraints are applied to h and the scalar components of the natural parameter vector $\bar{\sigma}$. The resulting constrained optimization problem, formulated

using discrete variational mechanics, is implemented using the sequential quadratic programming algorithm available in MATLAB's *fmincon* routine to compute a natural trajectory that resembles a desired reference path, as well as the corresponding dynamical environment via the values of the system natural parameters.

In contrast to alternative orbit computation techniques, the discrete variational methodology possesses numerous advantages in the construction of orbits with desired shape characteristics at various values of the natural parameters. In a multiple shooting scheme, the continuous dynamics that represent a nonlinear system are satisfied along each trajectory arc via numerical integration. However, an integrated trajectory in a chaotic system can exhibit significant sensitivity to both the initial state and the natural parameters. In fact, given a reference path, the computation of a similar orbit at a different combination of the system parameters likely requires the use of a continuation method and small steps in the parameter space. Nevertheless, corrections algorithms that employ multiple shooting typically leverage the state transition matrix, which either increases the computational burden when integrated numerically along the path, or introduces inaccuracies when an STM is approximated using finite differencing. Furthermore, it can be difficult to recover a desired shape characteristic along integrated arcs in a multiple shooting method. A collocation strategy, however, employs a set of polynomials to link neighboring nodes along a discrete path that must approximately satisfy the equations of motion at intermediate points along each arc [50]. In contrast to a multiple shooting method, a collocation approach can overcome some of the sensitivities associated with a poor initial guess and enable the recovery of desired shape characteristics via the nodes along the discretized path. In addition, this computational technique benefits from the use of algebraic relations to evaluate the constraints, rather than numerical integration. While offering advantages similar to those from collocation algorithms, discrete variational mechanics also benefits from the significant reduction in computational cost due to fewer design variables as each node is described solely in configuration space. Furthermore, variational techniques typically preserve the geometric properties of a Lagrangian flow [31].

Thus, discrete variational mechanics is employed in this investigation to aid in the recovery of trajectories that exhibit a desired behavior, as well as the associated natural parameters of the system.

5.4 Periodic Orbit Computation in the CR3BP

To demonstrate the utility of discrete variational mechanics for periodic orbit computation, consider the recovery of natural, planar behavior within the CR3BP. For the continuous time representation of this dynamical model, the planar state of the system is described by the two-dimensional configuration space vector $\bar{q} = (x, y)$ and the generalized velocity vector $\dot{\bar{q}} = (\dot{x}, \dot{y})$. Using this description of the state of the system, the continuous time Lagrangian is straightforwardly written as:

$$L(x, y, \dot{x}, \dot{y}) = \frac{1}{2}(\dot{x} - y)^2 + \frac{1}{2}(\dot{y} + x)^2 + \frac{1-\mu}{r_1} + \frac{\mu}{r_2} \tag{5.8}$$

where $r_1 = \sqrt{(x+\mu)^2 + y^2 + z^2}$ and $r_2 = \sqrt{(x-1+\mu)^2 + y^2 + z^2}$. Next, this continuous time Lagrangian is employed to evaluate the discrete Lagrangian across each segment using the midpoint rule, as summarized in Eq. (5.7), to produce:

$$L_d = hL\left(\frac{x_i + x_{i+1}}{2}, \frac{x_{i+1} - x_i}{h}, \frac{y_i + y_{i+1}}{2}, \frac{y_{i+1} - y_i}{h}, \mu, h\right)$$

where x_i and y_i are the discrete time configuration space variables at time t_i, and h is the constant time step between neighboring nodes. The expression for L_d is evaluated over the i-th and (i-1)-th segments and then differentiated and combined using Eq. (5.5) to form the discrete Euler-Lagrange equations, which must be satisfied at each of the interior nodes. Subsequently, the constrained optimization problem that is used to recover natural, planar periodic orbits in the CR3BP is summarized as:

$$\begin{aligned}\min \ J_d &= \sum_{i=0}^{N-2} C_d(x_i, x_{i+1}, y_i, y_{i+1}, \mu, h) \\ &= \sum_{i=0}^{N-2} \left(\frac{x_i + x_{i+1}}{2} - \frac{x_{i,ref} + x_{i+1,ref}}{2}\right)^2 + \left(\frac{y_i + y_{i+1}}{2} - \frac{y_{i,ref} + y_{i+1,ref}}{2}\right)^2\end{aligned}$$

subject to equality constraints in the form of the discrete Euler-Lagrange equations, which reflect the system dynamics:

$$\frac{\partial L_d(x_i, x_{i+1}, y_i, y_{i+1}, \mu, h)}{\partial x_i} + \frac{\partial L_d(x_i, x_{i+1}, y_i, y_{i+1}, \mu, h)}{\partial x_i} = 0$$

$$\frac{\partial L_d(x_i, x_{i+1}, y_i, y_{i+1}, \mu, h)}{\partial y_i} + \frac{\partial L_d(x_i, x_{i+1}, y_i, y_{i+1}, \mu, h)}{\partial y_i} = 0$$

for $i = 1, ..., N-2$. In addition, periodicity is enforced via the following position and momentum constraints:

$$x_0 - x_{N-1} = 0 \qquad y_0 - y_{N-1} = 0$$

$$\frac{\partial L_d(x_0, x_1, y_0, y_1, \mu, h)}{\partial x_0} + \frac{\partial L_d(x_{N-2}, x_{N-1}, y_{N-2}, y_{N-1}, \mu, h)}{\partial x_{N-1}} = 0$$

$$\frac{\partial L_d(x_0, x_1, y_0, y_1, \mu, h)}{\partial y_0} + \frac{\partial L_d(x_{N-2}, x_{N-1}, y_{N-2}, y_{N-1}, \mu, h)}{\partial y_{N-1}} = 0$$

At each of the interior nodes, this constrained optimization problem can affect the two position variables in this planar problem, $\bar{q}_i^* = (x_i, y_i)$. Furthermore, h and μ are assumed to be variables to allow modification of both the orbital period and the dynamical environment, resulting in a total of $2N+2$ design variables. This constrained optimization problem is implemented using the sequential quadratic programming algorithm available in MATLAB's *fmincon* routine to enable the recovery of planar periodic orbits possessing a desired geometry in the CR3BP.

To examine the validity of using discrete variational mechanics to compute periodic orbits in the CR3BP, a sample orbit is recovered from a significantly perturbed initial guess, along with the corresponding time interval, h, and the natural parameter μ describing the system. In fact, a retrograde exterior orbit of period $T = 27.4545$ nondimensional time units is selected from the composite stability representation in Figure 4.3. This orbit is known to exist in the CR3BP with a mass ratio equal to $\mu = 0.30$. The continuous orbit, depicted in Figure 5.1(a), is discretized into 400 nodes, each separated by a constant nondimensional time step of $h = 0.0688$. In this figure, the primaries are located via gray-filled circles, while the equilibrium points are identified using red-filled diamonds. As a test of the utility of discrete variational

mechanics for periodic orbit computation, an initial guess, plotted with black cross markers in Figure 5.1(b), is constructed using the actual time step, h, along with the original discretized reference path perturbed by randomly distributed errors in the range $[-0.05, 0.05]$ applied to the x and y variables describing each node. A mass ratio value of $\mu = 0.25$ is also employed in this straightforward test case, producing a poor initial guess for a natural periodic orbit in the CR3BP. In fact, integration of selected nodes along the discrete path using the first guesses for the natural parameters would reveal arcs that deviate significantly from the desired motion. This initial guess is then supplied to the constrained optimization problem implemented in Matlab, with the goal of computing a periodic orbit that resembles the original discretized periodic orbit as closely as possible. Recall that in the CR3BP, periodic orbits exist in continuous families over a range of mass ratios. Accordingly, exact recovery of the original periodic orbit and mass ratio is not expected. Rather, a discretized periodic orbit with a nearby value of the mass ratio and a similar geometry to the reference path is likely to be recovered. In correcting the initial guess for both the path and the natural parameter μ, the description of each node in configuration

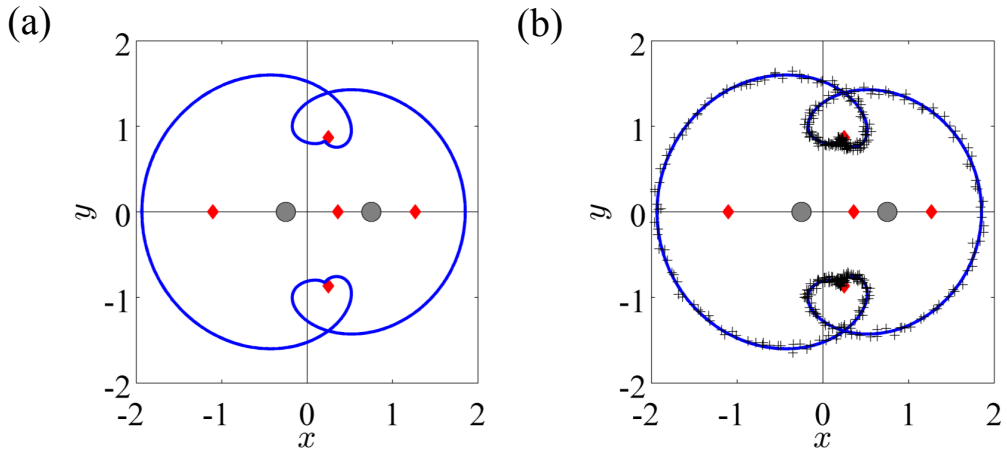

Fig. 5.1. (a) Reference periodic orbit (blue) and (b) perturbed initial guess (black cross markers) for demonstration of periodic orbit computation via discrete variational mechanics.

space, along with the values of h and μ are allowed to vary. One converged solution, represented by purple circles is overlaid on the original reference orbit, depicted in blue, in Figure 5.2(a). This locally optimal solution, which satisfies the constraints to within a tolerance of 5×10^{-11}, appears to closely match the original reference path, and possesses values of $\mu = 0.2996$ and $h = 0.0701$, which are close to the values corresponding to the true periodic orbit. In addition, note that the converged discrete path does not exactly reflect a periodic orbit in the continuous time system, but rather an approximation. This discrete approximation is, however, used to generate a truly periodic orbit via differential corrections for verification. In fact, a nearby periodic orbit, colored black, is overlaid on the converged discrete path, represented by purple circles, in Figure 5.2(b). In this example, the original continuous solution lies sufficiently close to the computed discrete approximation, thereby demonstrating the use of discrete variational mechanics in recovering a periodic orbit as well as the natural parameters of a dynamical system that may enable a desired type of motion to exist.

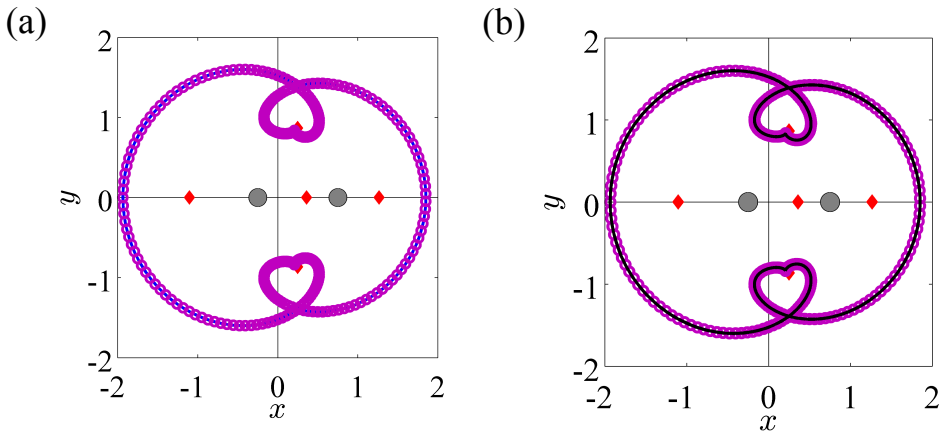

Fig. 5.2. (a) Original reference periodic orbit for $\mu = 0.30$ and $h = 0.0688$ (blue) and computed discrete solution for $\mu = 0.2996$ and $h = 0.0701$ (purple) possessing the desired geometry. (b) Overlaid on the converged discrete solution (purple), a nearby continuous periodic orbit (black) found via differential corrections for $\mu = 0.2996$.

6. APPLICATION: EXPLORING THE EFFECT OF A THREE-BODY INTERACTION

Consider a binary star system (e.g., pulsar-white dwarf, pulsar-pulsar) with a significantly smaller companion, such as an exoplanet, in orbit about the binary. Since binary star systems are located many light-years from the Earth, the characteristics of the binary, and any smaller companions, are determined using a variety of observational techniques, including pulsar timing measurements. A pulsar in complete isolation would rotate about its spin axis with a constant angular velocity, emitting pulses of radiation at a constant rate. However, in the presence of additional stars, the pulsar appears to rotate with a time-dependent angular velocity. Furthermore, smaller variations in the pulse timing data may provide clues to the existence of comparatively small exoplanets that are, at least temporarily, captured within the vicinity of the binary. Analysis of this observational data enables a prediction of the orbits followed by these exoplanets and, potentially, the presence and strength of additional force contributions such as gravitational wave radiation and magnetic fields.

Due to the strong gravitational field near a binary star, physicists have previously leveraged these systems as testbeds for examining the validity of gravitational and relativistic theories [65]. In this investigation, a preliminary analysis into the effect of an additional three-body interaction on the dynamical environment near a large mass ratio binary system is completed. Many-body forces are not an entirely new concept; in fact, the importance of three-body interactions in accurately modeling force fields on the atomic scale is well established in nuclear physics [7]. On a much larger scale, the motion of a small body orbiting a binary system serves as an interesting application for determining the potential existence and characteristics of a three-body interaction within the context of orbital dynamics. Assuming that the exoplanet possesses a negligible mass in comparison to the binary, the complexity of

the dynamical model may be reduced by considering only the pairwise, point-mass Newtonian gravitational contributions from the two stars. In addition, the two stars comprising the binary are assumed to possess similar mass, resulting in a mass ratio that is significantly larger than the mass ratios of objects considered within the solar system. Each star is assumed to follow conical paths about their barycenter, modeled with zero eccentricity. These assumptions enable the use of the CR3BP as a foundation for modeling the motion of an exoplanet in the vicinity of a binary star system. Since this model is inherently chaotic and nonlinear, analysis of the underlying dynamical structures is leveraged to identify unique characteristics that may be exhibited by an exoplanet within a dynamical environment that is influenced by a three-body interaction, potentially enabling detection or an estimation of the bounds on the strength of this additional force.

Identification and characterization of particular solutions for a nearby, small companion body enables a well-informed exploration of the impact of an additional force contribution on the dynamical environment near a binary star system. To enable a preliminary analysis of a many-body force in gravitational problems, an alternative dynamical model for the binary system is derived based on the CR3BP, augmented by an additional term in the potential function, producing a Modified Circular Restricted Three-Body Problem (MCR3BP). The three-body interaction, scaled using a constant k, is assumed to depend inversely on the product of the distances between the three bodies: the closer the bodies, the stronger the three-body interaction [8]. In this modified dynamical model, equilibrium points and families of periodic and quasi-periodic orbits still exist, but may evolve with the value of k in a manner that is not reproducible in the natural gravitational environment. Any unique effects of a three-body interaction may influence the underlying dynamical structures in a binary star system and, therefore, affect the potential motions of a nearby exoplanet. Through the identification of qualitative changes to natural particular solutions for the behavior of an infinitesimal body, a guided and well-informed exploration of the effect of an additional autonomous force contribution is completed. In particular,

structural and physical changes in the configuration of a family of periodic orbits are straightforwardly identified in the MCR3BP via composite stability representations. Features of interest are then examined using discrete variational mechanics over a range of natural parameters, enabling analysis of the uniqueness of the effect of a many-body interaction within a binary star system. Although a three-body interaction is modeled in this investigation, a similar analysis can be completed for any other alternative force that is both autonomous and derivable from a potential function, such as a time-averaged quantity or a higher-order gravitational term for a body fixed in a given coordinate frame.

6.1 Modified Circular Restricted Three-Body Problem

To explore the effect of a three-body interaction near binary star systems, an additional term is added to the potential function in the CR3BP, producing an augmented dynamical model that is labeled the MCR3BP. Given a system configuration consistent with the CR3BP, derivation of the differential equations governing the motion of P_3 in the MCR3BP requires the definition of the potential function. For this application, the nearby companion body, P_3, could take the form of an exoplanet, while the two primaries, P_1 and P_2, could each correspond to a star, such as a pulsar or a white dwarf. In the inertial frame, the dimensional scalar potential of P_3, per unit mass, is assumed to consist of the following terms:

$$\tilde{U}_3 = \underbrace{\frac{\tilde{G}\tilde{M}_1}{\tilde{R}_{13}} + \frac{\tilde{G}\tilde{M}_2}{\tilde{R}_{23}}}_{\text{pairwise gravitational potential}} + \underbrace{\frac{\tilde{K}}{\tilde{R}_{12}\tilde{R}_{13}\tilde{R}_{23}}}_{\text{three-body potential}} \tag{6.1}$$

where the tilde denotes dimensional quantities, $\tilde{G}$ is the universal gravitational constant, $\tilde{M}_i$ is the mass of the i-th primary, $\tilde{R}_{ij}$ is the distance between body i and body j, and $\tilde{K}$ is a constant that scales the contribution of the three-body interaction to the resultant potential with the associated dimensions $[length]^5[time]^{-2}$. Nondimensionalization via the characteristic mass, length and time quantities, m^*,

l^*, and t^*, as defined in Section 2.1 produces the following nondimensional scalar potential corresponding to P_3, per unit mass:

$$U_3 = \underbrace{\frac{1-\mu}{r_1} + \frac{\mu}{r_2}}_{\text{pairwise gravitational potential}} + \underbrace{\frac{k}{r_1 r_2}}_{\text{three-body potential}} \tag{6.2}$$

where k is the nondimensional constant that scales the three-body potential term [8]. Recall that r_i is the distance between P_3 and primary i, while μ is the ratio of the mass of the smallest primary to the total mass of the binary system. Although the three-body interaction is assumed to depend inversely on the product of the distances between all three bodies, the distance between P_1 and P_2 is equal to a constant value of unity in this model. Accordingly, only r_1 and r_2 appear in the denominator of the three-body potential term. Since the magnitude and sign of the constant k are unconstrained, it is assumed that k can be selected as either positive, negative or zero. When the value of the constant k is equal to zero, the potential in the MCR3BP reduces to the CR3BP potential; if k is positive, the three-body interaction is attractive, while a negative value of the coefficient corresponds to a repulsive interaction. Bounds are, however, placed on the value of k for numerical and dynamical reasons. For example, a lower limit of $k = -0.20$ is considered in this investigation: at $\mu = 0.30$, this value of k corresponds to a repulsive three-body interaction that is approximately half as strong as the gravitational attraction of the two primaries in some regions of configuration space. Positive values of k, however, are bound by the upper limit of $k = 0.70$ due to increased numerical sensitivities when integrating a path along with its state transition matrix.

From the derivatives of the potential function in Eq. (6.2), the equations of motion for P_3 are derived using a process similar to that in Section 2.1 and a constant of motion is subsequently identified. These nondimensional equations of motion, as expressed in the rotating frame, are written as:

$$\ddot{x} = 2\dot{y} + x - \frac{(1-\mu)(x+\mu)}{r_1^3} - \frac{\mu(x-1+\mu)}{r_2^3} - k\left[\frac{(x-1+\mu)}{r_1 r_2^3} + \frac{(x+\mu)}{r_1^3 r_2}\right] \tag{6.3}$$

$$\ddot{y} = -2\dot{x} + y - \frac{(1-\mu)y}{r_1^3} - \frac{\mu y}{r_2^3} - k\left[\frac{y}{r_1 r_2^3} + \frac{y}{r_1^3 r_2}\right] \tag{6.4}$$

$$\ddot{z} = -\frac{(1-\mu)z}{r_1^3} - \frac{\mu z}{r_2^3} - k\left[\frac{z}{r_1 r_2^3} + \frac{z}{r_1^3 r_2}\right] \tag{6.5}$$

where $r_1 = \sqrt{(x+\mu)^2 + y^2 + z^2}$ and $r_2 = \sqrt{(x-1+\mu)^2 + y^2 + z^2}$. For a detailed derivation of these equations of motion, see previous work by Bosanac [8]. Equivalently, the equations of motion are written in compact form as:

$$\ddot{x} - 2\dot{y} = \frac{\partial U_k^*}{\partial x}, \qquad \ddot{y} + 2\dot{x} = \frac{\partial U_k^*}{\partial y}, \qquad \ddot{z} = \frac{\partial U_k^*}{\partial z} \tag{6.6}$$

where the pseudopotential function is:

$$U_k^* = \frac{1}{2}(x^2 + y^2) + \frac{1-\mu}{r_1} + \frac{\mu}{r_2} + \frac{k}{r_1 r_2} \tag{6.7}$$

The resulting equations of motion retain the symmetry that is characteristic of the CR3BP. To prove this property, consider a change of variables:

$$\tau = -t \qquad x_\tau = x \qquad y_\tau = -y \qquad z_\tau = z$$

$$\dot{x}_\tau = -\dot{x} \qquad \dot{y}_\tau = \dot{y} \qquad \dot{z}_\tau = -\dot{z}$$

Substituting this change of variables into Eq. (6.6), the MCR3BP equations of motion remain unchanged:

$$\frac{d^2 x_\tau}{d\tau^2} - 2\dot{y}_\tau = \frac{\partial U_k^*}{\partial x_\tau}, \qquad -\frac{d^2 y_\tau}{d\tau^2} - 2\dot{x}_\tau = \frac{\partial U_k^*}{\partial(-y_\tau)}, \qquad \frac{d^2 z_\tau}{d\tau^2} = \frac{\partial U_k^*}{\partial z_\tau}$$

Thus, for a single natural solution to the MCR3BP equations of motion, a solution that is symmetric across the x-axis also exists. Furthermore, since this dynamical system is autonomous, a constant energy integral, C_k, can be derived using the same process as Section 2.1.1 to equal:

$$C_k = 2U_k^* - \dot{x}^2 - \dot{y}^2 - \dot{z}^2 \tag{6.8}$$

This integral of motion, C_k, is constant along any natural solution to the MCR3BP equations of motion and reduces to the Jacobi constant in the CR3BP when $k = 0$. Consistent with the CR3BP, the addition of a three-body interaction term still results in a chaotic nonlinear dynamical environment that admits a variety of particular solutions: equilibrium points, periodic orbits, quasi-periodic trajectories and chaos.

6.2 Existence, Location and Stability of Planar Equilibrium Solutions

Although the nonlinear differential equations that govern motion in the MCR3BP do not possess an analytical solution, planar equilibrium points offer significant insight into the resulting multi-body dynamical environment. Recall that in the rotating frame of the CR3BP, five equilibrium points exist, as summarized in Section 2.1.2. However, when an additional three-body interaction is incorporated into the dynamical environment, the existence, location and stability of these five equilibrium points may be impacted. Recall the form of the nondimensional pseudopotential function, as expressed in the rotating frame in Eq. (6.7). Figure 6.1 portrays level sets for: (a) the first three terms of the pseudopotential function in Eq. (6.7), inherited from the CR3BP; and (b) the final term in Eq. (6.7), representing the three-body interaction. In Figure 6.1(a), the level sets occur at positive values, admitting stationary points corresponding to the five L_i of the CR3BP as well as a singularity at each of the primaries, indicated by gray-filled circles. Isolating the three-body interaction term in Eq. (6.7), the potential field exhibits the form depicted in Figure 6.1(b) with singu-

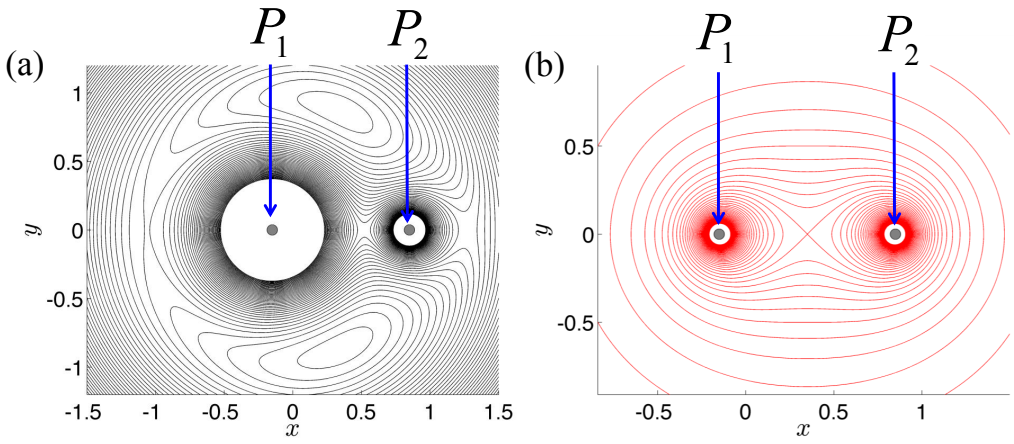

Fig. 6.1. Sample level sets of the components of the augmented pseudopotential function, U_k^*: (a) terms from the CR3BP and (b) the additional three-body interaction term for $k < 0$.

larities at each of the primaries. At negative values of k, corresponding to a repulsive three-body interaction, each level set occurs at negative values of $\frac{k}{r_1 r_2}$; the converse is true for positive values of k. As these two potential contributions are summed and the value of k is varied, the form of the augmented potential field in the MCR3BP evolves. Accordingly, the location, existence and form of the stationary points within the dynamical field are impacted. Since these equilibrium points play an integral role in defining the underlying dynamical structure within a binary system, any change in their properties and associated manifold structures may significantly influence the particular solutions that exist throughout the entire phase space. Thus, significant insight into the effect of a three-body interaction is obtained by characterizing the evolution of the equilibrium points.

With the inclusion of a three-body interaction, each of the planar equilibrium points inherited from the CR3BP appears shifted in configuration space, or may not even exist, as demonstrated via an initial analysis at a single mass ratio of $\mu = 0.30$. First, consider the locations of each of the five equilibrium points in the CR3BP, identified by green dots in Figure 6.2(a) for a system described by $\mu = 0.30$. At this mass ratio, for $k = [-0.20, 0.70]$, the five planar L_i still exist and are perturbed from their locations in the CR3BP, except for L_4 and L_5 which no longer exist for $k < -0.1985$. For positive values of k, the planar equilibrium points are numerically computed and located in the MCR3BP in Figure 6.2(a) using blue dots, while red dots are used to depict each L_i for negative values of k. Purple dots correspond to two additional equilibrium points, labelled L_{4b} and L_{5b} in this investigation, that exist over the small range of values $k \approx [-0.1985, -0.1839]$ as identified analytically by Douskos [66]. Analysis of Figure 6.2(a) reveals that, for an increasingly attractive three-body interaction, i.e., larger positive values of k, the collinear equilibrium points are located farther from P_2 [9]. In addition, the triangular equilibrium points, L_4 and L_5, are no longer located at the vertices of equilateral triangles as in the CR3BP. For negative values of k, however, each of the equilibrium points exists closer to P_2.

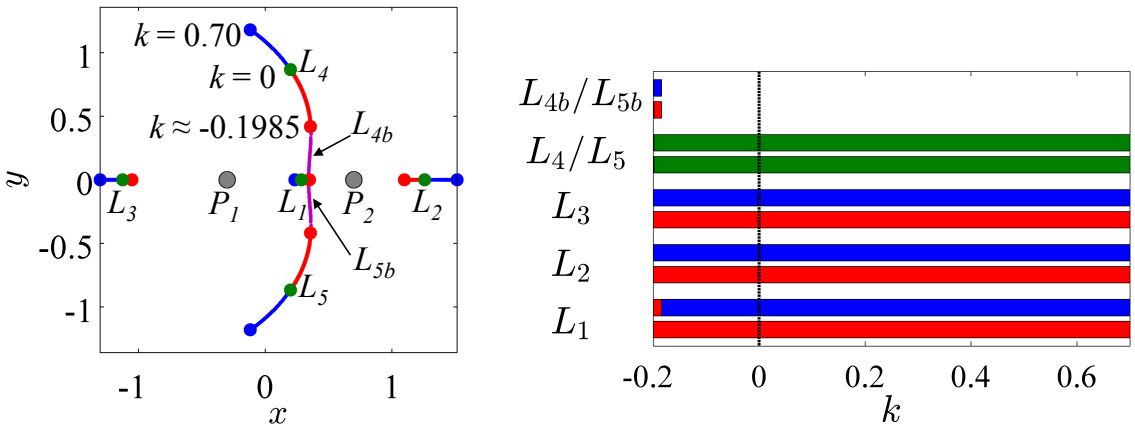

(a) Location of planar equilibrium points in the CR3BP (green) and MCR3BP for $\mu = 0.30$: $k > 0$ (blue), $k < 0$ (red), and $-0.1985 < k < -0.1839$ (purple).

(b) Stability of the two planar modes for each equilibrium point as a function of k for $\mu = 0.30$, with purely oscillatory modes (blue), real eigenvalues (red), or complex conjugate eigenvalues (green).

Fig. 6.2. Equilibrium points in the MCR3BP for $\mu = 0.30$.

To explain the appearance and disappearance of L_{4b} and L_{5b} over a small range of negative values of k, consider a summary of the stability of each equilibrium point at the sample mass ratio of $\mu = 0.30$. In Figure 6.2(b), the two colored bars for each of the labelled L_i reflect a qualitative measure of the linear stability of each of the planar modes. Specifically, blue portions along a bar indicate oscillatory modes corresponding to purely imaginary pairs of eigenvalues, while red reflects the presence of a stable and unstable pair of modes, and green locates complex conjugate eigenvalues at the corresponding values of k. Across the range $k = [-0.20, 0.70]$, indicated along the horizontal axis, this figure reveals that the stability of L_2 and L_3 remains qualitatively unchanged. For L_1, however, the oscillatory mode, which contributes to the existence of the planar Lyapunov family in the CR3BP, undergoes a pitchfork bifurcation at $k \approx -0.1839$. In addition to a change in the stability of L_1 due to this bifurcation, L_{4b} and L_{5b} are created and each possesses one pair of imaginary eigenvalues. As k becomes increasingly negative, the locations of L_{4b} and

L_{5b}, indicated by purple dots in Figure 6.2(a), symmetrically evolve away from L_1 on the x-axis, approaching L_4 and L_5 until the critical value of $k \approx -0.1985$, when the pairs of equilibrium points meet and disappear. For stronger attractive or repulsive three-body interactions, additional equilibrium points may appear within or normal to the plane of motion of the primaries, as derived analytically by Douskos [66].

Examination of the effect of a three-body interaction on families of particular solutions is enabled by a summary of the stability and existence of each planar equilibrium point inherited from the CR3BP for various large mass ratio systems. Figure 6.3 portrays the form of the (a) two planar eigenvalue pairs and (b) single out-of-plane eigenvalue pair associated with L_1 for values of k within the range $k = [-0.20, 0.70]$, represented on the horizontal axis, and mass ratios in the range $\mu = [0.10, 0.50]$ on the vertical axis. A blue point in each two-dimensional space indicates that the equilibrium point possesses only one pair of imaginary modes at the associated combination of μ and k, corresponding to the presence of nearby oscillatory motion. For Figure 6.3(a), at combinations of μ and k that lie within the blue regions, L_1 possesses one pair of planar imaginary modes as well as one pair of planar modes that are real, as inherited from the CR3BP. Red points correspond to values of the natural parameters at which an equilibrium point possesses no imaginary eigenvalues. For the planar modes in Figure 6.3(a), these red regions indicate that there are two pairs of real eigenvalues and, therefore, planar motion in the vicinity may not remain nearby indefinitely. Purple regions identify values of μ and k where the planar modes are comprised of two pairs of complex conjugate eigenvalues, causing nearby motion to spiral towards or away from the equilibrium point. Any white regions, however, locate combinations of μ and k where the associated equilibrium point does not exist. Analysis of the plot in Figure 6.3(a) reveals that, at large values of μ, L_1 undergoes a stability change for sufficiently negative values of k. During this stability change, the pair of planar imaginary eigenvalues inherited from the CR3BP shifts to the real axis. As a result, the well-known family of L_1 Lyapunov orbits no longer emanates from the equilibrium point. Beyond a sufficiently large negative value of k, L_1 disap-

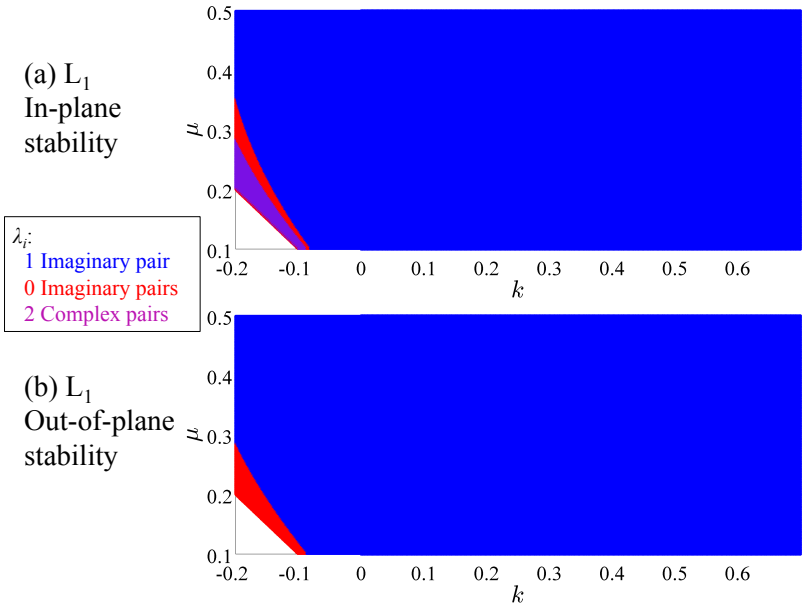

Fig. 6.3. (a) In-plane and (b) out-of-plane stability of L_1 for combinations of the natural parameters of the system.

pears, as indicated by the white triangular region. At positive values of k, however, the stability of L_1 is qualitatively consistent with the CR3BP. For the single pair of out-of-plane modes of L_1, represented in Figure 6.3(b), a stability change also occurs under the influence of a sufficiently strong repulsive three-body interaction. However, as evident from Figure 6.3(b), this stability change occurs at more negative values of k than for the planar modes. Nevertheless, this stability change corresponds to the out-of-plane modes of L_1 shifting from the imaginary axis to the real axis. Accordingly, the well-known three-dimensional family of vertical orbits no longer emanates from L_1. A similar analysis is also completed for L_2, which is located to the right of both primaries along the x-axis. A qualitative description of both the in-plane and out-of-plane stability of L_2 appears in Figure 6.4(a) and Figure 6.4(b), respectively. In both directions, for the combinations of μ and k at which this equilibrium point exists within the ranges considered in this investigation, L_2 possesses qualitative sta-

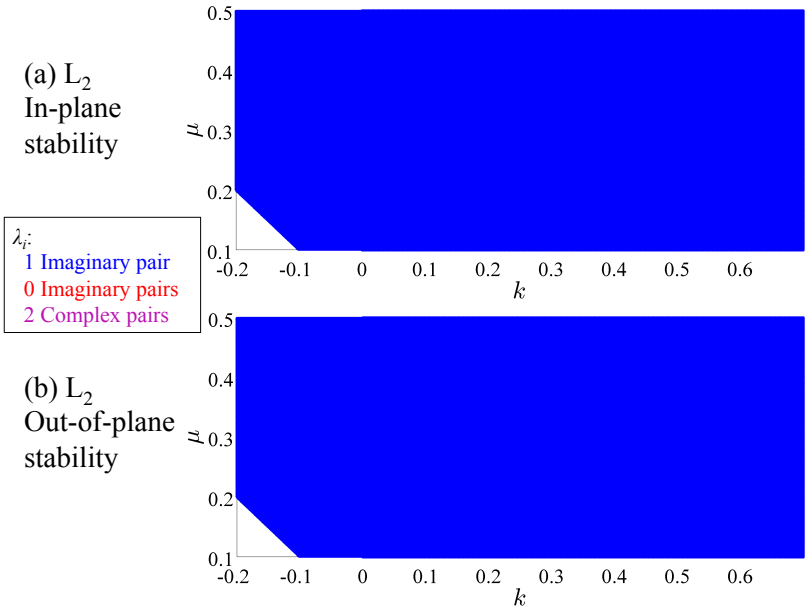

Fig. 6.4. (a) In-plane and (b) out-of-plane stability of L_2 for combinations of the natural parameters of the system.

bility properties that are consistent with the CR3BP. Accordingly, both the planar Lyapunov and three-dimensional vertical families continue to emanate from L_2.

To demonstrate the shift and subsequent disappearance of L_1 and L_2, consider a single value of the mass ratio equal to $\mu = 0.15$. For planar states that lie along the x-axis and possess zero velocity, the derivative of the pseudopotential function with respect to the x-coordinate is plotted in Figure 6.5 for various values of k. Specifically, Figure 6.5 is focused on the vicinity of P_2 to capture the locations of L_1 and L_2. In addition, P_2 is labeled as well as the locations of the equilibrium points in the CR3BP for $\mu = 0.15$. Recall that equilibrium points occur at stationary points within the configuration space. For states that lie along the x-axis, $U_y = U_z = 0$. Thus, a collinear equilibrium point is located by identifying values of x that correspond to zeros of the function U_x, a method also employed in an analytical study by Douskos [66]. As k becomes increasingly negative, the crossings of these curves with the line

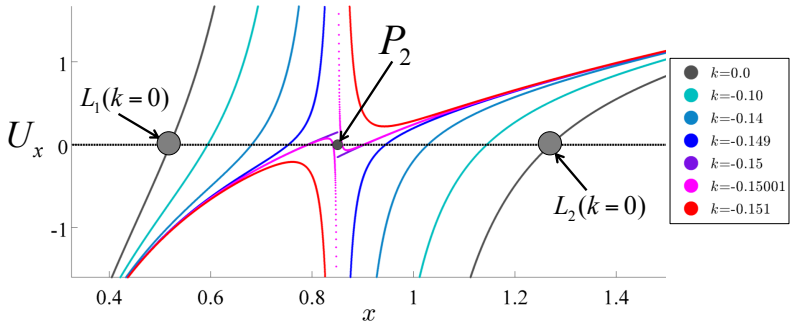

Fig. 6.5. Partial derivative of the pseudopotential function with respect to x, along the x-axis for $\mu = 0.15$ and various values of k.

$U_x = 0$, depicted in black in Figure 6.5, appear closer to P_2. Accordingly, both L_1 and L_2 are located closer to P_2 for an increasingly negative value of k. In the CR3BP, U_x monotonically increases or decreases between P_2 and each of L_1 and L_2. However, for a negative value of k, the pseudopotential field near P_2 deviates further from the CR3BP, impacting both the stability and location of the equilibrium points. For values of k slightly below $-\mu$, the pseudopotential function possesses a qualitatively different form. As an example, consider the curve for U_x corresponding to $k = -0.15001$, colored magenta in Figure 6.5 and in the zoomed-in view in Figure 6.6. At this combination of the natural parameters, the curve for U_x possesses an additional zero to the left of P_2 and, therefore, an additional equilibrium point exists between L_1 and P_2. The presence of this additional root of U_x is due to the inclusion of the term $\frac{k}{r_1 r_2}$ which, for $k < 0$, takes on values with a sign opposite to the pairwise gravitational terms in the pseudopotential function. This additional equilibrium point, analytically derived by Douskos, is located closer to the P_2 and only exists over a small range of values of k [66]. Although additional equilibrium points appear both within and out of the plane of motion of the primaries over small ranges of the system natural parameters and the traditional equilibrium points may reappear for larger magnitudes of k, the focus of this investigation is the equilibrium points inherited from the CR3BP

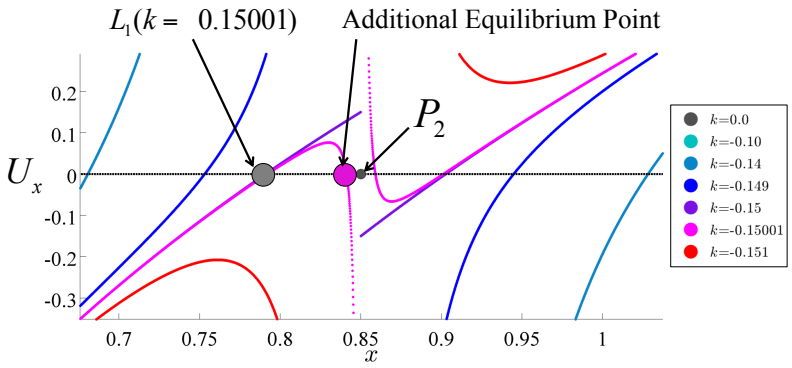

Fig. 6.6. Zoomed-in view of partial derivative of the pseudopotential function with respect to x, along the x-axis for $\mu = 0.15$ and various values of k. Location of equilibrium points to the left of P_2 indicated.

over the range of values of k that are examined here, representing smaller deviations to a natural gravitational environment. Nevertheless, as the value of k is decreased further, the local maximum of U_x along the curve displayed in Figure 6.5 also decreases until no zeros occur near P_2. A similar phenomenon occurs for L_2 at a similar, but not identical, critical value of k. Thus, as the pseudopotential field near P_2 changes for an increasingly repulsive three-body interaction, L_1 and L_2 eventually disappear, producing the triangular white regions in the bottom left of Figures 6.3 and 6.4.

Stability analysis completed for the collinear equilibrium point, L_3, which lies to the left of both primaries, reveals a relative insensitivity to the addition of a three-body interaction. Specifically, a qualitative representation of the form of the (a) planar and (b) out-of-plane eigenvalues appears in Figure 6.7. Referencing each of these figures, the two-dimensional (μ, k) space appears uniform in color. In fact, for each combination of μ and k encompassed by these figures, L_3 possesses stability properties that are consistent with the CR3BP. Accordingly, both the planar Lyapunov and three-dimensional vertical families continue to emanate from L_3. Furthermore, this equilibrium point continues to exist along the x-axis to the left of both primaries for each combination of the natural parameters examined in this investigation.

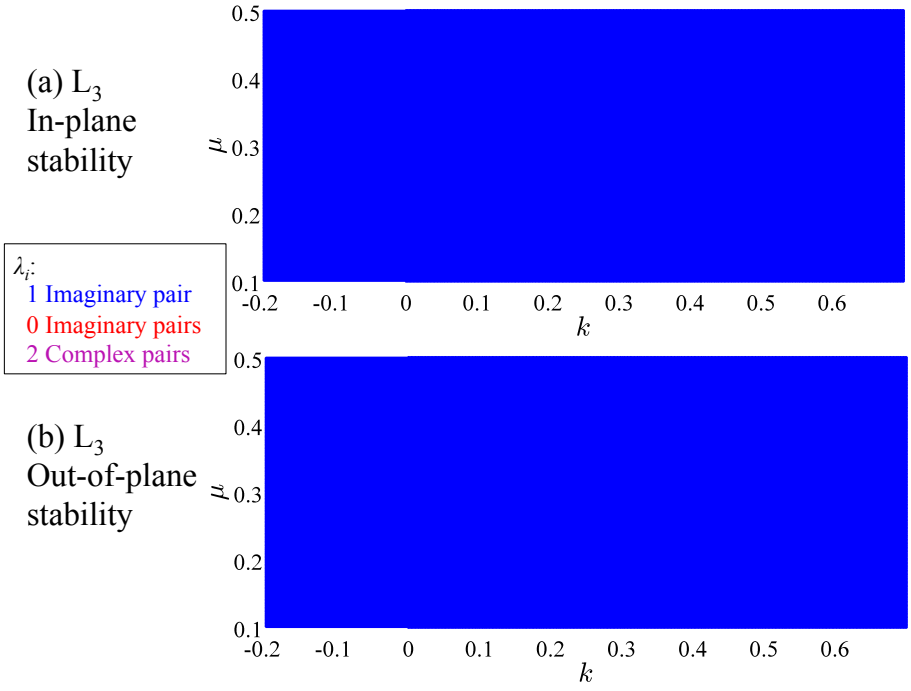

Fig. 6.7. (a) In-plane and (b) out-of-plane stability of L_3 for combinations of the natural parameters of the system.

The triangular equilibrium points, L_4 and L_5, possess identical stability properties due to the inherent symmetry of the MCR3BP, requiring only one pair of composite stability representations, displayed in Figure 6.8. For the range of values of μ and k considered in this investigation, both the in-plane and out-of-plane stability of L_4 and L_5 are predominantly consistent with the CR3BP. At large mass ratios in the CR3BP, L_4 and L_5 are known to possess two complex pairs of planar eigenvalues, causing motion in their vicinity to spiral towards or away from the triangular equilibrium points. Since Figure 6.8(a) is predominantly colored purple, the form of the planar eigenvalues of L_4 and L_5 remains largely unchanged. However, a small region in the bottom right of Figure 6.8(a), highlighted by a black box near $\mu = 0.10$ and $k = 0.70$, is colored green, which indicates the presence of two pairs of purely imaginary eigenvalues. Each pair of imaginary eigenvalues indicates the existence of a family of

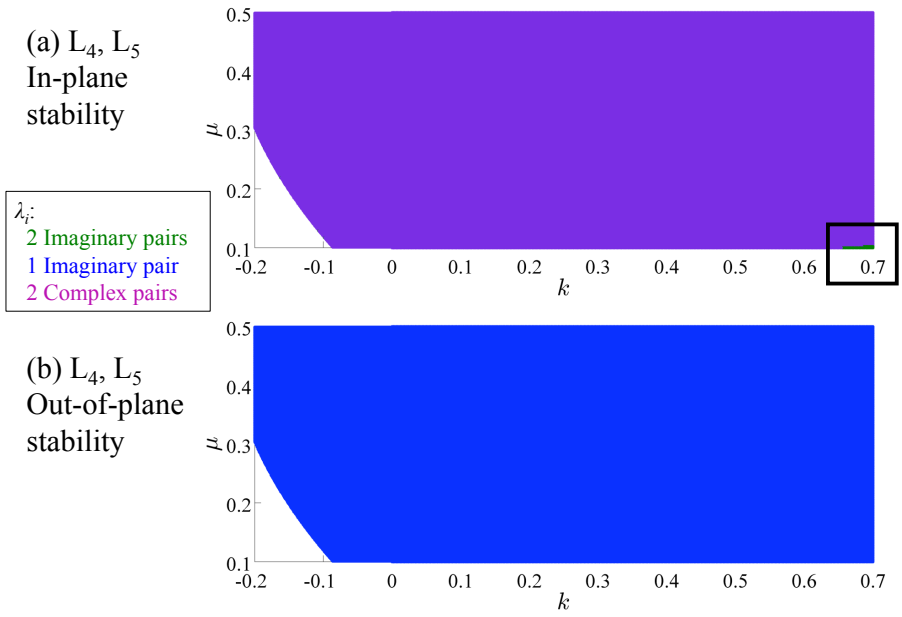

Fig. 6.8. (a) In-plane and (b) out-of-plane stability of L_4, L_5 for combinations of the natural parameters of the system.

planar periodic orbits. Such stability properties are only observed in the CR3BP for systems with a mass ratio below the critical value of $\mu \approx 0.03852$. However, with the addition of a significantly attractive three-body interaction, the qualitative stability of L_4 and L_5 can be modified within large mass ratio binary systems. Thus, an exoplanet orbiting within a large mass ratio binary star system that is adequately modeled by the MCR3BP and a large positive value of k may exhibit motion resembling a planar periodic orbit near L_4 or L_5. The existence of such motion may be used to place bounds on the strength and sign of the scaling constant for an additional three-body interaction within a given binary system.

Although the focus of this investigation is the evolution of the five equilibrium points inherited from the CR3BP, the two additional equilibrium points, L_{4b} and L_{5b}, play a role in the evolution of L_1, L_4 and L_5; thus, their existence and stability is of interest. Consider the in-plane and out-of-plane stability representations for the symmetrical equilibrium points, L_{4b} and L_{5b}, displayed in Figure 6.9. Using this

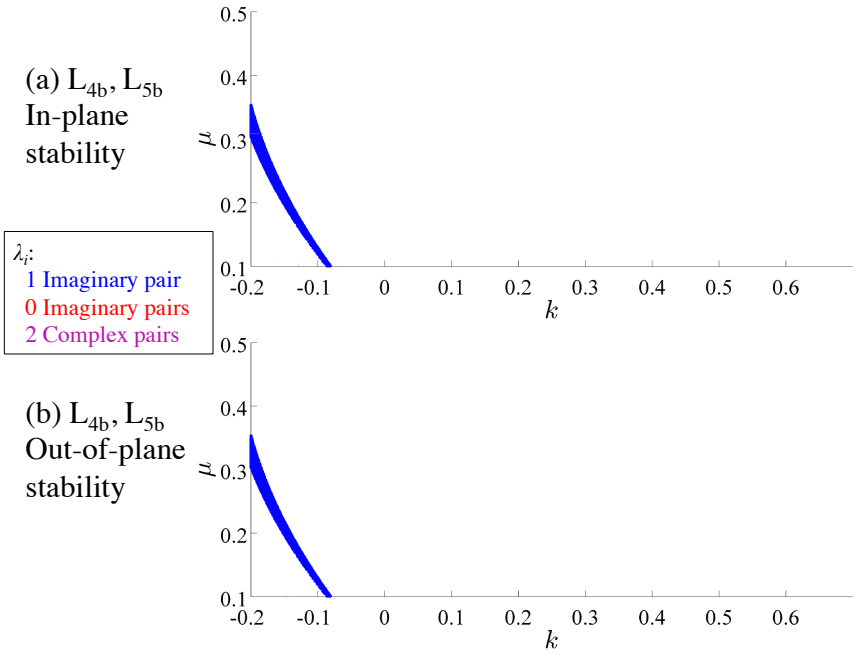

Fig. 6.9. (a) In-plane and (b) out-of-plane stability of L_{4b}, L_{5b} for combinations of the natural parameters of the system.

figure as a reference, analysis reveals that over the range of values for the natural parameters of the system that are examined here, these two equilibrium points exist over a small range of negative values of k. Recall that L_{4b} and L_{5b} are formed when L_1 undergoes a pitchfork bifurcation. Accordingly, for a given value of μ, the critical value of k at which the planar oscillatory eigenvalues associated with L_1 become real corresponds to the upper bound on k values for which L_{4b} and L_{5b} exist. Recall from Figure 6.2(a), that as k becomes increasingly negative, L_{4b} and L_{5b} evolve towards the triangular equilibrium points L_4 and L_5 until they coalesce and disappear. Thus, the lower bound on k for which L_{4b} and L_{5b} exist is equivalent to the values of k for which L_4 and L_5 disappear. In addition to a summary of the range of natural parameters for which the additional equilibrium points exist, an evaluation of their stability is also useful. At the upper bound on k, L_{4b} and L_{5b} inherit the stability of L_1 prior to its stability change, i.e., L_{4b} and L_{5b} each possess one pair of imaginary planar

eigenvalues, one pair of real planar eigenvalues, and one pair of imaginary out-of-plane eigenvalues. These qualitative stability properties are retained across the range of values of μ and k for which L_{4b} and L_{5b} exist, as apparent through the homogenously blue regions in Figures 6.9(a) and 6.9(b). Thus, L_{4b} and L_{5b} are each associated with a family of planar periodic orbits as well as a family of three-dimensional periodic orbits. Observations of such motions that do not otherwise exist in the CR3BP may point to the existence of a unique effect of a three-body interaction. Furthermore, shifts in the location, stability and existence of equilibrium points within a multi-body regime may uniquely impact particular solutions throughout the entire phase space and, therefore, the potential motions of an exoplanet near a binary star system.

6.3 Evolution of Families of Periodic Orbits

By combining composite stability representations with the capability to locate trajectories with desired shape characteristics via discrete variational mechanics, it is possible to explore the effect of an additional three-body interaction on families of periodic orbits and, therefore, the underlying dynamical structures within a multi-body system. First, composite representations of the in-plane and out-of-plane stability indices are employed to examine the evolution of selected families for a fixed value of the mass ratio, while allowing the strength of the three-body interaction to vary. These results are then compared to the composite stability representations produced in the CR3BP, as presented in Chapter 4, to identify potentially unique effects of a three-body interaction, as well as any other orbits of interest. Since the orbital stability within and out of the plane is decoupled for planar periodic orbits, the two corresponding stability indices are isolated and examined separately in each case. Using each composite stability representation, qualitative changes across each family are identified using colored structures that can reveal changes in the stability. Any orbits of interest that are identified using these exclusion plots are isolated and then explored using discrete variational mechanics. In astrodynamics, this computational technique

is typically employed to construct optimal paths for a spacecraft under the influence of a control force [34]. In this investigation, however, the underlying formulation is applied to the search for values of the system parameters, μ and k, that correspond to the existence of a natural trajectory (i.e., no active control forces) resembling a given reference path. The resulting constrained optimization problem delivers locally optimal solutions that supply approximations to trajectories in a wide variety of scenarios in both the CR3BP and MCR3BP, potentially avoiding some of the inherent sensitivities of a multiple shooting method when any natural parameters in a chaotic system are poorly known. This methodology is applied to the computation of orbits exhibiting desired shape characteristics in configuration space, along with the corresponding values of the natural parameters. By comparison to the stability and existence of equilibrium points across the range of values of μ and k at which a desired motion emerges, discrete variational mechanics facilitates exploration of the effect of a three-body interaction and identification of the conditions for reproducibility in the natural gravitational environment.

6.3.1 Retrograde Circumbinary Orbits

To model the motion of a small body that encircles both primaries in a binary system, a simply-periodic family of circumbinary retrograde orbits, one that exists in the exterior region, may be of interest. Referencing the evolution of the retrograde exterior family in the CR3BP, depicted in Figure 4.3, the effect of a three-body interaction is explored by varying the value of k, while holding the mass ratio fixed. Figures 6.10(a) and 6.10(b) depict the composite stability representation for values of k within the range $k = [-0.20, 0.70]$ and a mass ratio of $\mu = 0.30$. Since the two stability indices can be decoupled for planar, periodic orbits, initially consider the in-plane stability along the family. As k is increased in the positive direction, and the three-body interaction is increasingly attractive, the negative unstable periodic orbits that exist in the purple structure near $T = 9.42$ encompass a wider range of orbital

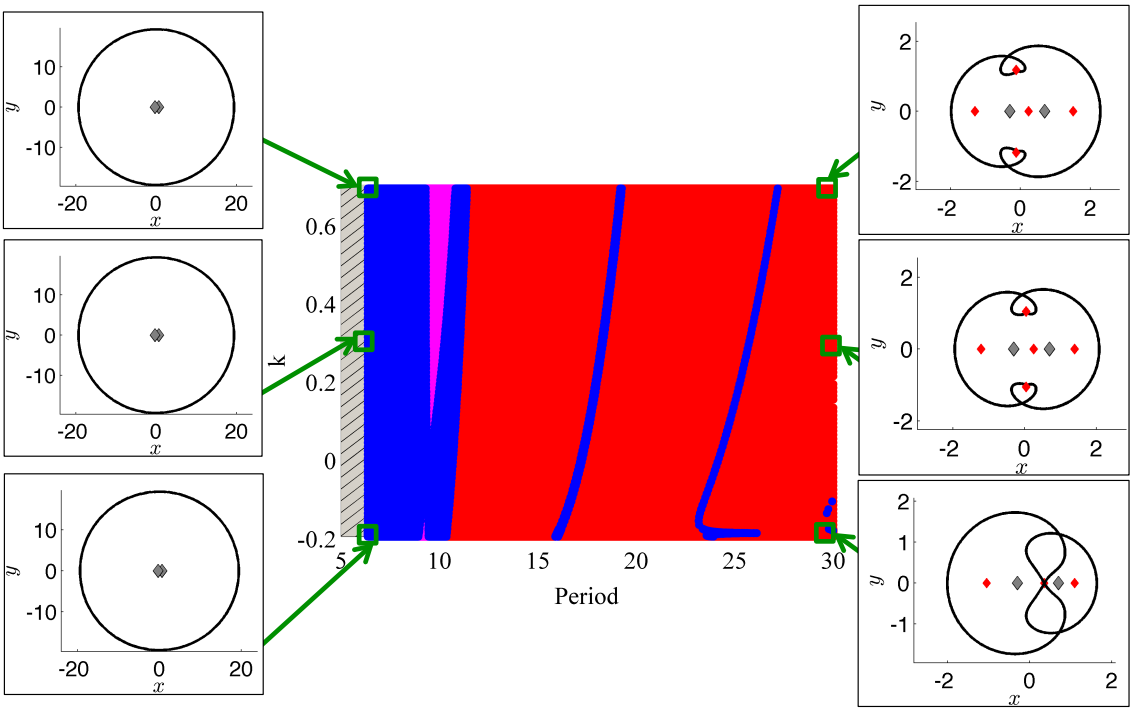

(a) In-plane stability.

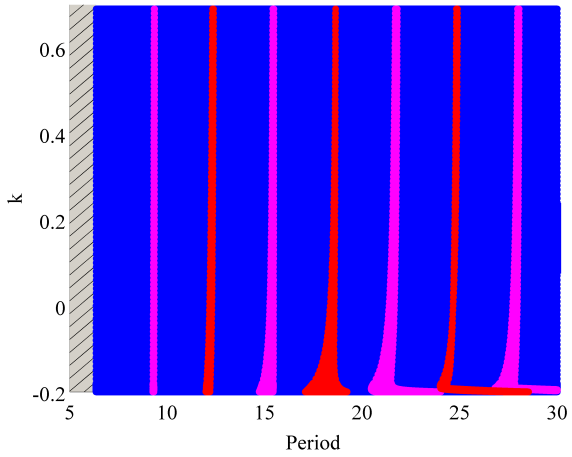

(b) Out-of-plane stability.

Fig. 6.10. Stability representation for the selected family of retrograde orbits in the exterior region for $k = [-0.20, 0.70]$ and fixed mass ratio, $\mu = 0.30$. Orbital stability is indicated via color: stable (blue), positive unstable (red), and negative unstable (purple).

periods. In comparison to the CR3BP, this effect occurs for a decreasing mass ratio close to $\mu = 0.30$. A similar expansion in the range of periods corresponding to negatively unstable orbits also occurs for decreasing values of k. Thus, the variation in the range of orbital periods corresponding to each region of stable or unstable orbits due to a nonzero value of k does not appear to exactly mimic the effect of modifying the mass ratio value around $\mu = 0.30$. Despite the varying size of these blue and purple structures, their consistent presence for orbital periods below approximately 10 nondimensional time units suggests that the three-body interaction may not qualitatively impact the in-plane stability curve of this family at low orbital periods. Similarly, the thin blue and purple structures that occur at higher orbital periods, inherited from the CR3BP at $k = 0$, seem to persist for the majority of k values represented in the composite stability representation. At large negative values, however, the thin blue structure at periods close to 25 nondimensional time units experiences a significant change in the corresponding orbital periods for a small perturbation in the value of k. In fact, this structural change is also apparent in the out-of-plane stability representation in Figure 6.10(b) as it impacts both the width and location of the purple and red structures. This significant change in the stability indices suggests that the physical characteristics of the orbits themselves may be influenced by the presence of a three-body interaction force.

Observing the physical configuration of the retrograde exterior orbits in the margins of the composite stability representations for the MCR3BP reveals some change in the appearance of the orbits as k varies. In Figure 6.10(a), low period orbits plotted to the left of the composite stability representation appear similar in their near-circular shape and large size, presumably because they exist far from the two primaries. However, the difference in the evolution of the retrograde exterior family between the CR3BP and MCR3BP is apparent through the examination of orbits with a larger period. In the CR3BP, Figure 4.3(a) reveals that, as the orbital period increases along the family for large values of the mass ratio, the orbits evolve towards the primaries and form loops in the vicinity of L_4 and L_5. Increasing the orbital pe-

riod even further, in multiples of 2π, additional loops form near these two equilibrium points in a fractal manner. In the MCR3BP, however, neither L_4 or L_5 exists at the vertices of equilateral triangles with respect to the two primaries. Accordingly, the loops that form along these retrograde orbits appear shifted in configuration space, as evident in the margins of 6.10(a). This effect of the three-body interaction can be attributed to the varied locations of the equilibrium points themselves. Furthermore, for large negative values of k, close to $k = -0.20$, these loops tend to exhibit 'pointed tips' which evolve towards L_1, as evident in the zoomed-in view in Figure 6.11. To explore this significant change in the physical configuration of the retrograde exterior family, recall that a straightforward stability analysis for the collinear equilibrium points, assuming large negative values of k, reveals a change in the stability of L_1. In fact, at the critical value of $k \approx -0.1839$, the pair of eigenvalues corresponding to the planar oscillatory mode inherited from the CR3BP undergoes a stability change, resulting in L_1 possessing only stable and unstable modes, and causing the disappearance of the L_1 Lyapunov family. These changes to the equilibrium points and, therefore, their manifolds and the underlying dynamical structures of the MCR3BP,

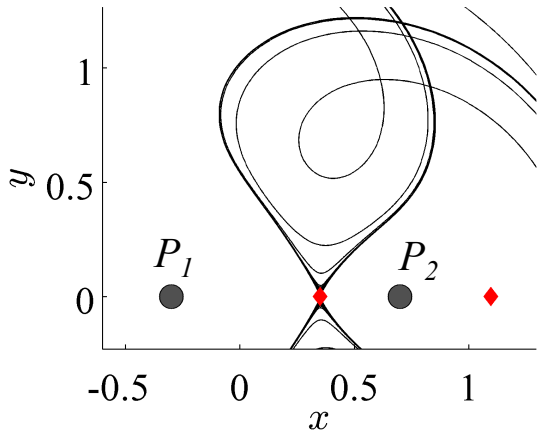

Fig. 6.11. Loops forming along the retrograde exterior family, with pointed tips directed towards L_1 for $\mu = 0.30$ and $k = -0.20$.

influence the physical configuration of this family of orbits. This observation suggests that the effect of the three-body interaction on these retrograde exterior orbits at large negative values of k may not be exactly reproduced within the CR3BP, but, rather, mimicked. Accordingly, discrete variational mechanics is used to explore the effect of this additional force and to investigate whether it is approximately reproducible in the CR3BP.

To explore the uniqueness of the effect of a three-body interaction, discrete variational mechanics is employed to search for an orbit in the CR3BP that exhibits 'pointed tips'. As an example, consider a retrograde exterior orbit existing in the MCR3BP for $\mu = 0.30$ and $k = -0.20$, with an orbital period of $T = 26.26$. This reference path is discretized into 500 nodes and depicted in Figure 6.12(a) using black dots, with the primaries located by gray-filled circles and the equilibrium point locations indicated with red diamonds. An arrow is used to represent the direction of the motion along the orbit. Since the assumed value of k is more negative than the critical value of $k = -0.1985$, neither of the triangular equilibrium points exists at this combination of the natural parameters. Furthermore, since the selected orbit exhibits pointed loops in the vicinity of the location at which these equilibrium points would exist in the CR3BP, this particular orbit from the MCR3BP may not be exactly reproducible in the CR3BP. Rather, the goal of this initial example is to determine if an orbit resembling this reference path in terms of its general geometry exists in the CR3BP, as well as the required value of μ. To achieve this goal, the discrete path in Figure 6.12(a) is supplied as a reference path for the constrained optimization problem formulated using discrete variational mechanics. When searching for a locally minimum solution that resembles this periodic orbit, the value of k is held constant at $k = 0$, consistent with the CR3BP, while the time step (and, therefore, the orbital period), the mass ratio and the path itself are all treated as variables. Without a lengthy continuation process in both natural parameters, which may not necessarily be successful, the value of μ at which a similar family of orbits might exist in the CR3BP is unknown. Furthermore, the addition of the three-body

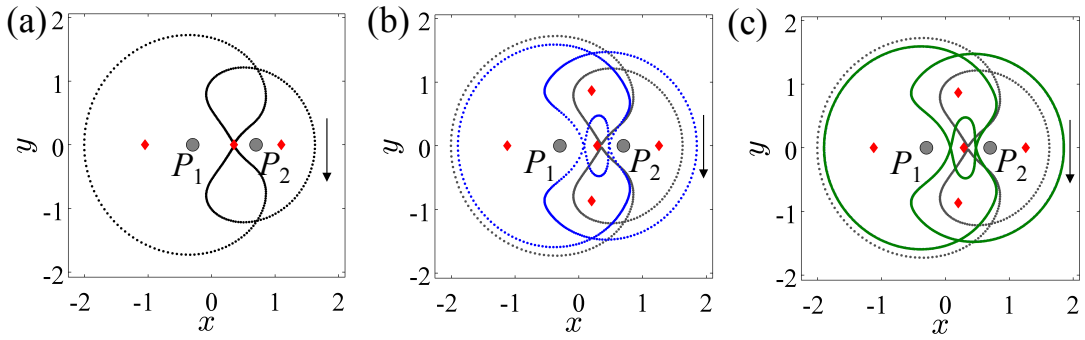

Fig. 6.12. Recreating a retrograde exterior orbit: (a) reference path (black) for $\mu = 0.30$ and $k = -0.20$, (b) closely reproduced in the CR3BP for $\mu = 0.30$ by a discrete path (blue), and (c) verified to exist near a continuous periodic orbit (green) in the CR3BP at $\mu = 0.30$.

interaction directly modifies the acceleration field, and, therefore, the velocities and periods of any orbits with a similar geometry in the CR3BP. To accommodate this effect, 500 unique initial guesses are input to the constrained optimization problem that is implemented using the sequential quadratic programming algorithm available in Matlab's *fmincon* routine. Each initial guess is constructed using the reference path with a small amount of random noise applied to the position variables at each node. In addition, each initial guess for μ is randomly selected to lie somewhere in the range $\mu = [0.10, 0.50]$, while the initial guess for the time step variable, h, lies within 25% of the value of h along the reference path. The constrained optimization problem is then solved, with $k = 0$ incorporated as an equality constraint, for each of these 500 guesses and the best locally optimal solution is selected.

The constrained optimization problem as formulated via discrete variational mechanics is leveraged to explore the selected retrograde exterior orbit that exists in the MCR3BP and deduce if it is approximately reproducible in the CR3BP. From the results of the multi-start constrained optimization algorithm, one of the converged solutions is plotted with blue dots and overlaid on the original reference orbit (gray) in Figure 6.12(b). Note that the primaries and the equilibrium points indicated in

this plot correspond to $\mu = 0.30$, the mass ratio at which the converged solution exists in the CR3BP. This locally optimal solution also possesses a period of $T = 28.74$, which is higher than the orbital period of the reference orbit. Although the computed solution is an approximation, it is straightforward to verify that this discrete path exists close to a continuous periodic orbit at $\mu = 0.30$ in the CR3BP. A nearby continuous periodic orbit, computed using a multiple shooting algorithm, is overlaid in green in Figure 6.12(c) and closely matches the discrete path. As expected, the presence of the three-body interaction impacts both the position and velocity along an orbit. Correspondingly, the converged orbit does not exactly follow the same path as the reference orbit. Furthermore, the loops around L_4 and L_5 for this converged solution in the CR3BP encompass the location of L_1, rather than exhibiting pointed tips that are characteristic of the reference path. This inconsistent behavior of the orbit close to L_1 can likely be attributed to a difference in the stability of the collinear equilibrium point for the dynamical environments corresponding to the reference and computed solutions. In fact, the periodic orbit for $\mu = 0.30$ and $k = 0$, plotted in green in Figure 6.12(c), encircles L_1 in a direction and shape that resembles the L_1 Lyapunov family itself. Recall that the L_1 Lyapunov family of orbits does not exist for $\mu = 0.30$ and $k = -0.20$. Accordingly, the 'pointed tips' along the reference orbit in the MCR3BP are likely a reflection of the absence of any oscillatory modes about L_1. Thus, while the exact characteristics of the motion along the reference orbit are not reproducible in the CR3BP, a somewhat similar geometry is certainly achieved. This observation, resulting from the complementary use of both composite stability representations and discrete variational mechanics, suggests that while large retrograde orbits of a given geometry may be inherited from the CR3BP, the presence of a three-body interaction may significantly affect their characteristics relative to the primaries in a binary system. Since no solutions recovered from the multi-start constrained optimization algorithm at various values of μ in the CR3BP possess 'pointed tips', additional analysis is required to ascertain the uniqueness of this behavior.

To further investigate the significant changes in the physical configurations of the orbits in the retrograde exterior family, retrograde exterior orbits with 'pointed tips' are reproduced at various values of the natural parameters, μ and k, using discrete variational mechanics. These results are then visualized in a (k, μ) two-dimensional space to determine the correlation between the stability of L_1 and the existence of this interesting behavior. By examining the values of μ and k at which an orbit resembling a given reference path exists, requirements on the dynamical environment for reproducibility can be determined. These bounds on the values of μ and k are valuable in providing further insight into whether motion exists only under the influence of an additional three-body interaction. Recall the retrograde exterior orbits depicted in Figure 6.12(a), existing in the MCR3BP for $\mu = 0.30$ and $k = -0.20$, and an orbital period of $T = 26.26$ nondimensional time units. This orbit, which exhibits the motion of interest, is discretized using 600 nodes and used as a reference path in the constrained optimization problem formulated using discrete variational mechanics. Periodic orbits exhibiting a similar behavior are then computed for various values of μ sampled within the range $\mu = [0.10, 0.30]$. For each value of the mass ratio, sampled within the given range, the minimization problem is solved using sequential quadratic programming in Matlab's *fmincon* for a single, unconstrained value of k. Then, the value of k is constrained and successively increased (or decreased) away from this initial value of k until the minimization problem either cannot be solved or produces an orbit that exhibits significantly different behavior, identified via an uncharacteristically large value of the cost function. The resulting process, applied to the reproduction of retrograde circumbinary orbits with the desired characteristics, recovers orbits within a specific region of the two-dimensional space of the natural parameters, μ and k, as displayed in Figure 6.13. In this plot, each black point in the (k, μ) space indicates the existence of an orbit that exhibits loops with 'pointed tips' that approach L_1, with two sample orbits at distinct values of μ and k displayed in the margins to confirm the recovery of the desired motion. Using Figure 6.13 as a reference, the desired motion only appears to exist for negative values of k, i.e.,

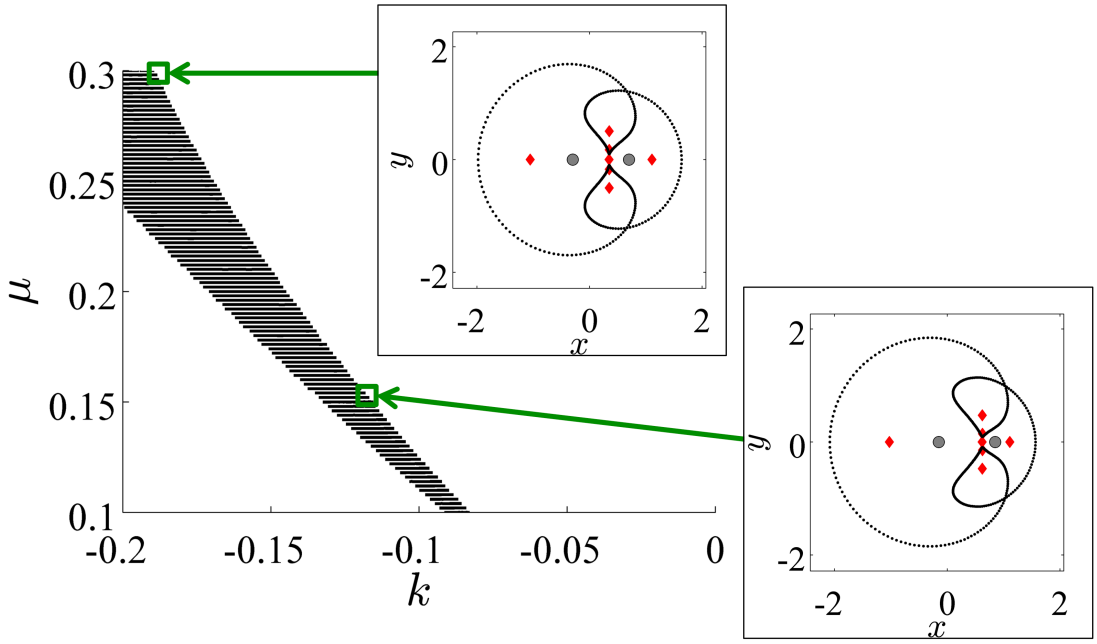

Fig. 6.13. Existence of retrograde circumbinary orbits with loops that exhibit 'pointed tips' for combinations of k and μ that are indicated via black points. Sample orbits are displayed in the margins.

when the three-body interaction is repulsive. However, to explore the specific nonzero values of k bounding this region, additional analysis using concepts from dynamical systems theory is useful.

To explain the existence of 'pointed tips' that occur along the retrograde exterior family for a repulsive three-body interaction, a comparison to the stability of L_1 is valuable. Recall from Figure 6.3 that a straightforward stability analysis for L_1 reveals a change in stability for values of μ within the examined range of $\mu = [0.10, 0.30]$. In fact, for sufficiently negative values of k, the pair of eigenvalues corresponding to the planar oscillatory mode inherited from the CR3BP undergoes a stability change, resulting in L_1 possessing only stable and unstable modes, and causing the disappearance of the well-known L_1 Lyapunov family that exists at all values of μ in the CR3BP. These changes to the equilibrium points, their manifolds and, therefore, the

underlying structure of the MCR3BP, influence the foundational dynamical environment near a binary system. For instance, this change in the stability of L_1 may cause the observed structural change along the retrograde exterior family of orbits. The combinations of μ and k at which this family of orbits exhibits 'pointed tips' that evolve towards L_1, as depicted in 6.13, are overlaid on the qualitative planar stability of L_1 using the same color scheme as in Figure 6.3: blue points indicate the existence of one imaginary pair and one real pair of eigenvalues, while red regions indicate the presence of only real stable/unstable modes, and purple shading corresponds to two pairs of complex conjugate eigenvalues indicating spiraling motion towards and away from the equilibrium point. The resulting plot, displayed in Figure 6.14, features black points for each combination of μ and k at which the observed motion exists. Using this figure as a reference, this motion of interest appears to exist only when L_1 possesses no oscillatory modes within the plane of motion of the primaries. Such

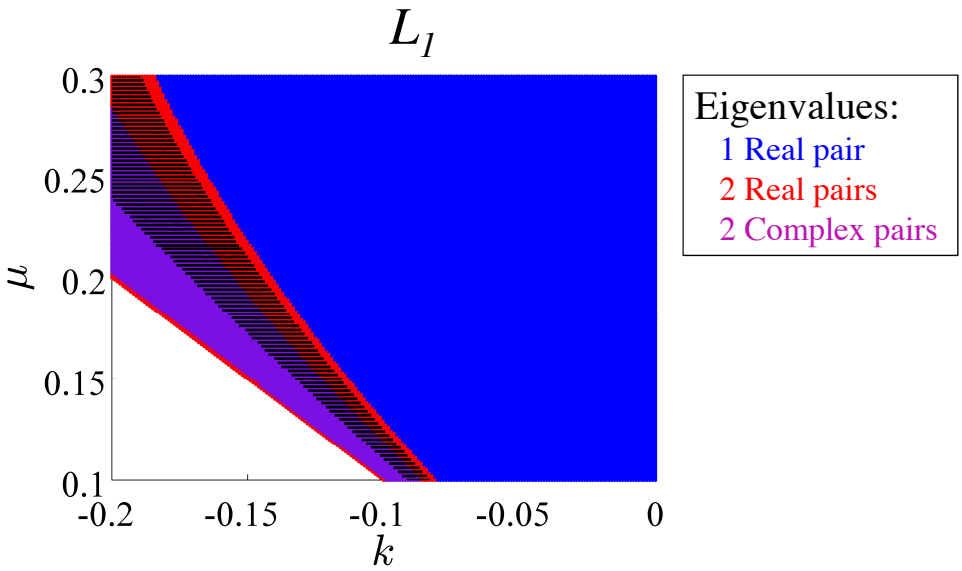

Fig. 6.14. Existence of retrograde circumbinary orbits with loops that exhibit 'pointed tips', indicated via black points, overlaid on a plot of the qualitative stability of L_1.

stability properties are not characteristic of L_1 at any value of the mass ratio in the CR3BP. Furthermore, since this black region does not encompass $k = 0$ for any large values of mass ratio, the effect of the three-body interaction on these retrograde exterior orbits at large negative values of k may not be exactly reproduced within the CR3BP, but, rather, simply mimicked. Accordingly, such motion may be a unique effect of the three-body interaction examined within this investigation.

6.3.2 Retrograde Circumstellar Orbits

Retrograde circumstellar orbits may describe potential motions of an exoplanet around the largest primary. To explore the effect of a three-body interaction, composite stability representations are first constructed at a fixed value of the mass ratio, $\mu = 0.30$. A qualitative representation of the (a) in-plane and (b) out-of-plane stability along this family, for various values of k, is depicted in Figure 6.15. Recall that on these plots, orbital stability is indicated via color: stable (blue), positive unstable (red) and negative unstable (purple). White regions, however, indicate that no orbits have been computed at the corresponding value of the orbital period either due to a close pass of one of the primaries, or due to the presence of a turning point along the stability curve. When an attractive three-body interaction is present in the dynamical environment near a binary, the stability evolution and physical configuration of the orbits in this family is relatively consistent with the CR3BP. Such an observation is reflected in the persistence of the red, blue and purple structures for positive values of k. When a sufficiently repulsive three-body interaction is introduced, however, a collision of bifurcations occurs and the family extends to large orbital periods. Simultaneously, loops form in the vicinity of L_4 and L_5 in a fractal manner. This structural change in the physical configuration, influenced by the motion emanating from the vicinity of the triangular equilibrium points, causes the family to extend to large orbital periods. Recall from Section 4.1 that this characteristic produces an alternating sequence of red and purple structures in the out-of-plane stability index as additional

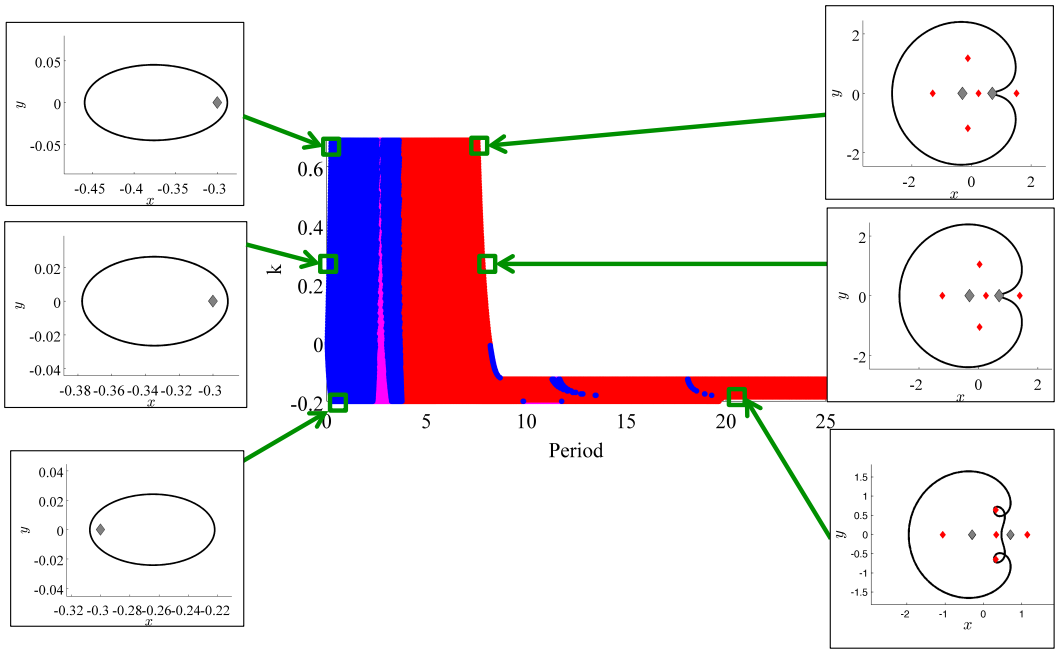

(a) In-plane stability.

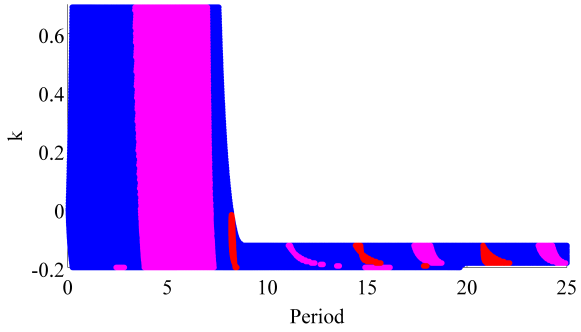

(b) Out-of-plane stability.

Fig. 6.15. Stability of retrograde orbits about P_1, for $\mu = 0.30$, $k = [-0.20, 0.70]$. Orbital stability is indicated via color: stable (blue), positive unstable (red), and negative unstable (purple).

loops form near L_4 and L_5 or, equivalently, additional revolutions occur around the primaries when visualized in the inertial frame. Furthermore, at low periods, the physical configuration of the retrograde circumstellar orbits when viewed in the rotating frame is impacted by the presence of a three-body interaction. In the CR3BP,

these P_1-centered orbits tend be small and circular. However, as evident in the left margin of Figure 6.15(a), the low period orbits appear elliptical with an apoapsis distance that is significantly larger than the periapsis distance. For positive values of k, the apoapsis along the orbit occurs to the left of P_1 as viewed in the rotating frame, while low period orbits under the influence of a repulsive three-body interaction possess an apoapsis to the right of P_1. This elliptical shape of the low period retrograde circumstellar orbits is a reflection of the modified form of the potential field. As the values of $U_k^*(x, y)$ are impacted by the addition of a three-body interaction term, possessing the form depicted in Figure 6.1(b), the path along a periodic orbit must adjust to maintain a constant integral of motion, C_k. This effect of k on the potential field is visualized by recalling the shift of the equilibrium points, depicted in Figure 6.2(a): for $k > 0$, L_3 exists further from P_1 while L_1 slightly shifts closer to the larger primary. Analogously, the apsis to the left of P_1 is raised, while the apsis to the right of P_1 is lowered. The converse is true for negative values of k. Using Figure 6.16 as a reference, the retrograde circumstellar family of orbits about P_2 experiences a similar evolution in the stability and physical configuration at $\mu = 0.30$. For a binary system that is adequately modeled by the MCR3BP, these changes to the physical configuration of orbits along the retrograde circumstellar family about P_1 may be used to deduce the existence and bound the strength of a potential three-body interaction.

As the value of the mass ratio is decreased towards $\mu = 0.10$, a significant structural change occurs along the retrograde circumstellar family about P_1 and interesting shape characteristics emerge. To visualize the evolution of this family of orbits within a binary system described by $\mu = 0.10$ and under the influence of a three-body interaction, consider the composite stability representation for the (a) in-plane and (b) out-of-plane stability indices as depicted in Figure 6.17. Using Figure 6.17 as a reference, the colored structures aid in deducing the stability evolution of orbits along this family as the value of k is varied for a fixed mass ratio. For various positive values of k, the blue, purple and red structures that pass through $k = 0$ continue to occur at similar values of the orbital period. Specifically, orbits close to P_1 with

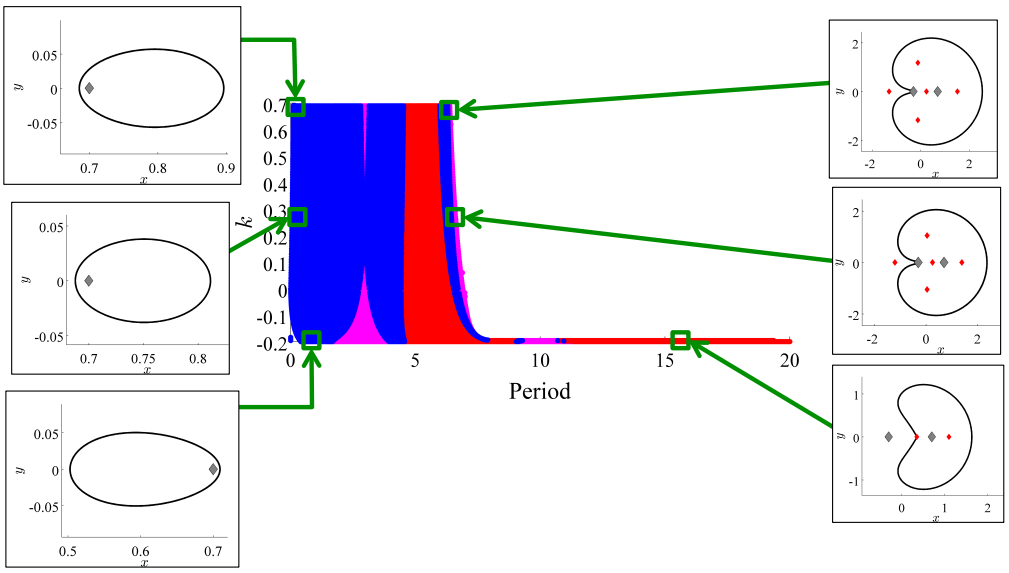

(a) In-plane stability.

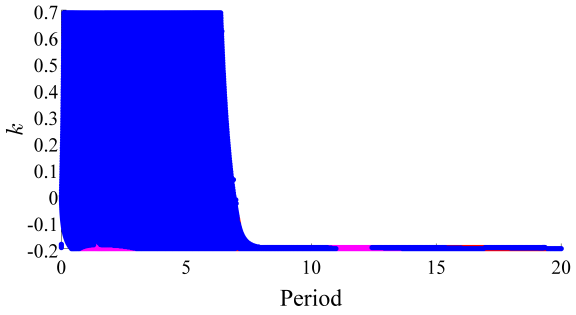

(b) Out-of-plane stability.

Fig. 6.16. Stability of retrograde orbits about P_2, for $\mu = 0.30$, $k = [-0.20, 0.70]$. Orbital stability is indicated via color: stable (blue), positive unstable (red), and negative unstable (purple).

a small orbital period are stable both within and out of the plane of motion of the primaries, indicating the existence of nearby quasi-periodic orbits. At larger orbital periods, with values between approximately 4 and 8 nondimensional time units, these retrograde circumstellar orbits possess only unstable nontrivial modes. Thus, under the influence of an attractive three-body interaction, the stability evolution of orbits

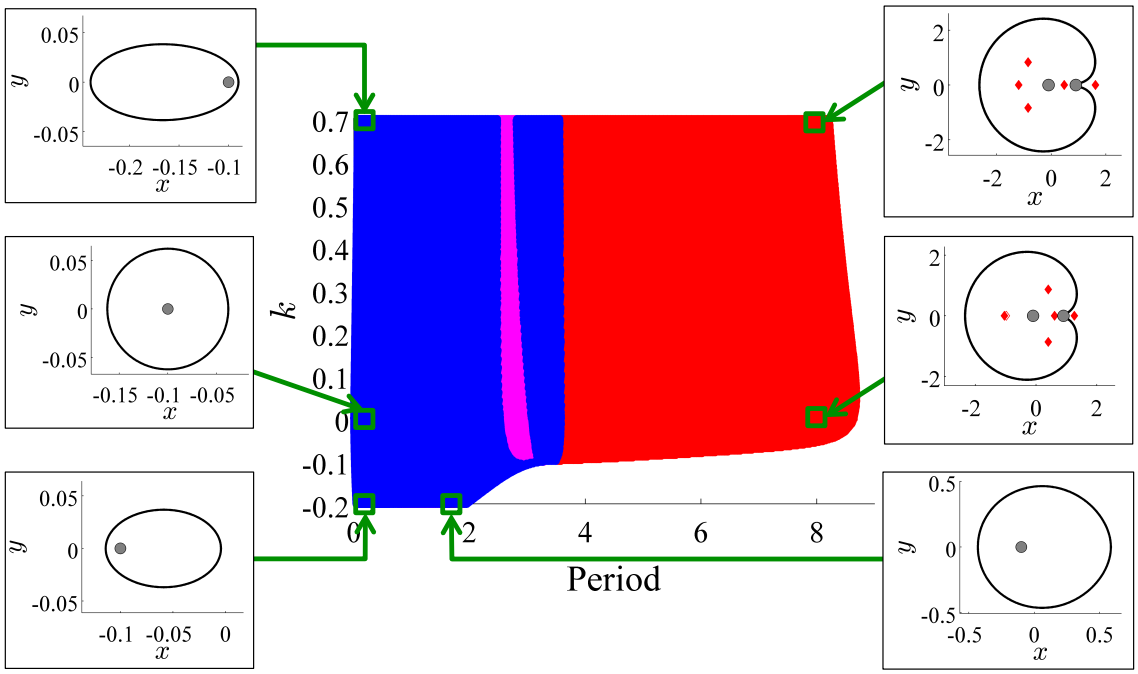

(a) In-plane stability.

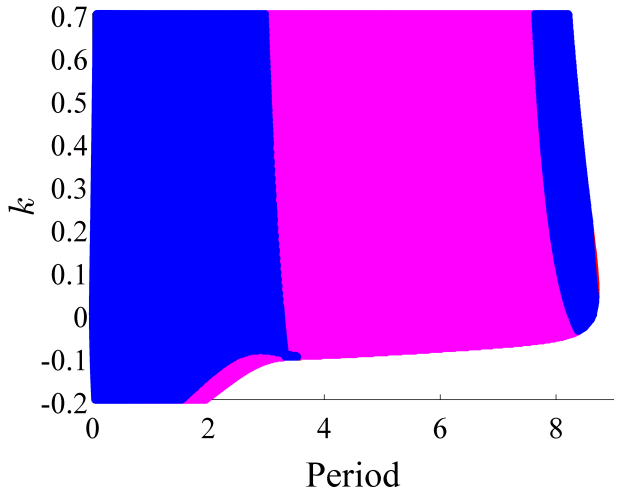

(b) Out-of-plane stability.

Fig. 6.17. Stability of retrograde orbits about P_1, for $\mu = 0.10$, $k = [-0.20, 0.70]$. Orbital stability is indicated via color: stable (blue), positive unstable (red), and negative unstable (purple).

along the retrograde circumstellar family about P_1 is qualitatively consistent with the CR3BP for $\mu = 0.10$. For a repulsive three-body interaction, however, the maximum period of orbits within this family drops significantly. In fact, for values of k slightly below -0.10, a turning point occurs along the family at the maximum orbital period. This change in the stability evolution is accompanied by a change in the physical configuration of the orbits along the family as visualized in the margins of the composite stability representation. Recall from Figure 4.6 that, as the value of the mass ratio is varied in the CR3BP, these retrograde circumstellar orbits about P_1 evolve from small and nearly circular to large orbits that encompass L_4 and L_5, while bending around P_2. The physical configuration of orbits along this family under the influence of a sufficiently repulsive three-body interaction, however, is visualized in configuration space in Figure 6.18(a). Specifically, orbits along this family tend to appear elliptical in the rotating frame. As additional members along this family are computed, the orbits evolve away from P_1 until a maximum amplitude in the y-direction is achieved. Further along the family, the apoapsis along each orbit tends towards P_2 while the y-amplitude decreases. Figure 6.18(b) displays the corresponding in-plane stability index along this family as a function of the orbital period. A turning point occurring

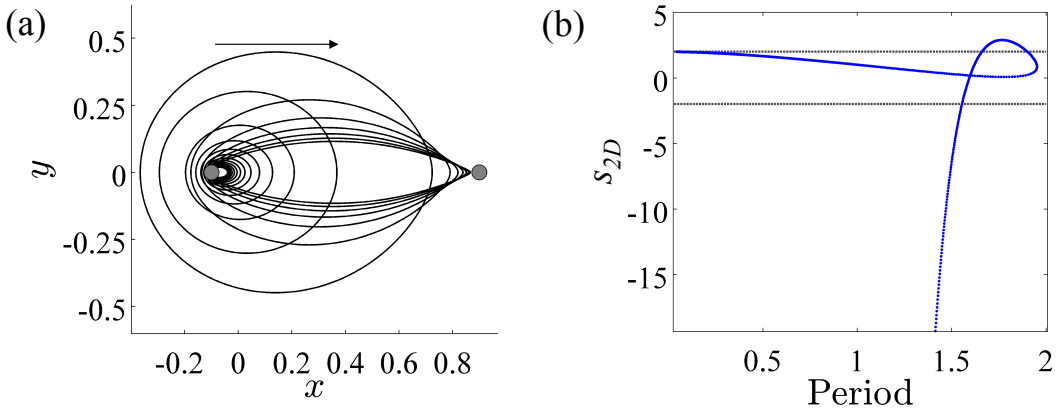

Fig. 6.18. Evolution of the retrograde circumstellar family of orbits about P_1 for $\mu = 0.10$ and $k = -0.20$ in (a) configuration space and (b) in terms of the planar stability as a function of orbital period.

at a local maximum in the orbital period is observed, producing the white region at the bottom of Figure 6.17. The stability evolution and resulting elliptical shape exhibited by these retrograde circumstellar orbits is not observed along the computed portions of the family in the CR3BP, as depicted in Figure 4.6. Thus, additional analysis is warranted to determine if such characteristics exist only under the influence of a three-body interaction.

To investigate the existence and uniqueness of the elliptically shaped retrograde circumstellar orbits about P_1, discrete variational mechanics supports the capability to reproduce these shape characteristics at various values of the natural parameters of the system. First, a reference path exhibiting the desired characteristics is selected and discretized into 500 nodes; the resulting orbit, which exists at $\mu = 0.10$, $k = -0.20$ and possesses an orbital period of 1.136 nondimensional time units, is depicted in configuration space in Figure 6.19. This orbit, which exhibits the motion of interest, is defined as a reference path in the constrained optimization problem in the formulation using discrete variational mechanics. Periodic orbits exhibiting a similar behavior

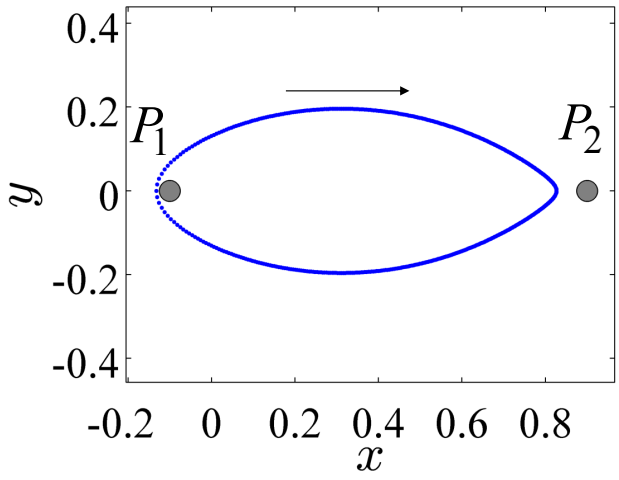

Fig. 6.19. Sample retrograde circumstellar orbit exhibiting desired shape characteristics for $\mu = 0.10$ and $k = -0.20$, used as a reference path in the constrained optimization problem.

are then constructed for various mass ratios and scaling constants, using the same process employed in Section 6.3.1. This procedure, used to reproduce retrograde circumstellar orbits about P_1 that appear elliptical in the rotating frame, recovers orbits within a bounded region in the two-dimensional (k, μ) space depicted in Figure 6.20. Recall that each black point in this natural parameter space indicates the existence of an orbit which exhibits the desired shape characteristics, while sample orbits are displayed in the margins. Analysis of Figure 6.20 reveals that the motion of interest is contained within a small triangular region at the bottom left slightly below the line reflecting $k = -\mu$. Thus, the retrograde circumstellar orbits about P_1 tend to exhibit an elliptical shape, as viewed in the rotating frame, for a sufficiently negative value of k. Accordingly, such motion appears to be unique to the presence of a three-body interaction within a large mass ratio binary system. However, to explore the

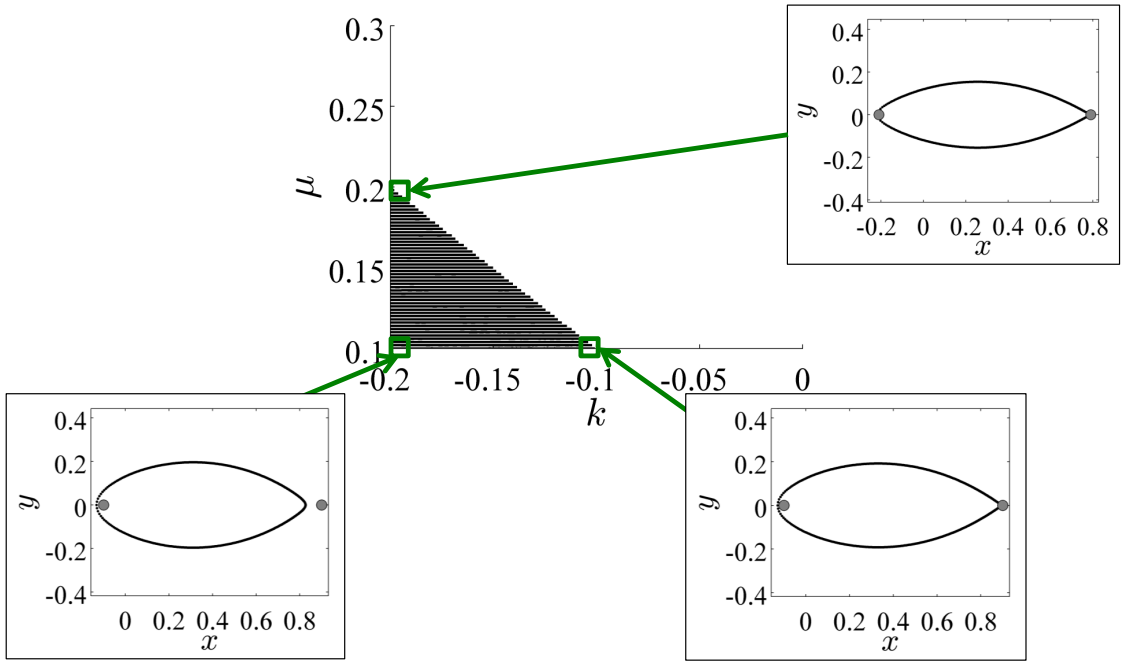

Fig. 6.20. Existence of retrograde circumstellar orbits about P_1 with the desired shape characteristics for combinations of k and μ that are indicated via black points. Sample orbits are displayed in the margins.

specific nonzero values of k bounding this region, additional analysis using concepts from dynamical systems theory is useful.

To explore the limiting values of the natural parameters at which the retrograde circumstellar family of interest exhibits an elliptical shape, a comparison to the stability of L_1 is valuable. Recall that L_1, as inherited from the CR3BP, does not exist at all negative values of k for mass ratios within the range $\mu = [0.10, 0.30]$. In fact, L_1 and its manifolds disappear at a critical negative value of k, as depicted in the zoomed-in view of the qualitative planar stability of L_1 in Figure 6.21(a). Recall, for this figure, that a white region in the (k, μ) two-dimensional space indicates that L_1 does not exist. To determine whether the retrograde circumstellar family of orbits is impacted by the disappearance of L_1, the combinations of μ and k at which the desired motion exists are overlaid on the qualitative planar stability representation of L_1. The resulting plot is displayed in Figure 6.21(b). Using this figure as a reference,

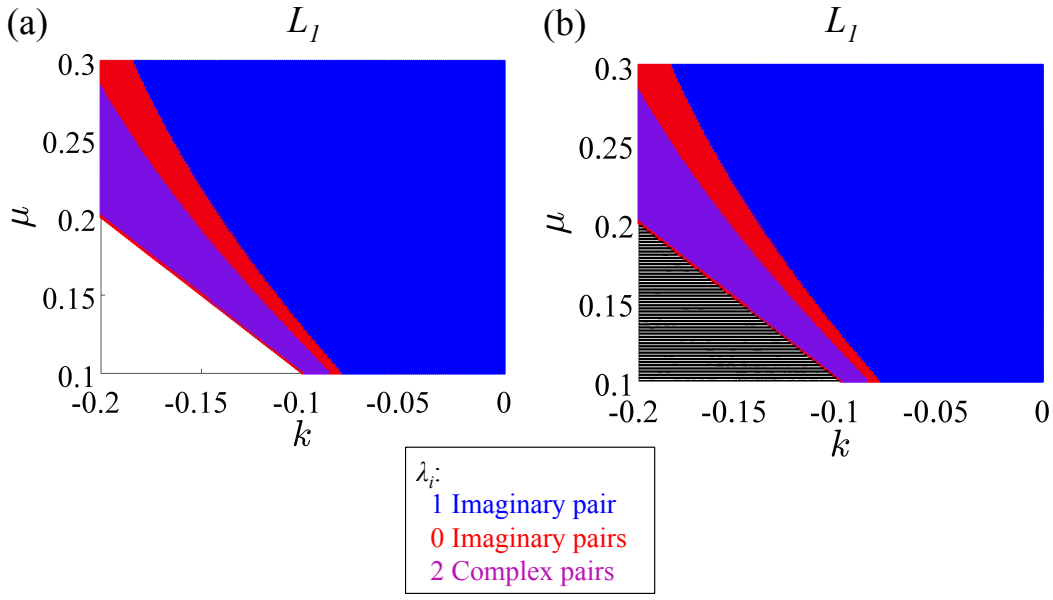

Fig. 6.21. (a) Planar stability of L_1 and (b) comparison of the existence of retrograde circumstellar orbits about P_1 with desired shape characteristics, for combinations of k and μ that are indicated via black points, with the existence and stability of L_1.

the motion of interest from Figure 6.20 for the planar retrograde circumstellar family of orbits appears to occur when L_1 does not exist. Since this equilibrium point exists at all mass ratios within the CR3BP, such periodic motion may be postulated to be reproducible only under the influence of a sufficiently repulsive three-body interaction.

6.3.3 Prograde Circumstellar Orbits

To explore circumstellar families of orbits that encircle the larger primary, P_1, note that two simply-periodic prograde families exist in the CR3BP for sufficiently large mass ratios. Recall from Section 4.4 that selected members along each family, labelled 'family 1' and 'family 2', are plotted in Figure 4.8 for $\mu = 0.30$. As discussed in Section 4.4, the evolution of the orbits along each of these families is governed by the stable and unstable manifolds emanating from the L_1 Lyapunov orbits [11]. For this application, consider 'family 1', which is explored in the MCR3BP using both composite stability representations and discrete variational mechanics.

Since 'family 1' exists in the CR3BP for $\mu = 0.30$, the evolution of this family of orbits is examined at this mass ratio in the MCR3BP. The resulting composite stability representations appear in Figures 6.22(a) and 6.22(b) for the in-plane and out-of-plane stability indices, respectively. Although this investigation examines values of the constant scaling factor representing the three-body interaction within the range $k = [-0.20, 0.70]$, this family only appears to exist for $k \approx [-0.0139, 0.1866]$. To understand these bounds on the value of k, first consider the case of a repulsive three-body interaction. With increasingly negative values of k, this family becomes closed and the two tangent bifurcations occurring at the minimum and maximum orbital periods approach each other. These tangent bifurcations collide at $k \approx -0.0139$, and the family disappears. Considering both the in-plane and out-of-plane stability, comparison of Figures 4.9 and 6.22 indicates that the effect of a repulsive three-body interaction on the existence and stability of this prograde family of orbits is qualitatively similar to the effect of decreasing the mass ratio below $\mu = 0.30$. When

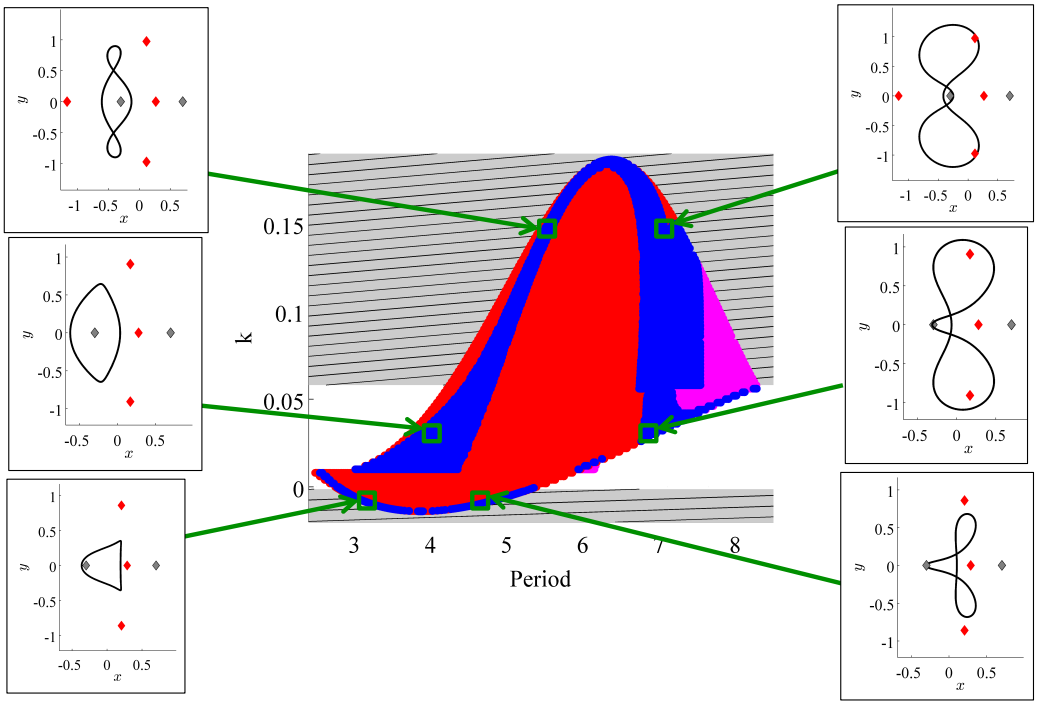

(a) In-plane stability.

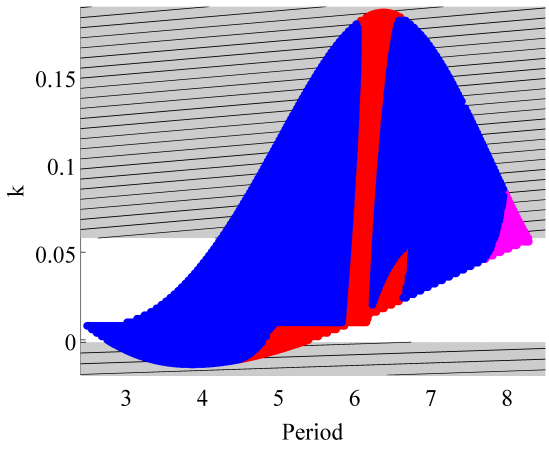

(b) Out-of-plane stability.

Fig. 6.22. Stability of 'family 1', comprised of prograde orbits about the larger primary, P_1, for $\mu = 0.30$, $k = [-0.0139, 0.1866]$. Orbital stability is indicated via color: stable (blue), positive unstable (red), and negative unstable (purple).

the three-body interaction is attractive, however, two discontinuities appear in the colored structures for the planar stability in Figure 6.22(a). These discontinuities are not numerical artifacts; rather, they reflect the occurrence of structural changes along the family. The first discontinuity occurs at $k \approx 0.01$, with a larger blue region of stable periodic orbits appearing at lower orbital periods. As in the CR3BP, this family often possesses two members at a given value of the orbital period. At $k \approx 0.01$, a small purple region also appears from behind the red and blue structures that are brought to the front in Figure 6.22(a), indicating that the family may no longer be closed. To explain these discontinuities, analysis of the in-plane stability index along 'family 1' reveals that by varying k, a local minimum in the stability index approaches the critical value $s = +2$ from above. At a critical value of k, a collision of tangent bifurcations occurs between two separate families as they exchange branches, thereby resulting in a discontinuity in the composite stability representation. As k is increased further, the blue structures corresponding to stable periodic orbits become smaller. Once k reaches another critical value, $k \approx 0.058$, the family is confirmed to be closed and a discontinuity appears in the blue structure, corresponding to periodic motion that is stable with respect to planar perturbations at higher orbital periods. In fact, the stable region encompasses a wider range of orbital periods than at lower values of k and, even, in the CR3BP for mass ratios close to $\mu = 0.30$. Further increasing the strength of the attractive three-body interaction, the two tangent bifurcations at the minimum and maximum orbital periods approach and eventually collide at $k \approx 0.1866$, causing the family to cease to exist. Examination of the out-of-plane stability in Figure 6.22(b) for positive values of k reveals a significant departure from the effect of varying the mass ratio. In comparison to the CR3BP, a larger portion of the family is stable in response to perturbations normal to the orbital plane for positive values of k. In addition, the structures corresponding to unstable orbits encompass a smaller range of periods. Together, these observations suggest that the evolution of the selected prograde family about P_1 appears relatively sensitive to the presence of a three-body interaction.

Further insight is gained from the plots of selected orbits in the margins of Figure 6.22(a), as viewed in the rotating frame. The physical configurations of orbits in this prograde family appear to be dependent upon the sign of k. For instance, orbits along this family tend to exhibit loops near L_4 and L_5. When the three-body interaction is attractive and the family disappears, the loops along the limiting orbit appear nearly above and below the largest primary. However, as the value of k becomes increasingly negative towards $k = -0.0139$, the limiting orbit possesses loops that are skewed towards P_2. This difference in the appearance of the limiting orbits at the minimum and maximum values of k for which this family exists can be attributed to both the change in the dynamical field due to the presence of the three-body interaction as well as the sequence of branch exchanges occurring during each collision of bifurcations as k increases or decreases away from zero.

Given the sensitivity of the evolution of the prograde orbits in 'family 1' to changes in μ and k, discrete variational mechanics is used to supplement the exploration of this family by recreating an orbit at a mass ratio not encompassed by this family in the CR3BP, and allowing k to be nonzero. By employing the discrete variational formulation to approximately recreate this type of orbit, the use of a lengthy continuation process in both natural parameters, which may be unsuccessful or computationally expensive, is avoided. Recall that this particular family of simply-periodic prograde orbits does not exist for mass ratios below $\mu \approx 0.26284$ in the CR3BP. However, assume that an exoplanet is discovered to move along a path resembling this type of prograde motion about the larger primary in a binary star system. Also assume, for this example, that the value of the mass ratio of this binary is accurately known to equal $\mu = 0.25$. The planar prograde motion typical of this family may not be followed by an object in the CR3BP, since this particular family does not exist at $\mu = 0.25$. This type of periodic motion may, however exist in the MCR3BP at $\mu = 0.25$ for some nonzero value of k.

To determine the value of k at which the periodic motions typical of the planar prograde family of interest may exist for $\mu = 0.25$, a periodic reference path from

the CR3BP is discretized and serves as an initial guess in the constrained optimization problem as formulated with discrete variational mechanics. An orbit is selected from 'family 1' at a sample mass ratio in the CR3BP and discretized into 600 nodes to supply a reference path that is representative of motion along this family. The selected discrete path, plotted in Figure 6.23(a) using black dots, exists at a mass ratio of $\mu = 0.274625$ and possesses an orbital period of $T = 2.97$ nondimensional time units. In this figure, P_1 is located using a gray-filled circle, while equilibrium points are indicated by red diamonds. As an input to the multi-start constrained optimization algorithm, 500 initial guesses are constructed using the reference path and a small amount of noise. Furthermore, each initial guess is assigned a value of the mass ratio equal to $\mu = 0.25$, while the value of k is randomly selected within the range $k = [-0.20, 0.70]$ and the initial guess for the time step variable, h, lies within 25% of the value of h along the reference path. Each initial guess is used in Matlab's *fmincon* routine to construct a locally optimal solution close to the reference path. The best locally optimal solution, existing closest to the reference orbit in configuration space, is retained and plotted using blue dots in Figure 6.23(b). The locations of the larger primary and L_1 now reflect the new values of the natural parameters corresponding to this particular solution, which exists at $\mu = 0.25$ and $k = 0.01134$, with a period of 2.915 nondimensional time units. Note that the computed solution is simply an approximation to a continuous periodic orbit. Accordingly, a verification step is completed using a multiple shooting method to ensure that a periodic orbit exists in the vicinity of the converged discrete path and in the prescribed dynamical environment. The resulting orbit, one that is periodic in the continuous time system, is represented by a green solid line in Figure 6.23(c). Note that, in this figure, the maximum y-excursions along the orbit differ slightly between the continuous and discrete paths. This discrepancy occurs due to the high orbital speed near the closest approach to P_1, which may not be accurately approximated using a first-order finite differencing. Increasing the number of nodes to the discretize the orbit reduces this discrepancy between the continuous and discrete motion. However, nodes added to

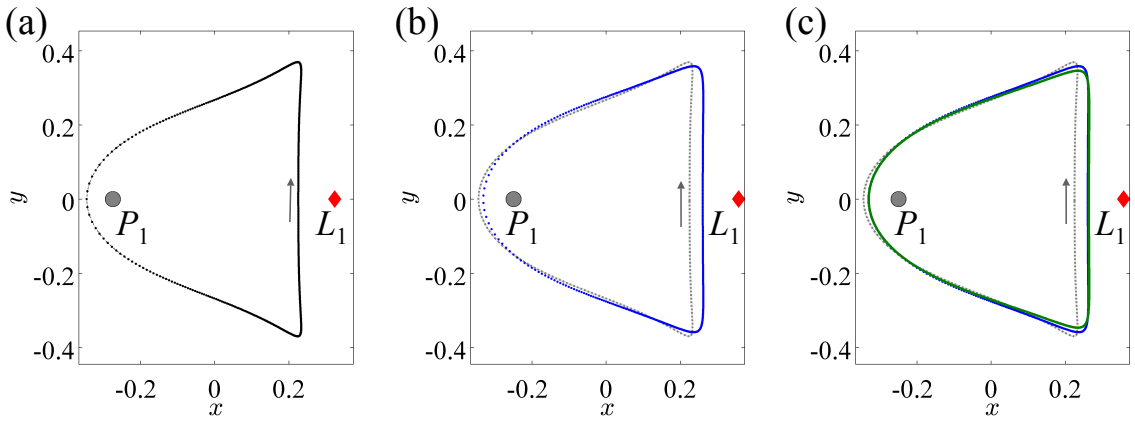

Fig. 6.23. Prograde orbit from 'family 1' in the rotating frame: (a) discretized reference path (black) for $\mu \approx 0.274625$ in the CR3BP, (b) discrete approximation (blue) of a periodic orbit existing at $\mu = 0.25$ and $k = 0.01134$, and (c) a continuous periodic orbit (green) corrected using the discrete path (blue).

this path mostly congregate near the maximum y-excursion locations where the velocities are significantly slower than near periapsis. Accordingly, such orbits would benefit from time-adaptive stepping to reduce the computational expense associated with using an excessively large number of nodes. Nevertheless, the discrete variational formulation accurately predicts the presence of periodic orbits at this combination of the natural parameters, (μ, k). Furthermore, the results from this example suggest that, in the presence of a small three-body interaction, prograde periodic motion typical of 'family 1' may be observed in binary systems with mass ratios at which the family does not normally exist in the CR3BP. Such analysis thereby demonstrates the utility of discrete variational mechanics as a supplement to stability analysis to add clarity in interpreting the effect of an additional autonomous force contribution added to the CR3BP. In addition, such analysis may aid in translating the existence of a given type of motion within a system described by an accurately known mass ratio to bounds on the strength of a three-body interaction.

6.3.4 Libration Point Orbits

Periodic motions within a binary system can also exist in the vicinity of the collinear equilibrium points. For L_1, which lies between the two primaries, the evolution of the associated planar family of Lyapunov orbits is examined. Both the (a) in-plane and (b) out-of-plane stability representations are visualized in Figure 6.24 for a fixed mass ratio of $\mu = 0.30$ and values of k within the range $k = [-0.142, 0.70]$; numerical difficulties prohibit reproduction of this family of orbits at even lower and more negative values of k. Note that since L_1 possesses a pair of imaginary eigenvalues for $k > -0.1839$ when the mass ratio is fixed at $\mu = 0.30$, the Lyapunov family of orbits cannot exist for $k < -0.1839$. Recall that gray shaded regions of this plot indicate a 'dynamical barrier' that prohibits orbits from possessing a given period. For the L_1 Lyapunov family, the minimum orbital periods are inherited from the equilibrium points and their associated imaginary eigenvalues. In the vicinity of L_1, the members of this family grow in size, while the orbital period increases away from this limiting value. For small positive values of k, the evolution of the planar stability along the L_1 Lyapunov family, as visualized qualitatively in Figure 6.24(a), resembles the effect of decreasing the mass ratio. The three-dimensional stability index, depicted in Figure 6.24(b), does not experience a qualitative change. Furthermore, observing the physical configuration of the orbits indicated in configuration space within the margins, no significant change occurs. Thus, the structure and stability of the L_1 Lyapunov family is relatively insensitive to uncertainty in a positive value of k. When a sufficiently repulsive three-body interaction is incorporated into the dynamical environment, however, the L_1 Lyapunov family undergoes a structural change. Specifically, members along this family develop loops in the vicinity of L_4 and L_5, which are shifted relative to their locations in the CR3BP. Similar to the evolution of the retrograde exterior orbits in the CR3BP, loops that form along periodic orbits near L_4 and L_5 tend to occur in a nearly fractal manner as the orbital period is increased. This structural change in the physical configuration, influenced by the

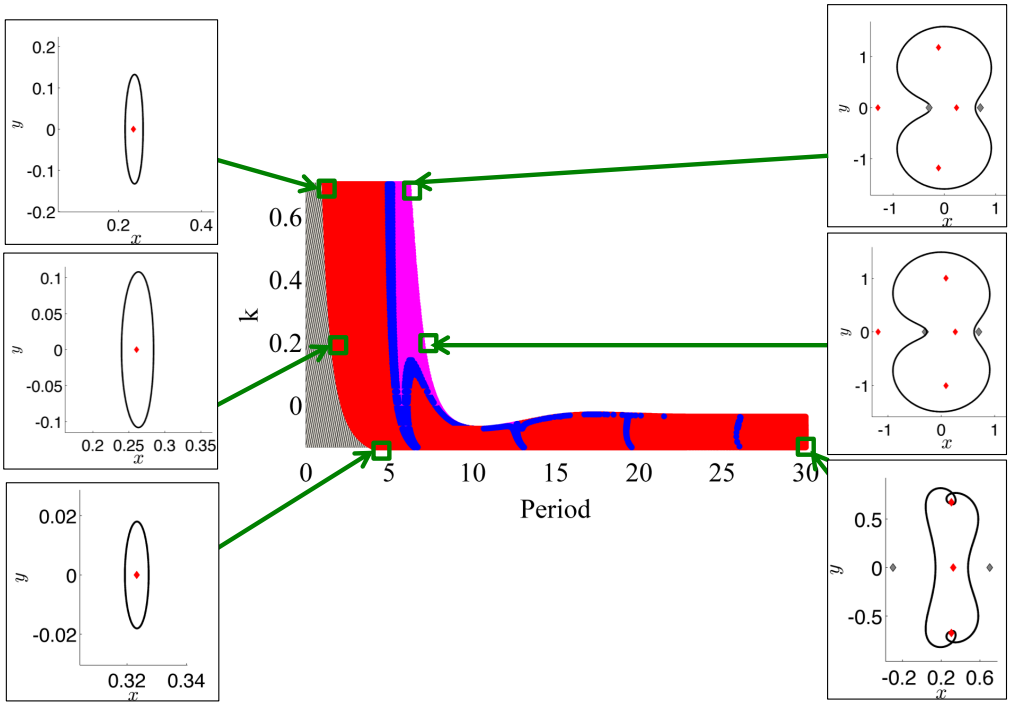

(a) In-plane stability.

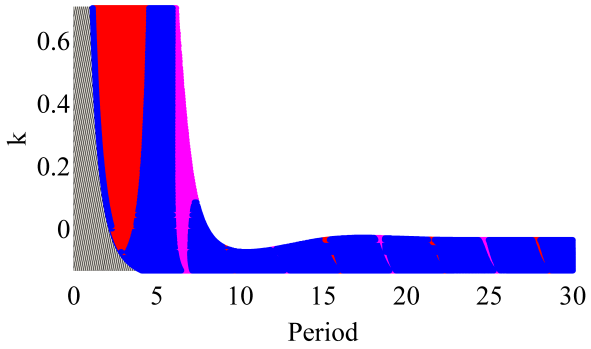

(b) Out-of-plane stability.

Fig. 6.24. Stability of L_1 Lyapunov orbits about P_1, for $\mu = 0.30$, $k = [-0.20, 0.70]$. Orbital stability is indicated via color: stable (blue), positive unstable (red), and negative unstable (purple).

motion emanating from the vicinity of the triangular equilibrium points, enables the family to extend to large orbital periods. Using Figure 6.24(b) as a reference, this

characteristic of the physical configuration of L_1 Lyapunov orbits for a sufficiently repulsive three-body interaction produces an alternating sequence of red and purple structures in the qualitative representation of the out-of-plane stability. Recall from Section 4.1 that the corresponding oscillation in the out-of-plane stability index occurs as additional loops form near L_4 and L_5 or, equivalently, with additional revolutions around the primaries when visualized in the inertial frame. Members of this family, at large negative values of k and large orbital periods can occur within the red regions of the (T, k) space in Figure 6.24(a). Accordingly, stable and unstable manifold structures may enable the capture of small bodies into these L_1 Lyapunov orbits. In contrast to the natural gravitational environment, the presence of a three-body interaction may result in such periodic motions repeatedly encountering the triangular equilibrium points over long time intervals.

The evolution of the L_2 and L_3 Lyapunov families at a mass ratio of $\mu = 0.30$ is similar as the value of k is varied. Specifically, the composite stability representations for the (a) in-plane and (b) out-of-plane stability for the L_2 and L_3 Lyapunov families appear in Figures 6.25 and 6.26, respectively. For both families, at small positive values of k, the stability evolution and physical configuration of its members is qualitatively similar to that in the CR3BP. However, at distinct critical values of k corresponding to an attractive three-body interaction, a structural change occurs along both the L_2 and L_3 Lyapunov families. In fact, loops form along each orbit family near L_4 and L_5. For each family, the orbital periods extend to large values, and the out-of-plane stability curve becomes oscillatory. This structural change is also observed along the L_1 Lyapunov family, but for negative values of k. Under the influence of a repulsive three-body interaction, both the L_2 and L_3 Lyapunov families exist over a smaller range of orbital periods before the occurrence of a close pass to their primaries. In the specific case of the L_2 Lyapunov family, however, a sufficiently repulsive three-body interaction has an additional effect: turning points occur along the family resulting in the orbital period initially decreasing as the family evolves away from the equilibrium point. Since the physical configuration of the

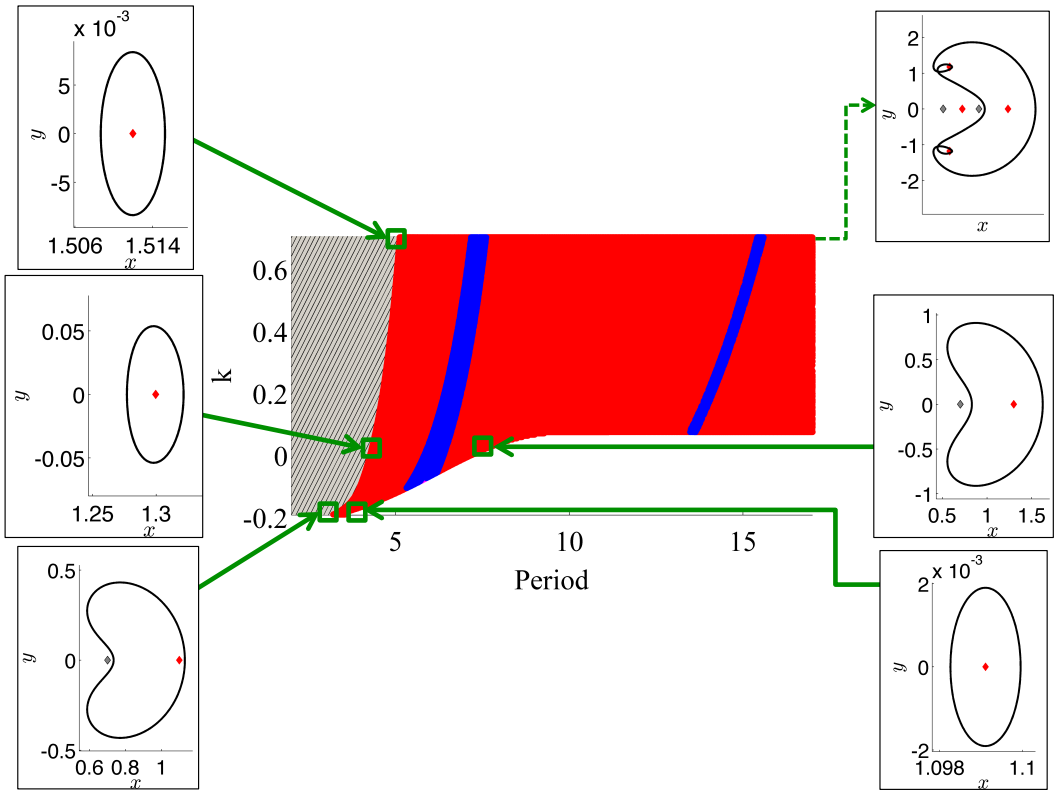

(a) In-plane stability.

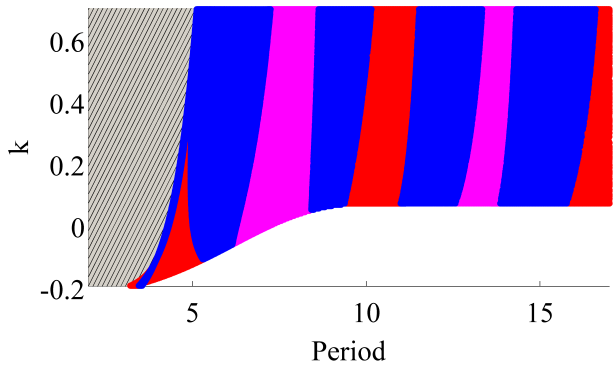

(b) Out-of-plane stability.

Fig. 6.25. Stability of L_2 Lyapunov orbits about P_1, for $\mu = 0.30$, $k = [-0.20, 0.70]$. Orbital stability is indicated via color: stable (blue), positive unstable (red), and negative unstable (purple).

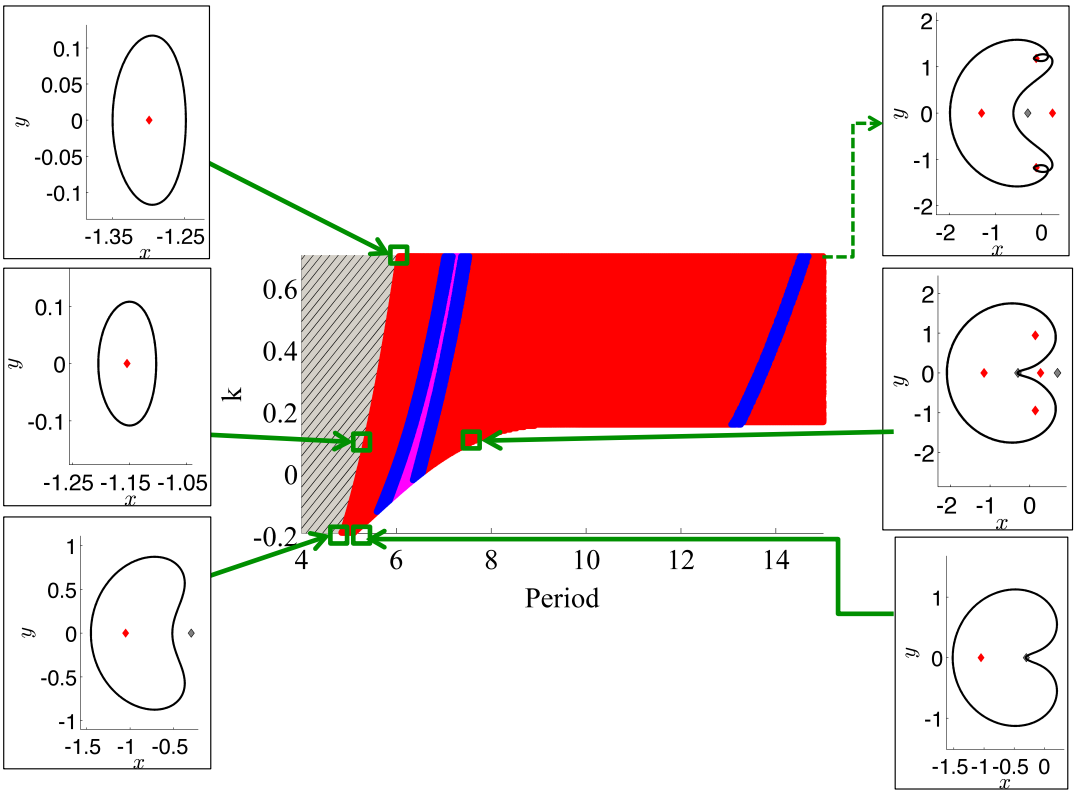

(a) In-plane stability.

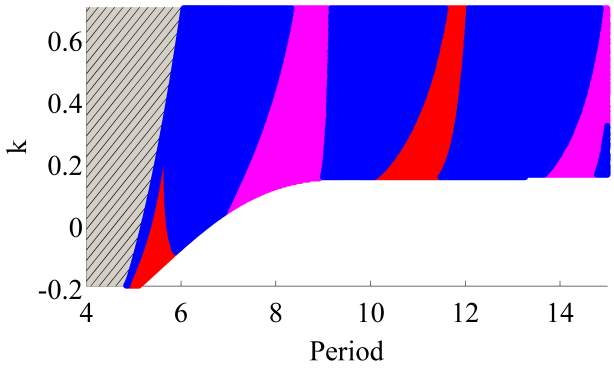

(b) Out-of-plane stability.

Fig. 6.26. Stability of L_3 Lyapunov orbits about P_1, for $\mu = 0.30$, $k = [-0.20, 0.70]$. Orbital stability is indicated via color: stable (blue), positive unstable (red), and negative unstable (purple).

corresponding orbits is not qualitatively dissimilar from those in the CR3BP, alternative methodologies are required to explore the existence and uniqueness of this effect, certainly warranting future investigation.

As new equilibrium points that possess oscillatory modes appear within the configuration space, additional libration point orbit families emerge. Recall from Section 6.2 that, as L_1 undergoes a pitchfork bifurcation for an increasingly negative value of k, two additional equilibrium points are created: L_{4b} and L_{5b}. As depicted in Figure 6.9, each symmetric equilibrium point possesses one pair of planar oscillatory modes indicating the existence of a planar libration point orbit family that does not exist in the CR3BP. The initial guess for the first orbit computed along the family is determined by linearizing the equations of motion near L_{4b} and isolating a periodic solution that lies within the center manifold. These approximations, constructed from the imaginary eigenvalues and their associated eigenvectors, are then corrected using a multiple shooting algorithm and continued via pseudo-arclength continuation. As an example of the physical configuration of orbits along this family, consider the following combinations of natural parameters: $\mu = 0.30$ and $k = -0.194995$. A portion of this family is computed and plotted in configuration space in Figure 6.27(a). Red circles indicate the location of L_4 and L_{4b}, while a black arrow denotes the direction of motion along each orbit. Using Figure 6.27(a) as a reference, this family of planar libration points emanates from L_{4b} and evolves towards a teardrop shape. As the family evolves further, loops form in the vicinity of L_4 in a fractal manner, corresponding to additional revolutions around the primaries when viewed in the inertial frame. Figure 6.27 also depicts the (b) planar and (c) out-of-plane stability along this family. Recall that stable modes are indicated by a stability index with a magnitude less than two; the critical values for the stability index, $s = 2$ and $s = -2$, are plotted as gray dashed lines in Figure 6.27(c). As evident from these figures, the L_{4b} libration point orbit family is predominantly unstable within the plane of motion of the primaries. The three-dimensional stability index, however, possesses a magnitude that predominantly lies below two, indicating the existence of quasi-periodic motion

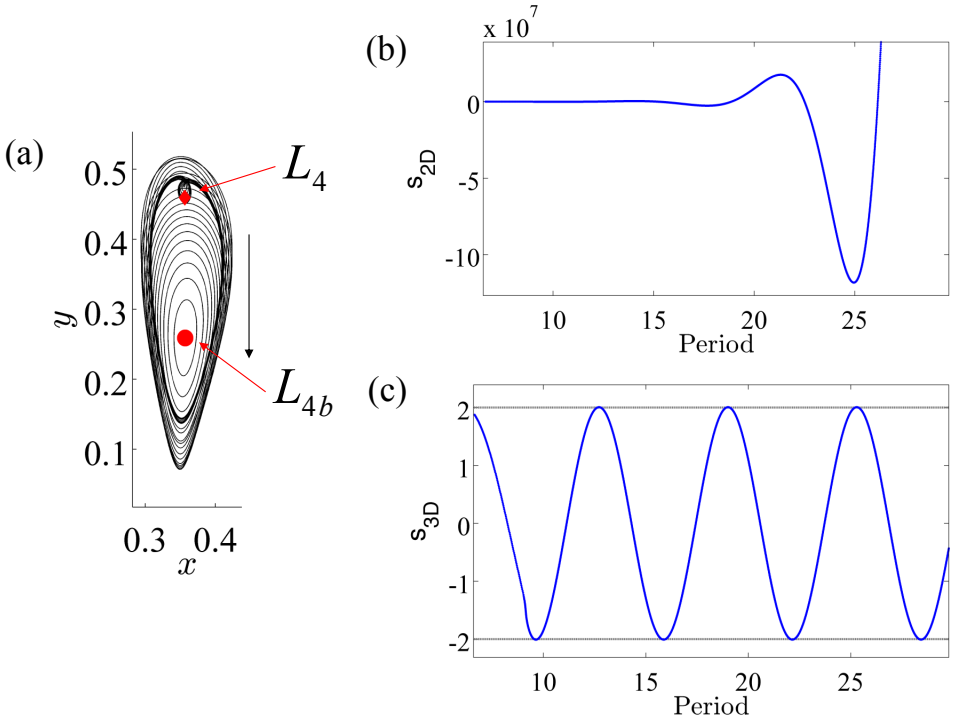

Fig. 6.27. Family of L_{4b} planar libration point orbits for $\mu = 0.30$ and $k = -0.194995$: (a) in configuration space, (b) planar stability index and (c) out-of-plane stability index.

out of the plane of motion of the primaries. The L_{5b} libration point orbit family is straightforwardly computed from the L_{4b} libration point orbit family by leveraging the symmetry properties of the MCR3BP. Nevertheless, observations of a small body exhibiting the motion typical of an L_{4b} or L_{5b} libration point orbit, for instance, may offer clues to the existence and bounds on the strength of an additional force contribution within a binary system.

6.4 Summary

By analyzing the underlying dynamical structures within a multi-body dynamical system, the effect of an additional perturbing force in the form of a three-body

interaction is explored. In this section, both equilibrium points and periodic solutions have been studied over a range of values of the natural parameters for large mass ratio binary systems. Specifically, the existence, location and stability of each of the equilibrium points inherited from the CR3BP are impacted by the presence of a three-body interaction and the resulting changes to the geometry of the potential field. This evolution of the equilibrium points significantly affects the existence and configuration of periodic motions throughout the entire phase space. Such changes in the structural evolution of a selected set of periodic orbits have been identified and analyzed by leveraging both composite stability representations and discrete variational mechanics. In many of the cases explored here, changes in the structural evolution of families of periodic orbits have been traced back to one of two sources: the occurrence of bifurcations with additional families, or changes in the existence, stability and location of the equilibrium points. Furthermore, in most of the examples presented in this section, a repulsive three-body interaction appears to alter the dynamical field more significantly than an attractive force with a scaling constant of the same magnitude, resulting in a larger deviation from the natural gravitational model. This insight into the effect of a three-body interaction within a nonlinear and chaotic system is obtained via a guided and thorough exploration of the underlying dynamics, demonstrating the value in leveraging natural dynamical structures to explore multi-body systems.

7. APPLICATION: TRAJECTORY DESIGN FRAMEWORK FOR A LOW-THRUST-ENABLED CUBESAT MISSION

With the emergence and increased development of miniaturized satellite technologies, CubeSats offer an alternative platform for unmanned exploration of cislunar space and, eventually, the solar system [1], [3], [4]. In fact, their reduced cost and development time in contrast to larger, traditional spacecraft supports a wide array of entities conducting scientific observation, technology demonstration and space exploration missions. Continued advancement in these small satellite technologies demands the innovative design of trajectories for spacecraft that require fewer resources, achieve more complex mission goals and visit farther destinations. Furthermore, small spacecraft typically ride as secondary payloads onboard a launch vehicle, producing significant uncertainty and variability in the launch date and deployment status. However, such uncertainty in the deployment state of a small spacecraft can severely constrain and complicate the trajectory design process during both the development and operational phases of the mission. Accordingly, the construction of a framework that leverages natural dynamical structures to enable efficient, rapid and well-informed trajectory design is warranted [12].

To demonstrate the value of a trajectory design framework, consider the Lunar IceCube mission led by Morehead State University and supported by NASA Goddard Space Flight Center (GSFC), Busek and Catholic University of America. This mission consists of a 6U CubeSat which is designed to detect and observe water and other volatiles near the lunar poles [3]. To achieve these scientific goals, an inclined, low lunar elliptical orbit is required during the observational phase of the mission. Currently, Lunar IceCube is scheduled for launch in late 2018 as a secondary payload onboard the upcoming Exploration Mission-1 (EM-1) vehicle. Following deployment

close to the Earth, the Lunar IceCube spacecraft, estimated to possess an initial mass of 14 kg, is placed on a high energy trajectory that would naturally depart the Earth-Moon system [69]. However, the spacecraft features a low-thrust propulsion system that is currently estimated to deliver 0.8 mN of thrust with an I_{sp} of 2500s [69]. Finite duration maneuvers can be leveraged, in combination with the natural dynamical structures associated with the gravity of the Sun, Earth and Moon, to design a complex path that delivers the Lunar IceCube spacecraft to its final lunar science orbit [12]. However, the constrained departure conditions, i.e., the launch date and deployment state, as well as the limited propulsive capability, may limit both the geometry and persistence of transfers within the phase space. Furthermore, as these departure conditions evolve during both the development and operational phases of the primary mission, a complete trajectory redesign may be required, necessitating the development of a framework for rapidly constructing an initial guess for a transfer that may satisfy the mission and hardware requirements.

To construct a trajectory design framework for a CubeSat with limited propulsive capability and constrained departure conditions, techniques from dynamical systems theory are leveraged. In fact, natural dynamical structures, along with Poincaré mapping strategies, are employed to design a complex path that delivers the spacecraft from a highly energetic deployment state to the final lunar science orbit [12]. With specific application to the Lunar IceCube mission, analysis of available point solutions reveals that the transfer trajectory can be split into three components: an Earth outbound segment, a phasing and energy adjustment segment that exploits solar gravity, and then lunar approach and capture. The first and final segments rely heavily on the low-thrust propulsion system to modify the spacecraft energy. However, given the limitations on the propulsive capability of the Lunar IceCube spacecraft, predominantly natural motions are sought to connect these two bounding segments. In addition, the phasing and energy adjustment segment exhibits the largest variability in terms of the available geometries and trajectory characteristics. To effectively design this transfer segment, a circular restricted three-body model of the Sun-Earth system is

employed to supply insight into the geometry of natural dynamical structures that can be incorporated into the design of an end-to-end trajectory. Furthermore, approximate bounds on the motion are established and transfer geometries are explained via analysis of the manifolds of libration point orbits. These natural motions are visualized and linked to the deployment and final lunar science orbit bounding conditions via Poincaré mapping strategies, thereby enabling rapid and efficient construction of a discontinuous initial guess. Depending on the deployment conditions, which frequently evolve throughout the development of the mission, the exact definition of the constructed maps may require update; however, a general framework that leverages mapping techniques is still useful. A differential corrections process is then formulated in a low-thrust-enabled ephemeris model to identify an end-to-end trajectory that generally retains the characteristics of the initial guess. The resulting continuous solution can be then be input to an operational-level model environment for further corrections or even an optimization algorithm. The constructed trajectory design framework, employed to link the highly energetic deployment state of the Lunar IceCube spacecraft to the final lunar science orbit, supports the identification of feasible transfer regions and rapid redesign. Implementation of this framework eliminates the challenges associated with searching for a solution via a grid search in a nonlinear and chaotic system. Moreover, this framework may be applicable to future CubeSat missions that must meet alternative mission goals, such as re-encountering the Moon with a specific energy and/or flight duration, attaining specific Sun-Earth or Earth-Moon orbits, or achieving a heliocentric trajectory that encounters an asteroid, as well as mission extensions.

7.1 Lunar IceCube Mission Overview

The Lunar IceCube mission leverages a 6U CubeSat developed by Morehead State University and supported by NASA Goddard Space Flight Center (GSFC), Busek and Catholic University of America. Specifically, the primary objective for this mission

is to observe water and other lunar volatiles at the poles of the Moon, furthering knowledge of the location and transportation physics associated with water in various forms [3]. Such insight may inform future in-situ resource utilization planning for missions as well as supply the science community with insight into the evolution and dynamical processes of the Moon. The scientific instruments onboard the Lunar IceCube spacecraft require that these measurements of lunar water and volatiles be performed from a low lunar science orbit. Currently, the nominal science orbit is highly elliptical with a perilune located over the equator at an altitude between 100 and 105 km [68]. Furthermore, to observe the lunar poles, the orbit is also constrained to possess a high inclination. However, the Lunar IceCube spacecraft, depicted in Figure 7.1 and currently estimated to possess an initial mass of 14 kg, will ride onboard the Exploration Mission-1 (EM-1) vehicle as a secondary payload. Accordingly, its deployment state is highly energetic and located close to the Earth. Naturally, this deployment state is associated with a trajectory that quickly departs the Earth-Moon system. To decrease the spacecraft energy and modify the trajectory to approach the final science orbit, an onboard low-thrust propulsion system is leveraged. This iodine-fuelled engine is a Busek Ion Thruster 3-cm (BIT-3) system, which is currently designed to deliver a maximum 0.8 mN of thrust with an I_{sp} of 2500s and a propellant mass of approximately 1.5 kg [67], [69]. During earlier phases of the design process, this low-thrust engine was estimated to impart 1.2 mN of thrust. Point solutions

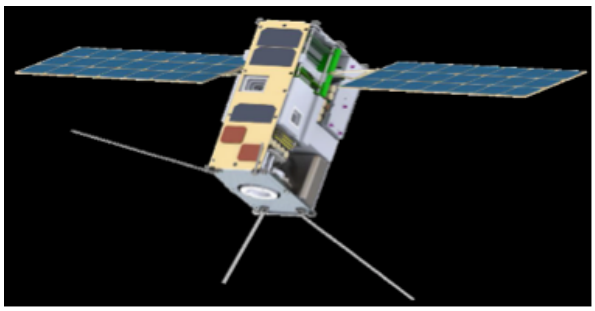

Fig. 7.1. Lunar IceCube preliminary spacecraft design.

for a trajectory to deliver the spacecraft from the highly energetic deployment state to the final lunar science orbit were designed for a thrust magnitude of 1.2 mN in an ephemeris environment by David Folta at NASA GSFC. These point solutions, displayed in a Sun-Earth rotating frame in Figure 7.2, illustrate some options for the itinerary of the Lunar IceCube spacecraft. In fact, each of these solutions exhibits a different geometry primarily along the segment of the transfer that exploits solar gravity for energy and phasing adjustment prior to lunar approach. In addition, these point solutions represent distinctly different trajectories in a large design space that is difficult to examine through the construction of single point solutions in an ephemeris environment, particularly as the spacecraft hardware and mission parameters evolve. Thus, a framework employing dynamical systems techniques is used to construct similar solutions based on insight into natural structures within the gravitational environment of the Earth, Sun and Moon.

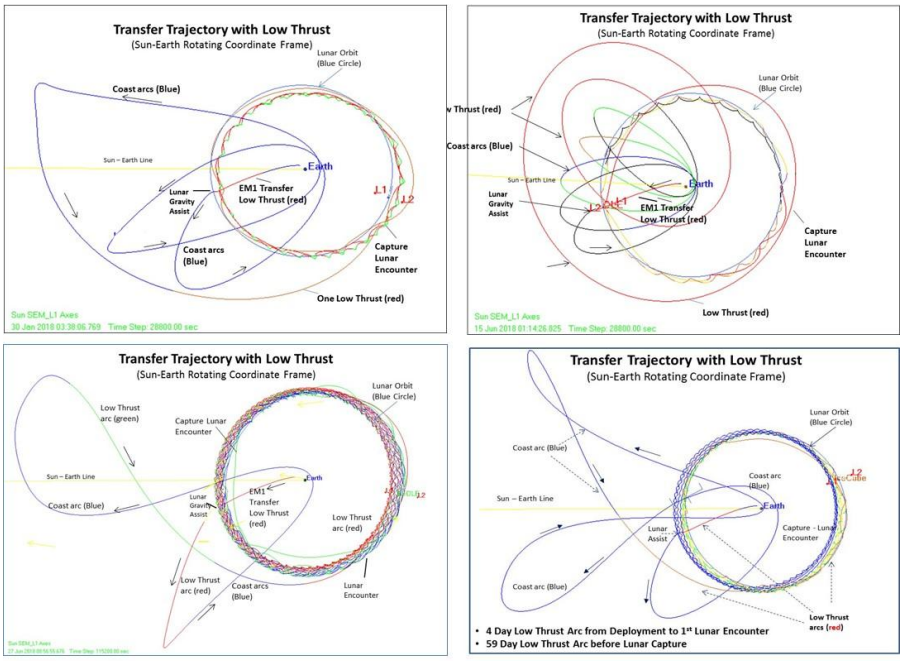

Fig. 7.2. Previous point solutions for the Lunar IceCube trajectory, constructed for a 1.2 mN low thrust engine by David Folta at NASA GSFC.

7.2 Low-Thrust-Enabled Motion in an Ephemeris Model

To recover an end-to-end trajectory, an ephemeris model is employed. In this section, the equations of motion are first derived for a spacecraft traveling under the point mass gravitational influences of the Earth, Moon and Sun. Then, an additional acceleration due to a low-thrust propulsion system is incorporated, leveraging a spacecraft-centered velocity-normal-conormal coordinate frame to describe the direction of the thrust vector. Development of the differential equations governing low-thrust-enabled motion within a point mass ephemeris model enables verification of the existence and characteristics of end-to-end trajectories constructed using multi-body dynamical structures.

7.2.1 Equations of Motion in a Natural Ephemeris Model

For applications within the solar system, a point mass ephemeris model enables verification of the solutions predicted by the restricted problem and serves as a basis for identifying an end-to-end trajectory in a higher fidelity dynamical environment. This nonautonomous model captures the true noncircular and nonplanar motion of each incorporated body. To develop this dynamical model, consider N_e bodies with dimensional mass $\tilde{M}_i$, each assumed to be spherically symmetric and, therefore, modeled as a point mass. These bodies are located in an inertial reference frame, $\hat{X}\hat{Y}\hat{Z}$, with a fixed origin at point O, as displayed in Figure 7.3. The notation used in this model is consistent with the development of the equations of motion for the CR3BP as formulated in the inertial frame. For instance, recall that the dimensional position vector locating the body of interest P_3, at the inertial coordinates $\bar{\tilde{R}}_3 = (\tilde{X}, \tilde{Y}, \tilde{Z})$, with respect to the body P_j, at the coordinates $\bar{\tilde{R}}_j = (\tilde{X}_j, \tilde{Y}_j, \tilde{Z}_j)$, is found as $\bar{\tilde{R}}_{j3} = (\tilde{X} - \tilde{X}_j)\hat{X} + (\tilde{Y} - \tilde{Y}_j)\hat{Y} + (\tilde{Z} - \tilde{Z}_j)\hat{Z}$. To formulate the differential equations governing natural motion within the point mass ephemeris model, the acceleration of the body of interest, P_3, is expressed relative to a celestial body P_q in P_q-centered J2000 inertial coordinates [76]. Accordingly, the relative dimensional

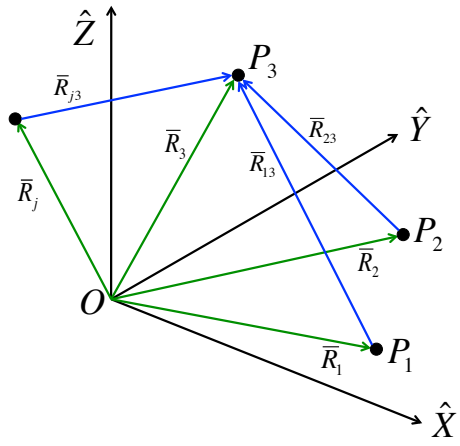

Fig. 7.3. Definition of the inertial coordinate frame and the position vectors locating each of the bodies in the N_e-body point mass ephemeris model.

equations of motion for P_3, subject to $N_e - 1$ point mass gravitational interactions and relative to an inertial observer, are written as:

$$\bar{\tilde{R}}''_{q3} = -\frac{\tilde{G}(\tilde{M}_q + \tilde{M}_3)}{\tilde{R}^3_{q3}}\bar{\tilde{R}}_{q3} + \tilde{G}\sum_{\substack{j=1 \\ j\neq q,3}}^{N_e} \tilde{M}_j \left(\frac{\bar{\tilde{R}}_{3j}}{\tilde{R}^3_{3j}} - \frac{\bar{\tilde{R}}_{qj}}{\tilde{R}^3_{qj}}\right) \tag{7.1}$$

When P_3 represents a spacecraft, $\tilde{M}_3 \ll \tilde{M}_q, \tilde{M}_j$. Thus, the spacecraft is assumed to have only a negligible impact on the paths of the celestial bodies. Accordingly, additional equations of motion are not required for the $N_e - 1$ celestial bodies if ephemerides are available. When modeling the natural motion of a spacecraft relative to the Earth within a Sun, Earth, and Moon point mass ephemeris model, Eq. (7.1) simplifies to:

$$\begin{aligned}\bar{\tilde{R}}''_{E,s/c} = &-\frac{\tilde{G}(\tilde{M}_E + \tilde{M}_{s/c})}{\tilde{R}^3_{E,s/c}}\bar{\tilde{R}}_{E,s/c} \\ &+ \tilde{G}\left[\tilde{M}_S\left(\frac{\bar{\tilde{R}}_{s/c,S}}{\tilde{R}^3_{s/c,S}} - \frac{\bar{\tilde{R}}_{E,S}}{\tilde{R}^3_{E,S}}\right) + \tilde{M}_M\left(\frac{\bar{\tilde{R}}_{s/c,M}}{\tilde{R}^3_{s/c,M}} - \frac{\bar{\tilde{R}}_{E,M}}{\tilde{R}^3_{E,M}}\right)\right]\end{aligned} \tag{7.2}$$

where the subscript E identifies the Earth, s/c identifies the spacecraft, M corresponds to the Moon and S indicates the Sun. These equations of motion are straight-

forwardly extended to incorporate additional accelerations due to sources such as additional bodies, higher order gravitational contributions, or a low-thrust engine.

7.2.2 Equations of Motion in a Low-Thrust-Enabled Ephemeris Model

Prior to augmenting the point mass ephemeris model equations of motion with the additional acceleration contributed by a propulsion system, the characteristics of a low-thrust engine are summarized. Specifically, a constant specific impulse low-thrust engine can be described by its thrust magnitude, T_{lt}, specific impulse, I_{sp}, and the thrust direction, $\hat{u}$. Recall that the iodine-fuelled BIT-3 system onboard the Lunar IceCube spacecraft is assumed to operate with the following parameters: $T_{lt} = 0.8$ mN and $I_{sp} = 2500$s [67], [69]. The assumed constant value of the available engine power, P, is then calculated from these quantities as:

$$P = \frac{T_{lt} I_{sp} g_0}{2}$$

where g_0 is the gravitational acceleration measured on the surface of the Earth, 9.81 m/s. It is also assumed that the mass of the spacecraft, $\tilde{m}(t)$, is initially equal to 14 kg. When the low-thrust engine is activated, the spacecraft mass decrements by the following mass flow rate [70]:

$$\frac{d\tilde{m}(\tilde{t})}{d\tilde{t}} = -\frac{T_{lt}^2}{2P} \tag{7.3}$$

Since the specific impulse of the low-thrust engine leveraged in this investigation is modeled as constant, the mass flow rate is also constant. The constant mass flow rate impacts the maximum time for operation of the low-thrust engine which is constrained by the initial propellant mass, assumed to be equal to 1.5 kg [12]. This description of a low-thrust engine is employed to augment the vector differential equation in Eq. (7.2) with the additional acceleration contributed by the propulsion system.

In this investigation, the direction of the thrust vector is described using a velocity-normal-conormal (VNC) coordinate system, which is often employed for spacecraft applications [71]. Specifically, the velocity direction, denoted by the $\hat{V}$ unit vector is

parallel to the inertial velocity vector of the spacecraft relative to a reference body. Then, the conormal direction, $\hat{C}$, is defined normal to the path of the spacecraft, while lying within the orbital plane. Finally, the normal unit vector, $\hat{N}$, is perpendicular to the orbital plane and completes the right-handed coordinate system. At any instant of time, assume that the spacecraft is defined by the dimensional inertial position and velocity vectors, $\bar{\tilde{R}}_{q,s/c}$ and $\bar{\tilde{V}}_{q,s/c}$, expressed relative to the body P_q in P_q-centered J2000 inertial coordinates. The corresponding $\hat{V}$, $\hat{N}$, and $\hat{C}$ directions are depicted as red unit vectors in Figure 7.4 for the motion of a spacecraft (yellow circle) defined relative to the Earth (blue circle), along with the corresponding position and velocity vectors (black arrows). Mathematically, these unit vectors are computed as:

$$\hat{V} = \frac{\bar{\tilde{V}}_{q,s/c}}{\tilde{V}_{q,s/c}} \qquad \hat{N} = \frac{\bar{\tilde{R}}_{q,s/c} \times \bar{\tilde{V}}_{q,s/c}}{|\bar{\tilde{R}}_{q,s/c} \times \bar{\tilde{V}}_{q,s/c}|} \qquad \hat{C} = \hat{V} \times \hat{N} \tag{7.4}$$

The engine thrust direction, $\hat{u}$, can then be projected into the VNC coordinate system and expressed using these three unit vector directions such that $\hat{u} = u_V \hat{V} + u_N \hat{N} + u_C \hat{C}$. By expressing the $\hat{u}$ unit vector in the VNC frame, an intuitive interpretation of the direction of the additional acceleration due to the low-thrust engine is possible. Furthermore, when working in the VNC frame, it is straightforward to constrain the

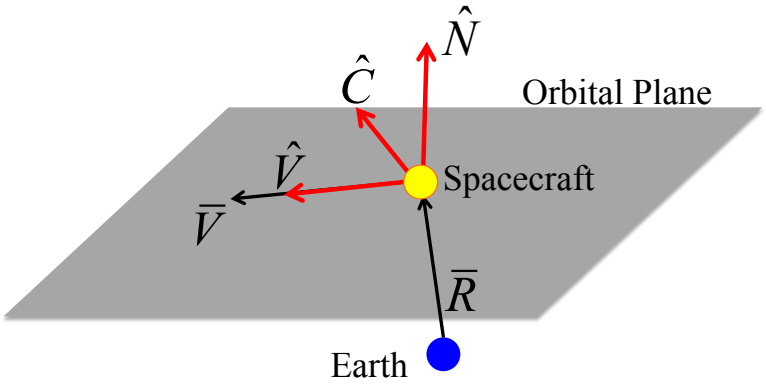

Fig. 7.4. Definition of the VNC coordinate system (red unit vectors) for the motion of a spacecraft (yellow) defined via position and velocity vectors expressed relative to the Earth (blue).

thrust direction relative to the spacecraft velocity or orbital plane. Then, the thrust vector, $\hat{u}_{VNC}$, expressed in the VNC frame can be converted into the P_q-centered J2000 inertial coordinates to produce, $\hat{u}_{XYZ}$, via the following transformation:

$$\hat{u}_{XYZ} = \begin{bmatrix} \hat{X}\cdot\hat{V} & \hat{X}\cdot\hat{N} & \hat{X}\cdot\hat{C} \\ \hat{Y}\cdot\hat{V} & \hat{Y}\cdot\hat{N} & \hat{Y}\cdot\hat{C} \\ \hat{Z}\cdot\hat{V} & \hat{Z}\cdot\hat{N} & \hat{Z}\cdot\hat{C} \end{bmatrix} \hat{u}_{VNC}$$

given the unit vectors $\hat{V}$, $\hat{N}$, and $\hat{C}$, computed from the spacecraft position and velocity vectors expressed in terms of the P_q-centered J2000 inertial coordinates via Eq. (7.4). This transformation is leveraged to incorporate a thrust vector that possesses a fixed direction in the VNC coordinate frame into the equations of motion for a point mass ephemeris model.

The additional acceleration of a low-thrust engine is incorporated into the differential equations governing the motion for a spacecraft relative to the Earth in a point mass ephemeris model including the Sun, Earth and Moon. First, to mitigate ill-conditioning between the position, velocity and time quantities in the equations of motion, nondimensionalization is employed. Specifically, the characteristic quantities m^*, t^*, and l^*, computed in the CR3BP for a primary system consisting of the bodies P_p and P_q, may be employed. For instance, for the Lunar IceCube spacecraft orbiting within the Sun-Earth-Moon system beyond the lunar radius, constant values of the characteristic quantities from the Sun-Earth system, calculated at an initial epoch or averaged over a given time interval, may be appropriate for nondimensionalization. Recall that, for nondimensional quantities, a tilde no longer appears above the variable of interest. For instance, the nondimensional position vector locating the spacecraft relative to the Earth is written in the Earth J2000 inertial coordinates as $\bar{R}_{E,s/c} = X_{E,s/c}\hat{X} + Y_{E,s/c}\hat{Y} + Z_{E,s/c}\hat{Z}$. Then, the acceleration due to the low-thrust engine is expressed in vector form as $T_{lt}^*/\tilde{m}(t)\hat{u}$ where the dimensional mass of the spacecraft, $\tilde{m}$, is employed, and the symbol T_{lt}^* represents the thrust magnitude nondimensionalized only in the length and time units for dimensional consistency such that $T_{lt}^* = T_{lt} \times (t^*)^2/l^*$. Then, the coefficient $T_{lt}^*/\tilde{m}$ is nondimensional. Once $\hat{u}$

is transformed into the same coordinate frame as the acceleration of the spacecraft relative to the Earth, this additional acceleration term is straightforwardly added to the second-order vector differential equation in Eq. (7.2). Since the mass of the spacecraft is assumed to be negligibly small compared to the mass of the Earth, the three scalar second-order differential equations are written as:

$$X''_{E,s/c} = -\frac{GM_E}{R^3_{E,s/c}} X_{E,s/c} + G\left[M_S\left(\frac{X_{s/c,S}}{R^3_{s/c,S}} - \frac{X_{E,S}}{R^3_{E,S}}\right) + M_M\left(\frac{X_{s/c,M}}{R^3_{s/c,M}} - \frac{X_{E,M}}{R^3_{E,M}}\right)\right] + \frac{T^*_{lt}}{m} u_X \quad (7.5)$$

$$Y''_{E,s/c} = -\frac{GM_E}{R^3_{E,s/c}} Y_{E,s/c} + G\left[M_S\left(\frac{Y_{s/c,S}}{R^3_{s/c,S}} - \frac{Y_{E,S}}{R^3_{E,S}}\right) + M_M\left(\frac{Y_{s/c,M}}{R^3_{s/c,M}} - \frac{Y_{E,M}}{R^3_{E,M}}\right)\right] + \frac{T^*_{lt}}{m} u_Y \quad (7.6)$$

$$Z''_{E,s/c} = -\frac{GM_E}{R^3_{E,s/c}} Z_{E,s/c} + G\left[M_S\left(\frac{Z_{s/c,S}}{R^3_{s/c,S}} - \frac{Z_{E,S}}{R^3_{E,S}}\right) + M_M\left(\frac{Z_{s/c,M}}{R^3_{s/c,M}} - \frac{Z_{E,M}}{R^3_{E,M}}\right)\right] + \frac{T^*_{lt}}{m} u_Z \quad (7.7)$$

Since these three equations of motion feature the time-dependent mass of the spacecraft, an additional first-order differential equation is required to completely describe the time evolution of the low-thrust-enabled spacecraft under the point mass ephemeris gravitational influence of the Sun, Earth and Moon. Furthermore, since the spacecraft mass variable $\tilde{m}$ remains dimensional, the mass flow rate equation from Eq. (7.3) is normalized using only t^* such that:

$$\dot{\tilde{m}}(t) = -\frac{T^2_{lt}}{2P} t^* \quad (7.8)$$

Together, Eqs. (7.5)-(7.7), (7.8) are used to numerically integrate the augmented state of the spacecraft, $\bar{X}_e = [X, Y, Z, \dot{X}, \dot{Y}, \dot{Z}, m]$, where the nondimensional position and velocity components are expressed relative to the Earth in the Earth J2000 inertial

coordinate system. At each epoch during the integration process, the position coordinates corresponding to each body, relative to a designated basepoint located at the Earth, are accessed using the Jet Propulsion Laboratory DE421 ephemerides via the SPICE toolkit [72], [73], [74]. Relative position coordinates are then used to integrate the motion of a spacecraft relative to the Earth in the low-thrust-enabled four-body point mass ephemeris model. A similar process can be employed to formulate the equations of motion relative to an alternate basepoint body.

The equations of motion for the low-thrust-enabled spacecraft within the point mass ephemeris model of the Sun, Earth and Moon are numerically integrated. In particular, a mex-ed integration file created using C++ within MATLAB is employed to reduce the computation time. This integration file is constructed by augmenting an existing natural ephemeris integration file, available within Purdue University's Adaptive Trajectory Design (ATD) software, to include low-thrust acceleration, thereby supporting a potential future transition of the developed framework to an interactive design environment [74]. Within this file, integration is performed using the Runge-Kutta Prince-Dormand (8,9) stepping function available through the GNU Scientific Library (GSL) [75]. Then, evaluation of the equations of motion for the Sun, Earth and Moon low-thrust-enabled point mass ephemeris model is described by the following general procedure:

- If the low-thrust engine is activated, construct the VNC frame unit vectors relative to a specified body: access the ephemeris position and velocity vectors relative to a user-selected basepoint body for defining the VNC frame, expressed in body-centered J2000 inertial frame; compute relative position and velocity unit vectors and, then, the $\hat{V}$, $\hat{N}$ and $\hat{C}$ unit vectors.

- If the low-thrust engine is activated, transform the thrust unit vector, defined in the VNC frame, to the Earth-centered J2000 inertial frame.

- Access and store the ephemerides for each body incorporated into the point mass ephemeris model, relative to the Earth.

- Evaluate Eqs. (7.5)-(7.7) and (7.8), to produce a set of first-order differential equations that is used to evolve the augmented state of the spacecraft, $\bar{X}_e = [X, Y, Z, \dot{X}, \dot{Y}, \dot{Z}, m]^T$.

This methodology is employed to evaluate the equations of motion, which are numerically integrated via GSL to recover either a natural or low-thrust-enabled path for a spacecraft moving under the influence of the gravity of the Sun, Earth and Moon.

7.3 Differential Corrections to Recover an End-to-End Trajectory

To construct a continuous trajectory for a low-thrust-enabled spacecraft traveling within a point mass ephemeris model of the Earth, Moon and Sun, a variable-time multiple shooting algorithm is employed. Recall the general procedure for a multiple shooting algorithm as summarized in Section 3.1.4: intermediate nodes, described by a set of free variables, are simultaneously integrated to produce a sequence of arcs and, then, iteratively corrected to recover a continuous trajectory that satisfies a set of constraints. To demonstrate the formulation of the multiple shooting algorithm employed in this application, the conceptual representation in Figure 7.5 serves as a reference. In this illustration, the path of a spacecraft relative to a central body is sought as it travels under the gravitational influence of the central body and any additional perturbing bodies, as well as the action of a low-thrust engine.

Consider n_e nodes, indicated via blue circles in Figure 7.5, to produce a sequence of arcs that, when integrated forward in time, form the initial guess for a trajectory. The i-th node is completely specified by the vector:

$$\bar{s}_i = [X_i, Y_i, Z_i, \dot{X}_i, \dot{Y}_i, \dot{Z}_i, \tilde{m}_i, T_{node,i}, T_{int,i}]^T$$

In particular, the description of each node includes its nondimensional position, (X_i, Y_i, Z_i), and velocity, $(\dot{X}_i, \dot{Y}_i, \dot{Z}_i)$, relative to a central body. For the purposes of describing this methodology, consider the Earth as the central body. Then, for convenience, each state component is expressed in terms of Earth-centered J2000 inertial coordinates. The mass of the spacecraft, $\tilde{m}_i$, is also recorded at each node to

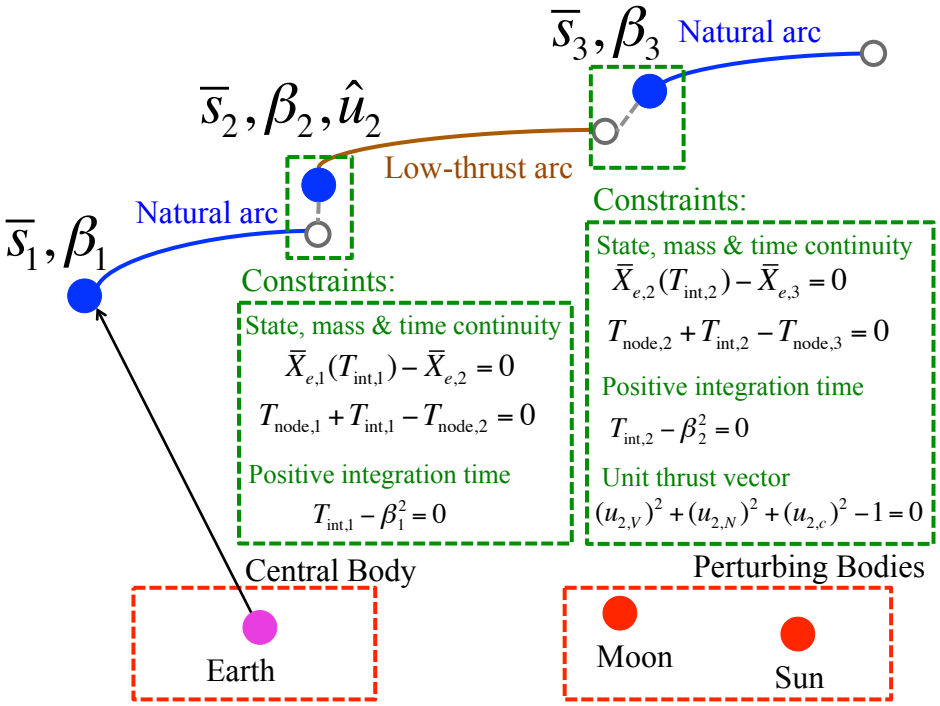

Fig. 7.5. Illustration of variable time multiple shooting formulation to target a continuous trajectory for a low-thrust-enabled spacecraft in an ephemeris model.

ensure mass continuity across arcs that employ low-thrust. In addition, the epoch at each node, $T_{node,i}$, is required to compute the ephemerides of the central and perturbing bodies. To ensure that the epoch possesses a similar order of magnitude in comparison to the remaining state variables, it is expressed relative to a fixed initial epoch and nondimensionalized via the characteristic time quantity, t^*, of the Sun-Earth system. Then, a nondimensional integration time, T_{int}, must be specified to compute the arc associated with a given node. Together, these variables completely represent each node. However, to completely describe the arc associated with a given node, a constant binary parameter is used to distinguish between a natural arc, displayed in blue in Figure 7.5, and a low-thrust arc, indicated in brown. Although this parameter must be predefined, the integration time along an arc is allowed to

vary towards zero, thereby enabling a low-thrust arc to be essentially eliminated if necessary to recover a continuous trajectory. For a low-thrust-enabled arc, the three components of the unit thrust direction vector, u_V, u_N, and u_C, must be specified. To identify arcs over which the low-thrust engine is activated, as well as the basepoint body used to express the position and velocity vectors, constant vectors with integers encoding this information are employed. Using this description, each of the arcs along a trajectory is completely defined.

Multiple arcs, computed by integrating a set of nodes forward in time, are iteratively refined until they satisfy a sequence of constraints that produce a continuous trajectory that leverages both natural and low-thrust-enabled motion. Regardless of whether the low-thrust engine is activated along an arc, connectivity between two neighboring arcs requires state, mass and time continuity. In particular, the position, velocity and mass at the end of the i-th arc, integrated forward for a time $T_{int,i}$, must equal the position, velocity and mass at the $i+1$-th node to within an acceptable tolerance. Due to the potential presence of low-thrust accelerations, dependent on the position and velocity vectors across an arc, the derivative of the augmented state constraints is calculated numerically using a first-order finite difference approximation. In addition, since the ephemerides of the central and perturbing bodies are time-dependent, the epoch, $T_{node,i} + T_{int,i}$, at the end of the i-th arc must equal the epoch, $T_{node,i+1}$, at the $i+1$-th node; this condition is labeled a time continuity constraint and its derivative is straightforwardly written as an analytical function of the time variables [76]. Furthermore, to ensure that the integration time along the i-th arc is positive, an inequality constraint is converted to an equality constraint that leverages a slack variable, β_i. This constraint is expressed in the form $T_{int,i} - \beta_i^2 = 0$, with a derivative that is an analytical function of only two variables. Then, for any arcs that leverage the additional acceleration of a low-thrust engine, an additional constraint is required: the thrust vector components, u_V, u_N, and u_C, must produce a unit vector. Thus, the unit thrust vector constraint is written as $u_V^2 + u_N^2 + u_C^2 - 1 = 0$. The derivative of this constraint is straightforwardly expressed as an analytical function

of the thrust direction components. The required constraints for the i-th segment are then summarized as follows:

$$X_i(T_{int,i}) - X_{i+1} = 0 \qquad Y_i(T_{int,i}) - Y_{i+1} = 0 \qquad Z_i(T_{int,i}) - Z_{i+1} = 0$$

$$\dot{X}_i(T_{int,i}) - \dot{X}_{i+1} = 0 \qquad \dot{Y}_i(T_{int,i}) - \dot{Y}_{i+1} = 0 \qquad \dot{Z}_i(T_{int,i}) - \dot{Z}_{i+1} = 0$$

$$\tilde{m}_i(T_{int,i}) - \tilde{m}_{i+1} = 0 \qquad T_{node,i} + T_{int,i} - T_{node,i+1} = 0 \qquad T_{int,i} - \beta_i^2 = 0$$

and over segments for which the low-thrust engine is activated:

$$u_{V,i}^2 + u_{N,i}^2 + u_{C,i}^2 - 1 = 0$$

Together, these constraints are used to recover a continuous trajectory for a low-thrust-enabled spacecraft under the influence of a point mass ephemeris model of the Earth, Moon and Sun.

In practice, additional constraints may need to be enforced at selected nodes along a trajectory. Such constraints, which may link to mission requirements or may be required for analysis, involve the epoch, spacecraft mass, inertial state components, apse conditions, energy via the Jacobi constant, rotating frame state components or orbital elements. First, the epoch, mass and inertial state component constraints are straightforwardly fixed to a constant value via an equality constraint. For instance, to fix the spacecraft mass at the i-th node to a value of 14 kg, a constraint can be formulated as $\tilde{m}_i - 14 = 0$. Next, to constrain a node as an apse relative to a body, P_q, an equality constraint is written as:

$$\bar{R}_{q,i} \cdot \bar{V}_{q,i} = 0$$

where $\bar{R}_{q,i}$ and $\bar{V}_{q,i}$ are, respectively, the position and velocity vectors locating the spacecraft at node i relative to body P_q and expressed in the inertial frame. To evaluate this constraint at a given epoch, the ephemerides locating P_q with respect to the central body must be accessed. Next, any constraints on the rotating frame components in the state vector or the Jacobi constant require a transformation from

the Earth-centered J2000 inertial coordinates to a rotating frame such as an instantaneously defined Sun-Earth rotating frame. Finally, the orbital elements of a spacecraft path relative to a body, P_q, are computed using concepts from the two-body problem. For a spacecraft located at node i with the relative position and inertial velocity vectors, $\bar{R}_{q,i}$ and $\bar{V}_{q,i}$, the following orbital quantities are calculated as:

$$\tilde{a} = \frac{-\tilde{G}\tilde{M}_q}{\tilde{V}_{q,i}^2 - 2\frac{\tilde{G}\tilde{M}_q}{\tilde{R}_{q,i}}} \qquad \hat{h} = \frac{(\bar{\tilde{R}}_{q,i} \times \bar{\tilde{V}}_{q,i})}{|\bar{\tilde{R}}_{q,i} \times \bar{\tilde{V}}_{q,i}|} \qquad i = \cos^{-1}(\hat{h} \cdot \hat{Z})$$

$$\tilde{p} = \frac{(\bar{\tilde{R}}_{q,i} \times \bar{\tilde{V}}_{q,i})^2}{\tilde{G}\tilde{M}_q} \qquad e = \sqrt{1 - \frac{\tilde{p}}{\tilde{a}}}$$

$$\theta^* = \cos^{-1}\left(\frac{1}{e}\left(\frac{\tilde{p}}{\tilde{R}_{q,i}} - 1\right)\right) \qquad \Omega = \sin^{-1}\left(\frac{\hat{h} \cdot \hat{X}}{\sin(i)}\right) = \cos^{-1}\left(-\frac{\hat{h} \cdot \hat{Y}}{\sin(i)}\right)$$

where $\tilde{a}$ is the semi-major axis, $\hat{h}$ is the specific angular momentum unit vector expressed in the body-centered inertial J2000 coordinates, i is the inclination relative to the equatorial plane of body P_q, $\tilde{p}$ is the semi-latus rectum, e is the eccentricity, θ^* is the true anomaly and Ω is the right ascension of the ascending node relative to the $\hat{X}$ reference direction in the body-centered inertial J2000 coordinates [77], [78]. Since the nodes along a trajectory can be expressed with respect to distinctly different bodies and nondimensionalized using either the Sun-Earth or Earth-Moon characteristic quantities, an additional system-to-system continuity constraint is defined. This constraint is typically enforced at the boundary between two trajectory segments that are recorded using different definitions: consider the final state along the first segment, expressed relative to body 1 and nondimensionalized by the characteristic quantities in system 1; and the first node of the second segment expressed relative to body 2 and normalized by m^*, l^* and t^* as defined in system 2. One strategy for implementing a continuity constraint between these two segments is to transform the time and state variables describing the first node of the second segment by shifting the basepoint and renormalizing each quantity to match the definition of the final state along the first segment. Accordingly, the first node of the second segment is transformed to produce state variables that are expressed relative to a basepoint located at body 1

and nondimensionalized by the characteristic quantities in system 1. With a consistent definition for the state and time variables at the end of the first segment and beginning of the second segment, a full continuity constraint is then directly applied. When required, each of these constraints are added to the continuity, positive time and unit thrust vector constraints in the multiple shooting algorithm implemented within MATLAB, and their derivatives may be computed using any combination of analytical expressions and numerical approximations.

7.4 Trajectory Design Framework

By leveraging known natural dynamical structures that exist in a simplified, autonomous dynamical model, a rapid and well-informed process for constructing a trajectory for a low-thrust-enabled small satellite is developed. In particular, the application of dynamical systems techniques enables the identification of known solutions that exist within a simplified natural gravitational environment. This insight offers a prediction of the bounds on the motion, while also supporting the construction of an initial guess for the trajectory prior to corrections in a operational-level modeling environment [12]. The capability for a rapid and guided exploration of the trajectory design space is particularly beneficial for CubeSat missions that possess limited propulsive capability and, as a secondary payload, are subject to significant uncertainty in their deployment conditions. Furthermore, the construction of a framework for CubeSat trajectory design, as demonstrated for the Lunar IceCube mission, enables rapid redesign as the deployment and spacecraft hardware parameters evolve during both the development and operational phases of the mission. This framework involves decomposing the trajectory into three segments:

- An Earth outbound segment, beginning at deployment
- A phasing and energy adjustment segment that exploits solar gravity, and
- A lunar approach and capture portion.

To illustrate this trajectory sequence, consider a sample point solution, designed by David Folta at NASA GSFC for a previous thrust magnitude of 1.2 mN, depicted in the top plot within Figure 7.6 [68]. In this figure, blue portions of the trajectory indicate natural motion while green curves correspond to arcs where the low-thrust engine is activated. In the three plots at the bottom of Figure 7.6, the arcs comprising each of the three segments are highlighted, while portions of this sample solution that are not included in the segment of interest are colored gray. Of these three segments within the trajectory sequence, the focus of this investigation is the phasing and energy adjustment arc, which exhibits the largest variability in terms of the available geometries and path characteristics. To explore and identify natural dynamical structures that may provide a pathway to link a high energy deployment state to a lunar

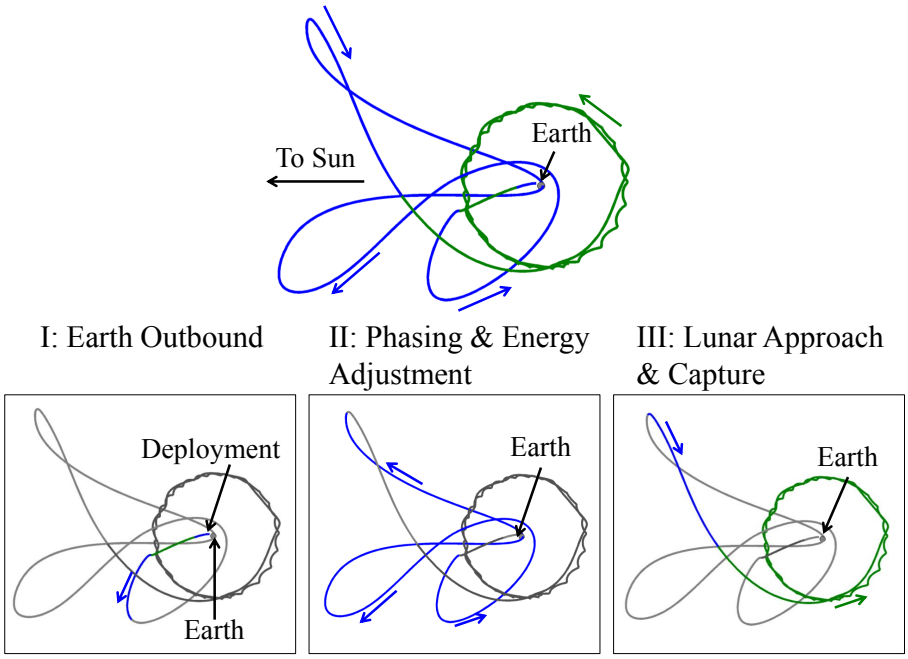

Fig. 7.6. Illustration of the trajectory sequence employed in this investigation, demonstrated using an existing point solution (top). Portions of the trajectory comprising each of three segments are isolated in the inset images (bottom).

capture arc, a Sun-Earth CR3BP model is leveraged, along with Poincaré mapping strategies. This framework is developed and subsequently employed to demonstrate the construction of an initial guess via dynamical systems techniques and insight. This initial guess trajectory is then corrected in a point mass ephemeris model that incorporates the additional acceleration of a low-thrust engine. The resulting trajectory supplies an initial guess for corrections and optimization within a higher fidelity dynamical model and, eventually, an operational-level modeling environment. Furthermore, the development and application of this framework demonstrates the value of a dynamical systems approach to trajectory design within chaotic multi-body environments, particularly for small spacecraft with limited propulsive capability and significant uncertainty in the deployment conditions.

7.4.1 Earth Outbound Segment

Integration of the Lunar IceCube deployment conditions (current as of August 2015) forward in time reveals that, naturally, the associated trajectory quickly departs the Earth vicinity. For a deployment epoch of December 15th, 2017, the initial state corresponds to a highly energetic path when integrated forward in time in a point mass ephemeris model. In fact, the associated trajectory is depicted in nondimensional coordinates in Figure 7.7 in (a) the Sun-Earth rotating frame and (b) the Earth-Moon rotating frame, with zoomed-in views near the Earth appearing in the insets. In Figure 7.7(a), a circular approximation to the lunar orbit is overlaid in black while Figure 7.7(b) includes the location of the Earth and Moon as gray-filled circles and the libration points as red-filled diamonds. As evident in both frames represented within this figure, the spacecraft undergoes a lunar flyby prior to quickly departing the Earth vicinity. Since the Lunar IceCube spacecraft must be delivered within a reasonable time frame to its final low lunar orbit to perform scientific observations, propulsive intervention is required.

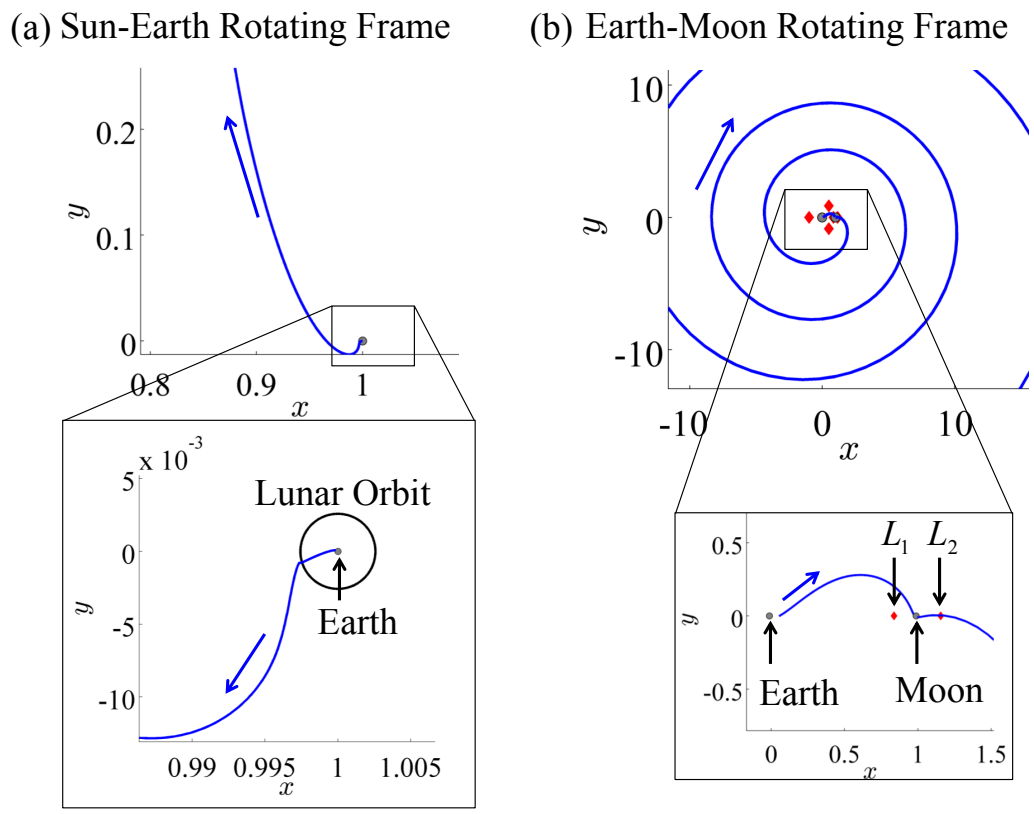

Fig. 7.7. Natural motion corresponding to forward propagation of the Lunar IceCube deployment conditions over 200 days in nondimensional coordinate in (a) a Sun-Earth rotating frame and (b) an Earth-Moon rotating frame.

By introducing a multi-day low-thrust arc shortly after deployment, the post-flyby conditions are sufficiently altered to produce a trajectory that remains within the Earth vicinity [68]. To demonstrate the impact of a short low-thrust arc near the beginning of the trajectory, consider a single sample arc: after approximately 8.5 hrs of natural motion, a low-thrust arc is introduced with the thrust vector aligned with the anti-velocity direction for 3.8 days, followed by a 2.5 hour coast arc until lunar periapsis and then natural motion until the first apogee. This sequence of arcs is depicted in Figure 7.8 in the (a) Sun-Earth rotating frame and (b) Earth-Moon rotating frame. In each figure, natural coasting segments are depicted in blue while

low-thrust arcs are indicated in green. In Figure 7.8(a), a circular approximation to the lunar orbit is overlaid in black while Figure 7.8(b) includes the location of the Earth and Moon as gray-filled circles and the libration points as red-filled diamonds. The motion of the spacecraft is integrated until the first apogee following the lunar flyby. For this example, the apogee is retrograde as viewed in the Sun-Earth rotating frame, i.e., the motion of the spacecraft is instantaneously clockwise. In fact, for this particular epoch and deployment state, the incorporation of a 3.8 day low-thrust arc raises the lunar periapsis radius to 6400 km from approximately 3000 km for the entirely natural trajectory depicted in Figure 7.7. Note that another deployment state and epoch may produce distinctly different behavior. Nevertheless, in addition to the reduction of velocity provided by the finite duration burn directed in the anti-velocity direction, raising the lunar periapsis reduces the acceleration boost provided by the Moon and, therefore, the velocity of the spacecraft after the lunar flyby. As a result, an apogee occurs within the Earth vicinity and the path remains, at least temporarily, captured. This apogee is leveraged to connect the Earth outbound portion of the transfer to the long phasing and energy adjustment segment.

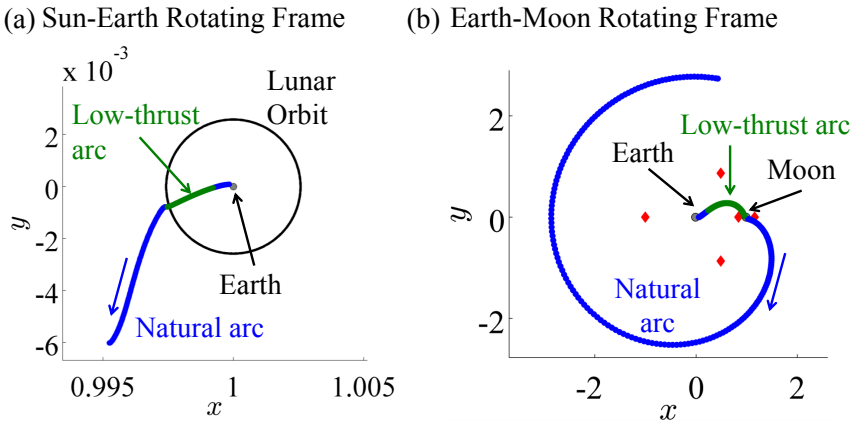

Fig. 7.8. Path of Lunar IceCube from deployment to apogee, produced by leveraging both the low-thrust engine and a lunar flyby in (a) a Sun-Earth rotating frame and (b) an Earth-Moon rotating frame.

By incorporating a second low-thrust arc shortly after the lunar flyby, the location and velocity of the first apogee along a temporarily captured path is significantly impacted. Assume the following trajectory sequence, similar to the previous example: after approximately 8.5 hours of natural motion post-deployment, a low-thrust arc with the thrust vector aligned with the anti-velocity direction for 3.8 days, a 2.5 hour coast arc until lunar periapsis, and a short post-perilune coasting segment followed by a low-thrust segment that continues until apogee. While the pre-flyby conditions are fixed, both the duration of the post-perilune coasting arc as well as the direction of the thrust vector during the post-perilune thrusting arc are varied, impacting the apogee conditions. Insight into the variation in the apogee condition is useful when connecting the Earth outbound segment to the phasing and energy adjustment segment, as well as the identification of feasible transfer regions. To explore the variation in the apogee conditions, consider the following two parameters of interest: T_{coast}, the duration of the post-perilune coasting segment; and $\hat{u}$, the direction of the thrust vector during the final segment prior to apogee. First, consider the effect of the duration of the post-perilune coasting segment by assuming this arc is followed by a finite duration burn that lasts until apogee, with the thrust vector aligned with the anti-velocity direction. Figure 7.9(a) illustrates a sample trajectory sequence from deployment until apogee as visualized in an Earth-Moon rotating frame, with natural arcs indicated by blue while low-thrust arcs are colored green. As the coasting time, T_{coast}, along the post-perilune natural arc is increased from 12 hrs to 16.5 days for the same fixed flyby conditions, the burn duration for the subsequent low-thrust arc is reduced; thus, the spacecraft velocity is reduced over a shorter time interval prior to apogee. In Figure 7.9(b), the planar projection of the location of the apogees, computed in a point mass ephemeris model, is displayed in the Earth-centered Sun-Earth rotating frame for coasting times between 12 hrs and 16.5 days. This figure is simply a planar projection for a Poincaré map constructed using an apoapsis surface of section. As expected for this epoch and deployment state, increasing the coast time and, therefore, decreasing the length of the final low-thrust arc, shifts the apogee

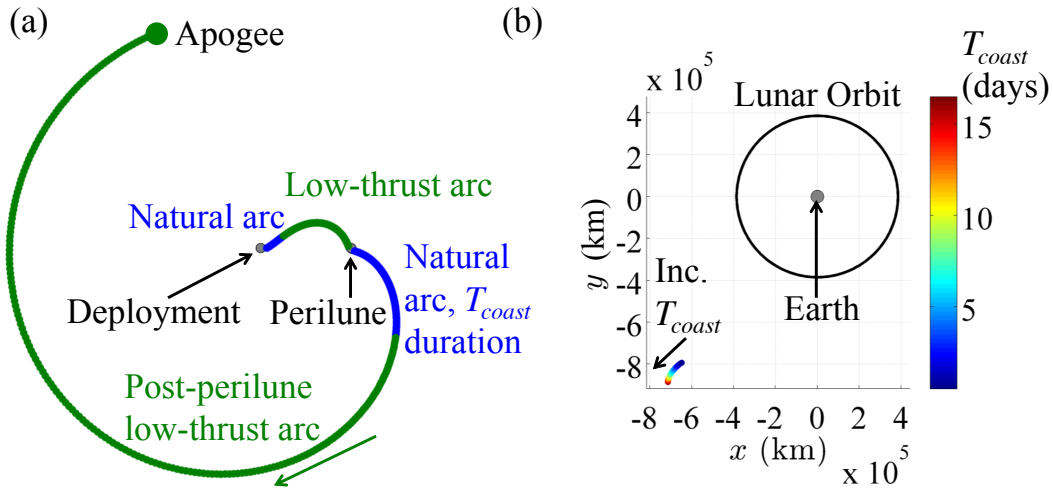

Fig. 7.9. Path of Lunar IceCube from deployment to apogee, produced by leveraging both the low-thrust engine and a lunar flyby in (a) a Sun-Earth rotating frame and (b) an Earth-Moon rotating frame.

further from the Earth. Accordingly, the Jacobi constant at this location is also decreased, producing a more energetic path at apogee. Next, the post-perilune coast time is held constant at 12 hours and the effect of the thrust direction during the final phase of the Earth outbound segment is explored. To avoid exacerbating the out-of-plane component of the spacecraft relative to the Earth-Moon plane, the thrust vector is constrained to the orbital plane of the spacecraft such that $\hat{u} \cdot \hat{N} = 0$. However, the $\hat{V}$ and $\hat{C}$ components of the thrust direction unit vector are varied within the ranges $\hat{u} \cdot \hat{V} = [-1, 1]$ and $\hat{u} \cdot \hat{C} = [-1, 1]$, subject to the unit vector constraint $(\hat{u} \cdot \hat{V})^2 + (\hat{u} \cdot \hat{C})^2 = 1$. A planar projection of the apogee map displaying the resulting trajectory segments appears in Figure 7.10 in the Sun-Earth rotating frame with a zoomed-in view in the inset image. A circular approximation to the lunar orbit is plotted in black, the Earth is indicated via gray circle. The set of apogees depicted in Figure 7.10 are colored by the value of the component of the thrust vector in the velocity direction. The inset image is a zoomed-in view of the curve of apogees produced by varying the constant thrust direction. The added arrows indicate the

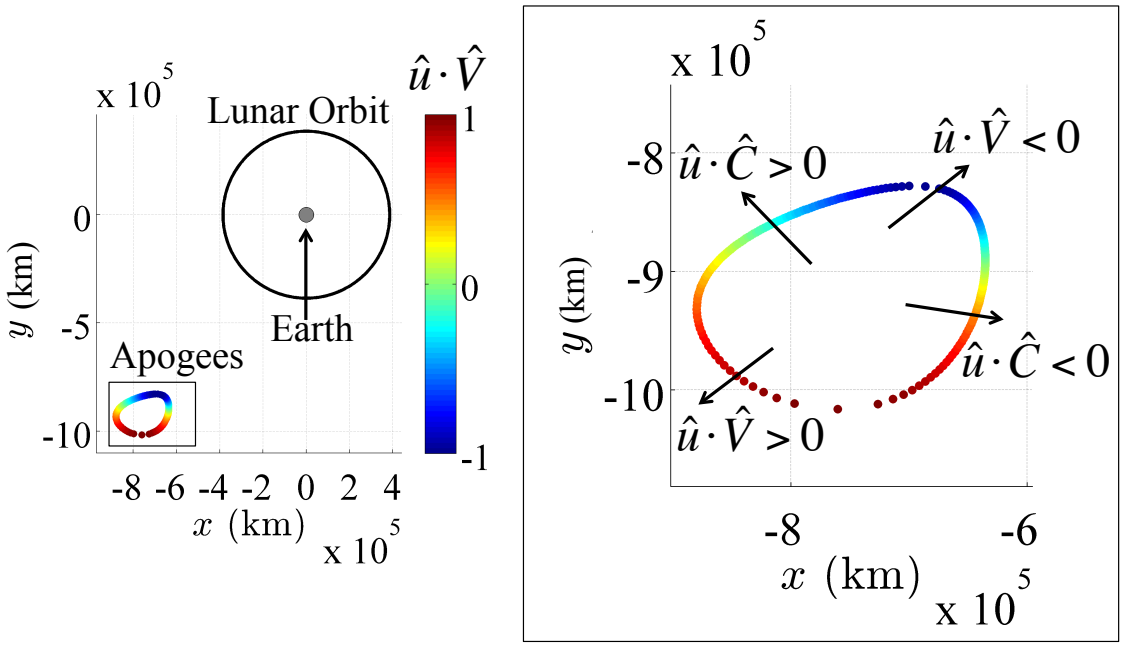

Fig. 7.10. Planar projection of the achievable apogees plotted in the Sun-Earth rotating frame for a fixed flyby condition, with a zoomed-in view in the inset.

sign of the velocity and conormal components of the thrust direction for various regions along the curve of apogees. For a fixed flyby condition and post-perilune coasting arc, these apogees appear as a one-dimensional curve. For post-perilune thrusting segments where the thrust vector possesses a positive component in the velocity direction, the apogees are shifted further from the Earth as depicted in the inset image in Figure 7.10. In addition, a thrust vector with a positive conormal component produces a path with an apogee that appears closer to the Sun-Earth line. From this figure, it is evident that varying the direction of the thrust vector can signficantly impact the location of the post-perilune apogee. By tuning these parameters, the geometry and availability of subsequent transfer segments may be significantly impacted.

7.4.2 Phasing and Energy Adjustment Segment

Following the post-deployment encounter with the Moon, one option for the Lunar IceCube trajectory design is leveraging the gravity of the Sun prior to approaching and capturing into the lunar science orbit. While this longest trajectory segment remains within the Earth vicinity, natural dynamical structures within the Sun-Earth system can be actively selected to modify both the energy and phasing of the spacecraft in its orbit. To reduce the number of deterministic thrusting arcs required along this portion of the Lunar IceCube mission trajectory, predominantly natural motions are sought. Accordingly, Poincaré mapping techniques are employed to explore the geometry of the natural flow corresponding to trajectories that persist within the Earth vicinity. These maps are constructed in the CR3BP, a model which offers a reasonable approximation to the dynamics in the true Sun-Earth system. Furthermore, these maps support a prediction of the geometry of the transfers that are constructed in this simplified dynamical model, as well as the corresponding regions of existence for transfers that link to a lunar capture arc.

To simplify the visualization of a large array of trajectories at a single energy level in the CR3BP, planar apoapsis maps are employed. Construction of these maps within the Sun-Earth CR3BP is demonstrated for a sample fixed value of the Jacobi constant, $C = 3.0008813$. At this value of the Jacobi constant, both the L_1 and L_2 gateways are slightly open and only a small number of trajectories depart the Earth vicinity, enabling a clear demonstration of the analysis employed in this investigation. First, feasible initial conditions in the Earth vicinity are seeded in the rotating frame using nondimensional configuration space coordinates that lie within the zero velocity curves, and between the L_1 and L_2 gateways. These feasible initial conditions are also represented as an apoapsis with respect to the Earth. For a state to be considered an apoapsis with respect to the Earth in the Sun-Earth rotating frame, it must possess a relative position vector $\bar{r} = [x - 1 + \mu, y, z]$, that is instantaneously perpendicular to the relative velocity vector, $\bar{v} = [\dot{x}, \dot{y}, \dot{z}]$, such that $\bar{r} \cdot \bar{v} = 0$. Furthermore, recall

from Eq. (3.34) that the radial acceleration at an apoapsis must be negative. For this investigation, only planar motion is considered when creating apoapsis maps in the CR3BP. Although feasible trajectories within the true ephemeris model exist in three dimensional space, the spatial component of motion along each sample transfer is small. Accordingly, planar motion in the CR3BP offers a valuable preliminary approximation with the added benefit of straightforward visualization. The direction of each apoapsis is selected uniformly across the entire map as either prograde with respect to the Earth or retrograde, i.e., counter-clockwise or clockwise, respectively. Thus, for various combinations of the planar position components, the direction of the velocity is determined via orthogonality. For a specified value of the Jacobi constant, the unit vector along the velocity direction is then scaled using the velocity magnitude, computed as $v = \sqrt{2U^* - C}$. Each initial apoapsis, seeded within the vicinity of the Earth, is then propagated forward for a specified number of revolutions about the Earth, from the perspective of the rotating frame, until the next apoapsis. Initial conditions that produce trajectories that either impact the Earth or pass through the L_1 or L_2 gateways are discarded. The remaining initial conditions are plotted in configuration space, producing a composite representation of the initial apoapses of trajectories that remain within the Earth vicinity, as predicted by the Sun-Earth CR3BP. As an example, two apoapsis maps are displayed in Figure 7.11 for the Jacobi constant value $C = 3.0008813$, representing trajectories that complete one revolution about the Earth without departing through the L_1 or L_2 gateways or impacting the Earth. In Figure 7.11(a), each initial apoapsis is prograde, while Figure 7.11(b) displays only retrograde apoapses. For convenience, these maps are represented in dimensional Earth-centered rotating coordinates. Gray shaded portions in each figure indicate forbidden regions, bound by the ZVCs, where motion cannot extend within the phase space of the CR3BP for the specified value of the Jacobi constant. Blue points locate apoapses that produce trajectories that remain within the Earth vicinity for one revolution and do not impact Earth. White regions, however, result in trajectories that do not fulfill these criteria. Furthermore, red di-

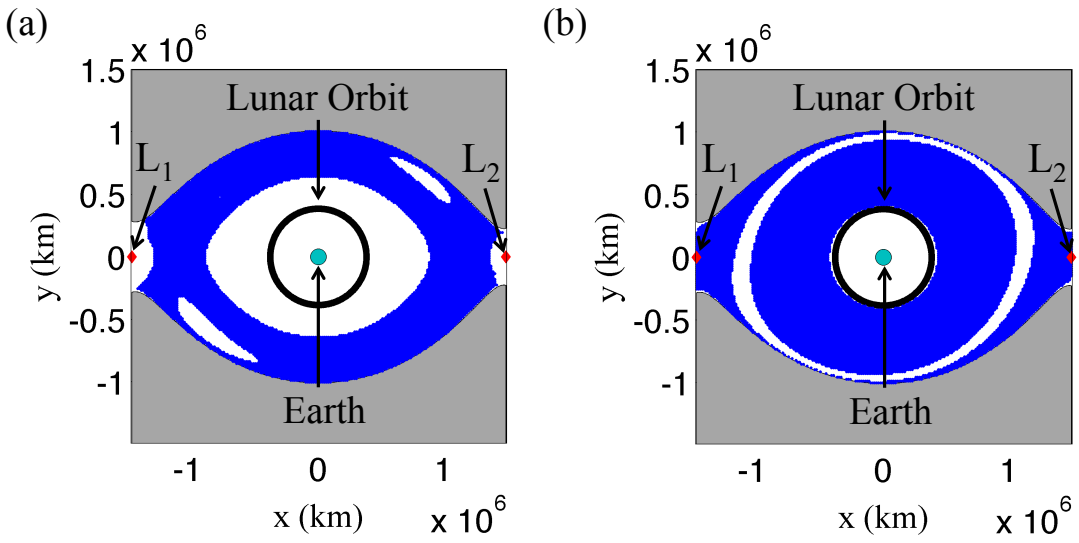

Fig. 7.11. Apoapsis maps in the planar Sun-Earth CR3BP for trajectories that encircle the Earth once at $C = 3.0008813$ for (a) prograde and (b) retrograde initial conditions.

amonds locate the equilibrium points, while a light blue circle indicates the location of the Earth and the black circle represents a circular approximation to the orbit of the Moon. These apoapsis maps supply an approximate, yet rapid, representation of natural motions that may be incorporated into a trajectory design strategy.

When supported by concepts from dynamical systems theory, apoapsis maps supply insight into some preliminary bounds on the feasible regions of motion near the Earth. For instance, consider the prograde apoapsis map in Figure 7.11(a). This map is repeated in 7.12(a) with additional information overlaid. In particular, the L_1 and L_2 planar Lyapunov orbits are overlaid in black, as well as a single stable manifold trajectory for illustration. The red curve represents the collection of the first apogees that occur along the L_1 Lyapunov stable manifold when integrated backwards in time. Similarly, the magenta curve indicates the first apogees that occur along the L_2 Lyapunov stable manifold. By overlaying these dynamical structures, comprised of solely prograde states, on an apogee map, the presence of the white regions is ex-

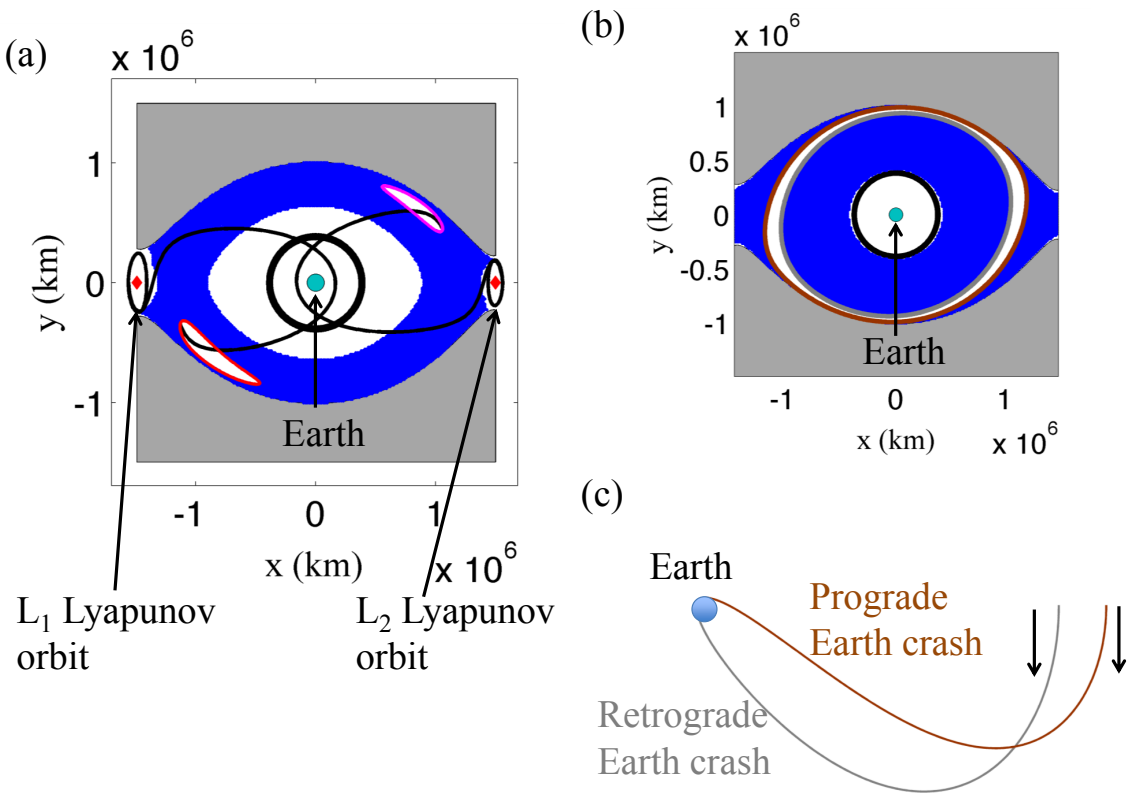

Fig. 7.12. Apoapsis maps in the planar Sun-Earth CR3BP for trajectories that encircle the Earth once at $C = 3.0008813$ for: (a) prograde initial conditions with apoapses corresponding to the manifolds of the L_1 and L_2 Lyapunov orbits overlaid; and (b) retrograde initial conditions with additional curves indicating trajectories that crash into the Earth, such as those depicted in (c).

plained. For instance, consider the white region in the lower left quadrant, contained within the L_1 Lyapunov stable manifold, depicted via the red curve. Specifically, each apoapsis within this white region quickly departs the Earth vicinity through the L_1 gateway. Similarly, the white region in the top right quadrant of Figure 7.12(a) is enclosed by the first apogees along the L_2 Lyapunov stable manifold at this value of Jacobi constant. For motion in the CR3BP to remain within the Earth vicinity, these two white regions should be avoided, creating approximate bounds on the motion during this segment along the transfer. Using Figure 7.12(b) as a reference, the set

of retrograde apoapses that produce feasible trajectories at the selected value of the Jacobi constant are separated by a thick white band. In fact, apoapses within this white region produce trajectories that resemble conics that quickly impact the Earth. Specifically, a gray curve indicates trajectories, propagated in the Sun-Earth CR3BP, that pierce the surface of the Earth with a state that is instantaneously retrograde as viewed in the Sun-Earth rotating frame. A sample trajectory that exhibits this behavior is plotted in gray in Figure 7.12(c). In addition, the brown curve in Figure 7.12(b) locates trajectories that pierce the surface of the Earth in a direction that is instantaneously prograde, with a sample path depicted in Figure 7.12(c). As the model fidelity is improved, these preliminary bounds shift and change size within the phase space. However, knowledge of these regions corresponding to dynamical structures supplies preliminary insight into the sensitivity of any nearby trajectories and facilitates explanation of the available transfer geometries, while also guiding the search for feasible transfer segments.

Regions in the apogee maps that correspond to transfers, predicted by the Sun-Earth CR3BP, but remaining in the Earth vicinity can be differentiated by their geometries. To demonstrate the identification of feasible transfer regions and their associated geometries, consider an apoapsis map constructed using prograde initial conditions at $C = 3.00088$ for trajectories that complete two revolutions around the Earth, as depicted in Figure 7.13. Recall that gray shaded portions of the figure indicate forbidden regions, while red diamonds locate the equilibrium points; the light blue circle at the center indicates the location of the Earth and the black curve depicts the lunar orbit, approximated as circular. On this apogee map, apoapses for each feasible transfer region are colored by the geometry of the subsequent transfer path, where the geometries are characterized by the velocity direction at each apoapsis in the rotating frame, i.e., prograde or retrograde. Specifically, blue regions in Figure 7.13 indicate transfers that possess only apoapses that are prograde, such as the transfer displayed in the bottom left inset. The feasible transfer regions colored green, however, correspond to trajectories that possess one retrograde apoapsis, as

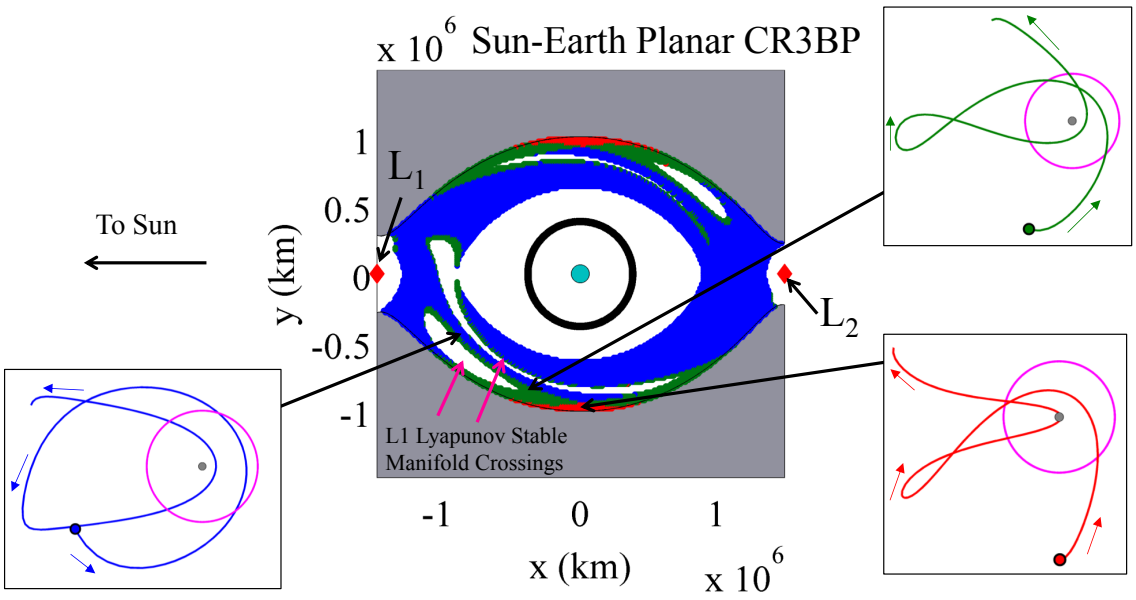

Fig. 7.13. Apoapsis map in the planar Sun-Earth CR3BP for trajectories that encircle the Earth twice at $C = 3.00088$ for prograde initial conditions, colored by the geometry of the transfer as viewed in the rotating frame. Sample trajectories are displayed in the inset images.

displayed in the top right inset of Figure 7.13. Note that these green feasible transfer regions appear to hug the white regions corresponding to the apoapses along the L_1 and L_2 Lyapunov stable manifolds, indicating that these transfers leverage the nearby natural dynamical structures. Finally, red-colored feasible transfer regions represent trajectories where the second and final apoapses are both retrograde as depicted in the bottom right inset of Figure 7.13. This feasible transfer region lies close to the zero velocity curves of the CR3BP and may exhibit significant sensitivity to uncertainty in the speed at apogee. This insight into the transfer geometry is useful when exploring the feasible transfer design space.

To identify an arc with the potential to link the phasing and energy adjustment segment to the Earth outbound and lunar approach segments, insight into the location and direction of the final state along a particular arc is useful. This information is straightforwardly visualized by introducing an alternative color scheme to the apoap-

sis map representation. Recall that each initial condition on an apoapsis map, when integrated forward in time, corresponds to a path that remains within the Earth vicinity for the specified number of revolutions without departing through the L_1 or L_2 gateways or crashing into the Earth. However, the apogee locations relative to the Earth, as viewed in the Sun-Earth rotating frame, may vary significantly. To select a path for this transfer segment and construct a good initial guess for an end-to-end trajectory that links all segments, the position of the final state along this path is of particular interest. This information is visualized via an alternative coloring scheme for each initial apse in an apoapsis map, correlating it with the angle of the final apoapse in the rotating frame relative to the Earth-L_2 line. A legend for this color scheme appears in Figure 7.14, with the Earth located at the center as a blue-filled circle. To mitigate the effect of complicating the map visualization, the colors in this scheme vary every 30 degrees, indicating whether the final apse along a trajectory arc lies in the center of a quadrant, or close to a neighboring quadrant. For instance initial conditions on an apoapsis map are colored teal, blue or dark blue if the final apse along the trajectory, propagated only for a specified number of revolutions around the Earth, possesses a state in the Sun-Earth rotating frame with $x - 1 + \mu < 0$ and

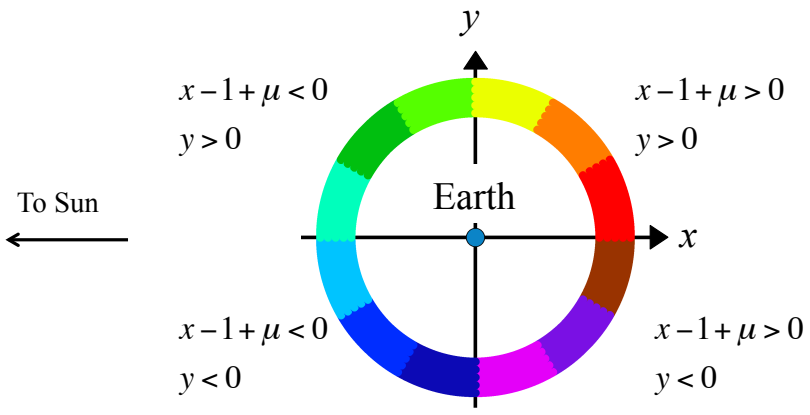

Fig. 7.14. Color scheme used in the mapping strategy, indicating the angular location of the final apogee relative to the Sun-L_2 line.

$y < 0$, i.e., it falls within the bottom left quadrant of the Earth-centered view. While this color scheme for the initial conditions on an apogee map does not capture the exact location of the final apses along the associated trajectories, it does enable rapid and straightforward evaluation of candidate transfers to identify those to be analyzed in further detail. This limitation is acceptable since the state corresponding to the final apoapsis shifts as the model fidelity is increased. To demonstrate the application of this color scheme to the planar apogee maps in the CR3BP, consider the map representations of prograde initial apogees with $C = 3.0008813$ and corresponding to trajectories that complete two revolutions around the Earth as depicted in Figure 7.15. Recall that gray portions indicate the forbidden regions, while red diamonds locate the libration points, a blue-filled circle locates the Earth and a black circle represents an approximate lunar orbit. Each initial condition in this figure is colored by the angular location of the final apse along the trajectory, which completes two revolutions around the Earth. The legend for this color scheme is repeated at the bottom of Figure 7.15. Sample trajectories, colored to match the regions in which their final apses lie, are displayed in the inset figures. From this figure, it is evident that, for the sample value of the Jacobi constant, a variety of transfer geometries exist for initial apogees that are prograde. These colored structures form elongated regions that mimic the curved nature of the L_1 and L_2 Lyapunov manifold crossings. Using this figure as a guide, a given transfer geometry may only deliver the spacecraft to a limited region of the configuration space, potentially impacting the existence and sensitivity of connections to a specific lunar approach segment. For instance, consider deployment conditions that produce trajectories with an apogee close to the ZVCs in the bottom left quadrant of the map in Figure 7.15. In this green-colored region, the initial apses correspond to arcs that encircle the Earth twice and possess a final apse in the top left quadrant of the map, similar to the green trajectory in the bottom left inset image. Initial apses for the subsequent lunar approach segment would need to fall within the top left quadrant of the apogee map at a given epoch to construct a good initial guess for an end-to-end trajectory. Less variability in the

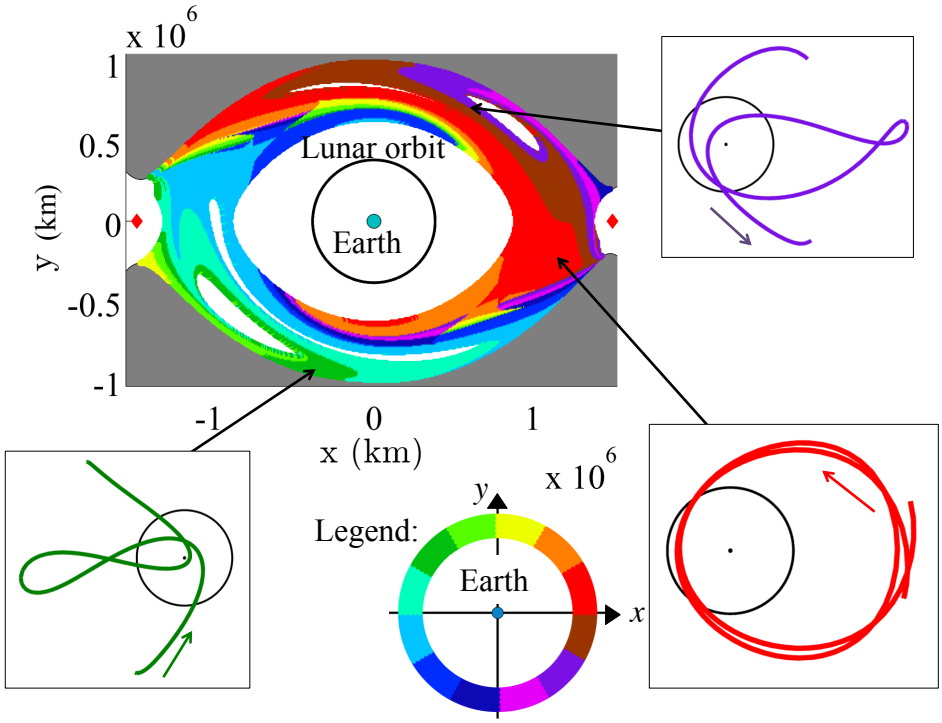

Fig. 7.15. Apoapsis map in the planar Sun-Earth CR3BP for trajectories that encircle the Earth twice at $C = 3.0008813$ for prograde initial conditions, colored by the angular location of the final apoapsis as indicated in the legend. Sample trajectories are displayed in the inset images.

colored structures is observed when applying the final apse location color scheme to the apogee map for retrograde initial conditions that encircle the Earth twice; this map is featured in Figure 7.16. Interior to the large white region corresponding to trajectories that crash into the Earth at either the first or second perigee, the apogees resemble a colorwheel. In fact, using the purple sample trajectory in the top right inset image as a guide, the final apse along the trajectory occurs nearly 90 degrees behind the initial apogee and exhibits a relatively straightforward geometry. Outside of the region corresponding to trajectories that crash into the Earth at either the first or second perigee, the feasible transfer regions are small and lie close to the ZVCs. Due to the consistency of the colored structures across the map, there may be little flexibility in selecting transfers that link the Earth outbound segment to a given lu-

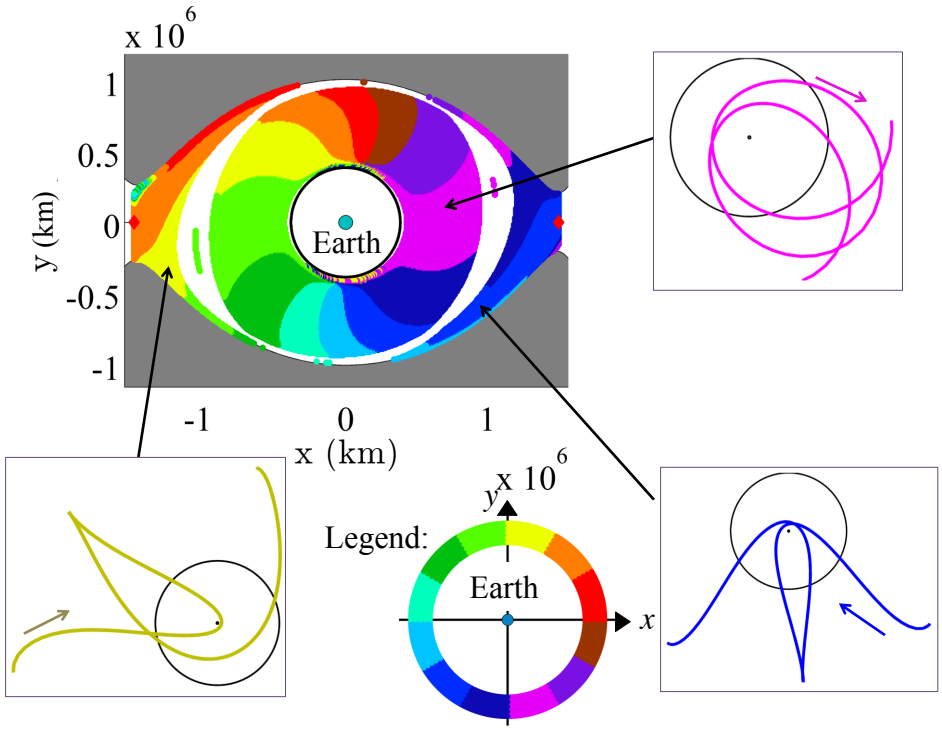

Fig. 7.16. Apoapsis map in the planar Sun-Earth CR3BP for trajectories that encircle the Earth twice at $C = 3.0008813$ for retrograde initial conditions, colored by the angular location of the final apoapsis as indicated in the legend. Sample trajectories are displayed in the inset images.

nar approach arc. The insight obtained through this application of Poincaré mapping strategies may guide the numerical targeting of outgoing lunar flyby conditions that subsequently deliver the Lunar IceCube spacecraft on a natural transfer that requires little propulsive effort. In a chaotic and nonlinear system, this capability to visualize and rapidly identify natural candidate arcs in a simplified, yet representative, dynamical model enables a well-informed process for constructing an initial guess for a trajectory that delivers the spacecraft from a highly energetic deployment state near the Earth to the vicinity of the Moon.

7.4.3 Lunar Capture Segment

To locate arcs that approach the Moon and eventually result in captured motion, techniques from manifold computations are leveraged [12]. Recall that the Lunar IceCube spacecraft is required to conduct observations from a low lunar orbit that is both elliptical and highly inclined. One strategy for reaching this orbit from a state that is located well beyond the lunar radius is to design a trajectory that passes through the L_2 gateway with a Jacobi constant that is only slightly below the value corresponding to the L_2 libration point, i.e., $C(L_2)$. Then, the low-thrust engine is activated in a direction close to the anti-velocity vector, effectively reducing the spacecraft velocity. Simultaneously, the Jacobi constant increases, with the L_2 and, then, L_1 gateways closing, effectively bounding the motion of the spacecraft to the vicinity of the Moon and producing captured motion. By modifying the thrust direction over a long time interval, the final science orbit is accessed. A significant challenge in designing a trajectory to deliver the spacecraft from a highly energetic deployment state to the final science orbit via this strategy is locating a trajectory that passes through the L_2 gateway. Since the Sun-Earth-Moon system is inherently nonlinear and chaotic, an uninformed search for trajectories that achieve this goal may be cumbersome, tedious and unsuccessful. However, techniques from manifold computation approaches are useful: a desired lunar orbit is discretized and each fixed point is integrated backwards in time, in a point mass ephemeris model, with the thrust vector directed in the anti-velocity direction [12]. Arcs that pass through the L_2 gateway are further integrated until apogee, and stored. These apoapsis states are then compared to the Sun-Earth transfer segment to construct a feasible guess for a complete trajectory. In this investigation, the focus for this segment is addressing one of the most significant hurdles in trajectory design for the Lunar IceCube spacecraft: identifying trajectories that deliver the spacecraft to the lunar vicinity with a Jacobi constant value above that of L_1 and L_2. To achieve this goal, it is sufficient to leverage an intermediate high altitude lunar orbit, rather than the required lunar science

orbit. Higher order gravitational models, which significantly influence motion close to the bodies, can be then be employed in future analyses to exactly target motion that subsequently reaches the low lunar orbit.

States along a high altitude lunar orbit are discretized and integrated backwards in time with the thrust vector aligned in the anti-velocity direction to identify trajectories that are eventually captured within the lunar vicinity. The intermediate orbit, with a Jacobi constant above that of L_1 and L_2, is described by a semi-major axis of 10,000 km, an arbitrarily selected eccentricity of 0.0, and a predefined final epoch. Since the final science orbit for Lunar IceCube is highly inclined, the inclination for this intermediate orbit is selected to be equal to 75 degrees. The right ascension of this orbit is sampled within the range $\Omega = [0, 360)$. Of course, these exact orbital elements may be varied to expand the set of identified trajectories that reach the lunar vicinity. However, this sample orbit supplies a good initial guess for arcs that pass through the L_2 gateway and maintain thrust in the anti-velocity direction while encircling the Moon until the ZVCs close at L_1 and L_2, guiding the corrections algorithm to compute a trajectory with similar characteristics. Nevertheless, states with true anomalies in the range $\theta^* = [0, 360)$, are sampled along this orbit and integrated backwards in time, in a point mass ephemeris model, and are only stored if they pass through the L_2 gateway and encounter an apogee beyond the lunar radius within a reasonable time frame. To further expand the set of apogees that result in lunar capture, the low-thrust engine remains activated for a time, T_{burn}, after passing through the L_2 gateway backwards in time. Then, the spacecraft coasts until apogee. To limit the amount of propellant expended prior to lunar capture, an upper bound is added on the additional burn time, T_{burn}; a reasonable value is selected as 20 days. In addition, a final spacecraft mass at arrival to the intermediate orbit must be set. Since this quantity is not known a priori, it is estimated iteratively using the average thrust time for the spacecraft to depart the L_2 gateway. This process is demonstrated for the selected intermediate orbit and a final epoch equal to 28390.5 in modified Julian date, with values for Ω and θ^* varied in increments of 30 degrees, and values for

T_{burn} between 0 and 20 days, in increments of 2 days. The final spacecraft mass is estimated to be equal to 13.7 kg. Trajectories that experience an apogee within 100 days of passing through the L_2 gateway are stored and plotted in Figure 7.17(a) in the Sun-Earth rotating frame. In this figure, green indicates thrusting segments while blue curves identify natural coasting arcs. Then, the recorded apogee for each of the stored trajectories is indicated by a circle colored by the epoch in terms of modified Julian date. These trajectories exhibit a variety of characteristics and possess apogees that occur in various regions of the phase space. To aid visualization and comparison to the phasing and energy adjustment segment, these apogees are also depicted on an apoapsis map in Figure 7.17(b). Each apogee, represented by a planar projection of the configuration space variables in the Sun-Earth rotating frame, is colored by its corresponding epoch to identify lunar approach arcs that begin at a similar time to the final state of the previous segment. From this set of apogees, paths that deliver

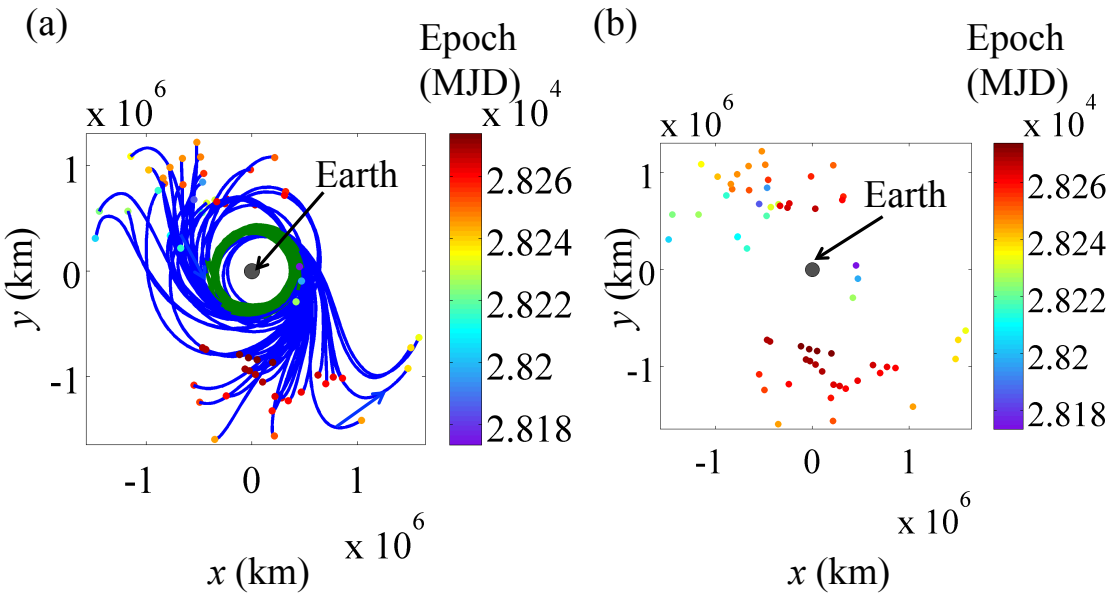

Fig. 7.17. (a) Trajectories that deliver the spacecraft to the lunar vicinity as viewed in configuration space in the Sun-Earth rotating frame and (b) representations of these paths on an apoapsis map colored by the apogee epoch.

the spacecraft to the lunar vicinity are straightforwardly identified and incorporated into the construction of an initial guess for a complete trajectory.

7.4.4 Sample Trajectory Construction

Arcs comprising each segment of the transfer sequence are selected using apoapsis maps to construct an initial guess for a path that delivers the spacecraft from an initial deployment state to the lunar vicinity and is then corrected in a low-thrust-enabled point mass ephemeris model. This process is demonstrated for a single transfer using a deployment state, current as of August 2015 and corresponding to a deployment epoch given as December 15th, 2017. As the deployment state and epoch continues to evolve throughout the EM-1 mission planning phase, the transfer sequence and map definition may require updates; however, the general framework, constructed and demonstrated in this investigation, remains useful.

An Earth outbound transfer arc influences the potential geometries for feasible transfers in the phasing and energy adjustment segment. For this example, a single sequence of coasting and thrusting arcs is selected from Figure 7.10. Consider the trajectory plotted as a planar projection in Sun-Earth rotating coordinates in Figure 7.18. Recall that blue arcs identify natural motion while green arcs indicate that the 0.8 mN low-thrust engine is activated and a black circle approximates the lunar orbit. This trajectory consists of the following sequence of arcs: 8.5 hours of natural motion immediately after deployment, a low-thrust arc with the thrust vector aligned in the anti-velocity direction for 3.8 days, a 2.5 hour coast arc until lunar periapsis, a 0.5 day post-perilune coasting segment, followed by a low-thrust segment that is maintained until apogee. This final thrusting segment corresponds to a thrust vector aligned with the unit vector $\hat{u} = -0.20\hat{V} + -0.979796\hat{C}$. The final apogee along this transfer segment is prograde when viewed in the rotating frame, possessing a Jacobi constant of approximately $C = 3.00088013$ and an epoch time corresponding to 28126.17 MJD. Furthermore, at the end of this segment, the spacecraft mass is

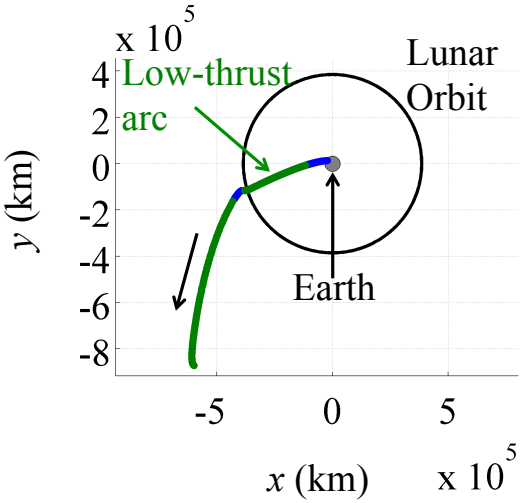

Fig. 7.18. Planar projection of the selected outbound segment in Earth-centered rotating coordinates in the Sun-Earth frame.

equal to 13.93 kg. Each of these characteristics significantly impact the construction of the remainder of the trajectory.

To identify a feasible path for the energy and phasing adjustment segment, the Poincaré mapping strategy outlined in Section 7.4.2 is employed. For this example, consider transfer arcs that encircle the Earth once, essentially reducing the time of flight along this portion of the path. An apoapsis map is then constructed for this type of transfer at $C = 3.00088013$ with prograde initial conditions, matching the Jacobi constant value and the direction of motion at the apogee designating the end of the Earth outbound segment. The resulting map is displayed in Figure 7.19. Recall that initial apogees that produce planar trajectories encircling the Earth once without departing through the L_1 or L_2 gateways or crashing into the Earth are plotted on this map in Earth-centered rotating coordinates. Each initial condition is colored, according to the legend displayed on the right of the Figure 7.19, by the angle of the final apoapsis state along the trajectory relative to the Sun-L_2 line. In addition, a circular approximation to the lunar orbit is plotted in black and the Earth is located

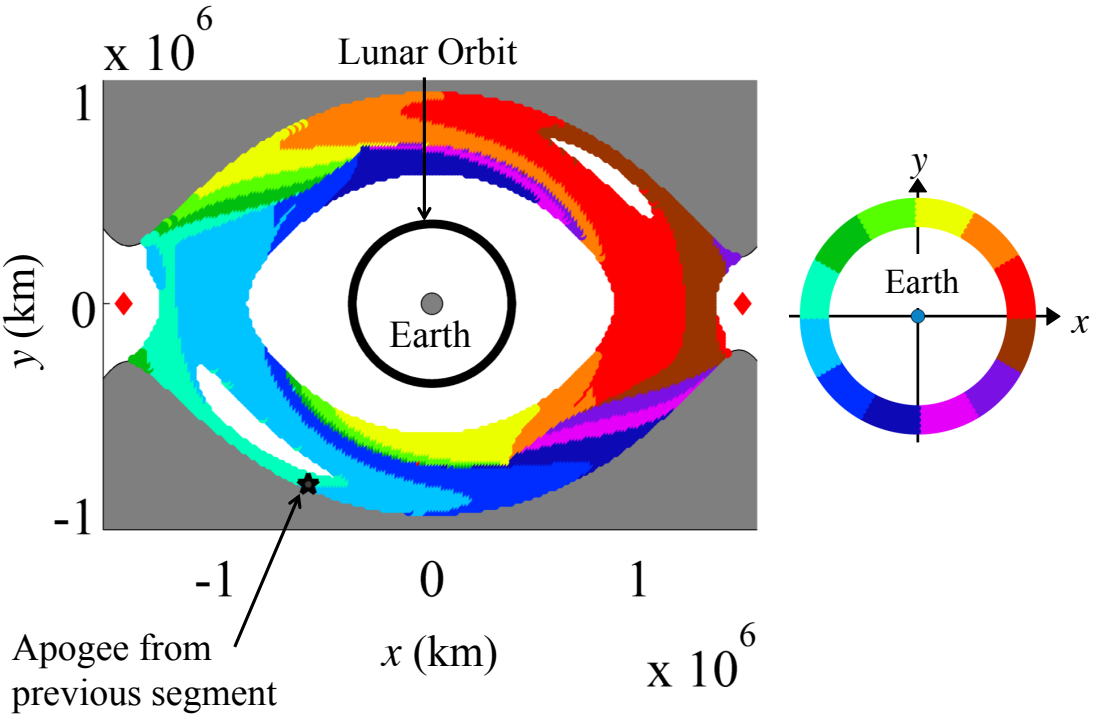

Fig. 7.19. Apoapsis map in the planar Sun-Earth CR3BP for trajectories that encircle the Earth once at $C = 3.00088013$ for prograde initial conditions, colored by the angular location of the final apoapsis as indicated in the legend. The final apogee along the Earth outbound segment is indicated by a gray star.

by a gray-filled circle; the equilibrium points are plotted as red diamonds. Then, forbidden regions are indicated by gray shaded regions. Overlaid on this apoapsis map is the location of the apogee state at the end of the Earth outbound segment, plotted as a gray star. Recall that the Earth outbound transfer arc is computed in a three-dimensional point mass ephemeris model, while the trajectories in this energy and phasing adjustment segment are propagated in a planar Sun-Earth CR3BP model. Thus, an exact match is not possible between the initial condition associated with the actual transfer arc in this segment and the end of the Earth outbound segment. However, the CR3BP does supply a reasonable approximation to the true dynamics in the Sun-Earth system and selecting an initial apogee that is as close as possible to

the final apogee along the previous segment should mitigate any necessity for a long thrusting arc to connect the two segments. Thus, this initial condition could lie in either a cyan or light blue region, both of which yield transfers that possess a final apogee close to the Sun-Earth line. In this example, the location of the final apoapsis along this transfer arc offers a rapid assessment of the approximate geometry for the transfer. This coloring scheme is also useful if the epoch at which the spacecraft must reach the final science orbit is constrained. An initial condition in the cyan region near the gray star is selected and propagated in the CR3BP to produce a planar trajectory that is plotted in the Sun-Earth rotating frame in Figure 7.20(a). This transfer, with a time of flight equal to 70 days, is then discretized into 10 subarcs, equally spaced in time. The state at the beginning of each arc, as computed in the CR3BP, is then propagated forward in the point mass ephemeris model of the Sun, Earth and Moon. In support of this simulation, an initial epoch, equal to the epoch at the end of the previous segment, 28126.17 MJD, is assumed. As an estimate, the final apogee at the end of this transfer arc is approximated as 70 days following the initial epoch, i.e.,

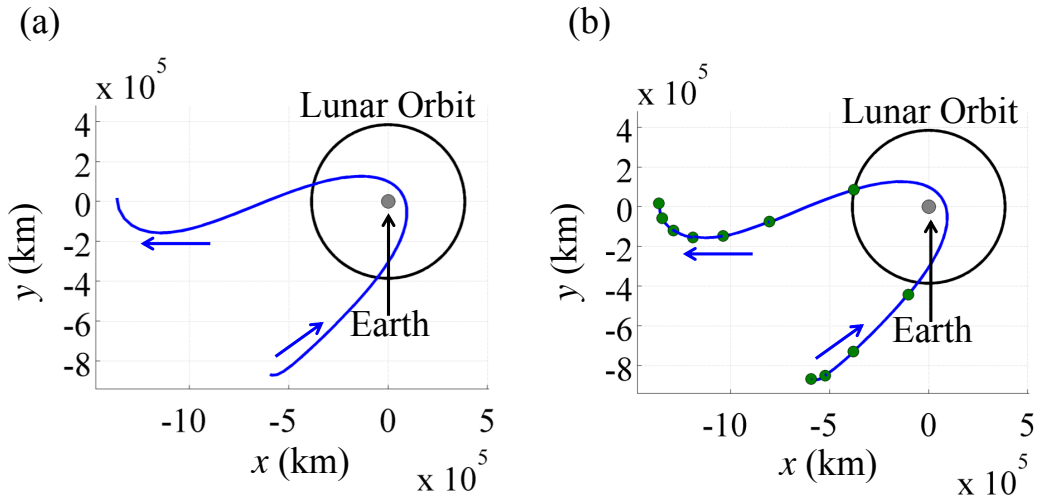

Fig. 7.20. Selected transfer arc for energy and phasing adjustment segment plotted in the Sun-Earth rotating frame: (a) propagated in the CR3BP and (b) discretized and integrated in the point mass ephemeris model.

28196.17 MJD. Note that, since only natural motion is leveraged along this segment, the spacecraft mass remains unchanged at the value of 13.93 kg. The resulting series of arcs is plotted in planar configuration space in Figure 7.20(b) with the nodes at the beginning of each segment located with green circles. Of course, each of these arcs is three-dimensional and no longer produces a single continuous path. However, these nodes serve as an initial guess for the Sun-Earth segment along the complete transfer, one that is later adjusted in a corrections algorithm.

A final transfer arc is then selected to deliver the spacecraft to the lunar vicinity. Recall that the transfer arc selected in the energy and phasing adjustment segment produces a final apogee that lies close to the L_1 side of the Sun-Earth line. Thus, lunar approach arcs that possess an initial apogee near the L_1 side of the Sun-Earth line with an epoch close to 28196.17 MJD are sought. Although a close match in energy between the beginning and end of neighboring segments is sought, the value of C is no longer constant in the ephemeris model, especially with the incorporation of an additional gravitational contribution. Thus, a prediction of the value of C at the end of the energy and phasing adjustment segment from the CR3BP may not be truly reflective of the actual value when corrected in an ephemeris model that also incorporates lunar gravity. Accordingly, the Jacobi constant is not currently employed as a filter for selecting the apogee that defines the lunar approach arc. Alternatively, the epoch, location and direction of motion are incorporated as selection parameters. To produce an apoapsis map for identifying a lunar approach arc, the process outlined in Section 7.4.3 is employed along with the specified intermediate orbit. The final epoch at this intermediate orbit is set equal to values within the range [28370.5, 28390.5] MJD, while the right ascension for the orbit and the true anomaly for discretization are sampled within the range [0, 360) in increments of 30 degrees. The resulting trajectories, in particular, those that pass through the L_2 gateway, are stored and plotted in Figure 7.21 in the Earth-centered Sun-Earth rotating coordinates. Each apogee is colored by the number of days past the desired epoch, i.e., the epoch at the end of the previous transfer segment and equal to 28196.17 MJD. Overlaid on

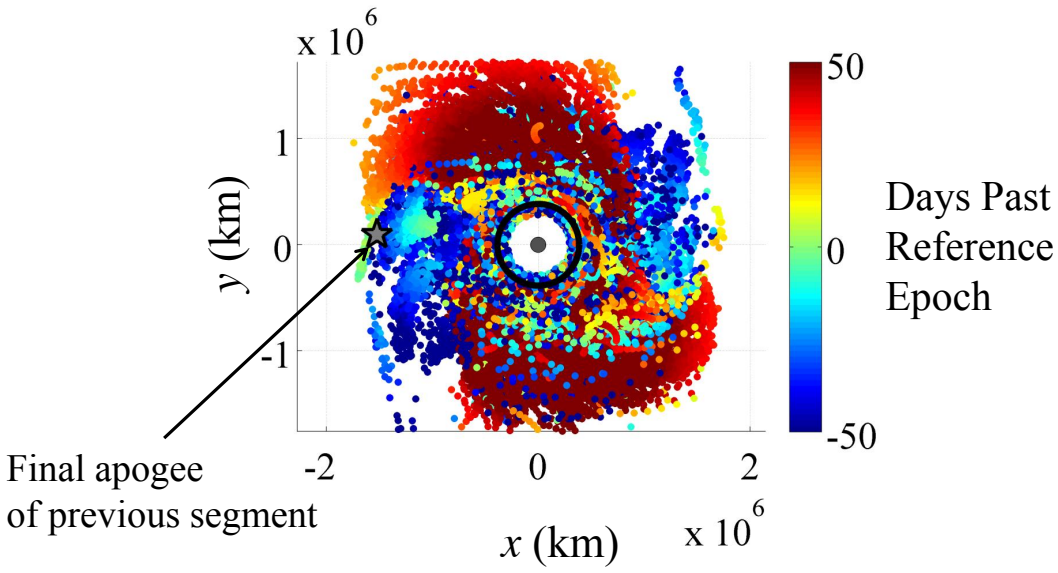

Fig. 7.21. Apoapsis map representing trajectories that approach the intermediate lunar orbit, projected into planar configuration space and colored by the epoch at each apogee.

this plot is a gray star which locates the final apogee of the previous arc. Since arcs selected from this map should possess an epoch similar to the reference epoch, an initial condition in a green region is sought. If no green regions are detected in the apoapsis map in the desired region, the final epoch should be iteratively modified and a new map constructed. Fortunately, in the current example, the final apogee along the previous segment lies near a green region. A lunar approach arc is selected in this vicinity, producing the trajectory plotted in Figure 7.22 in: (a) an Earth-centered view in the Sun-Earth rotating frame, (b) a planar zoomed-in view along the final portion of the transfer in the Moon-centered Earth-Moon rotating frame, and (c) a three-dimensional view of the final portion of the transfer in the Moon-centered Earth-Moon rotating frame. Along this trajectory, green indicates a low-thrust arc, while a blue line identifies a natural arc. Using this figure, the selected initial condition occurs at an epoch value equal to 28203.44 MJD with a spacecraft mass equal to 13.98 kg; this mass is approximately 0.05kg above the spacecraft mass at the end of

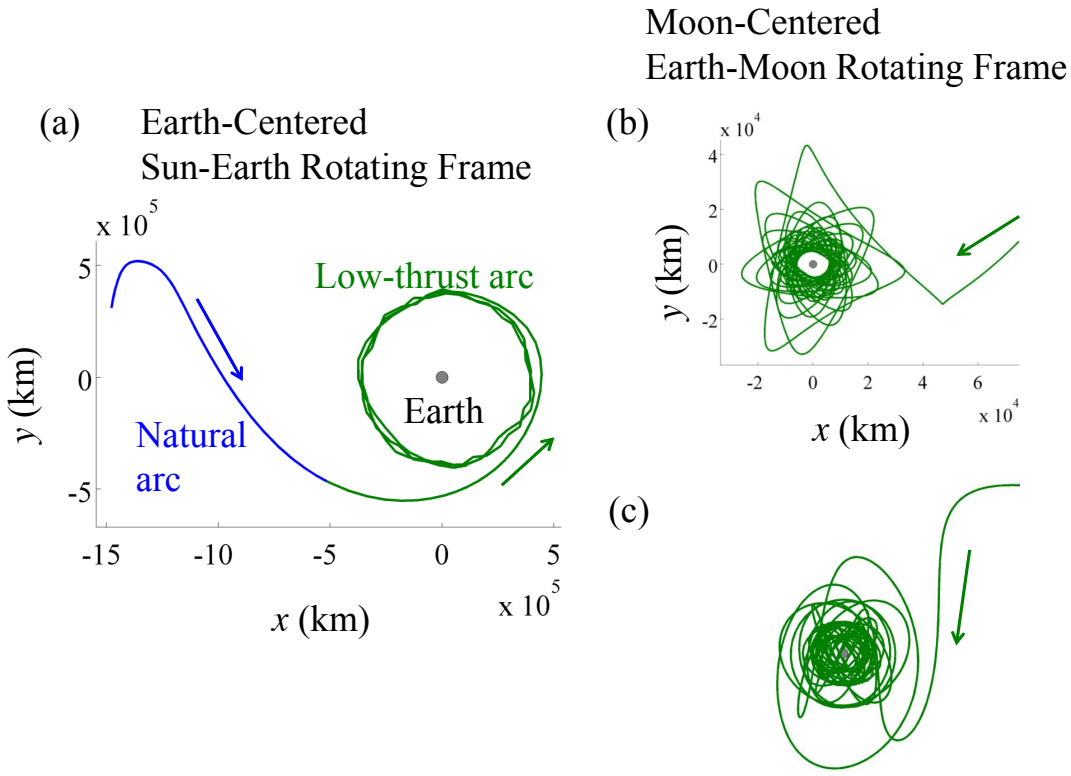

Fig. 7.22. Selected trajectory which approaches the lunar vicinity: (a) a view of the entire trajectory in an Earth-centered Sun-Earth rotating frame, (b) zoomed-in planar view of the final portion in a Moon-centered Earth-Moon rotating frame and (c) a three-dimensional view in the Earth-Moon rotating frame.

the previous transfer segment and the epoch is discontinuous by approximately one week. Of course, these parameters are adjusted during the iterations of a corrections algorithm. Since this step in the transfer design process is intended to identify a transfer that delivers the spacecraft to the lunar vicinity, the selected trajectory is clipped to only include a few revolutions of the Moon, rather than the entire lunar approach arc. In fact, these revolutions around the Moon serve to guide the corrector to a trajectory that reaches the lunar vicinity without the extra computational time associated with correcting a longer path. The exact trajectory to the final lunar science orbit, not the intermediate orbit employed here, can be identified in subsequent

analyses which incorporate higher fidelity models to also capture perturbations from lunar gravitational harmonics.

Each of the arcs selected via dynamical systems techniques enables the construction of an initial guess for a trajectory that is ultimately corrected in a low-thrust-enabled point mass ephemeris model. In particular, each of the three segments depicted in Figures 7.18, 7.20 and 7.22 are concatenated chronologically with short low thrust arcs between each segment, i.e., the Earth outbound segment is followed by a short low thrust arc to connect to the energy and phasing adjustment segment, and then an additional low thrust path is followed by the lunar approach arc. Recall that the corrections algorithm, outlined in Section 7.3, is formulated for simultaneous adjustment of a sequence of nodes described in terms of the body-centered position and velocity coordinates in a J2000 inertial frame, nondimensionalized by the characteristic quantities corresponding to the Sun-Earth or Earth-Moon system, as appropriate. Additional information that is recorded at each node includes the nondimensional time past a reference epoch, such as the deployment epoch, the integration time along the arc of interest as well as the spacecraft mass. For low-thrust-enabled arcs, the three components of the thrust direction unit vector are also stored as variables. To convert the initial guess in Figure 7.23 into a sequence of nodes, natural and low-thrust-enabled segments are first separated. Then, each segment is discretized by a user-defined number of nodes that are equally spaced in time. Three constant vectors are also defined with their elements recording the following quantities for each arc along the current solution: a binary description of whether the low-thrust engine is activated; for segments that leverage low-thrust, the body used as a basepoint for defining the VNC unit vectors; and the body used as a basepoint for the state information, which determines the two-body system used for nondimensionalization. Specifically, note that states that are defined relative to the Earth are nondimensionalized using characteristic quantities from the Sun-Earth system, while states expressed using the Moon as the basepoint are normalized using the Earth-Moon system parameters. For nodes that fall within either the Earth outbound segment

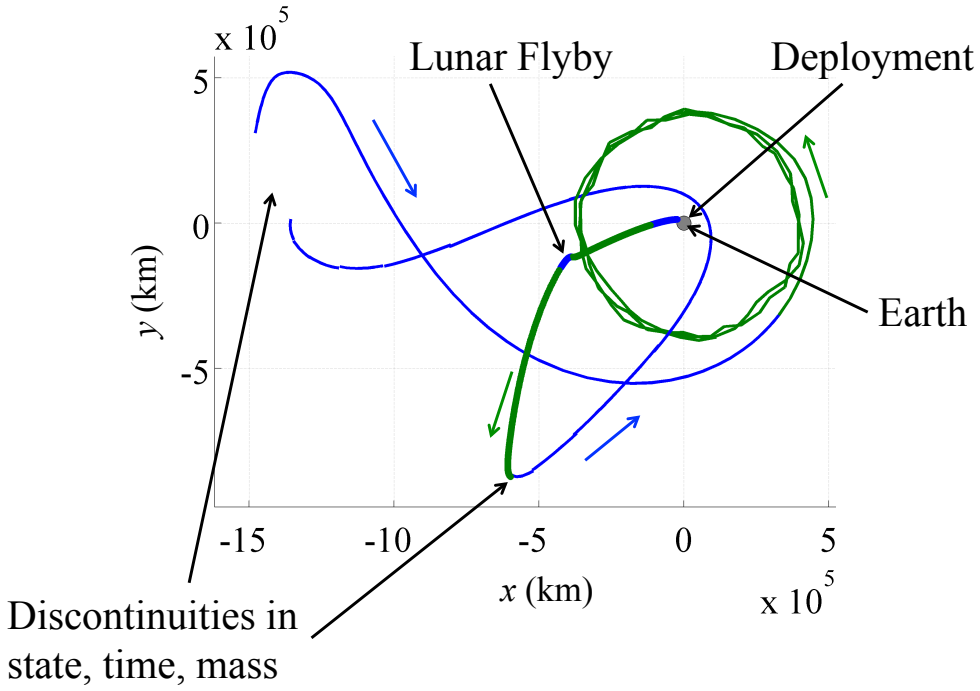

Fig. 7.23. Discontinuous initial guess for a complete trajectory, plotted in Earth-centered Sun-Earth rotating coordinates.

or the phasing and energy adjustment segment, the states are defined relative to the Earth, while nodes along the lunar approach arc are defined with respect to the Moon. These three constant vectors supply the corrections algorithm with information that is vital to integration and evaluating continuity across all arcs, as well as accurately incorporating the low-thrust engine when appropriate. This initial guess is displayed in Earth-centered Sun-Earth rotating coordinates in Figure 7.23. Recall that green arcs locate low-thrust-enabled segments while blue indicates natural motion. Although the free variables representing each state are formulated in the inertial frame when input to the corrections algorithm, the rotating view offers an intuitive representation for verification of the construction of the initial guess. Note that this initial guess exhibits significant discontinuities in the state, time and mass variables between the three phases of the trajectory. However, short low-thrust arcs are added

at these discontinuities to support the identification of a continuous path. Although selecting different arcs may reduce these discontinuities, this initial guess serves as an interesting example for demonstration purposes.

The initial guess that has been constructed is input into the corrections algorithm that leverages a low-thrust-enabled point mass ephemeris model, as outlined in Section 7.3. Since this complete trajectory is comprised of arcs that pass close to each of the primaries as well as those that exist beyond the lunar radius, numerical issues due to ill-conditioning may appear. To mitigate these problems, as well as to accommodate the visible discontinuities between each of the trajectory segments, the corrections process is introduced in steps. First, at each iteration of the corrections algorithm, if the absolute magnitude of the constraint vector is above a predefined threshold, a modified Newton's method is employed to update the free variable vector. Recall that the update equation for a Newton's method is formulated under the assumption that the current guess for a variable is close to the true solution. However, for an initial state that is not sufficiently close to a true solution for the constraint vector, the Newton strategy may diverge. Thus, an attenuation factor, γ, is introduced to the update equation for an underdetermined system such that, at each step, the free variable vector is iteratively modified as follows:

$$\bar{V}^{i+1} = \bar{V}^{i} - \gamma D\bar{F}(\bar{V}^{i})^{T}[D\bar{F}(\bar{V}^{i}) \cdot D\bar{F}(\bar{V}^{i})^{T}]^{-1}\bar{F}(\bar{V}^{i}) \tag{7.9}$$

for a free variable vector at the i-th iteration, $\bar{V}^{i}$, a constraint vector, $\bar{F}$, and a rectangular Jacobian matrix, $D\bar{F}$. Note that γ can be assigned any value between 0 and 1. Once the magnitude of the constraint vector falls below a threshold value, the update equation reverts to the traditional Newton's method, i.e., $\gamma = 1$. The exact value for both γ and the threshold on the constraint vector magnitude may be tuned by the user as the performance of the algorithm is evaluated. Furthermore, recall that for a sequence of nodes that are defined relative to two different basepoint bodies, i.e., the Earth and the Moon, a system-to-system continuity constraint in state, mass and time is enforced. For the sample initial guess in the current example, this constraint is applied at the boundary between the end of the phasing and energy

adjustment segment and the beginning of the lunar approach arc. Note that the final state along the last arc in the energy and phasing adjustment segment is expressed in terms of Earth-centered coordinates and is normalized by the characteristic quantities in the Sun-Earth system. The first state along the lunar approach arc, however, is expressed in terms of Moon-centered coordinates and is nondimensionalized using the characteristic quantities in the Earth-Moon system. To enforce continuity between these two states, the node at the beginning of the lunar approach arc is transformed into Earth-centered coordinates and renormalized by the characteristic quantities of the Sun-Earth system. Then, the system-to-system continuity constraint is enforced. Since the computation of these components of the system-to-system constraint involves a rotation as well as nondimensionalization by new characteristic quantities, the corresponding elements of the Jacobian matrix may be poorly scaled in comparison to the remaining elements, potentially creating numerical issues during inversion of the square matrix $D\bar{F}(\bar{V}^i) \cdot D\bar{F}(\bar{V}^i)^T$, which appears in the update equation. In contrast, the system-to-system constraint is scaled to increase the order of magnitude of the corresponding components of the Jacobian matrix. Alternative methods to eliminate any issues associated with ill-conditioning would serve as an interesting avenue of investigation in future analyses.

Corrections on the initial guess in Figure 7.23 enable the detection of a continuous trajectory in a low-thrust-enabled ephemeris model that follows the constructed itinerary and delivers the spacecraft from a highly energetic deployment state to the lunar vicinity. The constraints in the corrections algorithm are introduced gradually with updates performed until the trajectory is continuous to within a nondimensional tolerance on the constraint vector equal to 10^{-10}. Following the completion of this iterative process, a corrected trajectory is identified. This solution is displayed in Figure 7.24 in (a) Earth-centered Sun-Earth rotating coordinates, (b) a zoomed-in view of the lunar vicinity in Moon-centered Earth-Moon rotating coordinates and (c) Earth-centered J2000 inertial coordinates. Recall that green lines indicate low-thrust-enabled arcs while blue curves indicate natural motion. Comparison to the initial

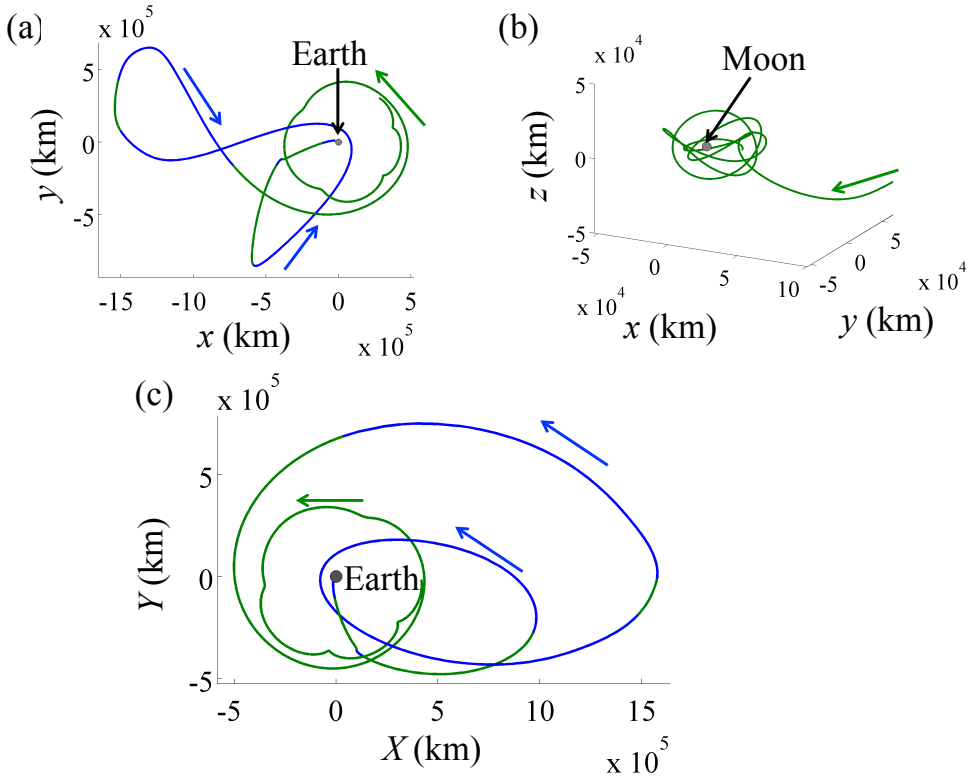

Fig. 7.24. Continuous sample trajectory (a) plotted in Earth-centered Sun-Earth rotating coordinates, (b) a zoomed-in view in Moon-centered Earth-Moon rotating coordinates and (c) Earth-centered J2000 inertial coordinates.

guess as constructed in Figure 7.23 reveals that the general geometry of the transfer is retained, demonstrating the value of leveraging natural dynamical structures within multi-body systems in the construction of a complex path for a low-thrust-enabled CubeSat. Although the final portion of the path has been significantly modified by the corrections algorithm, the goal of this investigation is certainly achieved: recovery of a path that delivers the spacecraft from a highly energetic deployment state to the lunar vicinity. Identification of a trajectory that eventually encircles the Moon, with a sufficiently high inclination and an energy at which the L_1 and L_2 gateways are closed, addresses the most significant challenges in the construction of an initial guess for a feasible end-to-end transfer. Future analysis in a higher-fidelity model

that more accurately reflects the lunar gravitational field can be leveraged to identify subsequent low-thrust-enabled arcs that reach the desired lunar science orbit. Additional corrections can then be employed to connect these two arcs. Nevertheless, this final portion along the path does capture into the vicinity of the Moon, as validated by the Jacobi constant computed in the Earth-Moon system. In fact, this quantity is plotted as a function of the epoch in Figure 7.25 for the lunar approach segment. The Jacobi constant values corresponding to L_1 and L_2 in the Earth-Moon system are overlaid on this plot. At the end of the continuous trajectory depicted in Figure 7.24(b), the Jacobi constant, as computed in the Earth-Moon system, is above $C(L_1)$, indicating that the ZVCs are closed at both the L_1 and L_2 gateways. Accordingly, the spacecraft is bound to the vicinity of the Moon. Although this transfer does not deliver the spacecraft to the final science orbit required by the Lunar IceCube mission, the final mass at the end of this trajectory is equal to 13.702 kg, corresponding to an expended propellant mass equal to 0.298 kg, which falls well below the current estimate for the available propellant mass of 1.5 kg. Thus, the remaining 1.202 kg can be employed to target the final lunar science orbit. Additional corrections and optimization processes may be applied to this solution to further increase the remaining propellant mass.

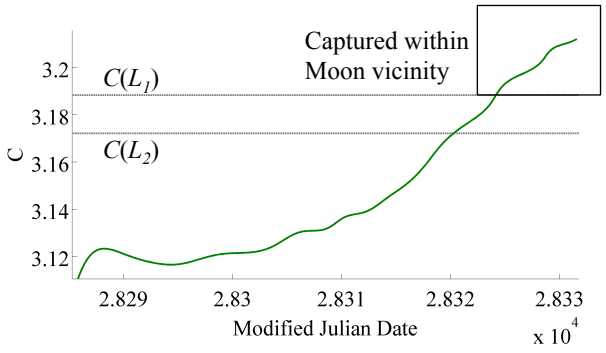

Fig. 7.25. Jacobi constant, as computed in the Earth-Moon system, for the lunar approach segment as a function of epoch in MJD form.

Transfers exhibiting various geometries and characteristics may be constructed using the trajectory design framework developed in this investigation, thereby enabling a well-informed exploration of the design space. To demonstrate such insight into the solution space, consider the same Earth outbound segment employed in the assembly of the initial guess in Figure 7.23. An alternative transfer option that connects to this boundary segment, but encircles the Earth twice, is designed used the process outlined within this chapter. To select an arc in the phasing and energy adjustment segment, an apoapsis map is constructed at a value of the Jacobi constant equal to $C = 3.00088013$ for prograde initial conditions. In contrast to the map in Figure 7.19, constructed at the same energy level, each initial condition is integrated until the spacecraft has encircled the Earth twice: the resulting map is plotted in Figure 7.26. Similar to the previous example, the final apogee of the Earth outbound seg-

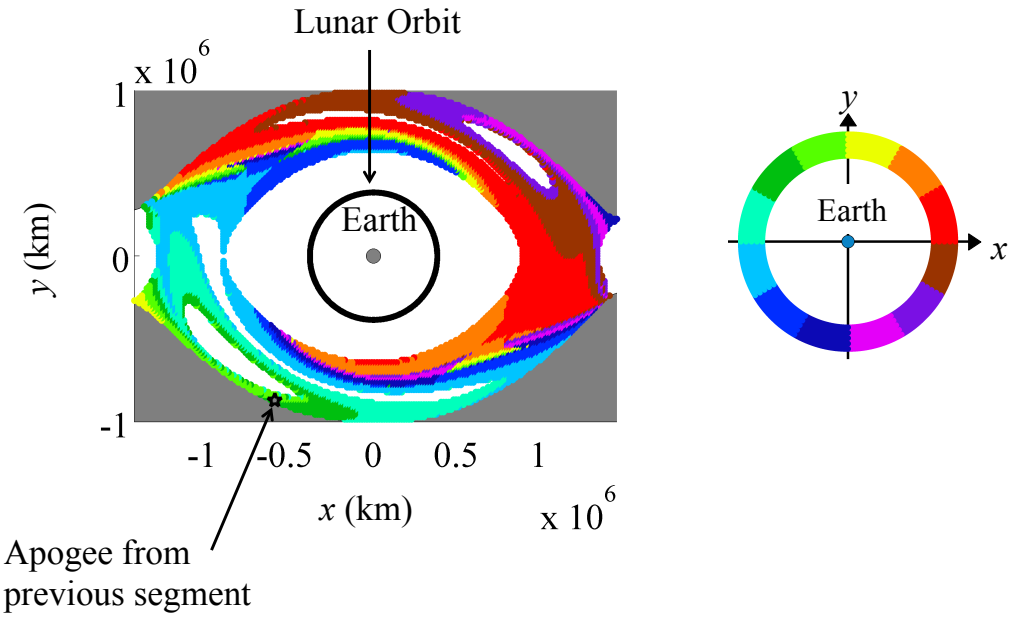

Fig. 7.26. Apoapsis map in the planar Sun-Earth CR3BP for trajectories that encircle the Earth twice at $C = 3.00088013$ for prograde initial conditions, colored by the angular location of the final apoapsis as indicated in the legend. The final apogee along the Earth outbound segment is indicated by a gray star.

ment, indicated via a gray star, lies within a large region of feasible transfers close to the ZVCs and the crossings of the L_1 Lyapunov stable manifold. Leveraging the color of the initial conditions near the gray star to supply insight into the geometry of the solutions within this region, it appears that trajectories that are initially prograde and encircle the Earth twice possess a final apogee that lies in the top left quadrant of the map. Of course, both the time of flight and exact location of the final apogee along the trajectories corresponding to initial conditions within this region may vary significantly. However, the existence of feasible arcs for the phasing and energy adjustment segment appears relatively robust to uncertainty in the location of the apogee from the previous segment and, potentially, small variations in the velocity. Such robustness in the existence of these arcs may be desirable given the uncertainty associated with the exact position and velocity of the CubeSat immediately after deployment. Nevertheless, using a path selected from the map in Figure 7.26 to possess an initial apogee close to the gray star and a time of flight of approximately 128 days, an initial guess for a complete trajectory is constructed. Following corrections, the resulting continuous trajectory is displayed in Figure 7.27,

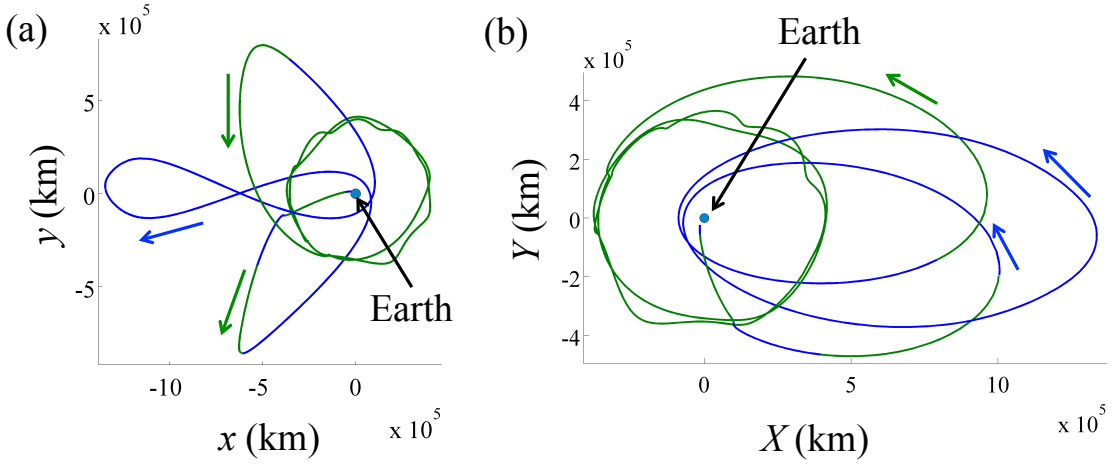

Fig. 7.27. Continuous sample trajectory that encircles the Earth twice (a) plotted in Earth-centered Sun-Earth rotating coordinates and (b) Earth-centered J2000 inertial coordinates.

with blue arcs corresponding to natural motion while green arcs indicate that the low-thrust engine is activated. Although this solution requires a longer time of flight than the trajectory plotted in Figure 7.24, it offers one of many alternative options for transfers within the chaotic dynamical environment of the Sun, Earth and Moon.

In addition to supplying the capability for rapid redesign, the developed framework enables a prediction of the robustness of alternative transfer options, supporting the exploration of a complex design space. In fact, consider an arc in the Earth outbound segment that possesses an apogee that is retrograde when viewed by an observer in the Sun-Earth rotating frame. An observer in the inertial frame, however, would observe the spacecraft traveling in a prograde direction at apogee. This trajectory is displayed in Figure 7.28 in Sun-Earth rotating coordinates, with a circular approximation to the lunar orbit indicated via a black circle. Such trajectory characteristics result from a reduction in the length of time that the low-thrust engine is activated between deployment and the lunar flyby, as well as a modification in the direction of the thrust vector during the post-flyby thrusting arc such that $\hat{u} = -0.60\hat{V} + 0.80\hat{C}$. The value

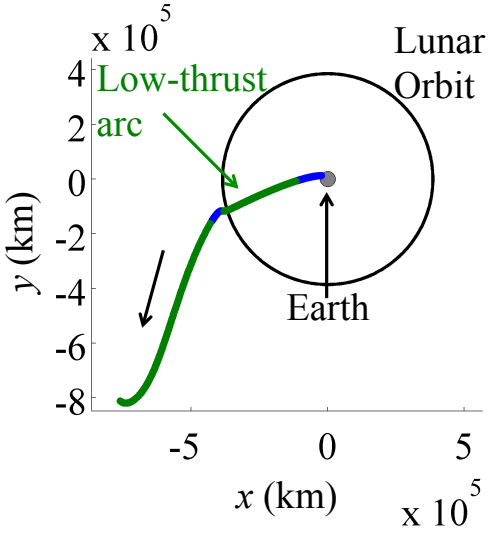

Fig. 7.28. Planar projection of the selected outbound segment, possessing a retrograde apogee as viewed from a Sun-Earth rotating frame.

of the Jacobi constant in the Sun-Earth system for this retrograde apogee is equal to $C = 3.000864$. Accordingly, an apoapsis map is constructed at this energy level for retrograde initial conditions that correspond to trajectories encircling the Earth once without departing through the L_1 or L_2 gateways or crashing into the Earth: this map is plotted in Figure 7.29. Analysis of this figure reveals that the location of the final apogee of the previous segment falls within a region that is bound by the ZVCs and a large white band that corresponds to trajectories that crash into the Earth. Initial conditions within this thin region are associated with trajectories that possess a perigee that is prograde for an observer in either the rotating and inertial frames, as displayed in the inset image. Insight into the size of the region of existence for a particular transfer geometry via the Sun-Earth CR3BP enables a prediction of the robustness of a transfer arc in the phasing and energy adjustment segment: a natural

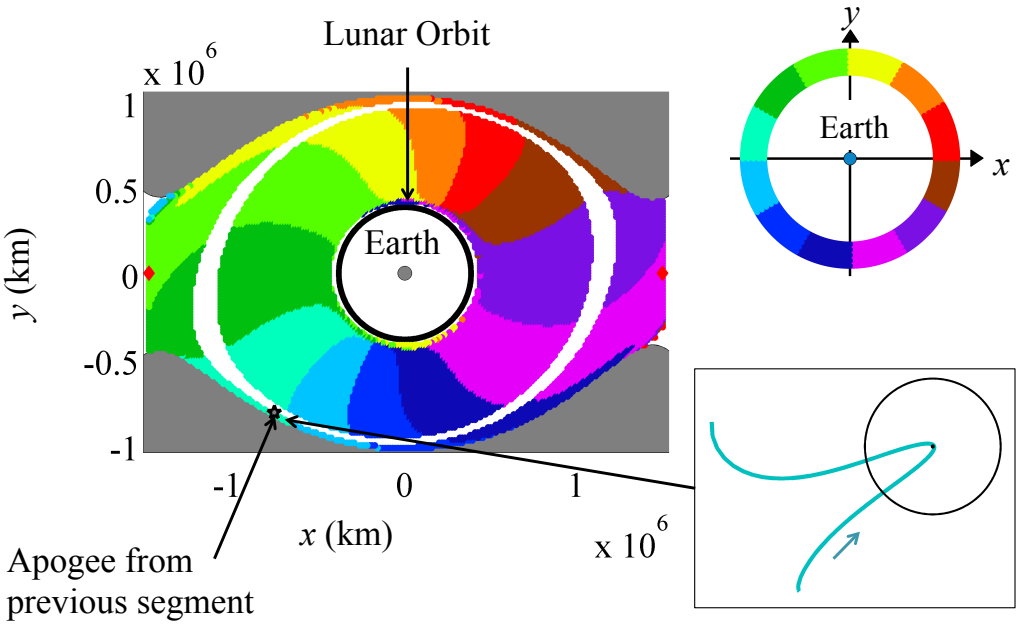

Fig. 7.29. Apoapsis map in the planar Sun-Earth CR3BP for trajectories that encircle the Earth once at $C = 3.000864$ for retrograde initial conditions, colored by the angular location of the final apoapsis as indicated in the legend. The final apogee along the Earth outbound segment is indicated by a gray star.

path with an apogee close to the gray star on the map in Figure 7.29, and encircles the Earth once, may produce a transfer that is sensitive to uncertainty in the state information at the post-flyby apogee. Given the limited capability associated with a 0.8 mN low-thrust propulsion system, a reference transfer with these characteristics, that does not pass too close to the Earth, would be challenging to target as the spacecraft and trajectory parameters evolve. Further exploration of the design space may reveal an alternative trajectory option that is more robust to uncertainty in the initial conditions.

7.5 Summary

The insight gained throughout this investigation demonstrates that a trajectory design framework, constructed using dynamical systems techniques, is valuable in designing a complex path for a spacecraft with limited propulsive capability within the chaotic gravitational environment of the Earth, Moon and Sun. In addition, the continuous solution constructed within this chapter serves as a suitable initial guess for corrections to a complete end-to-end trajectory in an operational-level modeling environment and, potentially, an optimization algorithm. Of course, the exact transfer sequence and map definition may require update as the deployment state frequently evolves throughout the development phase of the mission. However, the framework developed in this investigation remains useful for constructing trajectories for a small spacecraft that must be delivered from a high energy deployment state near the Earth to a low lunar orbit. In fact, the design framework enables rapid redesign of this trajectory as the deployment information or spacecraft hardware specifications evolve by mitigating the challenges associated with searching for a point solution in a chaotic dynamical regime, while also supporting the exploration of a large and complex design space.

8. CONCLUDING REMARKS

8.1 Summary

Identification and characterization of particular solutions that exist within a circular restricted three-body model enables a thorough and guided exploration of multi-body systems. Such analysis is supported by the application of numerical techniques that leverage dynamical systems theory, including: the computation of equilibrium points, periodic orbits, quasi-periodic motion, and manifolds; differential corrections; Poincaré mapping; stability analysis; and discrete variational mechanics. In fact, the utility of a dynamical systems approach is explored in this investigation in the context of both astrodynamics and celestial mechanics.

To explore the effect of a three-body interaction, inspired by nuclear physics, on the gravitational environment near a large mass ratio system, particular solutions are explored. Augmenting the pairwise gravitational potential in the CR3BP with a three-body interaction, scaled by a coefficient k, enables a preliminary analysis of any unique effects on the motion of a companion body orbiting near the binary system. As the strength and sign of this additional autonomous term is varied, a three-body interaction impacts the existence, location and stability of the fundamental equilibrium solutions that exist within a frame rotating with the two components of the primary. These equilibrium solutions are associated with stable and unstable manifold structures as well as periodic and quasi-periodic motion. Changes in the existence, location and stability of the equilibrium points affects it associated dynamical structures, which guide the flow throughout various regions of the phase space. Accordingly, the evolution and configuration of periodic orbits is also impacted. As observed in this investigation, unique effects of a three-body interaction are often attributed to the changes in the fundamental equilibrium solutions. Fur-

thermore, a repulsive three-body interaction results in a more significant impact on the dynamical environment than an attractive three-body interaction with the same magnitude scaling constant. A well-informed and guided exploration of an inherently chaotic multi-body system enables a thorough analysis of the effect of this additional autonomous force contribution.

Particular solutions that exist within a multi-body system enable the construction of a trajectory design framework for CubeSats with a limited propulsive capability and a constrained deployment state. With application to the upcoming Lunar IceCube mission, Poincaré mapping strategies are employed in a circular restricted model of the Sun-Earth system to locate natural solutions that connect a highly energetic deployment state to captured motion around the Moon. As demonstrated in this investigation, the developed trajectory design framework enables the construction of an initial guess that is corrected in a low-thrust enabled point mass ephemeris model. The continuous trajectory identified via this framework can be corrected later in the trajectory design process within an operational-level modeling environment and, potentially, optimized. This capability to rapidly design an intricate path enables redesign as the deployment information and spacecraft hardware parameters are updated throughout the development and operational phases of the mission, a common occurrence during small satellite missions. Furthermore, a dynamical systems approach supports future exploration of the complex trajectory design space that exists within the chaotic dynamical environment of the Earth, Moon and Sun.

8.2 Recommendations

Extending the analysis completed in this investigation may yield additional insight into the motion of a small companion body about a binary system, with a large mass ratio, under the influence of a three-body interaction. Recommendations for extending this investigation include:

- Incorporation of adaptive time-stepping strategies as developed by Moore to the discrete variational methodology for orbital computation, may reduce the required computational time and effort [34].

- Analysis of particular solutions that exist out of the plane of motion of the primaries would provide further information on the effect of an additional three-body interaction.

- Modification of the process leveraged in this investigation to accommodate a nonautonomous model where the eccentricity of the two primaries is nonzero would enable a higher fidelity analysis and an exploration of the conditions under which the current observations are valid.

In addition, further development of the trajectory design framework is valuable as the complexity of the mission objectives of CubeSats increases. Recommended extensions to the current analysis include the following items:

- Characterization of the behavior of the lunar approach arcs in a higher fidelity model may facilitate the development of targeting strategies once the spacecraft has passed through the lunar gateway.

- Weighting strategies for the constraints and free variables as well as an alternate formulation for the system-to-system constraint within the corrections process may facilitate improved convergence properties for an initial guess with significant discontinuities.

- When assembling the initial guess for the arcs within each of the trajectory segments, strategies for effective placement and definition of connecting low-thrust arcs may guide the corrections algorithm towards a continuous solution that remains as close to the initial guess as possible.

REFERENCES

REFERENCES

[1] Asteroid Impact Mission, Accessed June 2016: http://www.esa.int/Our_Activities/Space_Engineering_Technology/Asteroid_Impact_Mission/Asteroid_Impact_Mission2

[2] J.L. Margot, M.C. Nolan, L.A.M. Benner, S.J. Ostro, R.F. Jurgens, J.D. Giorgini, M.A. Slade, and D.B. Campbell, "Binary Asteroids in the Near-Earth Object Population," *Science*, Vol. 296, No. 5572, 2002, pp. 1445-1448.

[3] P.E. Clark, B. Malphrus, R. MacDowall, D. Folta, A. Mandell, C. Brambora, D. Patel, S. Banks, K. Hohman, V. Hruby, K. Brown, J. Kruth, R. Cox, "Lunar Ice Cube: Determining Volatile Systematics Via Lunar Orbiting Cubesat," *European Planetary Science Congress* Vol. 10, 2015.

[4] Mars Cube One (MarCO), Accessed June 2016: http://www.jpl.nasa.gov/cubesat/missions/marco.php

[5] D. Raghavan, T.J. Henry, B.D. Masion, J.P Subasavage, W. Jao, T.H. Beaulieu, N.C. Hambly, "Two Suns in the Sky: Stellar Multiplicity in Exoplanet Systems," *The Astrophysical Journal*, Vol. 646, 2006, pp. 523-542.

[6] S.E. Thorsett, Z. Arzoumanian, F. Camilo, A.G. Lyne, "The Triple Pulsar System PSR B1620-26 in M4," *The Astrophysical Journal*, Vol. 523, 1999, pp. 763-770.

[7] E. Fischbach, "Long-Range Forces and Neutrino Mass," *Annals of Physics*, Vol. 247, 1996, pp. 213-291.

[8] N. Bosanac, "Exploring the Influence of a Three-Body Interaction Added to the Gravitational Potential Function in the Circular Restricted Three-Body Problem: A Numerical Frequency Analysis," M.S. Thesis, School of Aeronautics and Astronautics, Purdue University, West Lafayette, Indiana, 2012.

[9] N. Bosanac, K.C. Howell, E. Fischbach, "Exploring the Impact of a Three-Body Interaction Added to the Gravitational Potential Function in the Restricted Three-Body Problem," *23rd AAS/AIAA Space Flight Mechanics Meeting*, February 2013, Hawaii.

[10] N. Bosanac, K.C. Howell, E. Fischbach, "A Natural Autonomous Force Added in the Restricted Problem and Explored Via Stability Analysis and Discrete Variational Mechanics," *AAS/AIAA Space Flight Mechanics Meeting*, Williamsburg, Virginia, January 2015.

[11] N. Bosanac, K.C. Howell, E. Fischbach, "Stability of Orbits Near Large Mass Ratio Binary Systems," *Celestial Mechanics and Dynamical Astronomy*, Vol. 122, Issue 1, 2015, pp. 27-52.

[12] D. Folta, N. Bosanac, A. Cox, K.C. Howell, "The Lunar IceCube Mission Design: Construction of Feasible Transfer Trajectories with a Constrained Departure," *AAS/AIAA Space Flight Mechanics Meeting*, Napa Valley, CA, February 2016.

[13] D. Folta, N. Bosanac, D. Guzzetti, K.C. Howell, "An Earth-Moon System Trajectory Design Reference Catalog," *Acta Astronautica*, Vol. 110, 2015, pp. 341-353.

[14] J. Barrow-Green, *Poincaré and the Three Body Problem, History of Mathematics Vol. 11.* American Mathematical Society, 1997.

[15] V. Szebehely, *Theory of Orbits: The Restricted Problem of Three Bodies.* London, UK: Academic Press, 1967.

[16] G. W. Hill, "Researches into the Lunar Theory," *American Journal of Mathematics*, Vol. 1, No. 1, 1878, pp. 5-26.

[17] J. H. Poincaré, *Les Méthodes Nouvelles de la Mécanique Céleste.* Vol. 1-3. Gauthier-Villars et fils, 1899.

[18] V.V. Markellos, "Numerical Investigation of the Planar Restricted Three-Body Problem," *Celestial Mechanics*, Vol. 9, No. 3, 1974, pp. 365-380.

[19] G. Contopoulos, *Order and Chaos in Dynamical Astronomy.* Germany: Springer-Verlag, 2002.

[20] M. Hénon, "Vertical Stability of Periodic Orbits in the Restricted Problem I. Equal Masses," *Astronomy and Astrophysics*, Vol. 28, 1973, pp. 415-426.

[21] M. Vaquero, and K.C. Howell,"Design of Transfer Trajectories Between Resonant Orbits in the Earth-Moon Restricted Problem," *Acta Astronautica*, Vol. 94, No. 1, 2014, pp. 302-317.

[22] A.D. Pinotsis, "Bifurcations, Stability and Universality of Families of Periodic Orbits in the Restricted Three-Body Problem," *Astronomy and Astrophysics*, Vol. 159, 1986, pp. 231-238.

[23] D. Guzzetti, N. Bosanac, D. Folta, and K.C. Howell, "A Framework for Efficient Trajectory Comparisons in the Earth-Moon Design Space," *25th AIAA/AAS Astrodynamics Specialist Conference*, San Diego, California, August 2014.

[24] M. Lara, R. Russell, and B. Villac, "Classification of the Distant Stability Regions at Europa," *Journal of Guidance, Control and Dynamics*, Vol. 30, No. 2, 2007, pp. 409-418.

[25] M. Lara, and R. Russell, "Concerning the Family "g" of the Restricted Three-Body Problem," *IX Jornadas de Trajabo en Mecánica Celeste*, Jaca, Huesca, Spain, June 2006.

[26] D. Benest, "Effects of the Mass Ratio on the Existence of Retrograde Satellites in the Circular Restricted Problem," *Astronomy and Astrophysics*, Vol. 32, 1974, pp. 39-46.

[27] D. Benest, "Effects of the Mass Ratio on the Existence of Retrograde Satellites in the Circular Restricted Problem: II," *Astronomy and Astrophysics*, Vol. 45, no. 2, 1975, pp. 353-363.

[28] D. Benest, "Effects of the Mass Ratio on the Existence of Retrograde Satellites in the Circular Restricted Problem: III," *Astronomy and Astrophysics*, Vol. 53, no. 2, 1976, pp. 231-236.

[29] D. Benest, "Effects of the Mass Ratio on the Existence of Retrograde Satellites in the Circular Restricted Problem: IV. Three-dimensional Stability of Plane Periodic Orbits," *Astronomy and Astrophysics*, Vol. 54, 1977, pp. 563-568.

[30] S. Ober-Blöbaum, O. Junge, J.E. Marsden, "Discrete Mechanics and Optimal Control: an Analysis," *ESAIM: Control, Optimisation and Calculus of Variations*, Vol. 17, 2011, pp. 322-352.

[31] J.E. Marsden, M. West, "Discrete Mechanics and Variational Integrators," *Acta Numerica*, Vol. 10, 2001, pp. 357-514.

[32] J.A. Cadzow, "Discrete Calculus of Variations," *International Journal of Control*, Vol. 11, 1970, pp. 393-407.

[33] O. Junge, J.E. Marsden, and S. Ober-Blöbaum, "Discrete Mechanics and Optimal Control," *Proceedings of the 16th IFAC World Congress*, Vol. 16, No. 1, 2005.

[34] A. Moore, "Discrete Mechanics and Optimal Control for Space Trajectory Design," Ph.D. Dissertation, California Institute of Technology, 2011.

[35] S. Ober-Blöbaum, "Discrete Mechanics and Optimal Control," Ph.D. Dissertation, University of Paderborn, Paderborn, Germany, 2008.

[36] S. Ober-Blöbaum, M. Ringkamp, and G. zum Felde "Solving Multiobjective Optimal Control Problems in Space Mission Design using Discrete Mechanics and Reference Point Techniques," *IEEE 51st Annual Conference on Decision and Control*, Maui, Hawaii, December 2012.

[37] M. Dellnitz, S. Ober-Blöbaum, M. Post, O. Schutze, and B. Thiere "A Multi-Objective Approach to the Design of Low Thrust Space Trajectories Using Optimal Control," *Celestial Mechanics and Dynamical Astronomy*, Vol. 105, No. 1-3, 2009, pp. 33-59.

[38] R. D. Mattuck, *A Guide to Feynman Diagrams in the Many-Body Problem: Second Edition*. New York: Dover Publications, Inc., 1976.

[39] S. Braibant, G. Giacomelli, M. Spurio, *Particles and Fundamental Interactions: An Introduction to Particle Physics*. Springer, 2012.

[40] P. Maris, J.P. Vary, P. Navratil, W. E. Ormand, H. Nam, D. J. Dean, "Origin of the Anomalous Long Lifetime of C^{14}", *Physical Review Letters*, Vol. 106, No. 20, 2011.

[41] W. S. Koon, M. W. Lo, J. E. Marsden, S. D. Ross, *Dynamical Systems, the Three Body Problem and Space Mission Design*, Springer-Verlag New York Incorporated, 2006.

[42] T.S. Parker, L.O Chua, *Practical Numerical Algorithms for Chaotic Systems*. New York: Springer-Verlag, 1989.

[43] L. Perko, *Differential Equations and Dynamical Systems*. Third Edition, New York: Springer, 2000.

[44] R. H. Abraham, C. D. Shaw, *Dynamics - The Geometry of Behavior. Part Two: Chaotic Behavior* Santa Cruz, CA: Fourth Edition, Aerial Press, 1990.

[45] R. Seydel, *Practical Bifurcation and Stability Analysis: From Equilibrium to Chaos*. New York: Springer-Verlag, 1994.

[46] E. Campbell, "Bifurcations from Families of Periodic Solutions in the Circular Restricted Problem with Application to Trajectory Design," Ph.D. Dissertation, School of Aeronautics and Astronautics, Purdue University, West Lafayette, Indiana, August 1999.

[47] W. Press, S. Teukolsky, W. Vetterling, B. Flannery, *Numerical Recipes: The Art of Scientific Computing, Third Edition*, New York: Cambridge University Press, 2007.

[48] B. Bradie, *A Friendly Introduction to Numerical Analysis*, Pearson Prentice Hall, 2006.

[49] A. Jorba, J. Villanueva, "Numerical Computation of Normal Forms around some Periodic Orbits of the Restricted Three Body Problem," *Physica D: Nonlinear Phenomena*, Vol. 114, No. 3, 1998, pp.197-229.

[50] G. Wawrzyniak, K.C. Howell, "Numerical Techniques for Generating and Refining Solar Sail Trajectories," *Advances in Space Research Special Issue: "Solar Sailing: Concepts, Technology, Missions"*, Vol. 48, 2011, pp. 1848-1857.

[51] D. Grebow, M. Ozimek, K.C. Howell, "Design of Optimal Low-Thrust Lunar Pole-Sitter Missions," *Journal of the Astronautical Sciences*, Vol. 58, No. 1, 2011, pp. 55-79.

[52] H. Keller, "Numerical Solutions of Bifurcations and Nonlinear Eigenvalue Problems," *Applications of Bifurcation Theory* (Edited by P.H. Rabinowitz), New York: Academic Press,1977, pp. 359-383.

[53] Z. Olikara and D. Scheeres. "Numerical Method for Computing Quasi-Periodic Orbits and their Stability in the Restricted Three-Body Problem," *Proceedings of the 1st IAA/AAS Conference on the Dynamics and Control of Space Systems*, Porto, Portugal, 2012.

[54] B.F. Villac, "Dynamics in the Hill Problem with Applications to Spacecraft Maneuvers," Ph.D. Dissertation, Aerospace Engineering, University of Michigan, Ann Arbor, Michigan, 2003.

[55] M. Paskowitz Possner, "Orbit Design and Control of Planetary Satellite Orbiters in the Hill 3-Body Problem," Ph.D. Dissertation, Aerospace Engineering, University of Michigan, Ann Arbor, Michigan, 2007.

[56] A. Haapala, "Trajectory Design Using Periapse Maps and Invariant Manifolds," MS Thesis, School of Aeronautics and Astronautics, Purdue University, West Lafayette, Indiana, December 2010.

[57] E. Fischbach, C.L. Talmadge, *The Search for Non-Newtonian Gravity*, New York: Springer-AIP, 1999.

[58] A. Kryszczynska, F. Colas, P. Descamps, P. Bartczak, M. Polinska, T. Kwiatkowski, J. Lecacheux, R. Hirsch, M. Fagas, K. Kaminski, T. Michalowski, A. Marciniak, "New binary asteroid 809 Lundia I. Photometry and modelling," *Astronomy and Astrophysics*, Vol. 501, No. 2, 2009, pp. 769-776.

[59] S. Sigurdsson, S. E. Thorsett, "Update on Pulsar B1620-26 in M4: Observations, Models, and Implications," *Binary Radio Pulsars, ASP Conference Series Proceedings*, Vol. 328, 2004, pp. 213-223.

[60] S. Sigurdsson, H. B. Richer, B. M. Hansen, I. H. Stairs, S. E. Thorsett, "A Young White Dwarf Companion to Pulsar B1620-26: Evidence for Early Planet Formation," *Science*, Vol. 301, No. 5630, 2003, pp. 193-196.

[61] A. Deprit, "Limiting Orbits Around the Equilateral Centers of Libration," *Astronomical Journal*, Vol. 71, No. 1337, 1966, pp. 77-87.

[62] M. Perryman, *The Exoplanet Handbook*. United Kingdom: Cambridge University Press, 2011.

[63] D.T. Greenwood, *Principles of Dynamics, Second Edition*, New Jersey: Prentice-Hall, 1988.

[64] C. Lanczos, *The Variational Principles of Mechanics*, Toronto: Courier Dover Publications, 2012.

[65] I. Stairs, "Binary Pulsars and Tests of General Relativity," *Proceedings of the International Astronomical Union*, Vol. 5, 2009, pp. 218-227.

[66] C.N. Douskos, "Effect of Three-Body Interaction on the Number and Location of Equilibrium Points of the Restricted Three-Body Problem," *Astrophysics and Space Science*, Vol. 356, 2015, pp. 251-268.

[67] Busek.com, "3cm RF Ion Thruster", Accessed January 2016: `http://www.busek.com/index_htm_files/70010819%20RevA%20Data%20Sheet%20for%20BIT-%3%20Ion%20Thruster.pdf`

[68] D. Folta, Private Communication, July 2015.

[69] D. Folta, Private Communication, November 2015.

[70] B.A. Conway, *Spacecraft Trajectory Optimization*, New York: Cambridge University Press, 2010.

[71] STK 10 Help, Accessed August 2015: `http://www.agi.com/resources/help/online/stk/10.1/index.html`

[72] W.M. Folkner, J.G. Williams, D.H. Boggs,"The Planetary and Lunar Ephemeris DE 421," *IPN Progress Report*, Vol. 42-178, 2009, pp. 1-34.

[73] SPICE Toolkit, Accessed May 2016: `https://naif.jpl.nasa.gov/naif/aboutspice.html`

[74] A. Haapala, "Trajectory Design in the Spatial Circular Restricted Three-Body Problem Exploiting Higher-Dimensional Poincaré Maps," PhD Dissertation, School of Aeronautics and Astronautics, Purdue University, West Lafayette, Indiana, December 2014.

[75] GNU Scientific Library, Accessed May 2016: `https://www.gnu.org/software/gsl/`

[76] T. A. Pavlak, "Trajectory Design and Orbit Maintenance Strategies in Multi-Body Dynamical Regims," Ph.D. Dissertation, School of Aeronautics and Astronautics, Purdue University, West Lafayette, Indiana, May 2013.

[77] C.D. Brown, *Spacecraft Mission Design, Second Edition*, Reston, VA: AIAA Education Series, 1998.

[78] D.A. Vallado, *Fundamentals of Astrodynamics and Application*, Microcosm Press and Kluwer Academic Publishers, 2001.

VITA

VITA

Natasha Bosanac received a Bachelor of Science in Aeronautics and Astronautics from the Massachusetts Institute of Technology in 2010. Natasha then moved to Purdue University to study multi-body gravitational environments with Professor Kathleen C. Howell. Here, Natasha received her Master of Science in Aeronautics and Astronautics in 2012. During her graduate career, Natasha has contributed to the construction of an orbit catalog module designing trajectories within the Earth-Moon system, currently incorporated into the Adaptive Trajectory Design software developed by Purdue University. In addition, Natasha has spent a summer working on-site at NASA Goddard Space Flight Center on the construction of a trajectory design framework for low-thrust enabled CubeSats under the guidance of David Folta. During this time, Natasha has also collaborated with Professor Ephraim Fischbach on exploring a many-body interaction in the context of orbital dynamics.